The Convergence of Parametric Resonance and Vibration Energy Harvesting

This dissertation is submitted for the degree of
***Doctor of Philosophy* in Engineering**

Yu Jia

Downing College

Nanoscience Centre, Centre for Smart Infrastructure and Construction

Department of Engineering, University of Cambridge

2014

The Convergence of Parametric Resonance and Vibration Energy Harvesting

Yu Jia

Declaration

This dissertation is solely the result of my own work and includes nothing which is the outcome of work done in collaboration except where specifically indicated in the text. This dissertation contains 118 figures, $\sim$ 44,000 words in the main text and $\sim$ 60,000 words in entirety.

Supervisor and advisor

Supervisor: Dr Ashwin A. Seshia
Advisor: Prof. Kenichi Soga

Examiners

Internal examiner: Prof. Arokia Nathan
External examiner: Dr. Paul Mitcheson

This dissertation is submitted for the degree of
Doctor of Philosophy in Engineering

Submitted: 28 November 2013
Viva voce: 29 January 2014
Final version approved: 5 February 2014

Downing College
Nanoscience Centre, Centre for Smart Infrastructure and Construction
Department of Engineering, University of Cambridge

Acknowledgements

Personal gratitude to

My kind and caring mother, Huiqing Lu, for her unwavering support in my studies; both emotionally and financially. She is everything for whom I am today.

My dear fiancée, Ying Miao, for her inspirational support during the hard and unfruitful times of my research as well as wholeheartedly sharing my joy during the successful times.

Sincere appreciation to

Dr Ashwin A. Seshia for his pivotal supervision, mentoring, guidance, support and regular critical review of the research; without whom, this research would have definitely taken many detours.

Prof. Kenichi Soga, for the initial admission into this research studies in Cambridge University and for his unreserved advice, support and constructive criticism. Also for Prof. Soga and team's vibration data measured from a Japanese railway bridge.

Dr Jize Yan for the continued mentorship and long fruitful discussions that were crucial for the realisation of the early parametric ideas explored in this research.

Dr Pradyumna Thiruvenkatanathan for all the help when I initially joined the Nanoscience Centre, initial help with learning the basics of COMSOL, organising the fabrication run, wire bonding of first generation MEMS devices and devising the in-house vacuum packaging technique.

Dr Xueyong Wei for the many fruitful discussions on early, although unused, MEMS designs and implementation.

Mr David Miller and Mr Gareth Ryder for helping to construct the electromagnetic experimental prototypes. The continued help on the experimental setup from Gareth was instrumental.

Mr Milkovic for consenting the employment of his two stage amplifier design that inspired the initial pendulum-lever prototype design.

Mr Alistair Ross and his team for assorted workshop help.

Mr Ian Ganney for helping to construct the experimental mounting apparatus for piezo-cantilever prototypes and xy-stage mounts for laser vibrometer.

Cambridge Centre for Smart Infrastructure and Construction (funded by EPSRC and TSB) for various project fundings.

Betty and Gordon Moore Library for purchasing the requested book: Parametric resonance in dynamical systems by T.I. Fossen and H. Nijmeijer (2012).

And last but definitely not the least, special thanks to all of my tutors, supervisors, lecturers, mentors and support staff at the University of Southampton for giving me a strong and unparalleled foundation; especially: Prof. Steve P. Beeby (my inspirational role model), Dr Paul H. Chappell, Prof. Alun S. Vaughan, Dr. M. John Tudor, Dr Dibin Zhu and Dr J. Neil Ross.

Abstract

Energy harvesting is an emerging technology that derives electricity from the ambient environment in a de-centralised and self-contained fashion. Applications include self-powered medical implants, wearable electronics and wireless sensors for structural health monitoring. Amongst the vast options of ambient sources, vibration energy harvesting (VEH) has attracted by far the most research attention. Two of the key persisting issues of VEH are the limited power density compared to conventional power supplies and confined operational frequency bandwidth in light of the random, broadband and fast-varying nature of real vibration.

The convention has relied on directly excited resonance to maximise the mechanical-to-electrical energy conversion efficiency. This thesis takes a fundamentally different approach by employing parametric resonance, which, unlike the former, its resonant amplitude growth does not saturate due to linear damping. Therefore, parametric resonance, when activated, has the potential to accumulate much more energy than direct resonance. The vibrational nonlinearities that are almost always associated with parametric resonance can offer a modest frequency widening.

Despite its promising theoretical potentials, there is an intrinsic damping dependent initiation threshold amplitude, which must be attained prior to its onset. The relatively low amplitude of real vibration and the unavoidable presence of electrical damping to extract the energy render the onset of parametric resonance practically elusive. Design approaches have been devised to passively minimise this initiation threshold.

Simulation and experimental results of various design iterations have demonstrated favourable results for parametric resonance as well as the various threshold-reduction mechanisms. For instance, one of the macro-scale electromagnetic prototypes ($\sim$1800 cm^3) when parametrically driven, has demonstrated around 50% increase in half power band and an order of magnitude higher peak power (171.5 mW at 0.57 ms^{-2}) in contrast to the same prototype directly driven at fundamental resonance (27.75 mW at 0.65 ms^{-2}). A MEMS (micro-electromechanical system) prototype with the additional threshold-reduction design needed 1 ms^{-2} excitation to activate parametric resonance while a comparable device without the threshold-reduction mechanism required in excess of 30 ms^{-2}. One of the macro-scale piezoelectric prototypes operated into auto-parametric resonance has demonstrated notable further reduction to the initiation threshold. A vacuum packaged MEMS prototype demonstrated broadening of the frequency bandwidth along with higher power peak (324 nW and 160 Hz) for the parametric regime compared to when operated in room pressure (166 nW and 80 Hz), unlike the higher but narrower direct resonant peak (60.9 nW and 11 Hz in vacuum and 20.8 nW and 40 Hz in room pressure).

The simultaneous incorporation of direct resonance and bi-stability have been investigated to realise multi-regime VEH. The potential to integrate parametric resonance in the electrical domains have also been numerically explored. The ultimate aim is not to replace direct resonance but rather for the various resonant phenomena to complement each other and together harness a larger region of the available power spectrum.

Contents

List of Figures

List of Tables

Abbreviations and Acronyms

MEMS	Micro-electro-mechanical system [16, 17, 18]
MOEMS	Micro-Opto-Electro-Mechanical System
NEMS	Nano-electro-mechanical system
VLSI	Very Large Scale Integration
HVAC	Heating, ventilation and air conditioning
WSN	Wireless sensor network
BAN	Body sensor network
EH	Energy harvesting
VEH	Vibration energy harvest.
PEVEH	Parametrically excited vibration energy harvest.
DPEVEH	Directly and parametrically excited vibration energy harvest.
EMF	Electromagnetic field
emf	Electromotive force
AC	Alternating current
DC	Direct current
DOF	Degree-of-freedom
LTCC	Low Temperature Co-Fired Ceramics
IC	Integrated circuit
PZT	Lead zirconate titanate
PVDF	Polyvinylidene fluoride
AlN	Aluminium nitride
ZnO	Zinc oxide
BeCu	Beryllium copper
NdFeB	Neodymium iron boron
RFID	Radio-frequency identification
RHS	Right hand side
LHS	Left hand side
FFT	Fast Fourier Transform
EPSRC	Engineering and Physical Sciences Research Council
TSB	Technology Strategy Board
IEEE	Institute of Electrical and Electronics Engineers
IET	Institution of Engineering and Technology
ASME	American Society of Mechanical Engineers
MIT	Massachusetts Institute of Technology

Symbols

P	Power
V	Voltage
Q	Electric charge
C	Capacitance
I	Current
R	Resistance
F	Force
A	Displacement amplitude
a	Acceleration amplitude
m	Mass
g	Acceleration due to gravity
θ	Angular displacement
ω	Angular frequency
ω_n	Angular natural frequency
f	Frequency
f_n	Natural frequency
Q_f	Quality factor
D_m	Mechanical parasitic damping
D_e	Electrical damping
c	Damping constant
ζ	Damping ratio
k	Stiffness constant
μ	Duffing coefficient
E	Young's modulus
I	Area moment of inertia
ν	Poisson's ratio

NB: Upon first appearance, each symbol will be introduced and defined in the context. Maximum effort has been made to avoid conflicting symbols throughout this dissertation. However, if conflicts still exist, local definition within the context overrides this list and other appearances. Some symbols such as ε and ρ reused several times (locally defined each time) due to the overlap of multiple mechanical and electrical disciplines within this research; and therefore, are not global symbols.

Units

E+xx	$\times 10^{xx}$
Hz	Hertz
kHz	Megahertz, 10^3 Hz
MHz	Megahertz, 10^6 Hz
rad	Radians
°	Degrees
s	Second
°C	Degree Celsius
K	Kelvin
kg	Kilogram
N	Newton
J	Joule
W	Watt
mW	Milliwatt, 10^{-3} W
μW	Microwatt, 10^{-6} W
nW	Nanowatt, 10^{-9} W
m	Metre
mm	Millimetre, 10^{-3} m
μm	Micrometre (Micron), 10^{-6} m
nm	Nanometre, 10^{-9} m
”	Inch
V	Volt
mV	Millivolt, 10^{-3} V
A	Ampere
Ω	Ohms
C	Coulomb
S	Siemens
H	Henry
F	Farad
Wb	Weber
T	Tesla
Pa	Pascal
atm	Standard atmosphere
Torr	Torr , 1/760 atm
mTorr	Millitorr, 10^{-3} Torr

Chapter 1

Introduction

1.1 Wireless

At the dawn of the wireless era, an ever increasing number of remote and mobile electronics have been deployed. This includes wireless sensor networks (WSN) that remotely monitor temperature, pressure, humidity and air quality in HVAC (heating, ventilation and air conditioning) systems; mass, strain, acceleration, displacement, tilt, fatigue and corrosion in civil infrastructures; structural health monitoring of critical transport systems such as lorries, rolling stocks, ferries, airplanes as well as rail tracks, bridges, tunnels and roads; traffic conditions to regulate traffic signals; implanted medical devices such as pacemakers or BAN (body area network); performance monitoring of athletes, conditions in water, oil and gas distribution systems and many more. These automation technologies are gradually becoming essential components of the modern world.
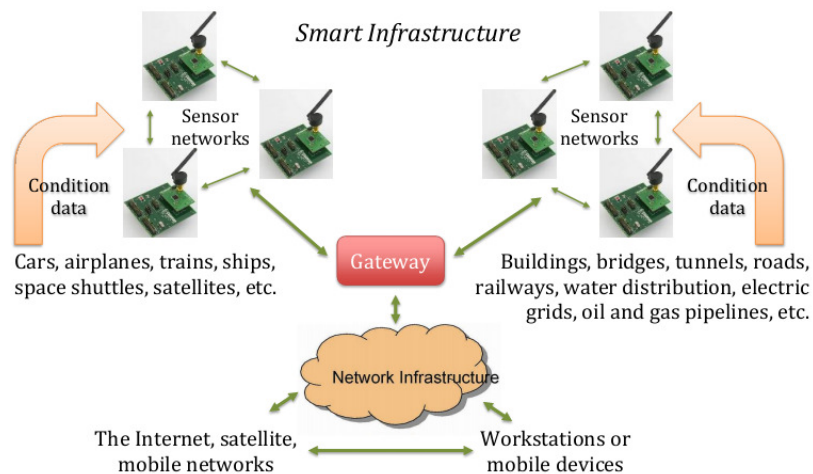
Figure 1.1: Smart infrastructure involves deploying wireless sensor networks to monitor, collect, make sense and coordinate critical information. Each mote requires batteries, which are impractical to maintenance.

Although these emerging technologies carry the 'wireless' tag in their names, their power supplies remain 'tethered'(either physically by cables or practically due to the need of periodic maintenance). Batteries are the most popular conventional option. However, they require regular replacements, which can be extremely costly (primarily skilled labour cost), tedious, environmentally unfriendly

and sometimes impractical to service; especially when dealing with vast infrastructures, embedded or buried systems and hazardous environments.

1.2 Energy harvesting

1.2.1 An emerging technology

A potential solution to complement battery technology is energy harvesting (also known as power harvesting or power scavenging). This is a technique of deriving useful electrical energy from ambient energy sources at the device-level. In contrast to the top down process of conventional power generation and distribution systems, the decentralised nature of energy harvesting provides a convenient onboard complement to batteries to prolong the lifetime of standalone micro-electronic systems.

In the past decade, energy harvesting has attracted an immense growth of interest from both the academia and the industry [9]. An evidential illustration of this can be seen from the publication search within ISI Web of Knowledge for titles with the term 'energy harvest*' that returned the result as shown in Figure 1.2.
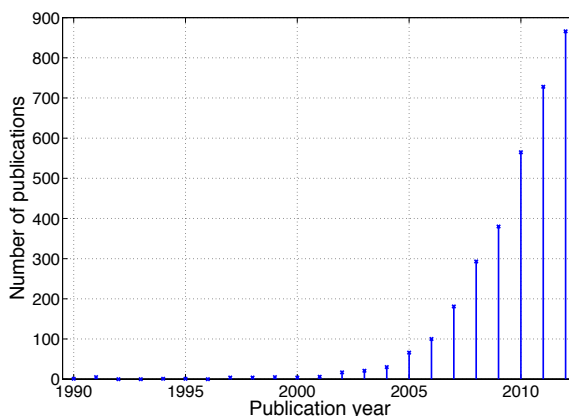
Figure 1.2: A few sparse energy harvesting publications existed in the 1980s and 1990s. Its academic emergence only took off from the early to mid 2000s.

Nonetheless, this technology is still far from perfect. The main challenges include insufficient energy densities to practically sustain the continuous operation of standalone devices as well as the specificity of the operational requirements in contrast to the random nature of real world ambient power sources. Although self powered wrist watches have been realised for decades [19], the practical and popular implementation of energy harvesting for more energy hungry devices, such as WSN, still require a technological leap forward [20].

Potential ambient power sources available for harvesting include solar, kinetic vibration, thermoelectric, fluidic flow, EMF (electromagnetic field), biochemical energy and many others (see Table 1.1). While solar energy has become a popular choice in the broader field of alternative energy and offers the most abundant energy density from the available selection, it is not always available or efficient for indoor and enclosed systems. Kinetic vibration and thermal energy on the other hand, are more practical options as many real world applications experience constant kinetic agitation and heat fluctuation [21], especially for civil infrastructural and transportation applications.

Table 1.1: Approximate power densities of various ambient energy sources; based on [9, 10, 11].

Energy source	Order of magnitude of potential power density
Solar (direct solar irradiation)	10's mW/cm^3
Solar (indoor illumination)	10's μW/cm^3
Mechanical vibration	100's μW/cm^3
Human motion	10's to 1,000's μW/cm^3
Temperature gradient (thermoelectric effect)	10's μW/cm^2
Temperature variation (pyroelectric effect)	1's μW/cm^2
Radio-frequency	100's nW/cm^3
Airflow or fluidic flow	100's μW/cm^3
Acoustic emission	100's nW/cm^3

1.2.2 Vibration energy harvesting (VEH)

This research looks at fundamentally novel techniques to tackle existing issues and enhance the potential performance of vibration energy harvesting for structural health monitoring applications. Vibration Energy Harvesting (VEH) is chosen as the core focus of this research due to the abundance of ambient vibrational sources in the context of civil infrastructures as well as the existing potential for further research explorations in terms of power density and frequency bandwidth enhancements.

The fundamental mode of directly excited resonance has become the unquestionable core physics of conventional resonant-based vibration energy harvesting [9]. However, it is far from being the sole or the best resonant phenomenon that can be exploited for mechanical amplification to maximise the mechanical-to-electrical energy conversion.

1.3 Parametric resonance for VEH

The work in this thesis employs an alternative candidate: parametric resonance, which instead of exhibiting a forced response, involves a time dependent modulation in at least one of the homogeneous system parameters at specific frequency and amplitude conditions. Once activated, unlike its direct resonant counterpart, the oscillatory amplitude growth of parametric resonance does not saturate due to linear damping and only settles with the rise of vibrational non-linearities at high amplitudes [8, 22]. The wider transducer community has dubbed this as the 'parametric amplification effect' employed to achieve higher input-to-output sensitivity than direct resonance [23, 24, 25, 26].

Figure 1.3 presents a basic demonstration using a simple pendulum to illustrate the difference between a system driven into resonance from direct excitation and the same system driven into parametric resonance through modulation of its system parameter (stiffness in this case). The theory behind this fundamentally distinct vibrational resonant phenomenon is explained in Chapter 3.

Alongside other alternative vibrational and resonant phenomena, such as bi-stability, implementation of these novel approaches at macro and MEMS (micro-electro-mechanical system) scales have been numerically and experimentally investigated to verify the feasibility for practical energy harvesting devices.
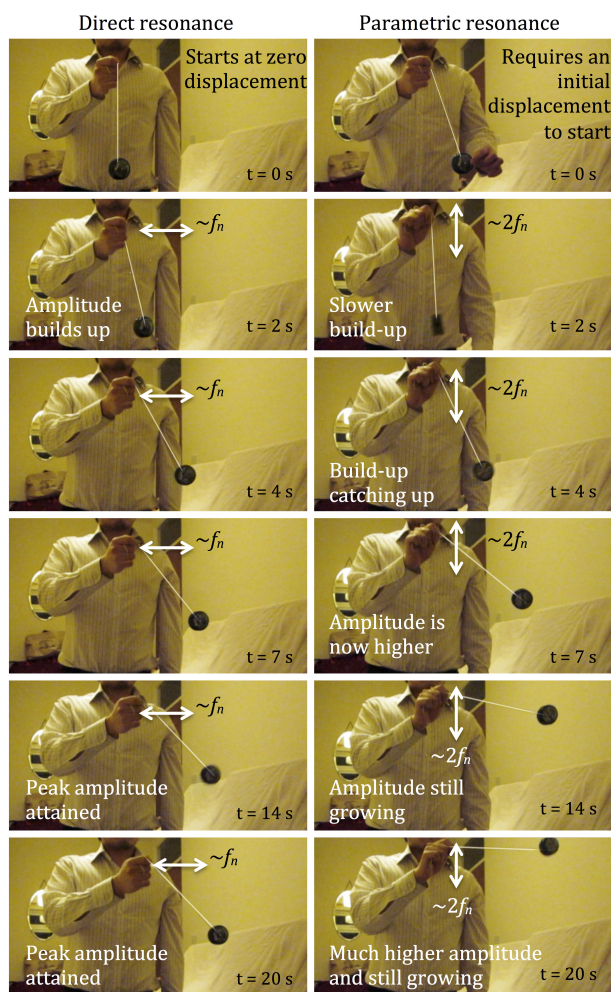
Figure 1.3: A demonstration of the difference between direct resonance (horizontal excitation at natural frequency f_n) and parametric resonance (vertical excitation at $2f_n$) using a simple pendulum (yoyo). The photos have been post-processed to improve the contrast of the yoyo string against the background. Each time-stamped frame shown here is when the pendulum attains its transient/steady-state oscillatory amplitude at the time. At first glance, vertical driving force at two times the natural frequency appears counter-intuitive, since it is, in a sense, driving 'in the wrong direction and at the wrong frequency' to achieve resonance; while in fact, a fundamentally different vibrational phenomenon: parametric resonance, is being activated, which allows the system to potentially attain a much larger amplitude for a comparable input amplitude.

1.4   Structure of the dissertation

The second and third chapters provide a review of the essential background on energy harvesting and basic principles of parametric resonance respectively. An attention to the specific applicability of parametric resonance for energy harvesting is explored in the later subsections of the third chapter. The consecutive two chapters cover macro-scale and MEMS investigations of pendulum-based and cantilever-based harvesters respectively, from both simulation and experimentation approaches. The sixth chapter looks at the correlation of bi-stability and parametric resonance as well as the integration of direct and parametric resonators to form a multi-resonant-regime harvester; the potential for utilising the advantages of parametric resonance in the electrical domain; as well as real vibration analysis of the established systems. The dissertation is then concluded with a discussion of possible future research directions and a summary of key findings.

Chapter 2

Background on vibration energy harvesting

This chapter covers the fundamental principles and provides a thematic review of the literature on the field of vibration energy harvesting (VEH). Some of the dedicated textbooks in the field include Priya and Inman (2009) [9], Erturk and Inman (2011) [27] and Kaźmierski and Beeby (2011) [28]. To be considered a practically feasible energy harvester (or an array of micro-scale harvesters) for the application context of the day, electrical power generated needs to be in the order of a milli-watt at device level in order to sustain some of the most efficient low power wireless sensor motes to date.

Kinetic vibration is observed almost everywhere; from railways to bridges, from rolling stocks to lorries, from industrial compressors to turbine engines and from walkways to human motions. The characteristics of kinetic vibration from human movements are generally defined by low frequency and (relatively) high displacement [29] while that of machinery are typically of (relatively) low displacement and high frequency [14, 20]. Certain sources are broadband such as passing traffic while others are less frequency-varying such as motors operating at a fixed speed. Therefore, VEH design is application specific.

In general, the conversion of mechanical power to electrical power of a mass-spring-damper system driven at resonance is summarised by Equation 2.1 [30].

$$P = \frac{ma^2\zeta_e}{4\zeta_T^2\omega_n} \tag{2.1}$$

where, P is the theoretical maximum electrical power from direct resonance after conversion, m is the seismic mass, a is the applied acceleration, ω_n is the angular natural frequency (equal to the angular excitation frequency at directly excited fundamental mode of resonance), ζ_e is the electrical damping ratio and ζ_T is the total damping ratio. Derivation is given in Equations 2.2 to 2.7.

$$P_{in} = Fv = mav \tag{2.2}$$
$$P_{in} = mA^2\omega_n^3 \tag{2.3}$$

where, P_{in} is the mechanical power based on mechanical forcing F, drive velocity v, drive displace-

ment amplitude A and excitation frequency at the natural frequency ω_n. The maximum mechanical power P_{out} accumulated by a resonator can be derived by adding quality factor Q_f to Equation 2.3, which acts as the mechanical amplification factor, in order to derive Equation 2.4 [31].

$$P_{out} = m(AQ_f)^2\omega_n^3 \tag{2.4}$$

$$P_{out} = \frac{mA^2\omega_n^3}{(2\zeta)^2} \tag{2.5}$$

where, ζ is the damping ratio ($\zeta = (2Q_f)^{-1}$). The effect of adding a transducer to convert this mechanical power into electrical power can be represented by introducing electrical damping ζ_e in addition to the purely mechanical parasitic damping ζ_m as shown in Equation 2.6.

$$P = \frac{mA^2\zeta_e\omega_n^3}{4(\zeta_e + \zeta_m)^2} \tag{2.6}$$

$$P = \frac{mA^2\zeta_e\omega_n^4}{4\zeta_T^2\omega_n} \tag{2.7}$$

Vibration energy harvesters can be broadly classified into resonant-based and non-resonant harvesters [32]. Resonant VEH relies on matching its natural frequency to the excitation frequency of the vibrational source. On the other hand, non-resonant VEH either employs zero restoring force or is designed to harvest impact or impulse forces [9].

VEH system typically consists of either one or more of the three major transduction mechanisms to convert mechanical kinetic energy into electrical energy [9], namely electromagnetic, piezoelectric and electrostatic (see Table 2.1). Although by far the most popular, this is not an exhaustive list and other alternative transduction mechanisms, such as magnetostriction [14], do exist. The following sections cover the major transduction mechanisms through a systematic review of their developments, challenges, shortcomings and remedial solutions thus far. Principles of kinetic vibration itself is further explored in Chapter 3.

Table 2.1: Comparing the theoretical maximum energy densities of the three major vibration transduction mechanisms (data and analysis based on [11, 12, 13, 14]).

	Electromagnetic	**Piezoelectric**	**Electrostatic**
Energy density	24.8 mJ cm^{-3}	35.4 mJ cm^{-3}	4 mJ cm^{-3}
Assumptions	0.25 T magnetic field	PZT 5H material	3E+07 Vm^{-1} electric field
Advantages	Well established technique. Easy to achieve high power densities at macro scales.	Simple and direct approach, highest potential, can be integrated with MEMS and IC.	Readily realisable with MEMS and are IC compatible, crucial for inexpensive realisation.
Shortcomings	Difficult to retain performance while scaling downwards to integrate with wafer-level systems.	Material is repeatedly strained. Lifetime and performance are limited by material selection.	Initial polarisation of the electrodes are required. Significantly lower power densities.

2.1 Electromagnetic

2.1.1 Introduction

Electromagnetic energy harvesting is based upon the long established principles of electromagnetism. Modern academia traces the roots of electromagnetic induction back to Michael Faraday [33] and Joseph Henry [34] in 1831. When an electrically conductive coil, connected to a closed looped circuit, cuts through the flux linkage lines of a magnet, electromotive force (emf) can be induced in the coil. The level of electricity being generated from such a transducer primarily depends on the strength of the magnetic flux density, the number of turns in the coil and the velocity of the relative motion between the magnet and the coil [14] as given by Equation 2.8.

$$\text{emf} = \frac{\mathrm{d}\Phi}{\mathrm{d}t} = N\frac{\mathrm{d}\phi}{\mathrm{d}t} \tag{2.8}$$

where, Φ is the total magnetic flux, N is the number of turns of the conductive coil assuming uniform wire diameter, ϕ is the magnetic flux per coil turn. Magnetic flux is measured in weber (Wb); where 1 Wbm^{-2} equates to 1 tesla (T), which is the unit for magnetic flux density B. Φ is given by Equation 2.9.

$$\Phi = NBS\sin\vartheta \tag{2.9}$$

$$\text{emf} = NS\frac{\mathrm{d}B}{\mathrm{d}t}\sin\vartheta \tag{2.10}$$

where, S is the surface area where the magnetic flux cuts through the coil and ϑ is the angle between the magnetic field lines and the normal to the coil surface area. For a given linear direction of magnetic against coil motion in the x-plane, emf can be expressed as Equation 2.11 [9].

$$\text{emf} = N\frac{\mathrm{d}\phi}{\mathrm{d}x}\frac{\mathrm{d}x}{\mathrm{d}t} \tag{2.11}$$

The instantaneous electrical power P_e extractable from the electromagnetic transducer can be calculated from the work done by time as given by Equation 2.12.

$$P_e = \frac{\mathrm{d}F_m(t)x(t)}{\mathrm{d}t} \tag{2.12}$$

where, F_m is the mechanical force required to overcome the Lorentz force. The work done by this force over x converts mechanical energy to electrical energy, dependent upon damping factors.

Traditionally, electromagnetic generators are of macro-scale and typically employed in power plants for top-down power generation and distribution systems. Device-level (few centimetres) or wafer-level (few millimetres or smaller) micro-generators are required for the scope of onboard ambient energy harvesting.

Established by Williams *et al.* [35], the following model is based on a second-order mass-damper-spring system with a linear damper and is suitable for electromagnetic transducer mechanism.

$$m\ddot{x}(t) + c\dot{x}(t) + kx(t) = -m\ddot{y}(t) \tag{2.13}$$

where, c is the damping constant, k is the spring constant and vibrational excitation $y(t) = Y\cos(\omega t)$, where Y is forcing displacement amplitude and ω is excitation frequency.

The total power dissipated in the damper assuming sinusoidal excitation:

$$P(\omega) = \frac{m\zeta Y^2(\frac{\omega}{\omega_n})^3\omega^3}{[1 - (\frac{\omega}{\omega_n})^2]^2 + [2\zeta(\frac{\omega}{\omega_n})]^2} \tag{2.14}$$

When a system operates at resonant frequency,

$$P_{max} = \frac{mY^2\omega_n^3}{4\zeta} \tag{2.15}$$

$$P_{max} = \frac{ma^2}{4\zeta\omega_n} \quad ; \text{where, } a = Y^2\omega_n^2 \tag{2.16}$$

Resonant (natural) frequency is given by,

$$\omega_n = \sqrt{k/m} \tag{2.17}$$

Damping ratio is given by,

$$\zeta = c/c_c = c/(2\sqrt{mk}) \tag{2.18}$$

where, c_c is the critical damping constant. The system is overdamped when $\zeta > 1$, underdamped when $\zeta < 1$ and critically damped when $\zeta = 1$.

Quality factor Q_f is the ratio of the periodic energy stored by the resonator and the energy dissipated. Quality factor Q_f is physically related to ζ by $Q_f = (2\zeta)^{-1}$; where $Q_f < 1/2$ corresponds to overdamped, $Q_f > 1/2$ is underdamped and $Q_f = 1/2$ is critically damped. Q_f can be experimentally measured from the ratio of the natural frequency and the half power bandwidth. Higher the Q_f, lower the energy loss and narrower the resonant frequency bandwidth. In other words, flatter curves also have lower peaks and vice versa. The ideal objective is to maximise both the peak and the frequency bandwidth.

In designing an electromagnetic transducer, the coil (number of turns and coil resistance) and magnets (positioning, strength and shape) are key factors. For instance, denser number of coil turns N and stronger magnetic flux density B lead to higher power density as seen previously from Equations 2.11 and 2.12. The ideal coil is one with minimum coil spacing fill factor while maximising number of turns. Parameters for a cylindrical coil is governed by Equations 2.19 to 2.22 [9].

$$V_{coil} = \pi(r_o^2 - r_i^2)t_{coil} \tag{2.19}$$

$$l_{wire} = \frac{4F_{coil}V_{coil}}{\pi D_{wire}^2} \tag{2.20}$$

$$R_{coil} = \rho_0\frac{l_{wire}}{A_{wire}} = \rho_0\frac{N^2\pi(r_o + r_i)}{F_{coil}(r_o - r_i)t_{coil}} \tag{2.21}$$

$$N = \frac{l_{wire}}{r_i + \frac{r_o - r_i}{2}} \tag{2.22}$$

where, V_{coil} is volume of the coil, A_{wire} is the cross-sectional area of the conducting coil wire, t_{coil} is the coil thickness, r_i is the coil inner radius, r_o is the coil outer radius, D_{wire} is the coil wire diameter, R_{coil} is the coil resistance, ρ_0 is the coil resistivity, N is the number of turns, F_{coil} is the coil spacing fill factor that can be used as a qualitative measure of coil turn density.

Key design considerations include the maximising of flux linkage gradient and matching the electrical damping to the mechanical damping. The later can be achieved through optimising the ensuing RLC circuit such as the load resistance. Maximum electrical power (at resonance) is when electrical damping D_e $(2m\zeta_e\omega_n)$ is equal to the total parasitic mechanical damping D_p and Equation 2.25 can be derived from Equation 2.6.

$$P_{maxelec} = \frac{ma^2\zeta_e}{4(\zeta_e + \zeta_e)^2\omega_n} \tag{2.23}$$

$$P_{maxelec} = \frac{ma^2}{16\zeta_e\omega_n} \tag{2.24}$$

$$P_{maxelec} = \frac{(ma)^2}{8D_e} \tag{2.25}$$

Electrical damping arising from electromagnetic transduction D_e is given by Equation 2.26 [14].

$$D_e = \frac{(Nl_{coil}B)^2}{R_{load} + R_{coil} + \mathrm{j}\omega L_{coil}} \tag{2.26}$$

where, l_{coil} is the length of the coil, L_{coil} is the inductance of the coil. The imaginary component of Equation 2.26 can be neglected for $f < 1$ kHz assuming circular coils for most cases.

2.1.2 Literature

One of the earliest electromagnetic self powered devices is the inertial generator that electrically winds a watch, by Seiko [36]. Studies on similar devices have reported power levels up to about 100 μW [20]. However, these mechanical devices are typically not compatible with integrated circuit (IC) technology and the power levels achievable are less than sufficient for more 'power hungry' devices such as wireless sensors.

One of the earliest documented study of micro-electromagnetic generators for harvesting ambient mechanical vibrations was reported by Williams *et al.* from the University of Sheffield in 1996 [35, 31, 37]. This early design employed a magnet attached to the centre of an elastic membrane hanging over a planar wafer-lever coil (see Figure 2.1). Their theoretical prediction placed the maximum power output from their device at the order of 1 mW while the actual tested device delivered a maximum power at the order of 0.3 μW. This serious discrepancy has been blamed on the non-linear effect of the spring with rising excitation amplitude. However, the nonlinear characteristics were not explored to verify the proposed explanation.

In 2008, a group [38] published results of a magnet on a diaphragm structure similar to that of Williams *et al.*. However, this device has planar coils integrated on micro-cantilevers at a lower level structure. A number of these micro-cantilevers surround the suspended magnet. Therefore, instead of being static, coils also oscillate along with the magnet during vibration; hence achieving dual resonant characteristics from the device. Theoretical estimates predicted around 25 μW peak
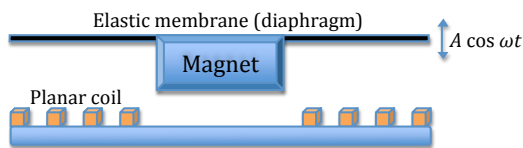
Figure 2.1: A generic electromagnetic micro-generator design: magnet on diaphragm displaces against coil.

power output while early prototypes only demonstrated a few nano-watts [39]. An optimised device reported in 2010 [40] also failed to demonstrate significant improvement in performance. Although this later design only marginally outperformed the Sheffield device in terms of power density, the dual resonant feature offered broader operational frequency bands.

A few other application-based design [41] and material fabrication [42] studies based on the similar working principle of planar coil and magnet on membrane structures have been investigated. However, the reported maximum power per device (wafer-level size) still lingered around a few hundred nano-watts to about one micro-watt. An optimised device of this working mechanism reported by Serre *et al.* in 2008 [43] was capable of producing a maximum of 55 μW. However, the power density is still significantly lower than the larger and non-IC compatible device level harvesters.

The main limiting factor for these micro-harvesters are directly dependent on the number of coil turns within the given volume. This implies that IC compatible planar coils are not the ideal option as only a few number of turns can be fitted onto the silicon wafer. Therefore, this limitation rapidly reduces the power efficiency of electromagnetic transducers when scaled down to wafer-level sizes.

Scherrer *et al.* from Boise State University [44] reported the possible employment of Low Temperature Co-Fired Ceramics (LTCC) technique to fabricate compact and multiple layered coils. Although they numerically predicted 7 mW from their micro-generator, no experimental verification (to the best of author's knowledge) had taken place. Wang *et al.* reported in 2009 [45] a device fabricated using MEMS technology. Although further miniaturisation was achieved, the planar coil design still highlighted the difficulties in scaling downwards.

A research group from the Chinese University of Hong Kong [46, 47] attempted to increase coil turns density by laser micro-machining. However, this did not experimentally yield any significant advancements in performance. On the other hand, micro-machining attempts by Lumedyne Technologies and Space and Naval Warfare Systems Center in San Diego [48, 49] produced relatively more motivating results in the order of several milli-watts for a coin sized device-level prototype.

Georgia Institute of Technology and University of Florida demonstrated in 2012 [50] various methods of producing micro-magnets using laser micro-machining techniques as well as thermo-magnetically patterned and sputtered Neodymium Iron Boron (NdFeB) magnetic films. A 2013 publication from Peking University [51] demonstrated promising results from a MEMS deposited array of permanent micro-magnets in an attempt to maximise the magnetic flux across the entire surface area of the wafer in contrast to a single large planar magnet that would otherwise concentrate the flux around its far edges.

A less than fruitful (in terms of absolute power level) investigation of cantilever-based electromagnetic micro-generators was reported by Mizuno and Chetwynd in 2003 [52]. Their design consisted of a coil integrated cantilever beam that oscillated in relation to a fixed permanent magnet (see Figure 2.2). The peak observed power values from both the theoretical model and experimental model were in the order of few nano-watts.

Figure 2.2: A generic electromagnetic micro-generator design: coil on cantilever beam displacing against externally fixed magnet.

However, several other cantilever design iterations that employed the magnet as the cantilever seismic mass (see Figure 2.3) reported significantly better results, especially those from the University of Southampton [53, 54, 55] and their spin-off company Perpetuum [56] that combined tungsten mass as the proof mass in addition to the already high deflection yielding magnetic mass.
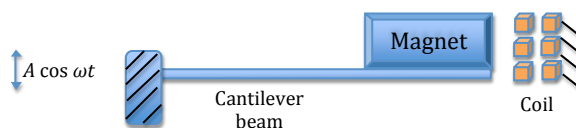
Figure 2.3: A generic electromagnetic micro-generator design: magnet as seismic mass on cantilever beam displacing against externally fixed coil.

A joint research effort by the University of Southampton and the Irish-based National Micro-electronics Research Centre [57] reported the integration of wound coils, rather than deposited coils, with a silicon device through micro-machining and assembling techniques. This attempt to overcome the planar coil limitation still yielded little advancement in power density, due to other downward scaling issues such as the rising dominance of air drag.

Various iterations of both micro (few millimetres in dimensions) [53, 54] and relatively macro (few centimetres in dimensions) [57, 58, 59] harvesters developed in Southampton employed orthocyclic coil winding techniques, which places maximum number of turns in the most compact arrangement (layer by layer): minimum coil spacing fill factor; as well as a magnet-coil-magnet arrangement where two attracting magnets are mechanically fixed apart to sandwich a coil in the middle with minimal air gap. This magnet-coil configuration allows the concentration of flux lines though the coil, which would otherwise be concentrated on the surface of the magnets and flux density rapidly decrease when moved further away from the surface.

Between 2011 and 2012, Zhu *et al.* from Southampton [60, 61, 62] published investigations of a Halbach array permanent magnet arrangement (consisting of opposing magnets mechanically forced together) to maximise the concentration of magnetic flux in a specific desired region (on the sides) by mechanically fixing an array of opposing magnets together. Simulations and experimental results have shown improvements in flux density and power output in the order of several 10's % over a single magnet configuration. Such an arrangement produces islands of concentrated flux regions but also voids several regions from magnetic flux within the array, which the coil could encompass as well. Therefore, non-trivial careful placement is required.

The miniaturisation of the traditional rotational electromagnetic generators dates back to the 1990s [32]. However, the use of rotational generators as a means of vibration energy harvester is rather recent. A few selected reports of rotational electromagnetic vibration energy harvesters include those from research groups in Imperial College London [63, 64], commercial manufacturer Kinetron [65] and MIT (Massachusetts Institute of Technology) [66]. The advantages of rotary generators are their low friction bearings, compact size and minimal air gap between coil and magnet. Therefore, it allows the maximisation of electromagnetic transducer efficiency in terms of energy conversion.

However, below a certain level of rotational velocity, the efficiency is rather limited as the system needs to first overcome the rotational inertia.

The Imperial and Kinetron devices employ eccentric loads similar to the long established self powered inertial generators developed by Seiko watches [36] in order to harvest power from irregular and intermittent human movements. Whereas, the MIT device reported in 2010 [66] employs the exact working principle of a traditional rotor and stator; but simply miniaturised. Although the MIT device reports significantly higher power density over the current state-of-the-art, the practicality of their device to harness real world vibration is yet to be demonstrated; and the generator is, at its core, a generating motor driven by a second actuating motor rather than kinetic vibration. Therefore, despite their claims, the MIT rotary generator does not strictly fall into the classification of vibration energy harvester in this dissertation. Practically, the effective conversion of linear motion into rotary motion is required in order to feasibly implement rotary generators for VEH.

Explored non-resonant harvesters include examples of rolling ball magnets around a coil cage [67] as well as rolling cylindrical magnet [68, 69] and eccentric pendulum magnet magnetically plucking transducer beams [70] through the use of either attached permanent magnet proof mass or magnetic shape memory alloy [71]. While these approaches are independent of frequency, they generally lack the high quality factor achievable in resonant approaches in terms of the mechanical amplification.

A summary of a few selected state-of-the-art resonant-based electromagnetic harvesters are presented in Table 2.2. A graphical representation of normalised power (power per squared of acceleration) versus volume is shown in Figure 2.4. As a device is scaled down, the power it can generate also decreases. The aim is to achieve the highest power density; that is, nearer to the upper left corner of the graph. The arbitrary straight line-of-best-fit shows how most devices have performed with various scaling factors. Any significant jump above this straight line demonstrates a notable improvement in the power density and hence the feasibility.

Table 2.2: Selected state-of-the-art electromagnetic vibration harvesters from the literature, listed in descending order of index (power density per squared of acceleration). Reported harvesters with insufficient acceleration or volume data are not presented in order to achieve fair comparison.

Reference	Year	Power (μW)	Acceleration (ms^{-2})	Frequency (Hz)	Volume (cm^3)	Index (μWcm^{-3}m^{-2}s^4)
Beeby *et al.* [58]	2007	4.60E+01	5.90E-01	52	1.50E-01	8.81E+02
Pepertuum [56]	2008	1.00E+03	2.50E-01	100	1.35E+02	1.19E+02
Lumedyne Tech. [49]	2008	1.00E+03	1.00E+00	53	2.70E+01	3.70E+01
Ferro Solutions [72]	2009	5.27E+03	9.80E-01	60	1.70E+02	3.23E+01
Zhu *et al.* [73]	2010	1.57E+02	5.90E-01	98	5.00E+01	9.00E+00
Hadas *et al.* [74]	2007	3.50E+03	3.10E+00	34.5	4.50E+01	8.09E+00
Waters *et al.* [48]	2008	1.80E+04	9.83E+00	90	2.70E+01	6.90E+00
Glynne-Jones *et al.* [2]	2001	2.80E+03	1.30E+01	106	3.66E+00	4.53E+00
Wang *et al.* [45]	2009	7.00E-01	4.94E+00	94.5	1.30E-01	2.21E-01
El-hami *et al.* [53]	2001	5.30E+02	1.02E+02	322	2.40E-01	2.12E-01
Huang *et al.* [41]	2003	1.40E+00	1.97E+01	100	3.00E-02	1.20E-01
Ching *et al.* [47]	2002	8.30E+02	9.55E+01	110	1.00E+00	9.10E-02
Li *et al.* [51]	2013	1.50E-02	1.18E+01	48	2.72E-03	3.98E-02
Li *et al.* [46]	2000	1.00E+01	1.62E+01	64	1.00E+00	3.83E-02
Beeby *et al.* [57]	2005	2.10E-02	1.92E+00	9500	3.00E-01	1.90E-02
Liu *et al.* [75]	2012	1.60E-02	9.81E+00	1400	3.60E-02	4.62E-03
Rodriguez *et al.* [42]	2005	1.44E+00	6.30E+01	400	2.50E-01	1.45E-03
Ju *et al.* [69]	2013	5.30E-01	2.94E+01	19	1.82E+00	3.37E-04
Shearwood *et al.* [76]	1997	3.00E-01	3.82E+02	4400	2.50E-02	8.22E-05
Zhang *et al.* [77]	2011	2.00E-06	4.83E+01	350	7.80E-02	1.10E-08
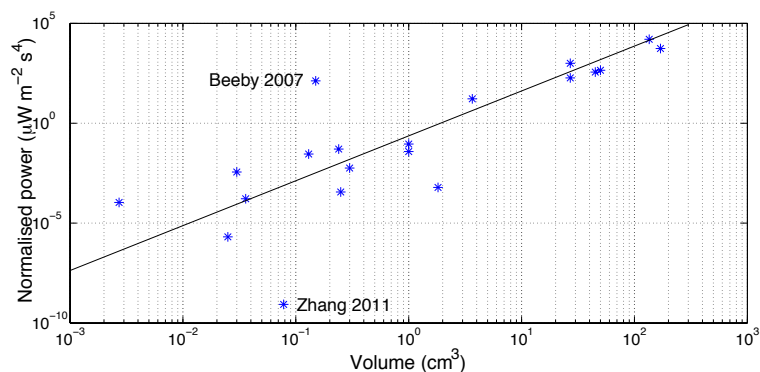
Figure 2.4: Normalised power versus volume of selected state-of-the-art resonant-based electromagnetic harvesters from the literature. The arbitrary line of best fit represents the current trend in technology. Any notable jumps above this line suggests a significant leap forward in performance.

A note on the figure of merit employed

The employed index (power)/(volume $\times$ acceleration^2) for comparison is a popular metric employed in the literature [9], however, it is not without its flaws [20] and other figures of merit do exist, such as normalising this index by frequency. However, within the context of this dissertation, this popular index is employed, along with excitation frequency information in the comparison table.

2.1.3   Summary

The principles of electromagnetic generators are well established and relatively straight forward to implement. Its commercial realisations already exist, such as devices from Seiko, Kinetron, Perpetuum, Ferro Solutions and Lumedyne. Throughout the academia, both impact-based, rotational and oscillatory electromagnetic generators have been employed to convert kinetic energy into electrical energy. While impact-based and rotational have been better implemented for harnessing human movements, their oscillatory counterparts are more feasible for scavenging ambient mechanical vibrations.

A major limitation with the electromagnetic option is the rapid fall in efficiency when scaled downwards in size. This is primarily due to the current limitation in fabrication technology to manufacture compact multi-layered coils with integrated circuit technology at wafer-level. On the other hand, device-lever miniaturised harvesters, although not readily compatible with IC for onboard VLSI, performs significantly better for practical implementation. Although the current state-of-the-art can marginally meet the power requirement of low power wireless sensors, this is further dependent on the maximum performance of the harvester under strict excitation frequency and amplitude conditions.

2.2   Piezoelectric

2.2.1   Introduction

One of the most popular transduction mechanisms for VEH, especially in recent years [27], is piezoelectricity, which is the intrinsic phenomenon of certain materials that can directly convert

stress-induced mechanical alterations (such as tension, compression and volumetric strain) of its physical structure into electrical charges. Therefore, unlike its electromagnetic and electrostatic counterparts that aim to maximise displacement, piezoelectric generators rely on maximisation of applied strain.

The earliest documented report of the piezoelectric effect was by Jacques Curie and Pierre curie in 1880 when they observed an electrical polarisation of certain crystalline minerals upon the application of mechanical forces [78, 79]. In the following year, Gabriel Jonas Lippmann mathematically deduced the converse relationship of this phenomenon while the Curie brothers experimentally verified the inverse piezoelectric effect.

Piezoelectric materials have symmetrically distributed and aligned electric dipole domains. Therefore, it has a net electrical neutrality. Under the application of mechanical force, this symmetry is disrupted and an internal dielectric displacement occurs; hence manifesting as either an internal electric polarisation or an external electric charge.

Apart from the naturally occurring piezoelectric minerals, piezoelectric materials can be produced by heating certain ceramics to a critical temperature known as the Curie point and inducing a direct current (DC) electric field to polarise and align the dipolar domains. After cooling, this polarisation will remain permanent even after the removal of the electric field. However, this also implies the operational temperature of piezoelectric materials are generally well below their Curie points.

Therefore, the piezoelectric effect, which is essentially the ability of a material to generate electrical charges under compression or tension, can be employed either in sensing applications such as accelerometers or in generating applications such as fuel-igniting devices. On the other hand, the inverse piezoelectric effect, which is the ability of a material to lengthen or shorten when exposed to an electric field, can be utilised in actuation applications such as motors. Within the context of harvesting energy from kinetic vibration, it is the forward piezoelectric effect that is of interest.

Equation 2.27 summarises the model constructed by Erturk *et al.* [80] for piezoelectric vibration energy harvesters based on a uni-morph (single layer of piezo-ceramics) cantilever structure.

$$
EI\frac{\partial^4 w_{rel}(x,t)}{\partial x^4} + c_s I\frac{\partial^5 w_{rel}(x,t)}{\partial x^4 \partial t} + c_a\frac{\partial w_{rel}(x,t)}{\partial t} + m\frac{\partial^2 w_{rel}(x,t)}{\partial t^2} + kv(t) \times \left[\frac{\mathrm{d}\delta(x)}{\mathrm{d}x} - \frac{\mathrm{d}\delta(x-L)}{\mathrm{d}x}\right]
$$
$$
= -\left[m + M\delta(x-L)\right]\frac{\partial^2 w_b(x,t)}{\partial t^2} \tag{2.27}
$$

where, E is the Young's modulus, I is the area moment of inertia, EI is the bending stiffness, $w_{rel}(x,t)$ is the transverse displacement response of the beam relative to the vibrating base, $w_b(x,t)$ is the effective displacement of the vibrating base, m is the mass per unit length, M is the seismic mass, $c_s I$ is the internal strain rate damping, c_a is the external viscous damping, $v(t)$ is the voltage response across the load resistance, k is the piezoelectric coupling and $\delta(x)$ is the Dirac delta function. The piezoelectric coupling coefficient, also known as the electro-mechanical coupling coefficient, k, relates to the conversion efficiency from mechanical energy E_m to electrical electrical energy E_e by the relationship: $k = \sqrt{E_e/E_m}$ [81].

Completing the circuit of the piezo-generator with a load resistance, the circuit equation can be

derived as shown in Equation 2.28.

$$\frac{\varepsilon_{33}bL}{h_p} \times \frac{\mathrm{d}v(t)}{\mathrm{d}t} + \frac{v(t)}{R_l} = -\int_{x=0}^{L} d_{31}h_{px}b\frac{\partial^3 w_{rel}(x,t)}{\partial x^2 \partial t}\mathrm{d}x \tag{2.28}$$

where, d_{31} is the piezoelectric charge constant, ε_{33} is the permittivity of the piezo-ceramic, b is the electrode width, L is the electrode length, h_p is the piezo-ceramic layer thickness, R_l is the load resistance and h_{pc} is the distance between the neutral axis and the centre of the piezo-ceramic layer.
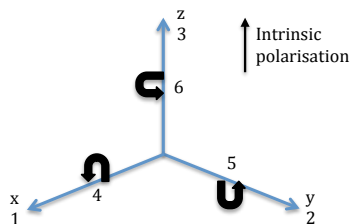
Figure 2.5: Direction of forces concerned with a piezoelectric element. Direction 3 is parallel to the direction of intrinsic polarisation.

The piezoelectric charge constant, also known as piezoelectric strain constant, d, is defined by either Equations 2.29 or 2.30.

$$d = \frac{\text{short circuit charge density}}{\text{applied mechanical stress}}; \quad \text{C N}^{-1}, \text{ forward piezoelectric effect} \tag{2.29}$$

$$d = \frac{\text{strain created}}{\text{applied electric field}}; \quad \text{m V}^{-1}, \text{ inverse piezoelectric effect} \tag{2.30}$$

The directions i and j of induced polarisation and applied stress respectively as shown in Figure 2.5 are denoted by subscripts for parameter d_{ij}. The most common modes adapted in piezoelectric VEH is shown in the list below (only forward piezoelectric effect is considered here for clarity purpose).

- d_{33}: induced polarisation in direction 3 per unit stress applied in direction 3.
- d_{31}: induced polarisation in direction 3 per unit stress applied in direction 1.
- d_{15}: induced polarisation in direction 1 per unit shear stress applied about direction 5.

Typically, d_{33} mode generates relatively more energy than d_{31} and others. However, d_{33} mode is harder to design. For instance, in order to harvest using the d_{33} mode when a thin piezo-layer is compressed, electrodes need to be fitted on either ends of the piezo-layer. The small cross-sectional area of the material between the electrodes implies maximisation of electrical resistance, which would compromise the recoverable electrical energy.

By sandwiching the piezo-material between two layers of electrodes, d_{31} mode can be achieved. Due to its significantly lower series resistance over the above mentioned d_{33} design, this arrangement yields higher levels of useful electrical energy; unless d_{33} mode is specifically designed to maximise performance.

While d_{ij} concerns with charge and polarisation, the piezoelectric voltage constant g_{ij} represents the electric field generated per unit of mechanical stress applied (V m N^{-1}). This constant also

adopts the directional mode subscripts explained above. Parameters k_{ij}, d_{ij} and g_{ij} are crucial terms concerned with the sensitivity of sensing and efficiency of generation applications.

Apart from modal direction, material selection is also an essential element during the design. Lead zirconate titanate PZT generally fares better in terms of typical d values than barium titanate BaTiO$_3$, polyvinylidene fluoride PVDF, aluminum nitride AlN and zinc oxide ZnO [14, 81, 82]. While softer and more elastic piezo-ceramics such as PZT-5H would generally have higher d values than harder materials such as PZT-5A [78, 79]. The efficiency of piezo-materials is also temperature sensitive. Beyond the Curie point for the specific material, the intrinsic polarisation would be lost.

Returning to the Erturk model [80], the steady state coupled voltage response under a harmonic driving excitation is given as [9],

$$v(t) = \frac{\sum_{r=1}^{\infty} \frac{\mathrm{j}\omega\varphi_r F}{\omega_n^2 - \omega^2 + \mathrm{j}2\zeta_r\omega_n\omega}}{\frac{1}{R_l} + \mathrm{j}\omega C_{piezo} + \sum_{r=1}^{\infty} \frac{\mathrm{j}\omega\varphi_r\chi_r}{\omega_n^2 - \omega^2 + j2\zeta_r\omega_n\omega}} \mathrm{e}^{\mathrm{j}\omega t} \tag{2.31}$$

where, ω is the excitation frequency, ω_n is the undamped natural frequency, F is the mechanical force applied in the desired modal direction, subscript $_r$ denotes the mode number, j is the unit imaginary number, e is the Euler's number, C_{piezo} is the piezo-ceramic's internal capacitance (defined in Equation 2.32), φ_r is the forward modal coupling term, χ_r is the backward modal coupling term, ζ_r is the mechanical modal damping ratio and $v(t)$ is the peak steady state voltage.

$$C_{piezo} = \frac{\varepsilon_{33} bL}{h_p} \tag{2.32}$$

Instantaneous peak power P across a load resistance R can be represented by the relationship $P = |v(t)|^2/R$. The room mean square voltage and average power are then given by $v_{rms} = |v(t)|/\sqrt{2}$ and $P_{average} = |v(t)|^2/2R$ respectively.

When operating in the vicinity of the fundamental mode of direct resonance where $\omega \approx \omega_n$, Equation 2.31 can be further simplified and combined with the power expression to give the steady state peak power response shown in Equation 2.33 [9].

$$|P(t)| = \frac{R(\omega\varphi_r F)^2}{[\omega_n^2 - \omega^2(1 + 2\zeta_r\omega_n RC_{piezo})]^2 + [2\zeta_r\omega_n\omega + \omega R[C_{piezo}(\omega_n^2 - \omega^2) + \varphi_r\chi_r]]^2} \tag{2.33}$$

2.2.2 Literature

One of the earliest studies on using piezoelectric material to generate useful electrical energy from kinetic energy was by Umeda *et al.* in 1996 [83]. Impact analysis of dropping steel balls onto a piezoelectric transducer was carried out to investigate the feasibility of this mechanism. Power conversion efficiency analysis of PZT showed an experimental value of 9.4% (most of the energy lost from bounce after initial impact) and simulated value of around 50% assuming inelastic collision and 'typical' electromechanical coupling and loss factors. The following year, Umeda *et al.* [84] reported a maximum of 35% conversion efficiency from the PZT upon connecting to a bridge rectifier and a storage capacitor.

Using a similar steel ball dropping test, Cavallier *et al.* [85] reported in 2005 the design incorporation of various shock-absorbing mechanical structures to capture maximum energy from impact.

Although no conversion efficiency analysis was undertaken, they qualitatively demonstrated a several folds increase in absolute power output over a comparable basic PZT structure. However, impact stressing of piezoelectric material is inefficient in practice due to the inevitability of elastic collisions and rapid fatiguing of the brittle nature of the material. On the other hand, compressive loading through cyclic application of stresses appeared to produce higher energy levels [86].

In terms of material selection, PZT and PVDF have been popular choices for macro-scale devices. PZT has been shown to experimentally confirm the higher power performance over PVDF [1, 87]. Therefore, PZT has been the material of choice by many studies [88, 89, 90, 91]. Additionally, study carried out by Funasaka *et al.* [92] reported a marginally higher efficiency from lithium niobate $LiNbO_3$ over PZT following a theoretical analysis. However, the values reported by these authors appeared relatively optimistic in contrast with other studies in the literature. In the past few years, lead magnesium niobate - lead titanate PMT-PT and lead zinc niobate titanate PZN-PT [82, 93] as well as the lead free potassium sodium niobate KNN [94] have also been demonstrated as alternatives with comparable efficiencies compared with the popular PZT.

Despite the significantly lower piezoelectric charge constant compared to PZT and the above mentioned alternatives, AlN has been a popular choice in integration with MEMS VEH and has shown by some studies [95, 96, 97, 98] to produce similar order of magnitude of 1's μW power output at wafer device levels while other studies [99, 100, 91] have demonstrated the superior conversion efficiency of PZT as well. These varied results are due to the far-from-perfected PZT MEMS fabrication technology thus far.

While progress have been made to fabricate MEMS PZT from PZT powder [101, 102], the process is yet to be perfected and the quality of the produced PZT has yet to demonstrate itself to the standard of its bulk counterpart. Therefore, despite the promising piezoelectric constant of PZT, AlN has still been pursued by many research groups at MEMS level [103, 104, 105, 106] due to the current non-trivial MEMS fabrication challenges of PZT MEMS [82, 93] and the presence of toxic lead [94] in PZT and other lead based piezoelectric materials.

In recent years, a few research groups from Japan [94, 107] have demonstrated KNN as a feasible candidate for MEMS piezoelectric VEH. Although the current experimental power performance of KNN operates at same order of magnitude as AlN, its power potential and piezoelectric charge constant is closer to that of PZT [108, 109]. Another group from Japan [110] demonstrated the development of a continuous fabrication process for an entirely polymer-based piezoelectric film (PVDF based) at MEMS level.

University of Michigan [100] realised PZT on SOI (silicon on insulator) through bonding of a thinned bulk PZT layer on an SOI wafer. Although the attaching of the bulk material adds complexity to the fabrication process, the performance of bulk PZT has been demonstrated by the Michigan device to be significantly higher than sol-gel PZT. In the meantime, University of Southampton has demonstrated screen printing of PZT from PZT pastes as an alternative over MEMS deposition or sol-gel techniques to more readily realise its higher conversion efficiency for micro piezoelectric VEH [111, 112] such as a credit card sized self-powered sensor node with RF transmitter [90]. While stacking of multiple layers were generally thought to maximise power, the Southampton group also observed optimal power density and conversion efficiency from dual screen printed layers of piezo-material. Further layer additions were deemed unworthy due to the diminishing returns. An explanation for this behaviour is the uneven distribution of strain from odd number of layers, relatively neutral principal axis strain towards the centre and losses in efficiency from

additional bonding layers.

Piezoelectric generators have been a popular choice for harvesting energy from human motions [20]. It is theoretically predicted that piezoelectric generators can harness a maximum of 1.27 W [81] from an average human gait energy generation of 67 W [29]. However, harvesting more energy from the human host induces higher parasitic effect. Parallels can be drawn to walking on sand or snow for such parasitic effects induced from electrical damping. Since the extra fatiguing load is generally undesirable, an optimum balance between maximum power output and user comfort is required while harvesting energy from human motions [113].

Human gaits with shoe-mounted harvesters [1, 87, 114] and motions from backpacks [115] have been investigated as possible sources. An early MIT design [1] that popularised [116] the concept of piezoelectric shoes employed multilayered PVDF foil (Figure 2.6) at the base of shoes to generate power for an active RFID. Other design approaches include compressive uni-morph [117, 80] or bi-morph [87, 118] structures. Uni-morph performs better for lower frequencies and load resistances while bi-morph (connected in series) performs better for higher frequencies and load resistances [119].
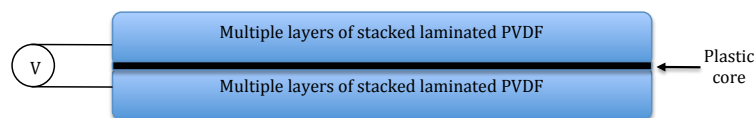
Figure 2.6: Stacked multi-layered piezo-transducer based on the MIT shoe-mounted harvester [1].

Some uni-morph or bi-morph structures [117, 87] employed Thunder piezoelectric transducers by Face International Corporation [120], which was originally developed by NASA (National Aeronautics and Space Administration). These piezoelectric layers are pre-stressed and pre-heated to achieve a thermal expansion, which results in a curved structure (see Figure 2.7). Therefore, the thermal pre-stress maximises the susceptibility of the piezoelectric material to deform and attain high charge polarisation and voltage output under the application of stress; yet, able to spring back to the curved shape once the forces are lifted.
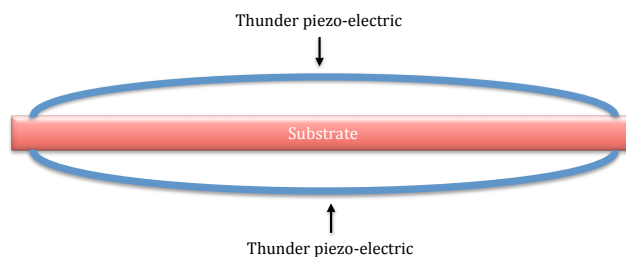
Figure 2.7: A typical bi-morph piezoelectric harvesters using pre-stressed and pre-heated piezoelectric transducers by Thunder. The curved structure enables higher susceptibility to deformation.

An EPSRC (Engineering and Physical Sciences Research Council) and DSTL (Defence Sciences and Technology Laboratory) funded joint research undertaken by the Universities of Liverpool, Sheffield, Leeds, Cranfield, Southampton, Bristol and Essex has targeted on harvesting energy of various gait and backpack motions in an attempt to replace the up to 20 kg of battery load for foot soldiers [121]. Research efforts included the analysis of the dynamics of biomechanics, mass-spring-damper systems such as pendula, non-linear cantilever beams and sliding or bouncing proof mass in a backpack, plucking of piezoelectric bimorphs in a rotary system for knee joints as well as footfall piezoelectric transducers on shoes with mechanical force amplifiers [122, 123]. Generally, the target

power is around the order of few watts for the macro-scale wearable devices, while reported values vary from a few milliwatts to a few watts for the various explored design options with gait being the most power abundant source. However, as mentioned already, harvesting too much power from humans would over fatigue the wearer.

Cantilever-based piezoelectric generators have been a popular design choice by many research groups [9, 14, 20, 124], including MEMS micro-machined iterations [95, 125]. Typically, the piezo-layer is sandwiched between two layers of electrodes [13]. The assembly itself rests on a substrate as shown in Figure 2.8 and usually a seismic mass rests on the free end to maximise displacement to induce maximum strain near the clamped end. The employment of attached tungsten mass has been popularly adopted by many designs due to its high mass density to maximise the induced strain [126, 12, 13, 100, 91] as illustrated in Figure 2.9.
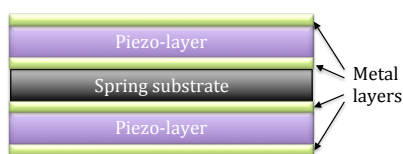
Figure 2.8: Typical cut out cross section of a piezoelectric cantilever harvester. (Not to scale)

(a) Schematic view   **(b)** COMSOL view
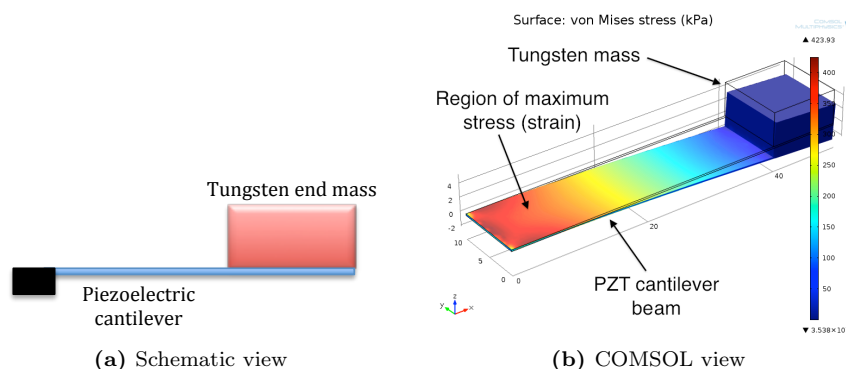
Figure 2.9: Typical piezoelectric cantilever harvester with tungsten end mass to maximise strain near the clamped end.

In 2001, University of Southampton [2, 3, 127] reported an asymmetrical design of a tapered thick-film PZT cantilever generator as illustrated in Figure 2.10. The triangular structure had a continuously narrowing width towards the free end. An optimised version of such a design ensures even distribution of strain along majority of the active length of the piezoelectric film (Figure 2.11) in order to maximise power conversion efficiency from the entire transducer layer. Conventional constant width cantilever only concentrates the strain near the clamped end while vast area of the beam near the free end is relatively strain neutral. For electromagnetic and electrostatic generators on the other hand, instead of maximising strain from the clamped-end, displacement of the free end is to be maximised. Therefore, the reverse tapered design can be applied for maximising the efficiency of electromagnetic and electrostatic cantilever-based VEH.

Other studies in the literature include bonding strands of piezo-material to stressed fibres [128], clamped-clamped beams or clamped circular plates [129, 130], carbon fibre epoxy plate bonded with piezoelectric layers [131, 27], piezoelectric walled container with freely rolling metal balls for impact-based harvesting [85] and self powered strain gauge to simultaneously take measurements and
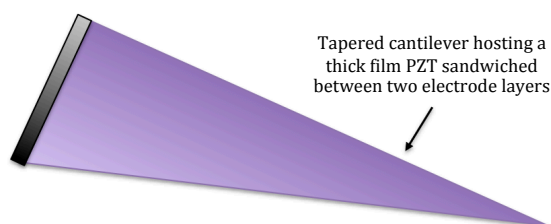
Figure 2.10: Tapered cantilever piezoelectric vibration harvester based on [2, 3]. The wider end (on RHS) is clamped. Such a structure would evenly distribute strain along the cantilever length.
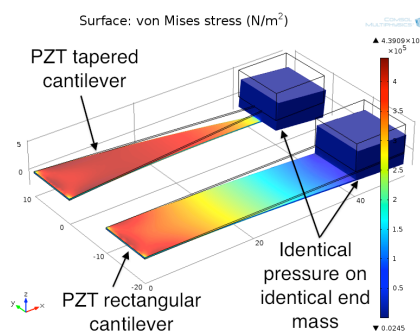
Figure 2.11: COMSOL simulated comparison of a tapered cantilever and a rectangular cantilever with identical end mass and applied pressure.

power the wireless sensor node [132]. A summary of a few selected state-of-the-art resonant-based piezoelectric harvesters are presented in Table 2.3 with the same index and normalisation used in the previous section. A graphical representation of normalised power versus volume is shown in Figure 2.12.

Table 2.3: Selected state-of-the-art piezoelectric vibration harvesters from the literature, listed in descending order of index (power density per squared of acceleration).

Reference	Year	Power (μW)	Acceleration (ms^{-2})	Frequency (Hz)	Volume (cm^3)	Index (μWcm^{-3}m^{-2}s^4)
Aktakka [100]	2011	2.74E+00	9.81E-01	167	2.70E-02	1.05E+02
		2.05E+02	1.47E+01	154		3.51E+01
Kok [101]	2011	4.00E+01	4.91E+00	229	1.61E-02	1.03E+02
Roundy [12]	2004	3.75E+02	2.50E+00	120	1.00E+00	6.00E+01
Erturk [88]	2008	2.39E+04	9.81E+00	45.6	3.52E+00	7.07E+01
Besse [91]	2012	6.37E+01	9.81E+00	41.1	1.88E-02	3.52E+01
Zhu [90]	2011	2.40E+02	3.90E+00	67	5.52E-01	2.86E+01
Tsujiura [94]	2013	1.60E+00	1.00E+01	393	3.90E-03	4.10E+00
Jeon [125]	2005	1.00E+00	1.06E+02	13.9	2.70E-05	3.30E+00
White [127]	2001	2.10E+00	2.30E+00	80.1	1.25E-01	3.18E+00
MinH [107]	2012	6.40E-01	1.50E+01	1412	1.40E-03	2.03E+00
Marzencki [95]	2007	3.00E-01	5.95E+01	1495	9.00E-04	9.43E-02
Kim [133]	2008	1.13E+00	7.84E+01	870	3.75E-03	4.90E-02
Cavallier [85]	2005	5.00E-01	1.37E+01	6	1.20E-01	2.21E-02

2.2.3 Summary

Piezoelectric material is a direct and convenient material to harvest kinetic energy, regardless of whether the source is oscillatory or impact-based. When under compression or tension, it can directly generate electrical charges. Most of the reported harvesters have demonstrated 1's μW to
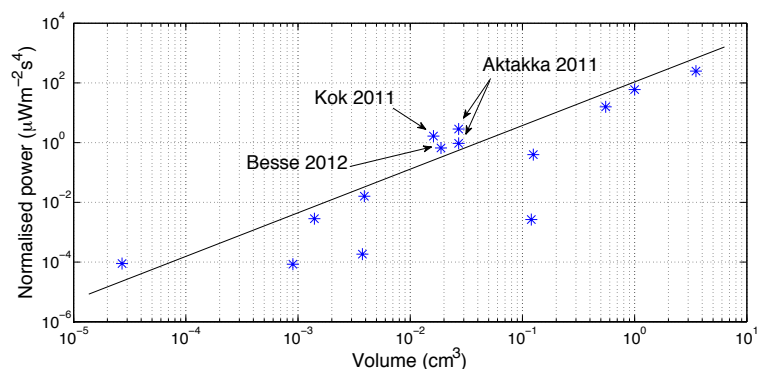
Figure 2.12: Normalised power versus volume of selected state-of-the-art resonant-based piezoelectric harvesters from the literature. The arbitrary line of best fit represents the current trend in technology. Any notable jumps above this line suggests a significant leap forward in performance.

10's μW at MEMS scale and 10's mW at device-level scales of around 1's cm^3 device volumes [134]. Its experimental power density closely rivals that of electromagnetic transducers. Theoretically, it marginally outperforms electromagnetic transducers in terms of power density [11, 30] but this has yet to be experimentally demonstrated.

At MEMS scales, the reported power densities of piezoelectric harvesters easily outperforms electromagnetic transducers not due to its own merit but due to the shortcoming of electromagnetic generators at smaller dimensions. The working mechanism of piezoelectric is not compromised at smaller scales, however, its full potential has yet to be realised due to various fabrication challenges.

2.3 Electrostatic

2.3.1 Introduction

The fundamental principle of electrostatic generators is based on Coulomb's law (Equation 2.34) and involves oppositely electrically charged plates isolated from each other by a dielectric, which essentially makes it a capacitor. Comparable to magnets, electrical charges either attract or repel each other by the electrostatic force, depending on their respective electrical polarity. By utilising external vibration to physically drive the plates relative to each other's positions, the energy stored in the capacitive plates change and mechanical energy can be converted into electrical energy.

$$F = \frac{\kappa Q_1 Q_2 r}{|r^3|} \tag{2.34}$$

where, κ is the Coulomb's constant (also known as the electrostatic constant) and r is the distance between two quantities of electric charges Q_1 and Q_2. κ is given by $\kappa = (4\pi\varepsilon_0)^{-1} = 8.99E + 09$ Nm^{2}C^{-2}, where ε_0 is the permittivity of free space.

The electric field strength E_f (measured in newton per coloumb) for a given electric charge q away from another electric charge Q is given be Equation 2.35.

$$E_f = \frac{F}{q} = \frac{\kappa Q r}{|r^3|} \tag{2.35}$$

Capacitance of a parallel plate separated by air is given by Equation 2.36.

$$C = \frac{Q}{V} = \varepsilon \frac{A}{d} = \varepsilon_r \varepsilon_0 \frac{A}{d} \tag{2.36}$$

where, C is the capacitance, V is the voltage, ε is the permittivity of the material, ε_0 is the permittivity of free space, ε_r is the relative permittivity of the dielectric material (≈ 1 in air), A is the area of the plates and d is the normal distance of separation between the capacitive plates. Since κ for vacuum is 1 and for air is approximately 1, the voltage across the capacitive plates in vacuum or air can be defined by Equation 2.37.

$$V = \frac{Qd}{\varepsilon_0 A} \tag{2.37}$$

The worked done to store E_e electrical energy into a capacitive plates is given by Equation 2.38.

$$E_e = \frac{Q^2}{2C} = \frac{Q}{2}V = \frac{C}{2}V^2 \tag{2.38}$$

With constant charge on the plates, a perpendicular electrostatic force, F_e, exist between the plates (Equation 2.39).

$$F_e = \frac{Qd}{\varepsilon A} \tag{2.39}$$

where, ε is the permittivity of the dielectric medium (usually air for most electrostatic VEH).

With constant voltage between the plates, the electrostatic force is defined by Equation 2.40.

$$F_e = \frac{1}{2} \frac{\varepsilon A V^2}{d^2} \tag{2.40}$$

Electrostatic VEH relies on vibrational sources doing work against F_e in order to generate electrical energy to accumulate on to E_e. For a pair of parallel plates, usually one is anchored while the other moves against the first. As the free plate moves, depending on the orientation of motion, either charge or voltage is altered. Generally, the net energy gained from the motion is defined by Equation 2.41 when voltage is constrained, Equation 2.42 when charge is constrained and Equation 2.43 when a hybrid of both exist [135].

$$E_{voltcons} = \frac{1}{2}(C_{max} - C_{min})V_{max}^2 \tag{2.41}$$

$$E_{charcons} = \frac{1}{2}(C_{max} - C_{min})V_{max}V_{start} \tag{2.42}$$

$$E_{charcons} = E_{voltcons} = -\frac{(\Delta Q)^2}{2(C_{para} + C_{max})} \tag{2.43}$$

where, $E_{voltcons}$ and $E_{charcons}$ are the net energies gained when voltage and charge are held constant respectively, C_{max} and C_{min} are respective maximum and minimum capacitance stored in the plates throughout the motion cycle, V_{start} is the starting voltage across the plates, V_{max} is the maximum voltage attained during the motion, C_{start} is the starting capacitance in the plates and C_{para} is a secondary capacitor connected in parallel to the capacitive plates. This model is based on the work done by Meninger *et al.* [135], but does not include an electromechanical coupling term.

2.3.2　Literature

Roundy *et al.* [4] classified electrostatic harvesters into three classes as summarised in Table 2.4. Generalised schematics of these three topologies are shown in Figures 2.13, 2.14 and 2.15. Apart from these three topologies, there could also be a fourth topology: out-of-plane gap overlapping, as shown in Figures 2.16a and 2.16b (and the mechanism explored later in Chapter 5).

Table 2.4: The relation of electrostatic force F_e to displacement x of the capacitive plate for the three classes of electrostatic generators. (Based on [4, 15])

Topology	Charge constrained	Voltage constrained
In-plane gap closing	$F_e \propto x$	$F_e \propto \frac{1}{x^2}$
In-plane overlap varying	$F_e \propto \frac{1}{x^2}$	F_e constant
Out-of-plane gap closing	F_e constant	$F_e \propto \frac{1}{x}$
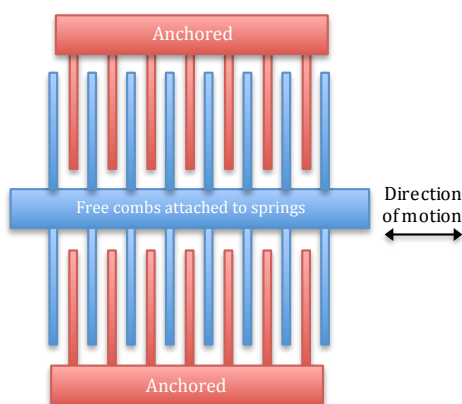
Figure 2.13: Top-down view of a generalised schematic for MEMS in-plane gap closing electrostatic vibration energy harvester topology. (Based on [4])
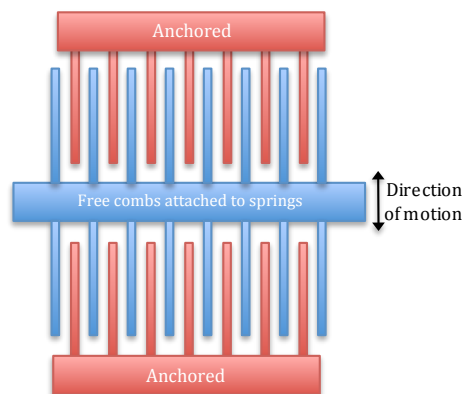
Figure 2.14: Top-down view of a generalised schematic for MEMS in-plane gap overlapping electrostatic vibration energy harvester topology. (Based on [4])

Roundy *et al.* summarised that in-plane gap closing could potentially yield the highest power density of around 100 μW cm^{-3}, while out-of-plane gap closing is the second most rewarding mechanism. This could be a result of the additional difficulty to control and minimise gap distance as precisely as its in-plane counterpart. Gap-overlapping mechanisms on the other hand, appeared to generate relatively less energy due to the limited freedom to close in on the normal gap distance. Although minimising gap increases the electrostatic force and the power output of the generator, when
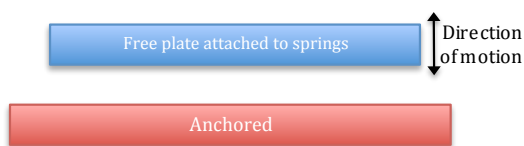
Figure 2.15: Cross-sectional view of a generalised schematic for MEMS out-of-plane gap closing electrostatic vibration energy harvester topology. (Based on [4])

(a) Top-down view

(b) Cross-sectional view
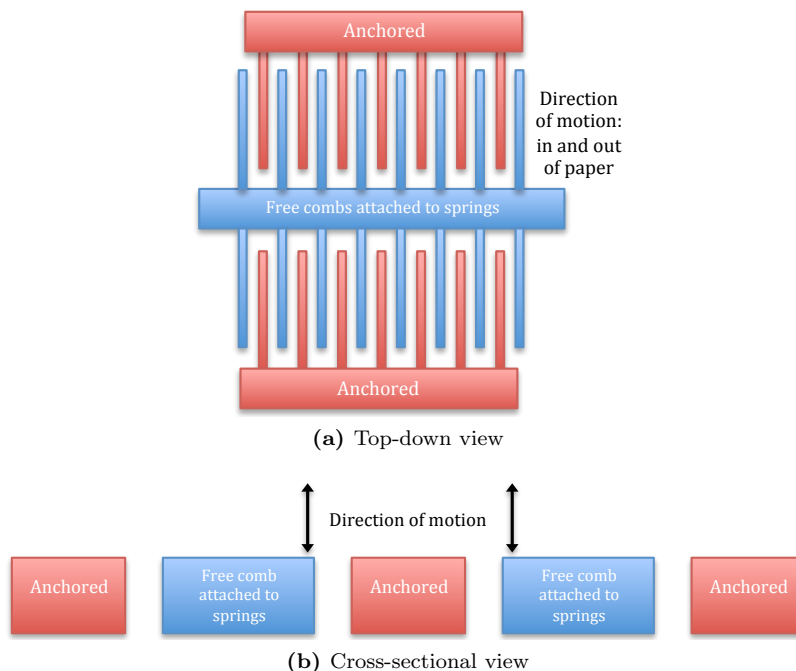
Figure 2.16: Generalised schematic for MEMS out-of-plane gap overlapping electrostatic vibration energy harvester topology.

the gap is too small, the electrostatic force collapses the plates onto each other in a phenomenon known as 'pull in'. Due to the presence of high stiction between silicon surfaces at MEMS level, such a behaviour could render the device inoperable as the plates refuses to part even after the removal of the electric field [4].

For a displacement of x varying gap distance d, the capacitance is represented by $C = \varepsilon A/(d-x)$. Therefore, the total energy E_T is given by Equation 2.44 [136].

$$E_T = -\frac{\varepsilon A V^2}{2(d-x)} + \frac{kx^2}{2} \qquad (2.44)$$

where, V is the bias voltage across the plates, k is the coefficient of the restoring force term (spring constant) of the oscillating plate. Therefore, the force acting on the moveable plate can be derived as Equation 2.45.

$$F = \frac{\varepsilon A V^2}{2(d-x)^2} - kx \qquad (2.45)$$

The system is in equilibrium when the spring restoring force equals the electrostatic attractive

force of the plates ($F = 0$). Henceforth, Equation 2.46 can be derived for a system in equilibrium.

$$\frac{\delta F}{\delta x} = \frac{2kx}{(d - x)} - k \tag{2.46}$$

The first part of Equation 2.46 represent the electrostatic restoring term while the second part is that of the mechanical restoring term. Therefore, the locus of pull in takes place when $\frac{\delta F}{\delta x} = 0$ and is given by $x = (3d)^{-1}$. Substituting back to Equation 2.45 for an equilibrium scenario $F = 0$, the pull in voltage V_p is given by Equation 2.47. When $V > V_p$, pull in instability takes place.

$$V_p = \sqrt{\frac{8kd^3}{27\varepsilon A}} \tag{2.47}$$

Some of the earliest documented studies on using electrostatic combs for energy generation were reported by research groups at MIT in 1999 [137], Terumo Corporation in 2000 [138] and University of California, Berkeley in 2002 [4]. Since then, various designs reported by other groups typically employ one or more of the above mentioned structural mechanisms; such as Hitachi in 2003 [139], Imperial College London in 2003 [140], University of Warwick in 2003 [52], the University of Tokyo in 2004 [141], IMEC in 2004 [142], the University of Hong Kong in 2005 [143], France-based LETI [15] in 2005 and many more. A few selected atypical designs are briefly mentioned below.

A joint research effort in Japan by Tashiro *et al.* [138, 144] employed a honeycomb structure to create a network of folded and interlinked spring sheets between two capacitive plates in order to realise an out-of-plane gap closing harvester to harness non-resonant random human motions for medical applications. Minakawa *et al.* from the University of Tokyo [145, 146] recently reported an X-shaped parylene spring supporting a large out-of-plane gap-closing plate (acting as the moving plate as well as a seismic mass). This design allows flexible springs to minimise frequency while in the same time suppressing displacements in undesired directions (such as rotational) to prevent unwanted modes and energy loss. Around the same time, Lin *et al.* from the University of Missouri [147] demonstrated a dual cavity process to fabricate an out-of-plane gap-closing mechanism with the moving plate suspended in between the bottom and top fixed plates. This enabled the same gap tightening in both directions of motion as that observable from conventional in-plane gap closing comb fingers. However, the out-of-plane structure allows larger surface area to increase the active capacitive region.

Researchers from Imperial College London [20, 140, 148] presents a relatively macro-sized (0.75 cm^3) 'Coulomb force parametric generator', which employs the non-resonant region of the frequency response, ideally when the excitation amplitude is larger than the maximum allowable displacement of the proof mass inside the packaging; therefore rendering the requirement of resonant peak redundant. Nonetheless, power density is extremely low since it operates outside the resonant range. However, the large active capacitive surface area achievable from such out-of-plane parallel plate mechanism has inspired several similar out-of-plane gap closing designs in recent years [149, 147, 150, 146, 151].

Several research groups [52, 141, 142, 152], especially in recent years with employment of various materials [149, 153, 154, 145, 146, 155, 156, 157, 151, 158], have also investigated electrets, which are quasi-permanently charged capacitive plates that can be seen as the electrical equivalent of permanently polarised magnets. Therefore, instead of constantly providing an external polarising electric field across the capacitive plates, the intrinsic polarisation of the electrets is self sufficient to maintain the electrostatic force. One of the key optimisation factors in this technique is to

maximise the initial polarisation voltage and the induced surface charge density [155, 151]. Where polarisation limit of the practical device has reached, stacking of electrets have been shown as a possible alternative to further maximise charge density [159, 160]. Power output has experimentally been shown to increase at a higher polynomial relationship to the number of stacks and the charge density thus achieved.

The conventional charging technique is applying a high voltage electric field across the plates. Bipolar charging of the both moving and ground plates allows lower absolute electric fields to achieve the same effect [161]. The triode corona discharge scheme [160, 162] can be employed to realise full wafer charging and has been shown to realise fast and stable results. The charger includes a patterned grid electrode that sits between a high voltage corona electrode and the grounded plate. This creates vastly different charge densities on different regions of the wafer depending on the positioning and patterning of the grid. Additionally, the charging scheme can be potentially incorporated into a continuous manufacturing process.

To maximise power generation of electrostatic generators in general [142], the main research interests surround maximising the capacitance variation per unit displacement of the proof mass and optimising damping to enable the proof mass to achieve maximum allowable displacement within the packaging structure [157]. Table 2.5 and Figure 2.17 present a brief summary of selected current-of-the-state electrostatic (including electret) vibration harvesters reported in the literature.

Table 2.5: Selected state-of-the-art resonant-based electrostatic vibration harvesters from the literature, listed in descending order of index (power density per squared of acceleration). Reported harvesters with insufficient acceleration or volume data are not presented in order to achieve fair comparison. Most volume values are estimated from various drawings, graphs and mass information provided in the cited source.

Reference	Year	Power (μW)	Acceleration (ms^{-2})	Frequency (Hz)	Volume (cm^3)	Index (μWcm^{-3}m^{-2}s^4)
Boisseau [153]	2011	5.00E+01	1.00E+00	50	1.22E+00	4.11E+01
Roundy [12]	2003	1.10E+02	2.25E+00	120	1.00E+00	2.17E+01
Wong [163]	2009	1.70E-02	1.76E+00	1400	3.19E-04	1.72E+01
Tashiro [144]	2002	3.60E+01	1.00E+00	6	3.38E+00	1.07E+01
Fujii [164]	2011	2.30E-01	9.80E-01	10	4.68E-02	5.12E+00
Wada [160]	2012	1.20E-01	1.96E+01	20	1.50E-04	2.08E+00
Chu [165]	2005	3.23E+01	4.00E+01	800	2.00E-02	1.01E+00
Despesse [15]	2005	1.05E+03	8.88E+00	50	1.80E+01	7.41E-01*
Guillemet [166]	2012	2.30E+00	9.81E+00	250	4.18E-02	5.72E-01
Arakawa [141]	2004	6.00E+00	3.90E+00	10	8.00E-01	4.93E-01
Lin [147]	2012	2.25E-01	4.91E+01	500	2.00E-04	4.68E-01
Renaud [157]	2013	1.60E+02	2.84E+01	728	1.00E+00	1.98E-01
Wang [151]	2013	1.50E-01	9.80E+00	96	1.07E-02	1.46E-01
Minakawa [146]	2013	1.50E+00	4.91E+00	28	4.43E-01	1.41E-01
Suzuki [149]	2010	1.00E+00	1.96E+01	63	5.86E-02	4.44E-02
Mitcheson [140]	2003	3.70E+00	5.00E+01	30	7.50E-01	1.97E-03
Ma [143]	2005	6.50E-02	7.66E+02	4200	7.55E-05	1.47E-03

* Acceleration was estimated from response rather than drive displacement, so index is under-estimated here.

2.3.3 Summary

In terms of MEMS fabrication, electrostatic harvesters are still the most straight forward to realise amongst the three major vibration transduction mechanisms. Although more complicated fabrication processes are required [167], the gap between piezoelectric and MEMS is closing fast. Therefore, electrostatic transducers are increasingly facing the competition from its piezoelectric
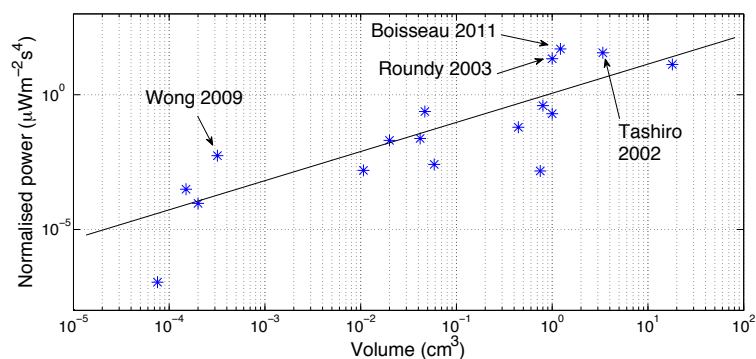
Figure 2.17: Normalised power versus volume of selected state-of-the-art resonant-based electrostatic harvesters from the literature. The arbitrary line of best fit represents the current trend in technology. Any notable jumps above this line suggests a significant leap forward in performance.

counterpart. Although MEMS electromagnetic VEH research currently exists [51], but it has yet to demonstrate itself as a competition for electrostatic VEH. In recent years, there have been significant attention drawn towards highly polarised elecrets that has demonstrated competitive power levels and has rekindled the electrostatic VEH interests.

Concurring with the theoretical predication in Table 2.1, the experimental power performance of electrostatic VEH are generally an order of magnitude lower than electromagnetic and piezoelectric VEH. This is shown in Table 2.6, which presents the order of magnitude of the Index (volumetric power density by squared of acceleration) of the state-of-the-art listed in Tables 2.2, 2.3 and 2.5. Nonetheless, current MEMS fabrication technology enables electrostatic VEH as an easily mass producible harvesting option.

Table 2.6: Comparing the order of magnitude of the normalised power densities of the current state-of-the-art of the three major vibration transduction mechanisms. Piezoelectric and electromagnetic is an order of magnitude higher than electrostatic, which agrees with the theoretical maximum energy density prediction shown in Table 2.1.

Current state-of-the-art	Electromagnetic	Piezoelectric	Electrostatic
Index order of magnitude $(\mu\mathrm{Wcm}^{-3}\mathrm{m}^{-2}\mathrm{s}^4)$	10^2's	10^2's	10's

2.4   Alternative transduction mechanisms

Apart from the three major transduction mechanisms mentioned thus far, a few research groups have investigated alternative approaches. These mechanisms are usually a combination or a derivative of these three approaches, such as the piezoelectric-electromagnetic coupled harvester reported by Challa *et. al* in 2009 [168] and piezo-magneto-elastic broadband harvester reported by Erturk *et al.* in 2009 [169]. These techniques are targeted at maximising power density and/or widening operational frequency range. However, a jump in the order of magnitude range of the Index (Table 2.6) over current state-of-the-art of the big three has yet to occur.

A rather distinct mechanism is the use of magnetostrictive materials. These materials deform when they experience a magnetic field. When a vibration-driven spring-housed magnet moves against such a material, this material would respond to the motion of the magnet with synchronised cyclic deformation. One of the early documented report of using magnetostrictive materials for VEH was

by Huang *et al.* in 2003 [170]. In general, the various designs explored by these authors or other authors [171] all primarily involved sandwiching PZT between two layers of these materials: Terfenol-D. Huang *et al.* experimentally achieved 1.2 mW for their >1 cm^3 device under half g of excitation acceleration. The normalised power density of such approach achieved around the same order of magnitude as the current state-of-the-art piezoelectric and electromagnetic. However, it does not share scaling limitation of electromagnetism since there is no coil.

In recent years, Ju *et al.* [71, 69] has reported the use MSMA (magnetic shape memory alloy) attached to a piezoelectric material. With a non-restoring magnetic ball rolling along a single axis inside a tight silicon container, which is walled by MSMA on the outside. As the magnetic ball moves, the MSMA/piezoelectric layer becomes responsive to its motion.

The common theme here is the presence and reliance of a piezoelectric transducer to eventually convert the magnetic energy into electrical energy through the mechanical coupling of the magnetostrictive and piezoelectric materials. Furthermore, the presence of bulk magnets complicate its compatibility and integration with MEMS and IC technologies. Therefore, the potential of such an approach to out rival piezoelectric harvesters, especially in MEMS scales, is yet to be demonstrated.

2.5 Existing issues and challenges

Power density has been the core focus throughout the literature review in the previous sections. Currently, Seiko [36] has realised electromagnetic inertial watches that harvest human motion to power wrist watches that require around 10's μW while Perpetuum [56], Lumedyne [49] and other energy harvesting-based emerging companies have realised VEH capable of producing power around a few mill-watts of net power for less than 1 g of acceleration; though, some of them are bulky in size.

However, these self powered wireless sensors typically require a strict power management regime with significant sleep-mode periods in order to conserve power [58]. The physical range of wireless transmission is also limited due to the scarcity of power supply. Continuously active low power wireless sensors typically require few tens of mill-watts (low power, short to medium range wireless sensors such as IEEE 802.15.4 ZigBee standards.) to a few watts (long range transmissions such as IEEE 802.11 Wi-Fi standards.).

In addition to its inadequate power levels, the expensive nature of the current commercialised vibration harvesters could serve as a demotivating factor to challenge the existing battery technologies in wireless sensors. Although an argument can be made regarding the additional maintenance costs associated with large scale battery deployments, the current limited performance of VEH hinders its claim as the replacement for batteries. Therefore, a further jump in the performance of the current state-of-the-art is required to further motivate the feasible realisation and popularisation of VEH implementations.

Another major issue is the limited operational frequency bandwidth of a typical resonant-based vibration harvester. This is because a resonator usually operates best within a narrow resonant peak to enable a high quality factor, which relates to the energy conversion efficiency. Although a high quality factor helps to achieve a high peak power, operation of the harvester outside the resonant peak would yield an unsatisfactory result. However, real world vibration is generally random and continuously varying, in terms of both frequency and amplitude, a limited and narrow operational

frequency range can only recover a fraction of the available power spectrum. A literature review of the research attempts to tackle the frequency issue is presented in Section 2.6.

A summary of existing issues and challenges of vibration energy harvesting is delineated in Table 2.7, with proposed potential solutions.

Table 2.7: Summary of existing issues and challenges of vibration energy harvesting. This research aims to address the first two issues listed here.

Issues and challenges	Potential solutions
Inadequate power density.	Novel working mechanisms and/or materials to drastically increase energy conversion efficiency. Decreasing power requirements without compromising the performance of wireless sensors.
Narrow operational frequency range renders resonant harvesters less effective to real vibrations.	Frequency tuning, broadband, non-linear or non-resonant (impact-based) approaches.
High costs associated with current commercial solutions.	VLSI, MEMS and IC integration to enable mass production and economies of scale.
Popular adoption by existing system integrators, easy interchangeability and compatibility to rival existing power source technologies.	Development of industrial standards: ISA100.18 Power Sources Working Group.
Despite the promise of prolonged lifetime in contrast to batteries, material fatigue does not actually enable 'perpetual' operation.	Research in material enhancement, minimise mechanical complexity and moveable parts, complement batteries instead of replacing them.

2.6 Operational frequency band

The various research attempts to overcome or bypass the narrow operational frequency band of resonant-based VEH can be broadly classified as follows (major drawbacks in parentheses),

- Frequency tuning to target the natural frequency towards the excitation frequency

    - Active mechanical tuning, typically with a drive actuator (drains extra power)
    - Intermittent mechanical tuning (ineffective response to rapidly varying frequencies)
    - Passive electrical tuning or tuning via electronics (narrow tuneable bandwidth)

- Intrinsically broadband approaches

    - Harvester arrays (flatter Q-factor, reduced power density)
        * Uncoupled oscillators with various natural frequencies
        * Coupled oscillators to flatten quality factor
    - Mechanical stoppers (frequency-sweep-direction dependent, rapid fatigue)
    - Bi-stable structures (complexity in design and fabrication)
    - Non-linear vibration harvesters (complexity in design and fabrication)

An ideal tuning mechanism should have,

- Minimal net power consumption, at least lower than the power generated by the harvester.

- Reasonably wide operational frequency range for adaption to real vibration sources.

- Does not compromise maximum power output and power density: flatter and higher peak.

The remainder of this chapter shall briefly review the literature of these approaches. Review articles in this topic include Zhu *et al.* (2010) [73] and Tang *et al.* (2010) [172].

2.6.1　Frequency tuning

One solution to counter the frequency mismatch is to vary the natural frequency of the oscillatory harvester in order to match the excitation frequency. Any sort of tuning mechanisms consume additional power. This extra power requirement further strains the limited power budget generated from the harvester. Roundy and Zhang in 2005 [173] and Zhu *et al.* in 2010 [73] have all concluded, with analytical derivations, that the power drain to continuously match the resonant frequency for an active tuning mechanism will almost always exceed the net power from the harvester. While there are some truth to this due to the high power budget required to sustain active tuning, the increasing profitability of active tuning stemming from the further improvement of VEH power density and development of low power tuning mechanisms are not fundamentally prohibited.

At the current state of the art, if an active tuning approach is to be adopted, only intermittent tuning is affordable. However, the effectiveness of such an intermittent techniques is dependent on the time-dependent frequency consistency of the vibration source, which are typically fast varying and continuously fluctuating between a certain (relatively large) frequency range [174]. However, certain applications such as ferry engines operating with a fixed load for over an extended period of time has been shown to serve as a feasible candidate for intermittent active tuning [175].

Most of the research attention on active (involving actuators) frequency tuning of device-level oscillators have been surrounding cantilever-based harvesters. The natural frequency of such a cantilever-seismic mass system is given below.

$$f_n = f_{r1} = \frac{1}{2\pi} \sqrt{\frac{3EI}{(m_l + 0.24m_b)l^3}} = \frac{1}{2\pi} \sqrt{\frac{Ewh^3}{4(m_l + 0.24m_b)l^3}} \tag{2.48}$$

where, f_n and f_{r1} are the natural frequency and the frequency of the fundamental mode of direct resonance respectively, E is the Young's modulus of the cantilever beam material, I is the area moment of inertia, w, h, and l are the active beam width, thickness and length respectively, m_l is the seismic (proof) mass and m_b is the beam mass.

On a wider and more general assumption, most vibration harvesters essentially employ a mass-spring-damper system similar to the model above. Therefore, the control parameters for frequency tuning is generic and the spring stiffness can be varied by,

- altering physical dimensions of the spring.
- positioning of the centre of gravity or the size of the proof mass.
- application of mechanical, electrical, magnetic or thermal pre-stress.

Several research attempts employing an active tuning mechanism to mechanically alter the natural frequency already exist. For instance, Challa *et al.* [126, 176] demonstrated the use of magnet pairs above and below a ferromagnetic proof mass of a piezoelectric cantilever in order to magnetically vary the spring stiffness as illustrated in Figure 2.18. Distances d_a and d_r can be changed when the above and below magnets are mechanically moved by a displacement actuation mechanism. A proof-mass centre-of-gravity adjustable piezoelectric cantilever harvester was reported by Wu *et al.* in 2008 [177]; while Gieras *et al* in 2007 [178] presented an electromagnetic cantilever harvester whose cantilever length can slide along the clamp with a linear actuator.
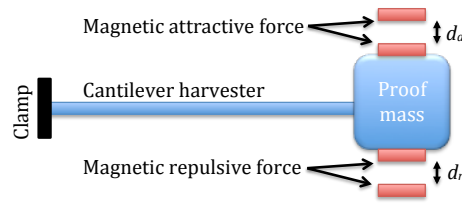
Figure 2.18: Magnetic tuning of a piezoelectric cantilever harvester spring stiffness.

Applying pre-stress (such as the example from Challa *et al.* [126, 176]), either mechanically, electrically, magnetically or thermally can all serve to alter the spring stiffness and tune the natural frequency of a resonator as illustrated by the generic models in Figure 2.19. Further examples of this include the clamp-clamped axial loading by Leland *et al.* in 2006 [179]; the cantilever proof mass tensile forcing by Garcia *et al.* in 2010 [180]; piezoelectric bi-morph and cantilever beam axial loading by Hu *et al.* [181] and Eichhorn *et al.* in 2009 [182] respectively; magnetically induced axial pre-stress on a cantilever end mass by University of Southampton and Imperial College London [183, 184, 185, 175]; the alteration of mechanical stiffness of piezoelectric resonator with an applied voltage across a piezoelectric tuning region (inverse piezoelectric effect to actuate the piezo-material) by Roundy and Zhang [173] and Peters *et al.* [186, 187]; the electrostatic softening of resonator springs by Scheibner *et al.* in 2005 [188]; the comb resonator with additional curved tuning fingers reported by Lee *et al.* in 2008 [189]; and the application of thermal stresses on electrostatic comb resonators [190, 191].

(a) Tuneable clamped-clamped beam employed by [179, 181].

(b) Tuneable cantilever beam employed by [182, 180, 183, 185, 175]
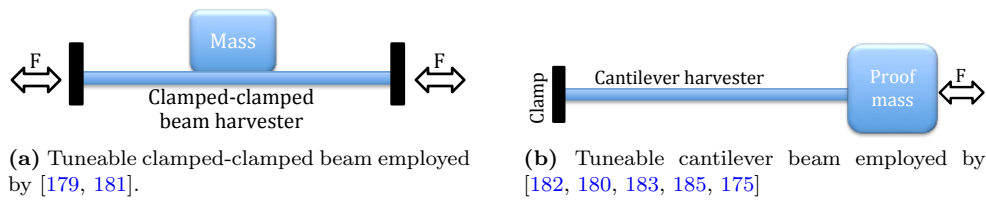
Figure 2.19: Applying pre-stress (tension and compression) either mechanically, electrically, magnetically or thermally to tune frequency.

The investigation of employing the capacitive nature of piezoelectric material to electrically tune its own stiffness has been undertaken by researchers from Pittsburgh [5] [6] [7] and Taiwan [192]. By connecting a capacitive array in parallel to a piezoelectric layer, the stiffness and hence the natural frequency, can be controlled by the passive electrical circuit (Figure 2.20). This passive method requires no mechanical actuators, but a switching mechanism is still needed to operate the shunt capacitive array during tuning. Also, the power efficiency of the piezoelectric tuning layer is sacrificed depending on the level of active capacitance; from no sacrifice when open circuited to completely sacrificed when short circuited. Therefore, the tuneable range is generally confined
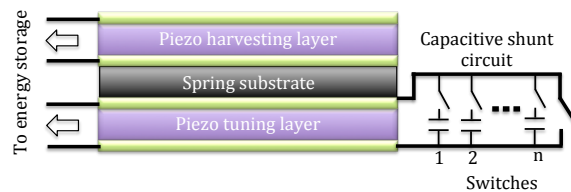
Figure 2.20: Electrical tuning of piezoelectric harvester. Stiffness is controlled by an array of shunt capacitors connected in parallel; based on [5, 6, 7].

Summary

Most mechanical frequency matching and tuning mechanisms yield a fine tuneable resolution and/or wide range. However, the additional power drain usually defeats the net-zero power target of the self-powered node. While intermittent and power budgeted tuning offers possible solutions to this, it is ineffective to keep up continuously and fast varying vibration frequencies. Although, electrical tuning of piezoelectric stiffness is a power efficient alternative, the tuneable range is still rather confined in contrast to the mechanical tuning options.

2.6.2 Broadband approaches

Instead of tuning and matching the natural frequency to the excitation frequency during operation, a harvester can also be designed to intrinsically operate across a broadband frequency response. The key advantage of such an approach is the obsoleteness of additional power drain for a tuning mechanism. However, the quality factor is generally flatter and poorer, thus compromising the conversion efficiency and peak power density.

Array of uncoupled resonators

Various researchers such as Feng and Hung in 2007 [193], Shahruz in 2006 [194, 195] and 2008 [196], Liu *et al.* in 2008 [197] and Xue *et al.* in 2008 [198] have employed an array of uncoupled cantilever harvesters, typically piezoelectric, with varying physical dimensions of the spring and/or the positioning or size of the proof mass to achieve a unique natural frequency for each individual beam resonator. Similar mechanisms were also reported by Sari *et al.* [199] in 2007 on a micro-machined electromagnetic coil-cantilever array surrounding a single permanent magnet and Ferrari *et al.* in 2008 [200] on a device-level ($\sim$1cm^3) assembly of commercially available piezoelectric bimorph cantilevers.

This approach results in an assembly of subsystem harvesters covering a broad range of frequencies in order to achieve a flatter and wider frequency response. At a particular operating frequency, the overall power output is derived by superimposing the output from all the sub-harvesters. However, typically only a few harvesters operating in the vicinity of resonance noticeably contribute to this total power output, while the majority experience diminished non-resonant responses. Main drawbacks of such an approach is the inevitably reduced power density because most of the cantilevers within the active volumetric space are not operating at their maximum potential.

Array of coupled resonators

Instead of mechanically uncoupled resonators, Petropoulos *et al.* in 2004 [201] and Wong *et al.* in 2009 [163] have investigated the effect of coupling the various mass-spring-damper systems to yield a multiple degrees-of-freedom system that has several resonant frequencies depending on the intrinsic properties of each constituting resonator. Erturk *et al.* presented in 2009 [202] an L-shaped beam where an orthogonal piezoelectric beam is attached to the end mass of a piezoelectric cantilever beam; thus achieving two degrees of freedom with two closely resonant peaks. By adjusting the coupling coefficient and natural frequencies of the individual oscillators, either frequency broadening or targeted-frequency superpositioning-accumulation of resonant peak responses can be achieved.

In other words, an infinitely strong coupled array is simply a single larger resonator with a single natural frequency.

The advantage of this approach over the uncoupled array is the significantly improved response for the resonators operating outside their natural frequencies due to the energy flow from the resonating springs. However, this flatter frequency response comes at the cost of lower power peak for the resonators supposedly operating in the vicinity of their respective natural frequencies, due to the increased damping (energy flow) thrust upon by the other resonators. The same scarcely spread out power density problem faced by their uncoupled counterparts still applies.

Mechanical stoppers

In an alternative attempt to widen the operational frequency bandwidth, the use of mechanical stoppers to impose a physical amplitude limit has been studied by Soliman *et al.* [203, 204]. The mechanical stoppers prevented the oscillating electromagnetic cantilever-based harvester to reach its potential peak; thus, achieving a flat and truncated peak from the resonant response. More than doubling of the operational frequency band was experimentally observed during a frequency upsweep with a peak power sacrifice of nearly one third. However, this broadening behaviour failed to manifest during downward frequency sweeps. Such a system compromises the peak power density and the physical impacts from the mechanical stoppers promotes structural fatigue.

2.6.3 Frequency up conversion

Miniaturisation of VEH is often desired to realise on-board system integration. However, at smaller dimensions, the natural frequency of the resonators are typically much higher than the frequency of the ambient vibration. Frequency up conversion is a design technique that can be incorporated in VEH to remedy this situation. Also, some transducers only attain optimal efficiency above a certain frequency. Additionally, the overall system can be responsive to multiple frequencies depending on the design.

A frequency up converter typically involves a primary resonator or dynamic system (either linear [205, 206, 207, 208] or rotational [209, 210] with potential to incorporate gear trains) responsive to a lower and/or wide band frequency, which is in turn coupled to a secondary resonating system that usually operates at a higher narrow band frequency with a high quality factor. As the larger primary resonator responds to vibration, energy flows towards the secondary resonator via a specific coupling mechanism, thus enabling the secondary resonator to oscillate and decay at its own natural frequency independent of the vibrational frequency.

Priya [209] and Rastegar *et al.* [205, 210] demonstrated mechanical plucking of secondary piezoelectric elements and Ferrari *et al.* [207] investigated smaller piezoelectric cantilever beams driven by mechanical impact from the oscillation of a neighbouring large and parallel drive cantilever, while Wickenheiser and Garcia [211] and Kulah and Najafi [212] employed magnetic coupling to actuate the secondary resonators. Jung *et al.* [213, 214] reported a larger clamped-clamped beam that houses multiple smaller subsidiary cantilever beams. This topology enables direct coupling of the primary and secondary resonators within the same structure rather than an external coupling mechanism that might dissipate additional energy.

2.6.4   Non-restoring non-resonant approaches

While any system driven out of resonance will qualify the non-resonant characteristic, there have been several studies that utilises some sort of non-restoring primary dynamic system to drive a secondary VEH resonator. In a sense, this is similar to the frequency converters, except the primary dynamic system here is not a resonator nor does it possess a restoring term. Such a harvester will be independent of frequency but more sensitive to amplitude. Therefore, despite the broader frequency bandwidth, the profitability of such devices diminishes for higher frequency but lower amplitude vibrations.

Examples include cylindrical ferromagnetic roller in a chassis that closely houses an array of small piezoelectric cantilevers with magnetic end mass [68] and ferromagnetic/magnetic rolling balls that are coupled mechanically by impact [85], magnetically [71, 69] or electrostatically [215] to a transducer.

Roundy and Tola [216] demonstrated a device with a single axis rolling ball inside a fixed tight container that mechanically pushes against a circular proof mass of a piezoelectric cantilever suspended and immersed at centre the container when the ball rolls across from one end to the other. Roundy and Tola also experimentally characterised the frequency behaviour of the single axis rolling ball inside its container. The rolling ball is responsive to low frequencies and becomes increasingly energetic with increasing frequency over a wide range (1's Hz to ∼25 Hz) until a specific high velocity is attained where the ball abruptly becomes motionless due to the overwhelming coulomb friction.

2.7   Nonlinear resonators

In recent years, nonlinear VEH has become a popular research topic [172] due to its potential to offer both higher peak and broader bandwidth [169, 217], albeit modestly, in contrast to a linear resonant response. This opens the possibility of accessing the previously untapped nonlinear regime of the power spectrum that is inaccessible by linear resonators. Recommended reference texts on non-linear vibration include Minorsky [218, 219], Nayfeh [8], Cartmell [220] and Thomson [221].

The various non-linear VEH approaches can be broadly classified into mono-stable resonators that rests at zero-displacement equilibrium and bi-stable or multi-stable resonators that usually has an unstable equilibrium at zero-displacement and hops between more than one potential intra-wells within the system. Further analysis of of the bi-stable behaviour is explored in Chapter 6.

2.7.1   Mono-stable resonators

Most of the mono-stable non-linear resonators explored employ an iteration or a variation of the duffing oscillator [73], which adds an amplitude-dependent cubic geometric duffing term or other higher order nonlinear stiffness term to a typical second order mass-spring-damper equation of motion. Depending on the sign of the duffing term, either spring softening or spring hardening effect manifest, which corresponds to a resonant peak bending towards lower frequency or towards higher frequency respectively.

The nonlinearity can be achieved through coupling of a resonator end mass (ferromagnetic) with closely placed magnets to induce either spring softening or hardening effect depending on the magnetic coupling orientation and topology [169, 222, 223, 224]; the employment of magnetic springs

instead of physical springs as the restoring force such as magnetically coupled rotary suspension [225] and nonlinear magnetic levitation where a magnetic is suspended in a single axis tube (coils wound from outside) by two opposing magnetics on either ends [226, 227]; and the application of axial pre-stress to a spring to induce softening or hardening [228].

In real vibrational systems, truly linear resonators are quite rare and most systems would have an amplitude dependent non-linear term. Therefore, nonlinearity will onset by simply driving an otherwise linear spring, such a simple cantilever, into high amplitudes [229, 217]. The amplitude at which the Duffing term becomes dominant is dependent on the geometry of the spring. However, to effectively utilise the non-linear phenomenon for VEH, the aim is to achieve the non-linearity at relatively low amplitudes and as few design complexities as possible.

Triplett *et al.* [230] demonstrated an intrinsically nonlinear piezoelectric composite due to the nonlinear coupling between the composite layers during manufacturing. This enabled a nonlinear VEH without the addition of external magnets or magnetic springs. However, the device experimentally deviated from a classical non-linear model described by the Duffing equation and further analysis is warranted to better understand the underlying nonlinearity.

Furthermore, Daqaq [227] experimentally compared a linear and nonlinear mono-stable harvester driven by broadband random vibration and observed no noticeable improvements despite the increased device complexity and promising theoretical predications. This could be a result of the presence of non-trivial boundary conditions required to access the potentially wider bandwidth of the non-linear regime. Therefore, the advantages of operating in the non-linear regime only becomes apparent when the various boundary conditions, dictated by the vibrational source, becomes favourable.

2.7.2   Bi-stable and multi-stable resonators

Bi-stable or multi-stable systems employ negative stiffness, which typically involves an unstable equilibrium at the zero-displacement position. Therefore, multiple intra system potential wells are created, which traps the resonators in one particular stable state. Energy can be harnessed through the normal resonant behaviour within any of the stable states, or from the instantaneous energy release when the system attains enough energy to hop from one potential intra-well to another across a potential barrier. This intra-well hopping is also known as the snap-through state.

The vibration required to induce the snap-through state is independent of the natural frequency of the system and only requires the forcing energy to be large enough to cross the potential barrier. Therefore, assuming ample amplitude, the snap-through mechanism is responsive across a wide range of frequencies, especially for low frequencies where displacement amplitude is high.

Dogheche *et al.* in 2006 [231] was one of the earliest to suggest the possibility of implementing bi-stability in VEH through the demonstration of a bi-stable piezoelectric micro-machined ultrasonic transducer originally designed as an acoustic sensor. Ramlan [229] and Moehils *et al.* [232] investigated the higher power output available from snap-through motion over a linear resonator. Bi-stability can be mechanically introduced or inherently configured into the system, such as the bistable carbon fibre piezoelectric composite plate by Aerrieta *et al.* [131], which was created by inducing thermal pre-stress in the composite; and the application of mechanical pre-stress to buckle clamped-clamped beams [233].

Magnets are a popular choice to realise bi-stable VEH. Examples include cantilever with magnet end mass and an opposing magnet in the zero-displacement position to push it away [234, 235, 236]; the use of ferromagnetic end mass on the pendulum and two attractive magnets placed on either sides to pull and nullify the stability of the zero-displacement position [169]; and two or more cantilevers with magnetically opposing end mass placed in close proximity to push each other into bi-stable [237, 236] or multi-stable [238] states. The bi-stable or multi-stable VEH thus created from magnetic coupling are not too unlike the use of magnetic coupling for enabling frequency tuning, multi-coupled resonators and non-linear resonators explored in the previous subsections. Therefore, a system that is simultaneously all of the above can be realised to exploit multiple resonant and vibration regimes, along with the snap-through mechanism.

2.7.3   Stochastic resonance

Stochastic resonance [239, 240] is the vibrational phenomenon where an excitation (signal) that is usually too small to yield a meaningful result (to detect), becomes meaningful with the addition of white noise. In sensing applications, it is popularly known as 'adding noise to remove noise', since the addition of white noise helps to boost the signal-to-noise ratio [241].

In the context of VEH, it can be easily explained by considering a bi-stable system experiencing a periodic forcing that is less than sufficient to cross the potential barrier. Although the system is trapped in a potential intra-well, when driven into resonance, it can still yield a meaningful power output. However, with the addition of noise (stochastic excitation) into this system, the extra energy in combination with the periodic forcing could activate the snap-through states and realise a much larger power output.

As mentioned above, the triggering of snap-through state is independent of the frequency, which renders the broadband nature of the noise, irrelevant. Therefore, the energy of the otherwise difficult to harvest noise is harnessed along with the onset of appreciable mechanical amplification from the snap-through states in contrast to the resonant response trapped in a limited potential well. In essence, the combination of two individually insignificant energy sources (periodic and stochastic excitations) yields a significant response. Although stochastic resonance is not limited by bi-stable system, this snap-through working mechanism has been the core of the theoretical and experimental investigations within VEH thus far [232, 233, 242, 243, 244].

Additionally, it should be noted that not all noise are stochastic excitations and a system designed to be responsive to noise/broadband vibration does not necessarily exhibit stochastic resonance. For further reading regarding stochastic resonance, please refer to the comprehensive theoretical analysis and literature review presented in the book by Ando and Graziani (2000) [239].

Chapter 3

Background on parametric excitation

This chapter explores the core principles behind the thesis of this dissertation: parametric resonance; and its applicability to VEH. Primary textbooks referenced include: McLackhlan (1947) [245], Minorsky (1947) [218] and (1974) [219], Nayfeh (1979) [8], Cartmell (1990) [220], Tondl (2000) [246] and Fossen (2012) [247].

Vibration energy harvesters are typically driven by excitation forces acting parallel to the direction of the oscillatory displacements. Resonance resulting from this forced excitation is classified as '*direct resonance*' in this dissertation. On the other hand, '*parametric resonance*' usually (but not exclusively) arises from orthogonal driving forces and a periodic variation in the system parameter is triggered instead of forced response.

3.1 Kinetic vibration

This section will give a general overview of kinetic vibration and resonance.

3.1.1 Introduction

The classification of kinetic vibration can be based on the interactions between the structural nature of the oscillating system and the external forcing applied to the system. In the real world, most dynamical systems are nonlinear multiple degree-of-freedom (DOF) in nature. Even when a vibrating system behaves linearly, it is generally because the nonlinear factors are negligible under the given excitation settings. Although pure linear systems are typically confined within theoretical grounds, the insignificant non-linearity in many practical systems such as the widely employed cantilever beams (assuming small displacements) in the field of vibration energy harvesting can be accurately approximated by linear models. The general form of the equation of motion for these systems is given in Equation 3.1.

$$M\ddot{x} + C\dot{x} + Kx + \mu(x) = F_1(t) + F_2(t)x \tag{3.1}$$

Where, x is the displacement, M is the mass matrix, C is the damping matrix, K is the stiffness matrix, $\mu(x)$ is the nonlinear vector (with polynomial expansion of x), $F_1(t)$ is applied force vector and $F_2(t)$ is the applied force matrix.

When the right hand side (RHS) of Equation 3.1 is zero, free vibration is observed where the oscillation would eventually decay to rest at an equilibrium position due to energy dissipation as a result of damping. Whereas when external periodic forces are experienced, vibrational energy input results and the equation of motion is represented by a function of time.

Following the onset of vibration, oscillatory amplitude starts to grow. However, amplitude growth has a higher order relationship directly proportional with damping. That is, damping grows faster than amplitude itself. Therefore, the amplitude dependant damping term would saturate the oscillatory amplitude growth.

3.1.2 Forced oscillation
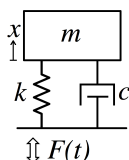
Figure 3.1: Model of a mass spring damper system under direct forcing.

Direct excitation of a mass-spring-damper system (figure 3.1) yields a forced response. A damped forced oscillator can be represented by Equation 3.2.

$$m\ddot{x} + c\dot{x} + kx = F \cos \omega t \tag{3.2}$$

where, m is the mass, c is the damping, k is the stiffness and F is the periodic force amplitude. A general solution is given by Equation 3.3.

$$x(t) = x_t(t) + x_s(t) \tag{3.3}$$

where, $x_t(t)$ is the transient solution and approaches zero when $t \rightarrow +\infty$; and $x_s(t)$ is the steady-state particular solution.

The particular solution for $x(t)$ is given by Equation 3.4 [248, 221].

$$x(t) = A_1 \sin(\omega t) + A_2 \cos(\omega t) \tag{3.4}$$

$$\text{where, } A_1 = \frac{c\omega F}{(k - m\omega^2)^2 + (c\omega)^2} \tag{3.5}$$

$$\text{and, } A_2 = \frac{(k - m\omega^2)F}{(k - m\omega^2)^2 + (c\omega)^2} \tag{3.6}$$

And the steady-state particular solution $x_s(t)$ that can be written as Equation 3.7 [248, 221].

$$x_s(t) = A_3 \cos(\omega t - \varphi) \tag{3.7}$$

$$\text{where, } A_3 = \frac{F}{\sqrt{(k - m\omega^2)^2 + (c\omega)^2}} \tag{3.8}$$

$$\text{and, } \varphi = \begin{cases} \tan^{-1}(\frac{c\omega}{k - m\omega^2}) & \text{if } k > m\omega^2 \\ \pi + \tan^{-1}(\frac{c\omega}{k - m\omega^2}) & \text{if } k < m\omega^2 \end{cases} \tag{3.9}$$

$A_3(\omega)$ is the forced amplitude where the maximum value of $A_3(\omega)$ is the particular value of the fundamental mode of direct resonance. For $c \geq \sqrt{2km}$, $A_3(\omega)$ is a decaying function while for $c < \sqrt{2km}$, A_3 attains a maximum value.

3.1.3   Resonance

When the driving frequency matches the natural frequency of the system, the system would experience a build up in stored energy and maximum oscillatory amplitude of Equation 3.7 could be achieved. This phenomenon is typically described simply as resonance arising from forced excitation and the primary resonant frequency is generally represented by Equation 3.10 and Equation 3.11 (in the case of a pendulum).

$$\omega_0 = 2\pi f_0 = \sqrt{\frac{k}{m}} \tag{3.10}$$

$$\omega_0 = 2\pi f_0 = \sqrt{\frac{g}{l}} \tag{3.11}$$

Where ω_0 is the fundamental mode angular resonant frequency, f_0 is the fundamental mode resonant frequency, g is acceleration due to gravity and l is the pendulum length. Resonance can be classified as follows with ω as the driving frequency [249],

- **Direct excitation**

  - Fundamental mode resonance: $\omega = \omega_0$

  - Higher resonant modes of vibration: ω dependent on topology of the system

  - Secondary resonance
    * Sub-harmonic: $\omega = 3\omega_0, ...$
    * Super-harmonic: $\omega = \frac{1}{3}\omega_0, ...$
    * Super-sub-harmonic: $\omega \pm \omega_1 \pm \omega_2 = \omega_3, ...$

- **Parametric excitation**

  - Heteroparametric resonance: $\omega = \frac{2\omega_0}{n}$; where n is a positive integer
    * Principal (1st) order: $\omega = 2\omega_0$
    * Fundamental (2nd) order: $\omega = \omega_0$

  - Autoparametric resonance: $\omega_2 = n\omega_1 (1 : n)$

3.2   Parametric excitation

Carrying on from the previous section, this section will focus further on the resonant phenomenon arising from parametric excitation.

3.2.1   Introduction

One of the earliest documented reports of this phenomenon was recorded by Michael Faraday in 1831 [250] upon observing that a vertically oscillating cylinder on the surface of a fluid had half the frequency of the excitation. The fundamental mathematics was initiated by Mathieu (1868) [251] and further established by the likes of Floquet (1883) [252], Hill (1886) [253] and many others. Experimental investigations were extensively carried out by Lord Rayleigh in 1880's using vibrating strings and wave propagation [254, 255]. Parametric resonance in the electrical domain was experimentally demonstrated by a motor controlled variable capacitor by Mandelstam *et al.* (1925) [256]. Since then, the fundamental principles have been comprehensively covered [8, 245, 219, 247].

Traditionally, the study of parametric resonance has circled around its control and prevention in regards to structural failure of mechanical systems such as aircraft wings, marine crafts, civil structures, etc. [246, 247]; as oscillations, en route to chaos, could accumulate to significantly larger amplitudes than direct resonance. This implies that it could potentially act as a mechanical amplifier to maximise the energy conversion efficiency of a given transducer and drastically improve its output power density for a given forcing amplitude.

The wider transducer community has dubbed this as the 'parametric amplification effect' employed to achieve higher input-to-output sensitivity than direct resonance [23, 24, 25]. To date, only a few sparse early investigations have been undertaken to incorporate parametric resonance for vibration energy harvesting [257, 26, 258] and significant performance enhancements have yet to be reported. Nonetheless, parametric resonance has the potential to facilitate the feasible and popular realisation of zero net power devices such as wireless sensor nodes for structural health monitoring.

Parametric resonance is distinct from most of vibrational resonances due to an instability phenomenon. Instead of energy build-up due to a forced response, parametric resonance involves a periodic variation in system parameter. There could be two types of parametric resonance; one is the externally induced heteroparametric resonance (which is generally known simply as parametric resonance) and the other is the internally excited autoparametric resonance [219].

Heteroparametric excitation is induced by the periodic modulation of certain system parameters in response to an external force. While autoparametric resonance arises from certain integer ratio relationships among the various natural frequencies of the multiple DOF system, resulting in one oscillating component of the system introducing a periodic modulation of system parameters on another. Mathematically, both types of parametric resonance reduce to the Mathieu equation. It is named after the elliptical membrane problem studied by M.E. Mathieu [251] and the canonical form is given by Equation 3.12 [245].

$$\frac{\mathrm{d}^2 y}{\mathrm{d}z^2} + (p - 2q\cos{(2z)})y = 0 \qquad (3.12)$$

where, y and z are generic variables and p and q are generic parameters.

3.2.2 Background

3.2.3 Motivation

This research aims to employ parametric resonance as a means of mechanical amplification for the achievable peak oscillatory displacement in order to improve the conversion efficiency of vibration energy harvesters. The motivation for this approach is based on a pivotal advantage that could potentially enable a significant leap forward in performance as illustrated below [22],

- Direct resonance: $E_{in} \propto A \propto \sqrt{E_{stored}} \propto \sqrt{E_{lost}}$

- Parametric resonance: $E_{in} \propto A^2 \propto E_{stored} \propto E_{lost}$

where, E_{in} is energy input, A is response amplitude, E_{stored} is energy stored in the system and E_{lost} is the energy dissipated by linear damping. In other words, more energy is stored into the system by parametric resonance over time. Therefore, theory predicts a higher order oscillatory amplitude growth in contrast to direct resonance.

3.2.4 Parametric modulation and instability

As mentioned, heteroparametric excitation is when a parameter of an oscillatory system modulates as a function of time as a result of an external non-direct forcing. When the parametric modulation frequency is twice the natural frequency (a typical identifier of this phenomenon) of the oscillator, principal parametric resonance can be observed.

Unlike direct excitation, the homogeneous parts of the equation of motion contain functions of time and Equation 3.13 can be assumed [218].

$$\ddot{z} + p(t)\dot{z} + q(t)z = f(t) \tag{3.13}$$

Parametric excitation here co-exists with external direct excitation $f(t)$. However, even with the absence of $f(t)$ in Equation 3.13, the parametric modulation of $p(t)$ and $q(t)$ can act as excitation from within the system.

Therefore, by assuming the absence of an external direct excitation and by introducing the variable x, Equation 3.13 becomes the following as explained by the Floquet theory [249, 218].

$$\ddot{z} + p(t)\dot{z} + q(t)z = 0 \tag{3.14}$$

$$\text{assuming: } z = x \exp(-\frac{1}{2}\int p \, \mathrm{d}t) \tag{3.15}$$

$$\ddot{x} + M(t)x = 0 \tag{3.16}$$

$$\text{where, } M(t) = q - \frac{1}{4}p^2 - \frac{1}{2}\dot{p} \tag{3.17}$$

Equation 3.16 is known as the Hill's Equation and $M(t)$ is a Fourier series. Alternatively $M(t)$ can be presented by Equation 3.18.

$$M(t) = \delta + 2\varepsilon \cos(2t) \tag{3.18}$$

From this, a system under sinusoidal parametric excitation can take a form of Mathieu Equation as shown in Equation 3.19 [218].

$$\ddot{x} + (\delta + 2\varepsilon \cos(2t))x = 0 \tag{3.19}$$

where, δ and ε are generic parameters related to the square of natural frequency and amplitude of the parametric excitation respectively. An example of such a system is a pendulum driven at suspension. This would be the principle employed in the initial stage of this research to realise and investigate the feasibility of a parametrically excited vibration energy harvester.

Due to the time dependent coefficients, the Mathieu Equation cannot be analytically solved despite being a linear differential equation. However, the Floquet theorem states that with a set of fundamental solutions x_1 and x_2, all other solutions can be numerically constructed.

Assuming fundamental solutions $x_1(t)$ and $x_2(t)$, the general solution shown in Equation 3.20 [249] can be formed.

$$x(t) = A_1 x_1(t) + A_2 x_2(t) \tag{3.20}$$

Where, A_1 and A_2 are arbitrary constants while $x_1(t + \pi)$ and $x_2(t + \pi)$ are further solutions; hence, giving the following [218].

$$x_1(t + \pi) = ax_1(t) + bx_2(t) \tag{3.21}$$
$$x_2(t + \pi) = cx_1(t) + dx_2(t) \text{ and} \tag{3.22}$$
$$x(t + \pi) = A_1 x_1(t + \pi) + A_2 x_2(t + \pi) \tag{3.23}$$

All solutions can be written as Equation 3.24 [249, 259].

$$x(t) = \exp(\gamma t)\varphi(t) \tag{3.24}$$
$$\text{where, } \varphi(t) = \varphi(t + \pi) \tag{3.25}$$

where, γ is the Floquet exponent or also known as the characteristic exponent. This is not a unique definition as any exponential factor can be absorbed into $\varphi(t)$ or $\exp(\gamma t)$.

Solutions for x is unstable and unbounded when the real part of γ is positive definite. Therefore, an exponential build up can be observed for the oscillatory amplitude (which would theoretically grow to infinity) until the system either reaches physical limits or nonlinearity is experienced. For zero and negative values of the real part of γ, x is stable and bounded with time, and decays to zero when damping is applied. Figure 3.2 illustrates examples of bounded and unbounded solutions of the Mathieu equation.

Hence, as the real part values of γ transitions from positive to zero and negative, the division between instability and stability forms. Figure 3.3 shows the stable and unstable regions divided by the transitions curves, which are the loci of ε and δ [249]. The diminishing size of each tongue (narrower operational frequency bandwidth) towards the right-hand-side (RHS) can be seen at higher orders (see Equation 3.26) of parametric resonance. Therefore, the left most positive δ tongue represents the principal parametric resonance.

(a) Unbounded

(b) Damped bounded   **(c)** Undamped bounded
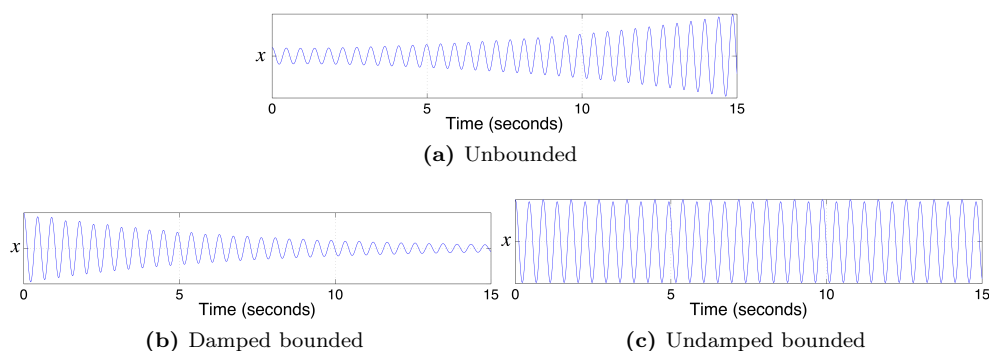
Figure 3.2: Unbounded (unstable) shown in (a) and bounded (stable) solutions shown in (b) and (c) of Mathieu equation. Unbounded solution (a) approaches infinity with or without linear damping.
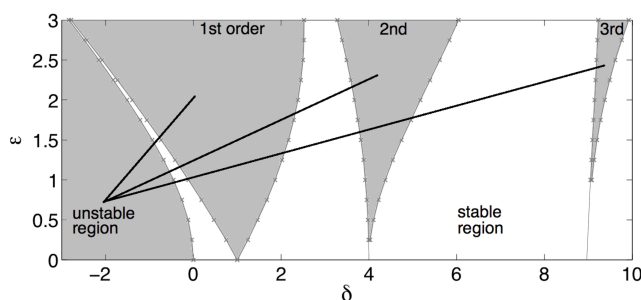
Figure 3.3: Stable (unshaded) and unstable (shaded) regions in the ε-δ stability chart (Strutt diagram) of the Mathieu Equation [8]. The unstable region signifies the activation of parametric resonance.

One of the identifying characteristics of parametric resonance is that the response frequency is always around the natural frequency regardless of the order of parametric resonance (excitation frequency). Figure 3.4 shows the 1st order parametric resonance where excitation frequency is twice that of the response frequency.

(a) Excitation at $2f_n$ **(b)** Parametric resonant response   **(c)** Zoom of (b) showing f_n
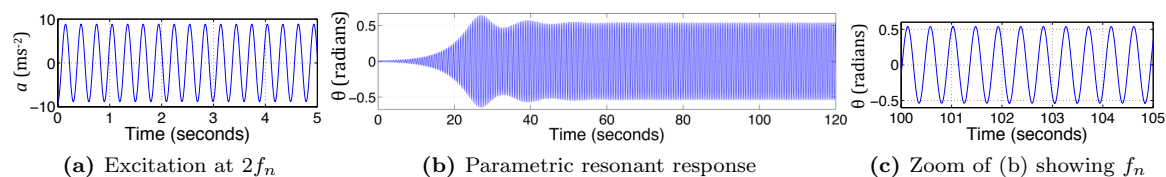
Figure 3.4: Excitation frequency of 1st order parametric resonance is twice the response (natural) frequency.

3.2.5   Conditions of parametric resonant onset

The system can potentially achieve parametric resonance (the shaded unstable region in Figure 3.3) when the condition in Equation 3.26 is met.

$$\omega = \frac{2\omega_0}{n}; \; n = 1, 2, 3, ...$$ (3.26)

When n = 1, the excitation frequency is at principal (1st order) parametric resonance ($\omega = 2\omega_0$), whereas n = 2 is the fundamental (2nd order) parametric resonance ($\omega = \omega_0$). At higher orders of n, less energy is delivered to the system during one period and the area of stable region takes dominance as seen in Figure 3.3.
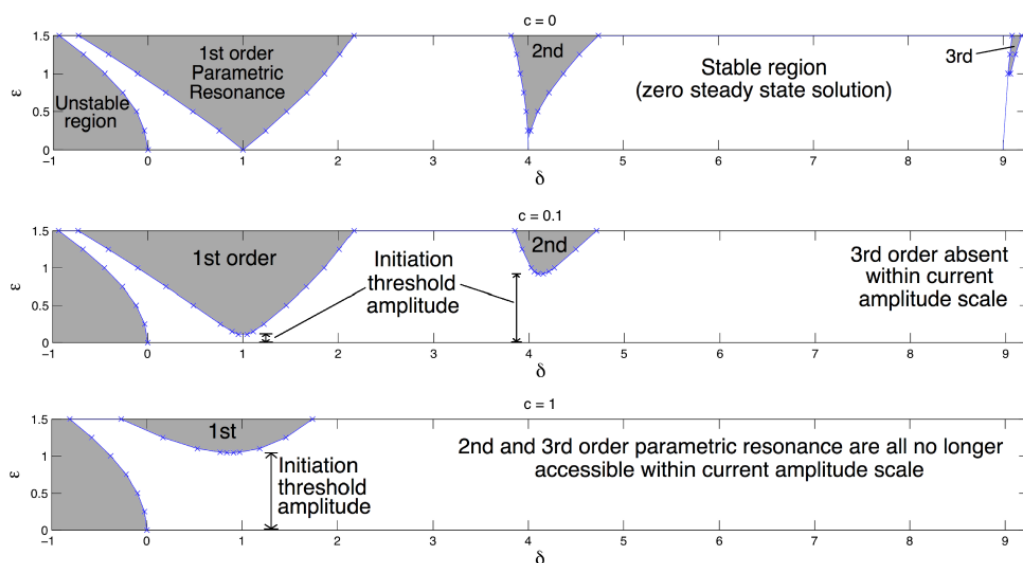
Figure 3.5: Effect of damping on the stability of the Mathieu Equation solutions. Shaded regions are unstable while c is damping [8]. A decrease in unstable area is observed as damping increases.

As damping c is introduced, the excitation amplitude A must meet the condition in Equation 3.27 [259] in order to enable the build up of parametric resonance. Otherwise, the system would remain in the stable region as long as excitation amplitude is below this damping-dependent initiation threshold amplitude. Figure 3.5 shows the damped version of the Strutt diagram, illustrating much more significant stable regions as damping increases. The damped version of the Mathieu equation is shown in Equation 3.28.

$$A \geq c^{\frac{1}{n}} \tag{3.27}$$

$$\ddot{x} + c\dot{x} + (\delta + 2\varepsilon \cos(2t))x = 0 \tag{3.28}$$

Apart from the frequency and amplitude prerequisites, the initial displacement of the system needs to be non-zero for the parametric excitation to onset the modulation in the system parameter. Otherwise, the system is trapped in a stable equilibrium regardless of the amplitude of the driving force, as no forced response theoretically results from parametric excitation. As the instability regions are accessed, oscillatory amplitude rapidly grows and mathematically approaches infinity with time in a linear system. The presence of linear damping cannot saturate such a system. Only higher orders of nonlinear damping can saturate the resonant growth at higher amplitudes.

Unlike direct resonance, purely linear damping does not saturate the oscillatory amplitude growth for parametric resonance. Hence, oscillatory amplitude can theoretically grow towards infinity or until the system is eventually destroyed. This phenomenon was demonstrated by Mandelstam and Papalexi (1934) [260] using a linear oscillating circuit with growing oscillatory amplitude that eventually resulted in its thermal insulation destroy at excessive voltage. In most real systems, nonlinearities become significant above a certain amplitude. Therefore, the nonlinear effects can eventually saturate the parametrically excited resonators and oscillatory amplitude can be maintained at a particular peak [219, 261].

Nonlinearities in systems can arise due to boundary conditions, nonlinear damping, geometric

nonlinearity, inertia nonlinearity, etc [262, 263]. Due to the amplitude dependent nature of eigenfrequencies in nonlinear oscillators, the eigenfrequency will shift out of resonance as amplitude grows. In other words, the resonant peak would bend towards a particular direction like that of a spring softening or spring hardening effect. Effectively, this would widen the frequency bandwidth of significant oscillatory amplitude.

3.2.6   Potential shortcomings and remedial solutions

Despite the promising potentials over direct resonance as a mechanical amplifier for vibration energy harvesting, parametric resonance has a few limiting disadvantages that need to be overcome.

Initiation threshold amplitude

One of this is the damping dependent initiation threshold amplitude, which has already been previously shown to be obstructive to accessing the profitable regions of parametric resonance within practical acceleration levels and damping conditions [257, 26]. This is especially true for energy harvesting as the technology relies on electrical damping to extract energy. Active actuators have been used in sensor applications to realise the parametric amplification effect [264, 265], however, extra power expenditure is counterintuitive and impractical for energy harvesting. In the meantime, the acceleration levels of real world civil infrastructural vibrations are typically small (from 0.1's ms^{-2} to 1's ms^{-2}).

Passive design approaches illustrated in Figure 3.6 are proposed to minimise this critical threshold in order to practically realise the profitable regions of the parametric resonance at lower acceleration levels. Detailed experimental investigations are given in the succeeding chapters.
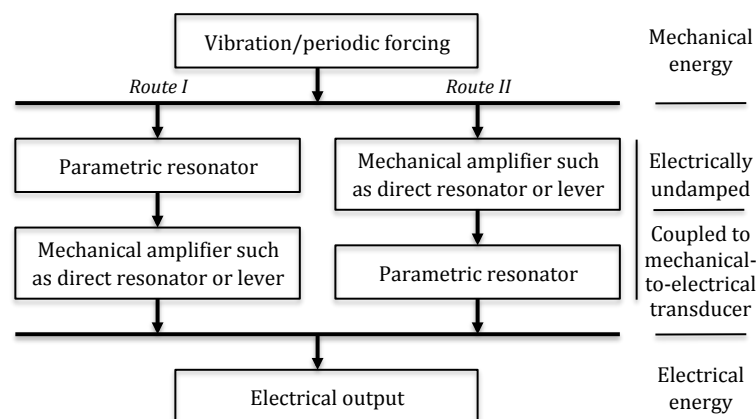
Figure 3.6: Design routes to minimise the initiation threshold amplitude to activate parametric resonance at lower acceleration levels.

Route I represents an electrically undamped parametric resonator coupled to a subsidiary mechanical amplifier where electrical damping is applied. The instability region in Route I is intrinsically lowered towards the horizontal axis of the Strutt diagram as shown in Figure 3.7b. Route II employs an electrically undamped mechanical amplifier as an initial mechanical amplifier to magnify the base excitation fed into the electrically damped parametric resonator. Here, the horizontal axis is brought up towards the instability region.

(a) Impact of damping   **(b)** Impact of design routes
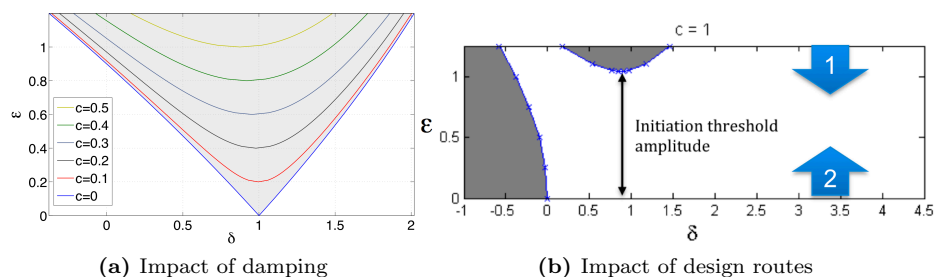
Figure 3.7: Increasing damping increases initiation threshold and the passive design routes 1 (electrically undamped parametric resonator) and 2 (amplification of base excitation) to minimise this threshold.

Initial displacement

A parametric excitation orthogonal to the oscillatory displacement is incapable to yield a forced response from the oscillator. Therefore, if the initial displacement rests at a zero position, oscillatory response from a parametric excitation, regardless of amplitude, cannot ensue as the system is stuck in a stable equilibrium. For such a system to experience the onset of periodic parametric modulation in its system parameter, an initial non-zero displacement is mandatory. Alternatively, a combination of direct excitation, either intentionally or an multi-axial leakage from the orthogonal driving force, can push the system out of stable equilibrium. The system can also be placed to rest in an unstable equilibrium such that a zero displacement is typically rare in the first place.

Frequency and time dependancy

At higher amplitudes, the instability regions becomes wider and the operational frequency bandwidth of parametric resonance becomes broader. Nonetheless, this is in essence still a resonant phenomenon and it suffers from the same limited operational frequency bandwidth as direct resonance. However, unlike direct resonance, when operating outside the operational frequency bandwidth, no parametric response can be accessed. Therefore, operation outside these frequency bands has to rely solely on non-resonant directly forced response.

In the time domain, like directly excited resonance, parametric resonance experiences a transient build-up until a steady-state resonant peak is attained. This transient build-up state is typically longer for resonance arising from parametric modulation rather than forced excitation as illustrated in Figure 3.8. However, once a parametric resonant peak has been achieved, frequency variation within the same instability region does not need to undergo the same prolonged build-up. Additionally, a relatively time-unvarying parametric excitation frequency is required to activate the dominance of the instability in the first place.

(a) Direct resonant build-up   **(b)** Parametric resonant build-up
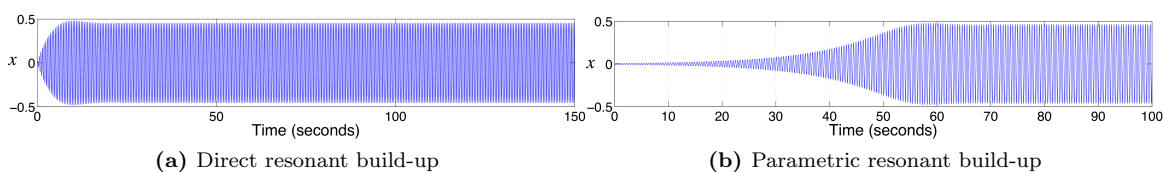
Figure 3.8: Time domain transient build-up of direct resonance and parametric resonance for the same system with the same damping and acceleration conditions.

Chapter 4

Pendulum-based parametrically excited vibration energy harvester

This chapter explores the first design route given in Figure 3.6 from Chapter 3 to passively reduce the initiation threshold amplitude for accessing parametric resonance by bringing down the instability regions towards the base axis of the Strutt diagram.

4.1 Concept

Figure 4.1 presents the general model of the design iteration explored, based on Route I as described in figure 3.6. The core mechanism involves a pendulum, which can be driven as either a direct resonator or a parametric resonator. Figure 4.1a is a simple pendulum where the oscillatory angular displacement is directly damped by a transducer. Figure 4.1b consists of an electrically undamped pendulum on the left-hand-side of the pivot, which is allowed to freely experience a an angular oscillatory build up with minimal effect from the dominant electrical damping of the transducer. As the pendulum oscillates, the periodic unbalancing of the lever beam oscillates the right-hand-side of the lever beam in the x plane, which is then electrically damped by a transducer.

(a) Pendulum (b) Pendulum coupled to a lever
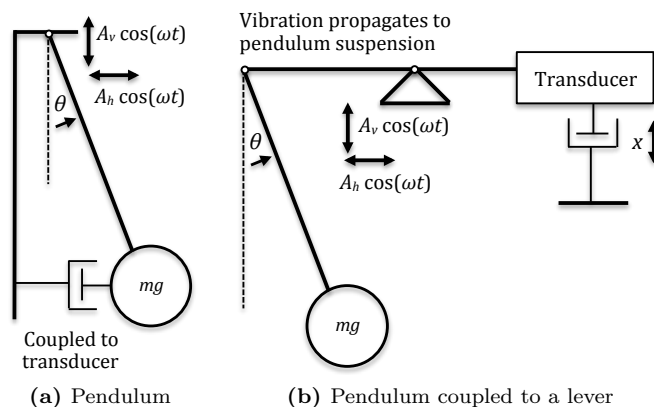
Figure 4.1: Design iteration where the parametric resonator (pendulum) is not directly electrically damped but connected to transfer energy to a secondary oscillating system in order to yield intrinsically low initiation threshold (b) compared to a system where the pendulum is directly damped by the transducer (a).

4.2 Analytical

4.2.1 Assumptions

Assumptions made for deriving the analytical model of the pendulum and pendulum-lever system are listed below.

- Lever beam
  - Perfectly stiff.
  - Does not vibrate as a free beam.
- Pendulum arm is
  - Perfectly stiff.
  - Moves in single plane.
- Friction at pivot points and air resistance included in damping c.
- Base and stand are perfectly stiff with no vibrational response.
- Vibrational excitations are propagated from the base to all points along the beam.
  - Input excitation at the base (pivot) is translated to the pendulum suspension with negligible loss.
  - Input excitation's amplitude and frequency at the base is the same as that at the pendulum suspension.
- Left-hand side (LHS) weight is dominated by the pendulum mass.
- Right-hand side (RHS) weight is dominated by the counter mass and the transducer.

4.2.2 Simple pendulum

Employing the Newtonian Second Law of Motion to describe the movement of a pendulum, Equations 4.1 and 4.2 can be derived.

$$F = -mg\sin\theta \tag{4.1}$$

$$a = -g\sin\theta \tag{4.2}$$

where, F is the applied force, m is mass, g is acceleration due to gravity, a is applied acceleration and θ is angular displacement. Assuming small angle approximation ($\theta \ll 1$ rad), differentiating arc length s and employing Equation 4.2, the velocity v and acceleration a can be derived.

$$s = l\theta \tag{4.3}$$

$$\frac{\mathrm{d}s}{\mathrm{d}t} = l\frac{\mathrm{d}\theta}{\mathrm{d}t} = v\theta \tag{4.4}$$

$$\frac{\mathrm{d}^2 s}{\mathrm{d}t^2} = l\frac{\mathrm{d}^2\theta}{\mathrm{d}t^2} = a = -g\sin\theta \tag{4.5}$$

Simple harmonic angular natural frequency ω_0 is given by Equation 4.6.

$$\omega_0 = 2\pi f_0 = \sqrt{\frac{g}{l}} \tag{4.6}$$

where, l is the pendulum active length and f_0 is the natural frequency. Simple un-damped pendulum is given by Equation 4.7 and damped pendulum is given by Equation 4.8.

$$\frac{\mathrm{d}^2\theta}{\mathrm{d}t^2} + \omega_0^2 \sin\theta = 0 \tag{4.7}$$

$$\frac{\mathrm{d}^2\theta}{\mathrm{d}t^2} + c\frac{\mathrm{d}\theta}{\mathrm{d}t} + \omega_0^2 \sin\theta = 0 \tag{4.8}$$

where, c is the damping constant. Equation 4.9 adds a periodic driving force to the damped pendulum.

$$\frac{\mathrm{d}^2\theta}{\mathrm{d}t^2} + c\frac{\mathrm{d}\theta}{\mathrm{d}t} + \omega_0^2 \sin\theta = \frac{A}{l}\omega^2 \cos(\omega t) \tag{4.9}$$

where, A is the excitation displacement amplitude and ω is the excitation frequency.

4.2.3 Pendulum driven at suspension

Equation 4.10 demonstrates the motion when the pendulum is driven at its suspension point.

$$\frac{\mathrm{d}^2\theta}{\mathrm{d}t^2} + c\frac{\mathrm{d}\theta}{\mathrm{d}t} + \omega_0^2 \sin\theta = -\frac{\mathrm{d}^2(\frac{x_0}{l})}{\mathrm{d}t^2}\cos\theta + \frac{\mathrm{d}^2(\frac{y_0}{l})}{\mathrm{d}t^2}\sin\theta \tag{4.10}$$

where, x_0 and y_0 are horizontal x-plane and vertical y-plane excitation.

When horizontally driven,

$$x_0 = A_h \cos(\omega_h t) \tag{4.11}$$
$$y_0 = 0 \tag{4.12}$$

where, A_h and ω_h are the horizontal excitation displacement amplitude and horizontal excitation frequency respectively.

When vertically driven,

$$x_0 = 0 \tag{4.13}$$
$$y_0 = A_v \cos(\omega_v t) \tag{4.14}$$

where, A_h and ω_h are the vertical excitation displacement amplitude and vertical excitation frequency respectively.

When rotationally (vertically and horizontally) driven,

$$x_0 = A_h \cos(\omega_h t) \tag{4.15}$$
$$y_0 = A_v \cos(\omega_v t) \tag{4.16}$$

Substituting these conditions into Equation 4.10, horizontally driven at suspension is given by Equation 4.17.

$$\frac{\mathrm{d}^2\theta}{\mathrm{d}t^2} + c\frac{\mathrm{d}\theta}{\mathrm{d}t} + \omega_0^2 \sin\theta - \omega_h^2 \frac{A_h}{l} \cos(\omega_h t)\cos\theta = 0 \tag{4.17}$$

Vertically driven at suspension is given by Equation 4.18.

$$\frac{\mathrm{d}^2\theta}{\mathrm{d}t^2} + c\frac{\mathrm{d}\theta}{dt} + (\omega_0^2 + \omega_v^2 \frac{A_v}{l} \cos(\omega_v t))\sin\theta = 0 \tag{4.18}$$

θ here has time domain in its coefficient is a variant of the damped Mathieu equation previously seen in Equation 3.28. Therefore, the excitation applied in this scenario (vertical excitation of pendulum) is parametric in nature when the frequency is in the vicinity of the instability regions.

Rotationally driven at suspension is given by Equation 4.19.

$$\frac{\mathrm{d}^2\theta}{\mathrm{d}t^2} + c\frac{\mathrm{d}\theta}{\mathrm{d}t} + (\omega_0^2 + \omega_v^2 \frac{A_v}{l} \cos(\omega_v t))\sin\theta - \omega_h^2 \frac{A_h}{l} \cos(\omega_h t)\cos\theta = 0 \tag{4.19}$$

In this scenario, both direct (horizontal) and parametric (vertical) excitation are present. For small angle approximation, $\sin\theta \approx \theta$ and $\cos\theta \approx 1$. Equations 4.17, 4.18 and 4.19 can be rewritten as Equations 4.20, 4.21 and 4.22 respectively.

$$\ddot{\theta} + c\dot{\theta} + \omega_0^2\theta - \omega_h^2 \frac{A_h}{l} \cos(\omega_h t) = 0 \tag{4.20}$$

$$\ddot{\theta} + c\dot{\theta} + (\omega_0^2 + \omega_v^2 \frac{A_v}{l} \cos(\omega_v t))\theta = 0 \tag{4.21}$$

$$\ddot{\theta} + c\dot{\theta} + (\omega_0^2 + \omega_v^2 \frac{A_v}{l} \cos(\omega_v t))\theta - \omega_h^2 \frac{A_h}{l} \cos(\omega_h t) = 0 \tag{4.22}$$

For large angle approximation, Taylor expansion can be employed to approximate the $\sin\theta$ and $\cos\theta$ terms as given in Equations 4.23 and 4.24.

$$\sin\theta = \theta - \frac{\theta^3}{3!} + \frac{\theta^5}{5!} - \frac{\theta^7}{7!} + \frac{\theta^9}{9!} - \frac{\theta^{11}}{11!}... \tag{4.23}$$

$$\cos\theta = 1 - \frac{\theta^2}{2!} + \frac{\theta^4}{4!} - \frac{\theta^6}{6!} + \frac{\theta^8}{9!} - \frac{\theta^{10}}{10!}... \tag{4.24}$$

4.2.4   Pendulum coupled to lever beam

The core mechanism of the pendulum-lever design is illustrated by Figure 4.2 and involves the propagation of vibrational energy from the anchored pivot to drive the pendulum at its suspension.
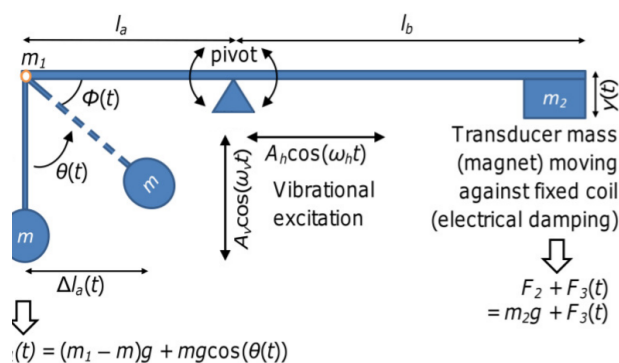
Figure 4.2: Working mechanism of the pendulum-lever system. Horizontally driving ($A_h \cos \omega_h t$) the pendulum equates to direct excitation, which allows the activation of direct resonance when ω_h equals the pendulum's natural frequency ω_0. On the other hand, vertically driving the pendulum ($A_v \cos \omega_v t$) is a form of parametric excitation and can activate parametric resonance when $\omega_v \approx 2\omega_0$. Displacement induced by pendulum motion is further mechanically amplified onto the transducer side by the lever.

A lever beam is balanced in a static scenario when the moments about the pivot are balanced. When angular displacement $\theta(t)$ is non-zero in dynamic motion, the lever beam (acting as an additional mechanical amplifier) is unbalanced and drives the transducer in the vertical direction. $F_1(t)$ is the force exerted by the weight of pendulum, F_2 is the counterweight of the transducer side and $F_3(t)$ is the dynamic force acting on the lever beam due to the electrical damping of the transducer.

The equilibrium equations describing the lever beam balanced at rest ($\theta(t) = \theta(0) = 0$) is given by Equations 4.25 to 4.29.

$$F_1(t)l_a(t) = F_2 l_b \tag{4.25}$$

$$\text{where, } F_1(t) = (m_1 - m)g + mg\cos(\theta(t)) \tag{4.26}$$

$$\text{and, } F_1(0) = (m_1 - m)g + mg\cos(0) = m_1 g \tag{4.27}$$

$$\text{also, } F_2 = m_2 g \tag{4.28}$$

$$\text{therefore, } m_1 g l_a(0) = m_2 g l_b \tag{4.29}$$

where, m is the pendulum mass, m_1 is the total mass of the pendulum side, m_2 is the total mass of the transducer side, $l_a(t)$ is the active length between the centre of mass of the pendulum and the pivot, $l_a(0)$ is the constant parameter of static l_a at rest and l_b is the active length between the centre of mass of the transducer side and the pivot. Under dynamic response, $l_a(t)$ is represented by Equation 4.30 and unbalance is induced in the lever beam.

$$l_a(t) = l_a(0) - \text{sgn}(\theta(t))\Delta l_a(t) \tag{4.30}$$

$$\text{where, } \Delta l_a(t) = l\cos(\phi(t)) \tag{4.31}$$

where, $\Delta l_a(t)$ is the change in active length $l_a(t)$ when pendulum is in motion and $\phi = 0.5\pi - \theta$. As the lever beam rocks about the pivot as a function of time, the transducer side mass experiences displacement in the y plane. For $l_b \gg y(t)$, small arc angle can be assumed and $y(t)$ can be approximated as simple vertical displacement.

4.2.5   Mechanical-to-electrical

The mechanical work done against the electrical damping by the transducer and the electrical power extractable from the system can be estimated by the dynamic forces about the lever beam. Therefore, the governing equation of the system sums up to the following.

$$((m_1 - m)g + mg\cos(\theta(t))) \cdot l_a(t) = l_b(m_2 g + F_3(t)) \tag{4.32}$$

The $F_3(t)$ term here is assumed to be approximately equal to the mechanical force from the resultant torque due to imbalance in the lever when θ is non-zero. This assumption is true for an ideal transducer where conservation of energy holds during mechanical-to-electrical power conversion, while taking into account the various damping terms. The squared of displacement is directly related to electrical power output P_{elec} [31], therefore is: $\theta^2 \propto y^2 \propto P_{elec}$. An estimate of the theoretical maximum electrical power output achievable $P_{maxelec}$, under ideal electrical impedance conditions (when electrical damping D_e equals parasitic damping D_p) is assumed in equation 4.33. Detailed electromechanical derivation is explored in Chapter 2 and [31].

$$P_{maxelec} \approx \frac{(m'a')^2}{8D_p} \tag{4.33}$$

where, m' is a generic mass and a' is the time-varying-acceleration of this mass. The generic '$m'a'$' term from this equation is the mechanical force experienced by an ideal mechanical-to-electrical transducer. Therefore, $m'a' \approx F_3$ and an estimate of the maximum electrical power output can be calculated by substituting this term back into equation 4.32 to obtain the $\theta(t)$ dependent power output relationship in equation 4.34. $\theta(t)$ itself is determined by one of the equations 4.17 to 4.19, depending on the excitation criteria.

$$P_{maxelec}(t) \approx \frac{1}{8D_p} \cdot \left(\frac{((m_1 - m)g + mg\cos(\theta(t))) \cdot l_a(t)}{l_b} - m_2 g\right)^2 \tag{4.34}$$

The actual maximum power extractable at the load ($P_{maxload}$) also depends on the impedance conditions of the transducer as defined in Equation 4.35 [9, 14].

$$P_{maxload} = P_{maxelec} \cdot \frac{R_{load}}{R_{load} + R_{coil}} \tag{4.35}$$

where, R_{load} is the resistive load and R_{coil} is the resistance of the coil. While electrical damping directly resists $y(t)$, it also has a fractional effect on $\theta(t)$ as it restricts the dynamic motion of the lever. The actual operating efficiency of the system and the transducer as well as additional nonlinear damping factors further reduce the maximum power estimated above. Therefore, various fitted numerical factors (either constants or polynomial functions of displacements for higher order nonlinearities) are required as coefficients for variables such as $F_3(t)$, D_p, D_e and the feedback damping from D_e to the pendulum damping in order to numerically provide a more realistic estimate and to match the experimental model.

4.3   Numerical

This section employs MATLAB and SimuLink to numerically calculate and simulate direct resonant and parametric resonant response of the pendulum-lever system for vibration energy harvesting. A sinusoidal signal of $\omega^2 A \cos \omega t$ is assumed as the excitation, where ω and A are the excitation frequency and displacement amplitude respectively.

The investigation of the dynamic response of angular displacement of the pendulum subjected to direct and parametric excitations serves as the primary source of evaluation. Generally speaking, beyond the initiation threshold excitation amplitude, the oscillatory amplitude growth of the parametric resonance experiences prolonged transient build-up time but can accumulate to a higher steady state value at certain boundary conditions.

The direction of the curvature of the transient state is specific to the respective resonant build-up and can serve as an identifier for parametric resonance. This is a result of the varying influence from linear and nonlinear damping. The plots shown in Figure 4.3, 4.4, 4.5 and 4.6 contrast the characteristics of the direct and parametric responses under various linear damping conditions while consisting of a high amplitude-dependent eigenfrequency shift and nonlinear damping factor (negligible at low amplitudes).

(a) Direct resonance   **(b)** Parametric resonance
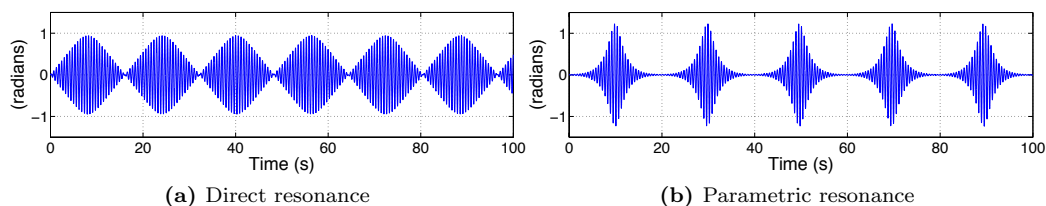
Figure 4.3: Pendulum undamped oscillatory amplitude build up.

Without the presence of the dominant linear damping in Figure 4.3, neither cases are able to achieve a constant steady state solution. The modulation is a back-and-forth power transfer with other degrees-of-freedom as the resonator (vibration absorber) is incapable of 'holding onto' the stored energy.

(a) Direct resonance   **(b)** Parametric resonance
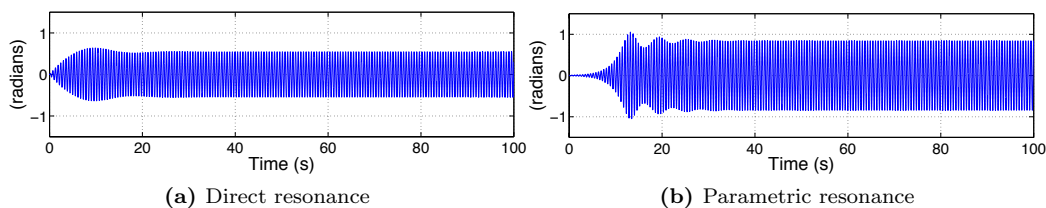
Figure 4.4: Pendulum mildly damped oscillatory amplitude build up.

When mild damping is introduced in Figure 4.4, an initial beating effect can be seen prior to settling to a constant steady-state value. This initial instability at higher amplitudes act as the oscillating over-shoots by the less-than critical damping and is more significant for parametric resonance.

When damping is higher and near critical in Figure 4.5, the response is more stable and smooth. With increasing linear damping, the system approaches the stability boundaries of the instability region for parametric resonance. Therefore, the peak attainable becomes smaller and the transient

(a) Direct resonance   **(b)** Parametric resonance
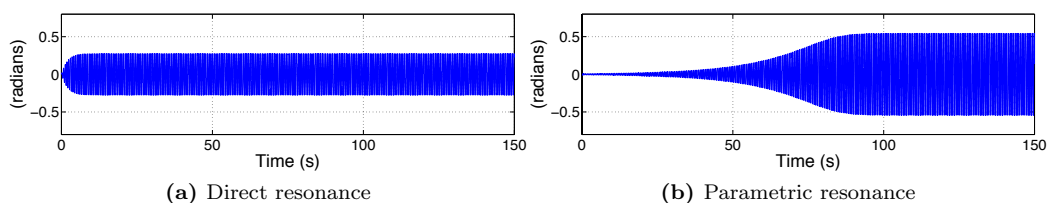
Figure 4.5: Pendulum near critically damped oscillatory amplitude build up.

build-up time required to attain that peak becomes longer. Despite the much prolonged build-up state compared to direct resonance, parametric resonance has the potential to saturate at a much higher peak with the same given damping and excitation conditions.

(a) Direct resonance   **(b)** Parametric resonance
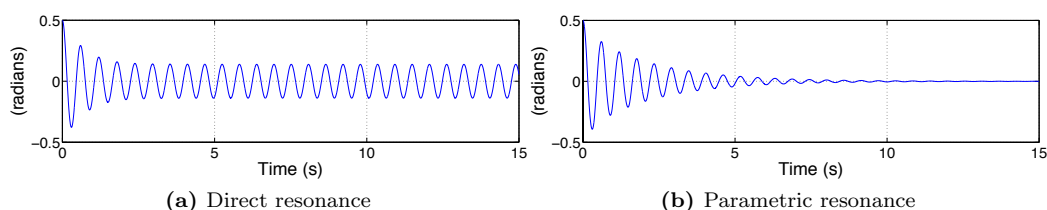
Figure 4.6: Pendulum over damped oscillatory amplitude build up with an initial displacement of 0.5 rad.

In Figure 4.6, overdamping of direct resonance is contrasted with parametric resonance where its excitation amplitude is lower than the damping-dependent initiation threshold amplitude. Upon overcoming inertia, the direct resonator will always exhibit a response regardless of the magnitude of the excitation. However, parametric excitation yields zero steady-state response for this excitation scenario as the system operates inside the stable regions of the Strutt diagram and has bounded solutions.

A full numerical model using MATLAB Simulink was constructed with parameters in Table 4.1 to investigate the behaviour of the pendulum-lever vibration energy harvester subjected to various excitation conditions.

Table 4.1: System parameters employed in the numerical simulation of the pendulum-lever VEH.

m (kg)	0.51	R_{coil} (kΩ)	5.00
m_1 (kg)	0.61	R_{load} (kΩ)	5.00
m_2 (kg)	0.31	c (Nsm^{-1})	0.2
l (m)	0.06	D_p (Nsm^{-1})	3
$l_a(0)$ (m)	0.100	Feedback D_p to c	1
l_b (m)	0.200	Power efficiency	0.5
f_n (Hz)	2.04		

The angular displacement θ is directly related to vertical displacement, and henceforth the voltage output, of the transducer end lever beam y as established in Section 4.2. However, the alternating current (AC) voltage output waveform is not symmetrical about the base axis due to the asymmetrical lever unbalancing effect from the periodic variation in active length l_a. With positive θ, the lever displaces in the preferred direction of the counterweight, but a cancelling out of opposing forces can be observed when θ displaces away from the pivot. Therefore, a full wave rectification of the voltage output from the pendulum-lever transducer will yield a waveform where the flipped negative half waveform is smaller than the accompanying positive waveform as shown in Figure 4.7.

54
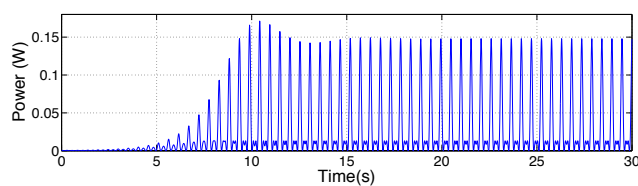
Figure 4.7: Full wave rectified power output of the pendulum-lever generator. The flipped negative output is smaller than the positive side due to asymmetrical effect of pendulum displacement θ on active length $l_a(t)$ and the lever beam motion.

Figure 4.8b compares the qualitative characteristics of the frequency domain power response of the same system operating at 1st mode of direct resonance and principal parametric resonance.

(a) Ordinary resonance   **(b)** Parametric resonance
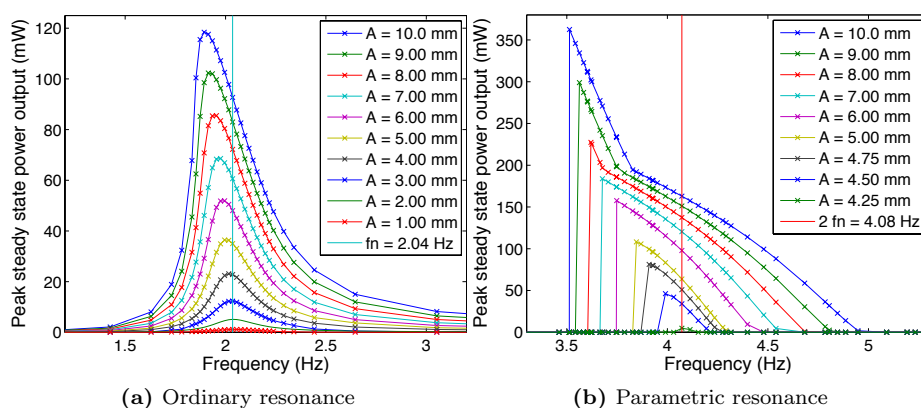
Figure 4.8: Comparison between the numerically computed response for parametric resonance and direct resonance in the frequency domain. Onset of nonlinearity, and therefore the widening of frequency band, around natural frequency f_n is relatively gradual for direct resonance with increasing excitation amplitude A. On the other hand, parametric resonance demonstrates relatively more significant nonlinearity even at low A followed with the onset of higher orders of nonlinearity (steeper peaks) at higher A. However, the latter has zero steady state response immediately outside the frequency band and/or when A is below an initiation threshold amplitude, which is around 4.25 mm in this setting.

Vibrational non-linearities and eigenfrequency shifts play a more significant role in parametric resonance, especially at low amplitudes. Direct resonance on the other hand, only experiences duffing nonlinearities at high amplitudes as shown by the spring softening effect in Figure 4.8a. Therefore, for a given excitation, parametric resonant peak can exhibit a relatively, albeit mildly, wider operational frequency band. However, the higher instability regions on the left-hand-side (LHS) of the natural frequency mark line in Figure 4.8b are only accessible when an appreciable initial displacement is present or during a downwards frequency sweep. This is because during an upward frequency sweep, initial system displacement is absent upon reaching these otherwise operational frequency band; in other words, the system is trapped at a lower bifurcation point.

Parametric resonance experiences a steep increase in nonlinear response at high excitation amplitudes as shown by the elongated peak on the LHS of Figure 4.8b. This region in the frequency domain, again, is only seen with presence of large initial displacement or during downwards frequency sweep and matches the experimental observation made by Requa (2006) [261] on a MEMS cantilever driven into parametric resonance. A theoretical explanation for this higher order of nonlinear instability is that at large amplitudes, parametric oscillation no longer approximate to simple harmonic motion but undergoes Hopf bifurcation to a limit cycle motion [246], hence, yielding an even faster resonant growth.

Figure 4.9 illustrates the power response in respect to excitation amplitude. With increasing excitation amplitude, the power response increases with a second order polynomial relationship since θ^2 is directly proportional to power output. However, parametric resonant response is non-existent below the initiation threshold amplitude for the given damping condition. Beyond this threshold, parametric resonance rapidly outperforms direct resonance with a much steeper nonlinear growth gradient. Furthermore, the additional steep jump in amplitude growth rate at high excitation amplitudes is present, which is the same effect seen from the elongated peak in Figure 4.8b.
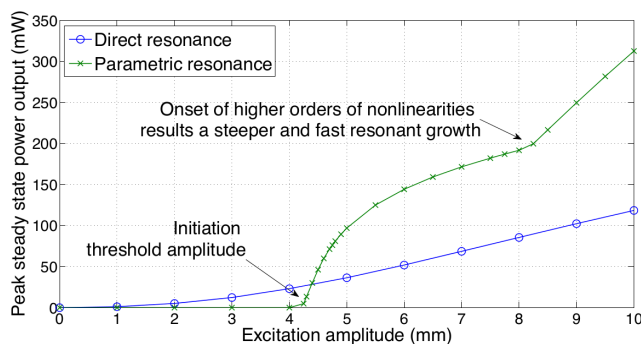
Figure 4.9: Quantitative numerical comparison between the peak power response for direct and parametric resonance to varying excitation amplitudes. Beyond a certain threshold of the excitation amplitude, parametric resonance rapidly outperforms direct resonance.

Numerically, parametric resonance has been shown to possess the potential to operate in a region where its mechanical-to-electrical conversion efficiency outperforms direct resonance. However, due to the presence of the initiation threshold amplitude, a region where direct resonance is superior also exist. Also, outside the operational frequency bands, response from parametric resonance is non-existent. Therefore, parametric resonance becomes increasingly rewarding at higher excitation amplitudes due to the higher order polynomial growth behaviour demonstrated in Figure 4.9.

4.4 Experimental

4.4.1 First generation macro pendulum-lever VEH

Design

Figure 4.10 illustrates the first generation macro-scale parametrically excited vibration energy harvester (PEVEH) prototype design schematic drawn by SolidWorks. The component volume calculated by SolidWorks is approximately 500 cm^{-3} and the minimum practical device volume is around 1800 cm^{-3}. An electromagnetic transducer is employed with a component volume of $\sim$50 cm^{-3} and a practical volume of $\sim$90 cm^{-3}.

The system primarily constituents a lever beam with pendulum resting on the right-hand-side (RHS) and the magnet of the transducer resting on the left-hand-side (LHS). The RHS lever length is shorter than that of the RHS in order to enable displacement amplification via the lever beam. Displacement and therefore velocity amplification aids the magnification of emf induced from the electromagnetic induction. Variable and tuneable parameters include pendulum length, lever beam active length on either sides as well as pendulum mass and counterweight mass. Lubricated ball
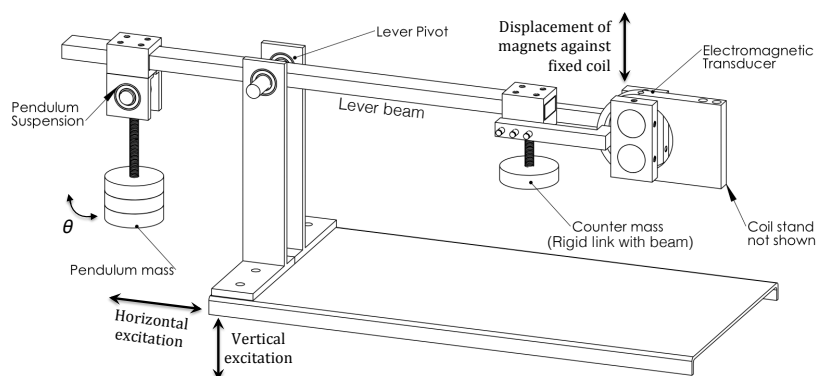
Figure 4.10: Dimetric view of the initial macro PEVEH prototype design schematic.

bearings have been employed to enable angular motion for the pendulum suspension and lever pivot with minimal mechanical damping and parasitic energy dissipation.

Prototype

The experimental prototype is shown in Figure 4.11, mounted on an air cooled shaker and the driving force is quantified by an accelerometer attached to the vibrating platform with charge sensitivity of 26∼29.7 pC$_{pk}$/g$_{pk}$ and voltage sensitivity 15.92∼18.33 mV$_{pk}$/g$_{pk}$.
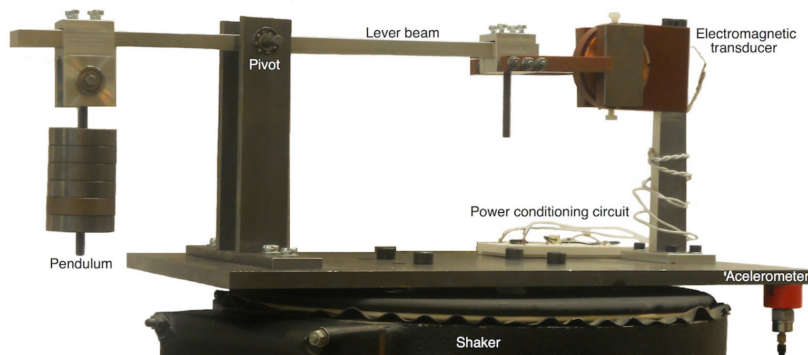
Figure 4.11: Preliminary PEVEH prototype.

The electromagnetic transducer is based on the sandwiched magnet-coil-magnet configuration [58, 59]. This configuration, shown in Figure 4.12, involves pairs of attracting magnets mechanically held apart and the coil rests in the high flux density air gap in between. Magnetic keepers (mild steel plates) on two away sides further help to concentrate the flux linkage within the transducer.

The magnets used in this prototype are disc-shaped sintered grade N38H Neodymium Iron Boron (NdFeB) with dimensions of 22 mm diameter and 10 mm depth. The orthocyclically wound copper coil is also cylindrical in shape with dimensions of 50 mm outer diameter, 5mm inner diameter, 10 mm depth, 90 microns wire diameter, an estimated coil turns in the order of one hundred thousand and coil resistance of approximately 15.5 kΩ ± 0.5kΩ. The housing of the coil and the magnets are made from a non-magnetic and non-conductive material: a type of machinable stiff plastic polymer.

The AC voltage output from the coil is fed into a simple full wave rectifier (Figure 4.13) and DC voltage can then be measured by a voltage probe of a digital oscilloscope across the parallel load resistance to calculate the DC power output of the PEVEH prototype with $P = \frac{V^2}{R}$.

(a) Configuration

(b)   Electromagnetic flux field simulation
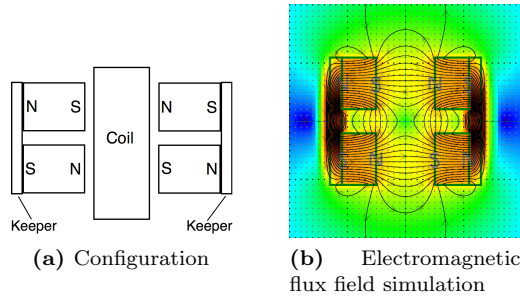
Figure 4.12: Magnet-coil-magnet configuration with magnetic keeper (mild steel) on either sides. Magnetic flux lines are concentrated in the space in between the magnet pairs where the coil is to be placed.
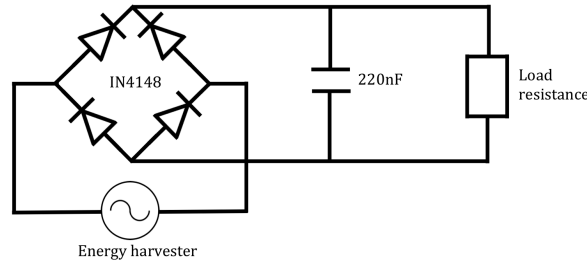
Figure 4.13: Full wave rectifier assuming VEH as an AC source.

Result

Following resistance matching, the ideal load resistance was experimentally found to be in the order of 5 kΩ. At this electrical load condition, excitations in excess of ∼0.4 ms^{-2} brought about the onset of the principal order parametric resonance. Higher orders of parametric resonance was not experimentally observed, potentially due to their increasingly narrower operational frequency bands and higher initiation threshold amplitudes. Figure 4.14 shows the AC voltage output build up from the transducer for the same prototype driven by comparable excitation acceleration levels. The qualitative characteristics matches the numerical simulation observed in Section 4.3.

(a) Direct, V$_{pp}$ = 21.8 V

(b) Parametric, V$_{pp}$ = 56.4 V
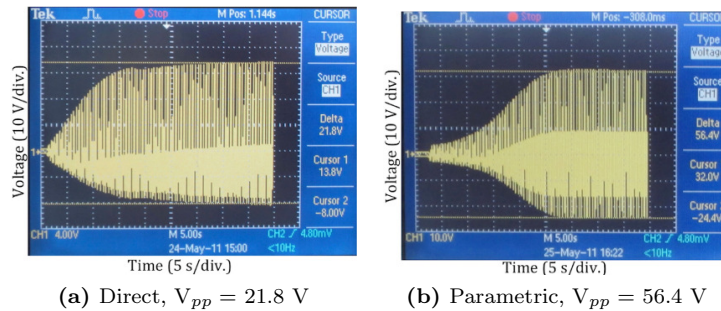
Figure 4.14: Experimental results of the oscillatory voltage amplitude build up (in time domain) driven by comparable excitation acceleration levels. Parametric resonance has a longer transient state but is able to attain a higher amplitude.

The absolute peak power recorded (within physical limits of the shaker and the prototype) at parametric resonance (vertical excitation) is 956.6 mW at 1.70 ms^{-2} and at direct resonance (horizontal excitation) is 27.75 mW at 0.65 ms^{-2}. Furthermore, parametric resonance at this excitation setting (from which the peak power value was noted) did not reach a steady state but was rather

constrained by the physical limits of the design, which only permitted the pendulum to undergo a maximum angular displacement of $\pm\frac{\pi}{2}$ radians. If larger angular displacements or circular motion are accommodated, then even higher power levels can be expected for this scenario.

For a given set of configured system parameters listed in Table 4.2, measured peak power responses at varying excitation levels are presented in Figure 4.15 and Table 4.3. The unmeasured parameters in Table 4.2 were numerically estimated and fitted in order to match the numerical model with the experimental power response. The second order polynomial D_e coefficient is a fitted nonlinear amplitude-dependent parameter.

Table 4.2: System parameters of the experimental prototype and fitted values of the corresponding numerical model (to match the recorded power response).

Measured		Numerically fitted	
m (kg)	0.71	c (Nsm^{-1})	0.2
m_1 (kg)	1.0	D_p (Nsm^{-1})	5.4
m_2 (kg)	0.41	D_e (Nsm^{-1})	100
l (m)	0.07	D_e coefficient	$0.06(|\theta|+1)^2$
l_a (m)	0.102	Feedback D_p to c	0.15
l_b (m)	0.255	Peak power efficiency (parametric)	0.45
f_n (Hz)	1.88	Peak power efficiency (ordinary)	0.15
R_{coil} (kΩ)	15.20		
R_{load} (kΩ)	5.40		

(a) Direct resonance   **(b)** Parametric resonance
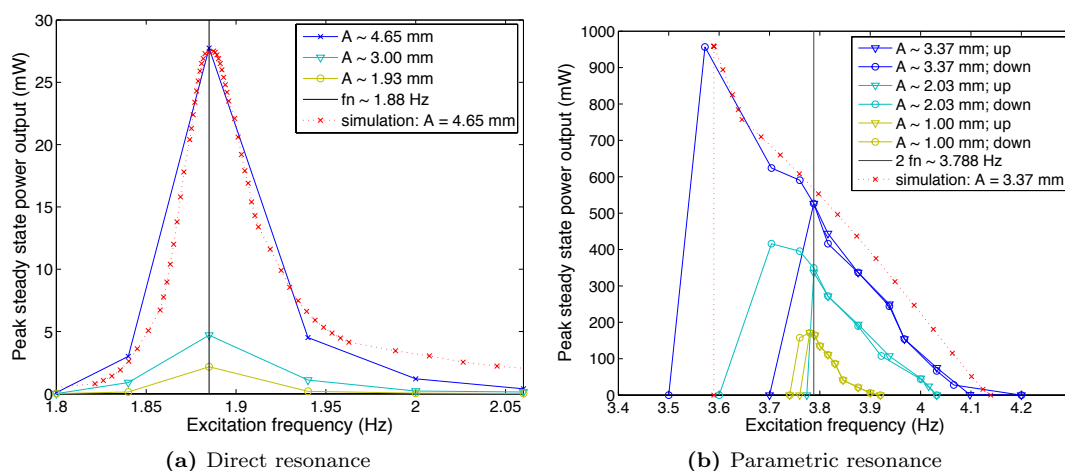
Figure 4.15: Experimental power response in frequency domain for various excitation amplitudes A. The fitted simulation equivalent of the recorded peak power data are also plotted. With higher A, nonlinearity associated with parametric resonance rapidly becomes significant and results in the widening of frequency bandwidth, while that of direct resonance remains relatively confined. The LHS nonlinear peaks have different responses for frequency upward and downward sweeps as these resonant responses are only achievable when significant initial displacements are present to allow the system to jump to the higher bifurcation point.

Within the physical limit of the shaker, direct resonance shown in Figure 4.15a did not exhibit observable vibrational nonlinearities while parametric resonant peak shown in Figure 4.15b demonstrated appreciable nonlinear peaks during downward sweeps. This bifurcation characteristics of the LHS of the natural frequency mark line of the parametric bode plot matches with the numerical model from Section 4.3. The steep jump of the nonlinear peak associated with parametric resonance at high amplitudes as described in figure 4.8b can also be seen for the highest amplitude peak here.

At similar excitation levels (see Table 4.3), parametric resonance yielded over 6 times higher

Table 4.3: Comparison of the experimental performance of direct and parametric resonances. Higher accelerations for direct resonance were not measured due to the physical amplitude limit of the employed shaker ($\sim$ 5 mm).

	Peak power (mW)	Frequency (Hz)	Amplitude (mm)	Acceleration (ms^{-2})	Normalised Power Density ($\mu\text{Wcm}^{-3}\text{m}^{-2}\text{s}^4$)
Direct	2.17	1.88	1.93	0.27	1.65E+01
	4.70	1.88	3.00	0.42	1.48E+01
	27.75	1.88	4.65	0.65	3.65E+01
Parametric	171.5	3.78	1.00	0.57	2.93E+02
	415.9	3.704	2.03	1.1	1.91E+02
	956.7	3.572	3.37	1.7	1.84E+02

peak power than its direct counterpart. In terms of power density normalised against the squared of excitation acceleration demonstrated an order of magnitude higher in performance in favour of the device driven into parametric resonance.

Figure 4.16 contrasts the frequency bands and extractable power for both resonances at similar input acceleration levels ($\sim$0.6 ms^{-2}). The darker shaded region represent the power region above the half power points. In this scenario, the parametrically driven system exhibited around 50 % wider operational frequency band. Taking the half power points of direct resonance as reference, the parametric case power curve experienced nearly a 3-fold broader frequency bandwidth with the lighter shaded region as the additional power regions.
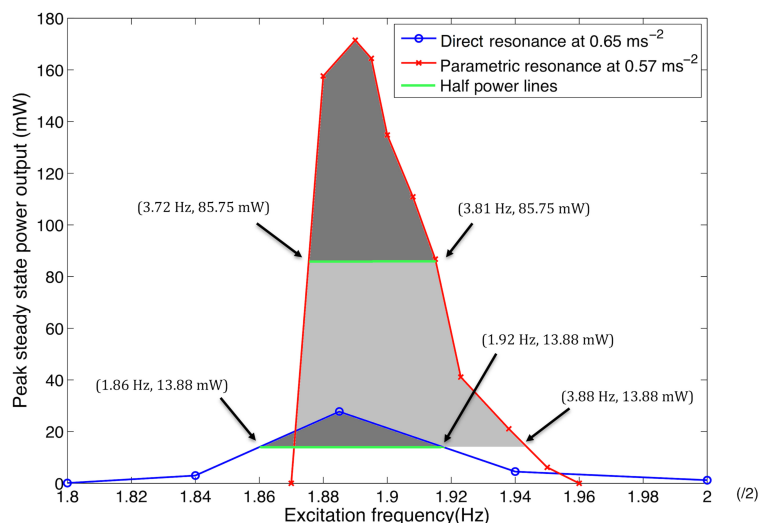
Figure 4.16: Experimental frequency bands and extractable power of parametric resonance (frequency scale halved for comparison) and direct resonance at comparable accelerations ($\sim$0.6 ms^{-2}). The darker shaded regions denote extractable power within the half power bands. The lighter shaded region represents the additional power extractable by parametric resonance above the half power points of direct resonance.

Table 4.4 briefly contrasts the power performance against selected current state-of-the-art macro-scale electromagnetic vibration energy harvesters, where all of them employ direct resonance. In terms of normalised power density, PEVEH driven into parametric resonance compares favourably against the current state-of-the-art. On the other hand, the less-than-top performance of the device driven into direct resonance suggests room for further transducer optimisation.

The principal source of damping (transducer) here acts on the secondary oscillating element (lever beam). Therefore, the initiation threshold amplitude for the primary oscillating element

Table 4.4: Comparing PEVEH with selected current state-of-the-art macro-sized electromagnetic vibration energy harvesters in terms of power density normalised against acceleration squared.

Reference	Peak power (mW)	Freq. (Hz)	Volume (cm^3)	Acceleration (ms^{-2})	Normalised Power Density (μWcm^{-3}m^{-2}s^4)
PEVEH (parametric)	171.5	3.57	1,800	0.57	***2.93E+02***
Perpetuum (2008) [56]	1.000	100	135	0.25	1.19E+02
Lumedyne (2008) [49]	1.000	53	27	1	3.70E+01
PEVEH (direct)	27.75	1.88	1,800	0.65	***3.65E+01***
Ferro Sol. (2009) [72]	5.270	60	170	0.98	3.23E+01
Hadas (2007) [74]	3.500	34.5	45	3.1	8.09E+00
Waters (2008) [48]	18.00	90	27	9.81	6.93E+00
Glynne-Jones (2001) [2]	2.800	106	3.66	13	4.53E+00

(pendulum) is intrinsically minimised due to the relatively low damping. In turn, a relatively higher initiation threshold exist if the principal source of damping acts on the same degree-of-freedom as the parametric excitation, which has been the main limiting factor that restricted notable absolute power improvements within practical acceleration levels for previous investigations [257, 26, 258].

The requirement of a non-zero initial displacement (to 'push' the system out of stable equilibrium) is another intrinsic property of most parametrically excited systems. A design that places the rest position in an unstable equilibrium could serve as a solution. This issue is addressed in Chapter 5.

(a) Corsair: pendulum-lever   **(b)** Swing: pendulum
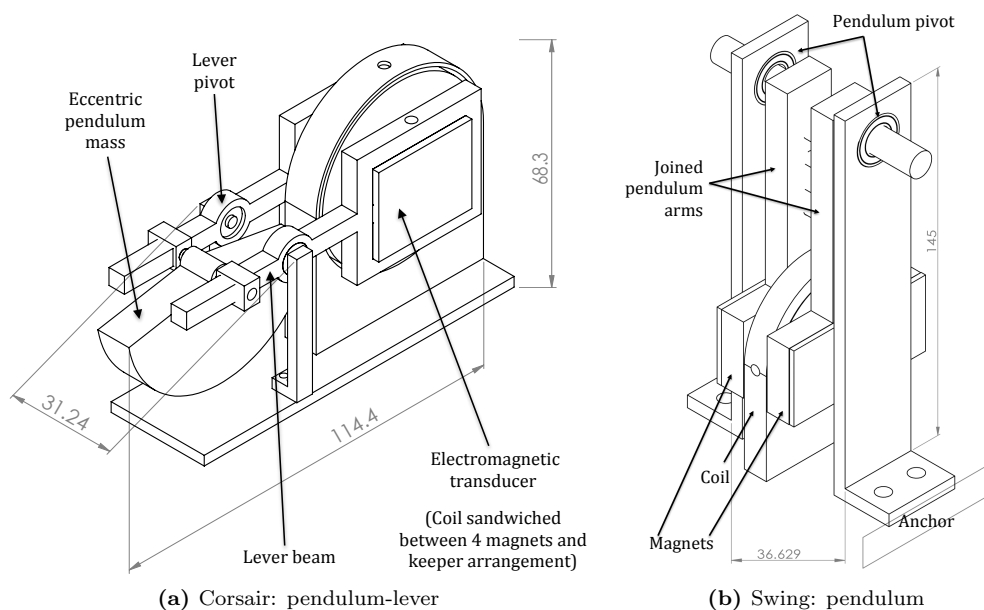
Figure 4.17: Second generation PEVEH design.

4.4.2   Second generation miniaturised pendulum and pendulum-lever VEH

Design

This section reports a miniaturised version of the pendulum-lever prototype investigated in Subsection 4.4.1 and a sole pendulum prototype of comparable volumetric size. The design schematic of the pendulum-lever VEH shown in Figure 4.17a is dubbed the Corsair while the pendulum VEH shown in Figure 4.17b is dubbed the Swing.

While the pendulum in Swing is directly damped by an electromagnetic transducer at the pendulum mass, the pendulum in Corsair is electrically undamped like the first generation macro-scale prototype. The eccentric pendulum is used to conserve volume and enable full rotational freedom that the macro-scale prototype did not possess. The estimated (by SolidWorks) practical device volume for both prototypes are approximately 300 cm^{-3} while the Corsair has ~80 cm^{-3} and Swing has ~150 cm^{-3} in component volume.

Prototype

The experimental prototypes of the Swing and the Corsair are shown in Figures 4.18 and 4.19 respectively. The harvesters were mounted on a shaking table and a 3-axis accelerometer was attached to the shaking platform to quantify the applied driving force with a sensitivity of 300 mV$_{pk}$/g$_{pk}$.
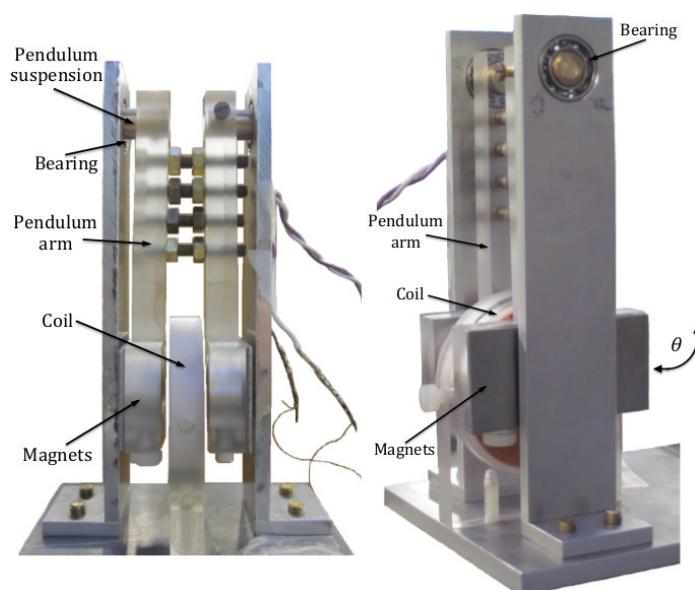
Figure 4.18: Electromagnetic pendulum harvester prototype: Swing.

The electromagnetic transducers of both harvesters employ the same coils used by the first generation prototype (Subsection 4.4.1). Corsair contains four rectangular NdFeB magnets (grade N35H) with individual dimensions of 30 mm length, 10 mm width and 5 mm depth. Swing consists of four circular magnets (grade N38H) with individual dimensions of 10 mm diameter and 10 mm depth. The four-magnet configuration was again employed to maximise flux density through the coil. The fixed coil is positioned in a sandwiched configuration in between each pair of magnets with an approximately 1 mm air gap. Additionally, two pieces of 1 mm thick rectangular mild steel plates have been magnetically attached the sides as magnetic flux keepers.

The simple full wave rectifier and parallel load resistance power conditioning circuitry was employed for the second generation prototypes as well. Optimal electrical load was experimentally found to be between 15 kΩ and 20 kΩ for both devices. Although the ideal load resistance varies depending on amplitude and the specific resonant regime, the change is still within the same order of magnitude. The Swing and Corsair possess measured natural frequencies around 1.7 Hz and 4.5 Hz respectively when subjected to horizontal excitation; thus, the expected principal parametric resonant frequencies are 3.4 Hz and 9.0 Hz respectively from vertical excitation.
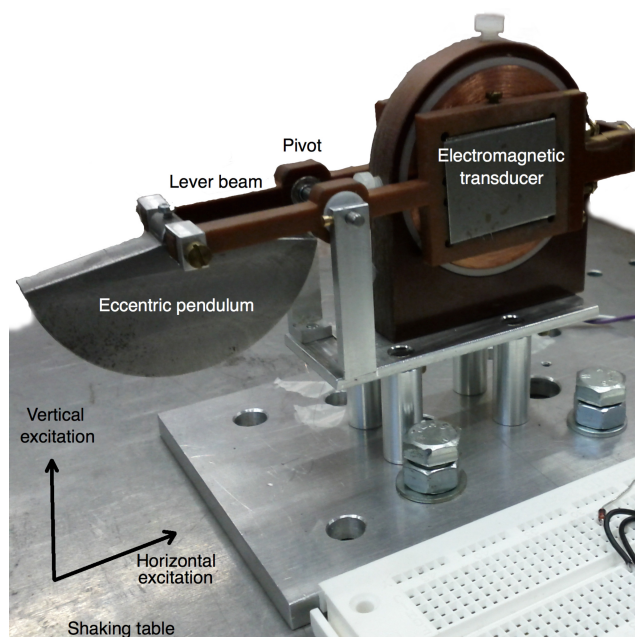
Figure 4.19: Electromagnetic pendulum-lever harvester prototype: Corsair.

Numerical analysis

Based on the numerical model previously established in Section 4.4.1 and the parameters listed in table 4.5, the initiation of parametric resonance was analysed for the two prototypes using ODE45 solver in MATLAB. A variation of the Strutt stability chart, plotting excitation frequency against input acceleration, for the Swing and Corsair prototypes are presented in figures 4.20 and 4.21.

Table 4.5: System parameters used to simulate the stability charts of the Swing and Corsair prototypes. Damping values are fitted to the experimental prototypes.

Parameter	Swing	Corsair	Units
Natural frequency	1.7	4.5	Hz
Pendulum length	86	12.2	mm
Lever length (pendulum side)	n/a	25	mm
Lever length (transducer side)	n/a	30	mm
Pendulum mass	0.205	0.097	kg
Lever counter mass	n/a	0.080	kg
Mechanical parasitic damping	84.4	18.8	N·s·m^{-1}
Electrical transducer damping	291	295	N·s·m^{-1}

It can be seen that the application of electrical damping, as the mechanical-to-electrical transducer is in operation, a noticeable increase in the initiation threshold of parametric resonance for the Swing prototype occurs. On the other hand, the presence of electrical damping has minimal effects on the Corsair prototype as the pendulum (the parametric resonator) is not directly subjected to the electrical damping of the transducer and is still allowed to freely build-up its oscillatory amplitude.

Result

Prototypes were subjected to direct (horizontal) and parametric (vertical) excitations. Parametric resonant onset at 3.4 Hz (twice the natural frequency) for the Swing has been observed for an

(a) Electrically undamped

(b) Electrically damped - significantly higher initiation threshold amplitude
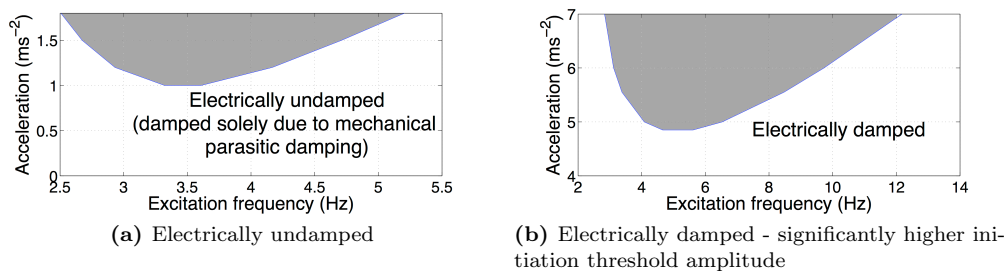
Figure 4.20: Simulated stability chart of the Swing prototype where the pendulum is electrically damped to complete the mechanical-to-electrical energy conversion. Shaded region represents the unbounded solutions of the Mathieu equation and the onset of parametric resonance. The addition of electrical damping pushed the initiation threshold from ~ 1 ms^{-2} to ~ 4.8 ms^{-2}.

(a) Electrically undamped

(b) Electrically damped - slightly higher initiation threshold amplitude
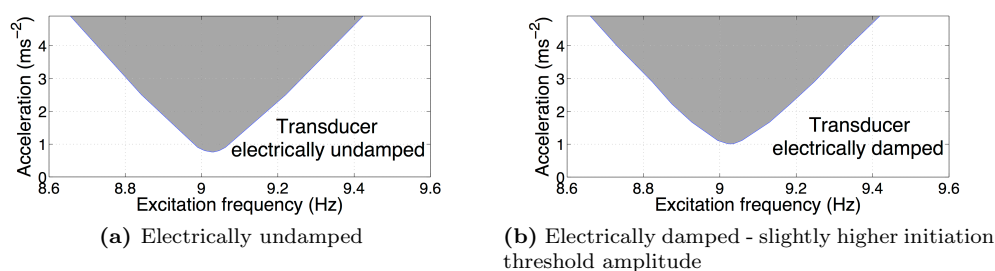
Figure 4.21: Simulated stability chart for the Corsair prototype where the pendulum is intrinsically electrically undamped and the lever beam is electrically damped as the transducer. Shaded region represents the unbounded solutions of the Mathieu equation and the onset of parametric resonance. The addition of electrical damping pushed the initiation threshold from ~ 0.76 ms^{-2} to ~ 1.0 ms^{-2}.

electrically undamped (open circuit) configuration when a minimum acceleration of approximately 1 ms^{-2} is attained. However, with the application of the resistive load ($\sim$17.6 kΩ, the ideal load for direct resonance), parametric resonance failed to initiate within the scanned acceleration range limited by the physical constraint of the shaking table (maximum displacement $\sim$10 mm, which translates to 4.56 ms^{-2} for 3.4 Hz).

On the other hand, the onset of parametric resonance for the electrically damped Corsair was much more readily at lower acceleration levels as shown in Figure 4.22. The pendulum can freely build up in oscillatory amplitude with relatively less damping restriction. The initiation threshold amplitude of the Corsair under ideal electrical load ($\sim$16.8 kΩ) was recorded at $\sim$1.1 ms^{-2} and the power performance of parametric resonance outraced direct resonance for accelerations in excess of $\sim$1.5 ms^{-2}. Figure 4.23 presents the frequency characteristics of the Corsair. At an excitation of 3.99 ms^{-2}, 12.21 mW (half power band of 0.17 Hz) and 35.67 mW (half power band of 0.20 Hz) were recorded for the direct resonant and parametric resonant peaks.

As acceleration increases deeper into the profitable region of parametric resonance, the power performance gap between parametric resonance and direct resonance widens increasingly. The onset of nonlinearities at high amplitudes help to mildly broaden the resonant peaks. No higher orders of parametric resonance were observed, potentially due to the fast narrowing of the frequency bandwidth of these higher orders. For larger than currently achievable excitation accelerations, the same parametric amplification characteristics is theoretically predicted for the Swing prototype as well. However, the onset of the profitable region for parametric resonance would be at a significantly larger
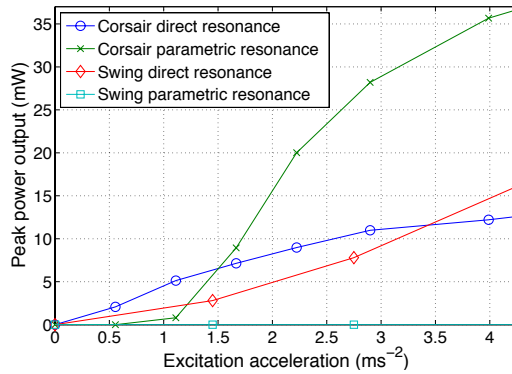
Figure 4.22: Power response per excitation acceleration levels for the electromagnetic Swing (pendulum) and Corsair (pendulum-lever) prototypes.

(a) Direct resonance	**(b)** Parametric resonance
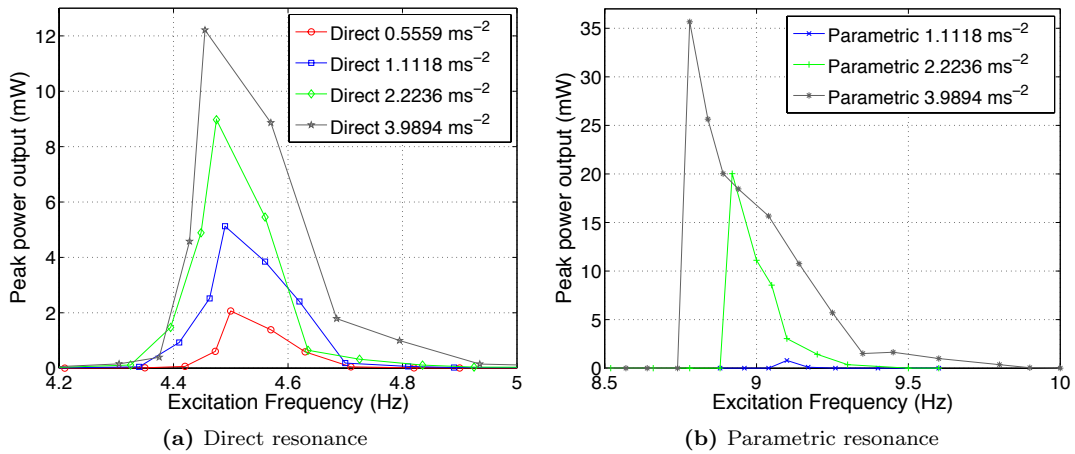
Figure 4.23: Power response of Corsair ($f_n \sim 4.5$ Hz) in the frequency domain.

acceleration level and only if the physical limit of the transducer was not reached before then.

4.5 Summary

A summarised comparison of the two resonant phenomena for VEH are presented in Table 4.6.

Table 4.6: A summarised comparison between direct and parametric resonances.

	Direct	**Parametric**
Peak power density normalised against acceleration	lower	an order higher
Increase in nonlinearity and frequency bandwidth with amplitude growth	minimally	immediately observable
Transient state	short	prolonged
Initiation threshold amplitude requirement	no	yes
Non-zero initial displacement requirement	no	yes
Response outside frequency bands	small	decays to zero

Parametrically driven harvesters, despite their potential capabilities of exhibiting significantly higher power performance, are not perfect. Therefore, the integration of both direct and parametric excitations to compensate and complement each other, can serve as an ideal solution.

Chapter 5

Cantilever-based parametrically excited vibration energy harvester

This chapter explores the second design route given in Figure 3.6 from Chapter 3 to passively reduce the initiation threshold amplitude for accessing parametric resonance by elevating the base axis towards the instability regions of the Strutt diagram.

5.1   Concept

Figure 5.1 presents the general model of the design iteration of Route II described in Figure 3.6. Unlike the design approach explored in Chapter 4, the parametric resonators here are directly subjected to electrical damping from a mechanical-to-electrical trasnducer.

(a) Cantilever   (b) Addition of initial spring
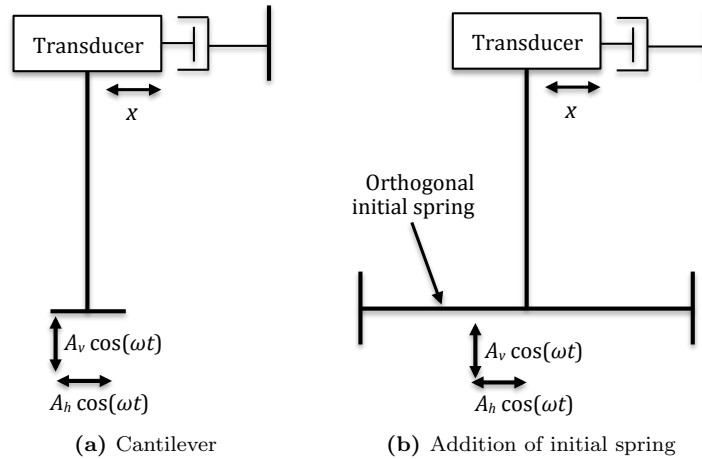
Figure 5.1: Design iteration with the addition of initial spring to amplify the base excitation fed into the parametric resonator (cantilever beam).

Figure 5.1a illustrates a simple cantilever whose oscillatory displacement in the x plane is electrically damped. Horizontal forcing along the same x plane corresponds to a direct excitation, while orthogonal driving force such as in the vertical direction can potentially act as the parametric excitation. In Figure 5.1b, an orthogonal clamped-clamped beam is added to the structure prior to the

anchor. This additional initial spring directly displaces along the same direction as the parametric excitation in the vertical axis. Therefore, the base vibration of parametric excitation along the vertical axis undergoes additive mechanical amplification before being fed into the vertically upright cantilever beam.

5.2   Amplification of base excitation

This section analytically and numerically explores a cantilever beam subjected to direct excitation and parametric excitation; as well as the influence of adding an initial spring structure in an attempt to minimise the initiation threshold amplitude of parametric resonance.

5.2.1   Cantilever resonator

The cantilever resonator is a common design choice for VEH [9]. Large displacements are achievable at the free end (ideal for electromagnetic and electrostatic transducers), while simultaneously high levels of strain can be induced near the clamped end (ideal for piezoelectric transducers) and offer lower natural frequencies than many other device configurations.

Like any harmonic resonator, such as the pendulum explored in Chapter 3, a cantilever resonator can be represented by the second order differential equation of a mass-spring-damper model as shown in Equation 5.1

$$\frac{\mathrm{d}^2 x}{\mathrm{d}t^2} + 2\zeta\omega_0 \frac{\mathrm{d}x}{\mathrm{d}t} + \omega_0^2 x + \mu x^3 = 0 \tag{5.1}$$

According to the classical beam theory, elastic deflection δ_x of a cantilever beam in the x plane (Figure 5.1a) is given by Equation 5.2.

$$\delta_x = \frac{Fl_a^2(3l - l_a)}{6EI} \tag{5.2}$$

where, F is the force applied to the free end tip of the beam, l is the active length of the cantilever beam, l_a is the length to point a along l from origin, E is the Young's modulus and I is the area moment of inertia.

In the context of MEMS cantilevers, factors such as gravity is not influential while other factors that are considered negligible for macro-cantilevers such as internal stress becomes more dominant. Stoney's equation shown in Equation 5.3 can be used to approximate the deflection of MEMS cantilevers [266].

$$\delta_x = \frac{3\sigma l^2(1 - \nu)}{Eh^2} \tag{5.3}$$

where, σ is the applied stress, ν is the Poisson's ratio and h is the thickness of the beam.

The natural frequency of cantilevers, both micro and macro, can be represented by Equation 5.4.

$$\omega_0 = \sqrt{\frac{3EI}{ml^3}} \tag{5.4}$$

where, m is the effective mass of the load at the free end of the beam. This m directly feeds into F in Equation 5.2 and σ in Equation 5.3. The fundamental mode natural frequency of an unloaded cantilever beam with significant beam mass m_b is given by Equation 5.5 [221, 267, 268].

$$\omega_0 = 1.875^2 \sqrt{\frac{EI}{m_b l^3}} \tag{5.5}$$

Therefore, by substituting Equation 5.5 back into Equation 5.4, the effective mass of the beam alone is given by $0.2427 m_b$. Henceforth, the natural frequency of a cantilever beam with significant beam mass m_b and load mass m_l is given by Equation 5.6.

$$\omega_0 = \sqrt{\frac{3EI}{(0.2427 m_b + m_l) l^3}} \tag{5.6}$$

With the application of a direct driving force, the equation of motion in the x plane can be written as Equation 5.7.

$$\ddot{u} + 2c_1\dot{u} + c_2\dot{u}|\dot{u}| + \mu u^3 + \omega_0^2 u = \omega^2 X \cos(\omega t) \tag{5.7}$$

where, u and X are the dimensionless quantities of response displacement in the x axis and direct excitation displacement A_h normalised against beam length l respectively, c_1 and c_2 are the linear viscous damping parameter and quadratic damping representing the dominant higher order damping nonlinearity respectively and μ is the duffing parameter representing cubic geometric non-linearities. The mass parameter has been absorbed into c_1, c_2 and μ.

Parametric excitation applied orthogonally to x is given by equation 5.8 [257, 269].

$$\ddot{u} + 2c_1\dot{u} + c_2\dot{u}|\dot{u}| + \mu u^3 + (\omega_0^2 - \omega^2 Y \cos(\omega t))u = 0 \tag{5.8}$$

where, Y is the parametric excitation displacement A_v normalised against l. Figure 5.2 numerically (using ode45 solver in MATLAB with 'Relative tolerance' of 1E-05) contrasts the resonant peaks of a micro-cantilever when subject to either types of excitation at varying acceleration levels.
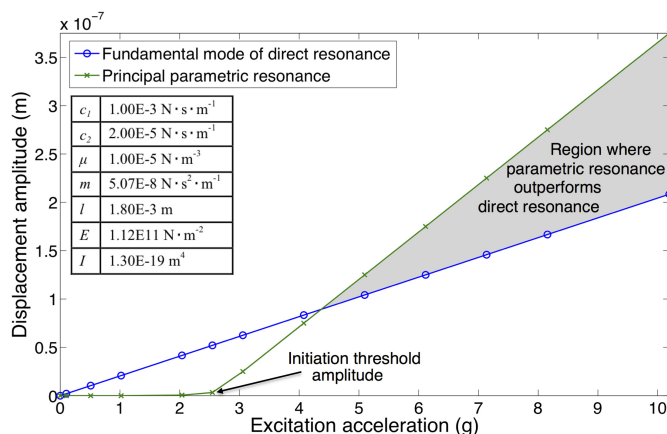
Figure 5.2: Numerical comparison of the steady-state resonant peaks between direct and parametric excitations at various excitation levels.

While direct excitation almost always yields a response regardless of the excitation level, its parametric counterpart converges to a zero steady-state response below the initiation threshold amplitude. In this lower excitation region, direct resonance is more profitable. However, with increasing excitation amplitudes beyond this activation barrier, parametric resonance rapidly outperforms the fundamental mode of resonance.

5.2.2   The addition of Initial Spring

The addition of an orthogonal directly excited spring structure prior to the parametric resonator as shown in Figure 5.3 acts as a base excitation amplifier to elevate the base axis of the Strutt diagram towards the instability regions.
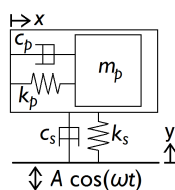
Figure 5.3: Mass-spring-damper model of the threshold-aided PEVEH with the addition of initial spring.

Here, c_s, k_s, c_p, k_p, m_p, y and x are damping of the additional initial spring, stiffness of the initial spring, damping of the parametric resonator spring, stiffness of the parametric resonator spring, effective mass of the system, displacement of the initial spring and displacement of the parametric resonator spring respectively. The initial spring is able to pass along energy absorbed from the mechanical excitation to the subsidiary cantilever spring. However, as mentioned in Chapter 4, x must possess an initial displacement for any orthogonal propagation of vibration into the parametric resonator to take place.

This study employs a clamped-clamped beam design, such as the one shown in Figure 5.4, as the initial spring for a cantilever-based parametric resonator. However, any spring designs for both the initial spring and the parametric resonator are all theoretically valid.
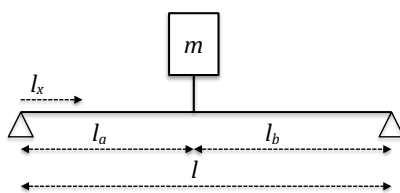
Figure 5.4: A clamped-clamped beam with mass placed at distance l_a along active length l from the origin.

For a clamped-clamped beam with centred mass, natural frequency is given by Equation 5.9.

$$\omega_0 = \sqrt{\frac{48EI}{ml^3}} \tag{5.9}$$

The fundamental mode natural frequency of an unloaded clamped-clamped beam with significant beam mass is given by Equation 5.10 [221, 267, 268].

$$\omega_0 = \pi^2 \sqrt{\frac{EI}{m_b l^3}} \tag{5.10}$$

69

Therefore, substituting Equation 5.10 back into Equation 5.9, the effective mass of the beam alone is given by $48m_b/\pi^4$. Henceforth, the natural frequency of a clamped-clamped beam with significant beam mass m_b and load mass m_l is given by Equation 5.11.

$$\omega_0 = \sqrt{\frac{48EI}{(\frac{48m_b}{\pi^4} + m_l)l^3}} \tag{5.11}$$

For a clamped-clamped beam with asymmetric mass, the natural frequency is given by Equation 5.12.

$$\omega_0 = \sqrt{\frac{9\sqrt{3}lEI}{ml_b(l^2 - l_b^2)^{\frac{3}{2}}}} \tag{5.12}$$

Where, $l_a + l_b = l$ and the mass is placed at distance l_a from the origin.

Deflection of a clamped-clamped beam with centred mass is given by Equation 5.13.

$$\delta_x = \begin{cases} \frac{-Fl_x(4l_x^2 - 3l^2)}{48EI} & \text{for } 0 \leq l_x \leq l/2 \\ \frac{F(l_x - l)(l^2 - 8ll_x + 4l_x^2)}{48EI} & \text{for } l/2 \leq l_x \leq l \end{cases} \tag{5.13}$$

$$\text{and maximum } \delta_x = \frac{Fl^3}{48EI} \quad \text{at } l_x = l/2 \tag{5.14}$$

Deflection for clamped-clamped beam with asymmetric mass at l_x long l from the origin is given by Equation 5.15.

$$\delta_x = \begin{cases} \frac{Fl_bl_x(l^2 - l_b^2 - l_x^2)}{6lEI} & \text{for } 0 \leq l_x \leq l_a \\ \frac{Fl_bl_x(l^2 - l_b^2 - l_x^2)}{6lEI} + \frac{F(l_x - l_a)^3}{6EI} & \text{for } l_a \leq l_x \leq l \end{cases} \tag{5.15}$$

$$\text{and maximum } \delta_x = \frac{Fl_b(l^2 - l_b^2)^{\frac{3}{2}}}{9\sqrt{3}lEI} \quad \text{at } l_x = \sqrt{\frac{l^2 - l_b^2}{3}} \tag{5.16}$$

By applying a direct excitation on the clamped-clamped beam, the same driving force acts as an orthogonal excitation for the cantilever beam resting on the clamped-clamped beam. Displacement of the clamped-clamped beam in y direction adds to the driving displacement amplitude Y. Equations 5.17 and 5.18 can be derived based on Equations 5.7, 5.8, 5.12 and [246] for directly driving the initial spring (clamped-clamped beam) and parametrically driving the parametric resonator.

$$\ddot{y} + c_1\dot{y} + c_2\dot{y}|\dot{x}| + \mu_1xy^2 + \left(\frac{9\sqrt{3}lEI}{m(l_b - x)(l^2 - (l_b - x)^2)^{\frac{3}{2}}}\right)y - \omega^2Y\cos\omega t = 0 \tag{5.17}$$

$$\ddot{x} + c_3\dot{x} + c_4\dot{x}|\dot{y}| + \mu_2yx^2 + (\omega_0^2 - \omega^2(Y + y)\cos\omega t)x = 0 \tag{5.18}$$

where, y displacement of the initial spring, x is the displacement of the subsidiary parametric resonator, Y is the excitation displacement parallel to the y displacement and normal to the x displacement, ω_0 of Equation 5.18 represents the transverse natural frequency of the parametric resonator (taking into account the now more flexible anchor of the cantilever) and the coefficient of the 5th term of Equation 5.17 represent the natural frequency of the primary clamped-clamped resonator that consists of variable centre of mass dependent on the mass displacement x assuming small angular delfection.

5.2.3   Auto-parametric resonance

Contrary to the external excitation induced hetero-parametric, auto-parametric resonance is triggered by aligning the longitudinal and transverse natural frequencies in a 2:1 ratio. The classical example is a pendulum suspended off an elastic spring with the natural frequency of the spring to be twice the natural frequency of the pendulum. The governing equation of such a system is given by Equations 5.19 and 5.20 [246].

$$m\ddot{y} + 2m\zeta_1\omega_1\dot{y} + ky + ml(\ddot{\theta}\sin\theta + \dot{\theta}^2\cos\theta) = F\cos\omega t \tag{5.19}$$

$$ml^2\ddot{\theta} + 2m\zeta_2\omega_2\dot{y} + mgl\sin\theta + ml\ddot{y}\sin\theta = 0 \tag{5.20}$$

where, ω_1 and ω_2 are the natural frequencies of the primary direct resonator (spring) and the natural frequency of the subsidiary orthogonal parametric resonator (pendulum) respectively, m is the mass of the pendulum while assuming negligible spring mass, c_1 and c_2 are the damping coefficients of spring and pendulum respectively, k is the spring constant of the spring, g is gravity, l pendulum arm length, y is spring displacement, θ is the pendulum displacement normal to y plane, F is the external driving force parallel to y and orthogonal to θ plane and ω is the frequency of the this driving force. The $\ddot{y}$ coefficient for $\sin\theta$ in Equation 5.20 consists of the time domain parameter from Equation 5.19.

For a scenario where $\omega = \omega_1 = 2\omega_2$, auto-parametric resonance can be activated. The energy stored in the primary spring from direct resonant build up can be internally transferred to the subsidiary pendulum in a parametric fashion. When oscillation of the parametric resonator dominates and operates deep within the instability region, the energy stored no longer returns to the primary direct resonator and the oscillatory amplitude of the direct resonator diminishes [219].

The addition of initial spring to the parametric resonator in Subsection 5.2.2 is a similar system and auto-parametric resonance can be achieved when the natural frequency of the clamped-clamped beam is twice the natural frequency of the subsidiary parametric resonator. When this criteria is met and auto-parametric resonance occurs, a resonant-based amplification of the base excitation can take place. This serves as a more efficient initiation threshold amplitude reduction mechanism than the additive base excitation amplification explored in Subsection 5.2.2. The equations of motion for such a two degrees-of-freedom direct-parametric system is given by Equations 5.21 and 5.22 [220].

$$\ddot{y} + 2\zeta_1\omega_1\dot{y} + \omega_1^2 y - \xi\mu(\dot{x}^2 + x\ddot{x}) = \omega^2 A\cos\omega t \tag{5.21}$$

$$\ddot{x} + 2\zeta_2\omega_2\dot{x} + \omega_2^2 x - \xi\ddot{y}x = 0 \tag{5.22}$$

where, ω_1 and ω_2 are the natural frequencies of the directly excited initial spring and parametrically excited subsidiary parametric resonator respectively, ξ is the coupling coefficient, ω is the drive frequency and A is the excitation displacement amplitude. An example of simulated time domain auto-parametric response is shown in Figure 5.5 with the system parameters in Table 5.1 and using Runge-Kutta solver in MATLAB.

Table 5.1: Parameters used for MATLAB simulation in Figure 5.5

ζ_1	0.0015	ζ_2	0.0015
ξ	1	μ	0.1
ω	$\omega_1,\ 2\omega_2$	A	0.01 m

(a) Direct resonator build-up   **(b)** Parametric resonator build-up

(c) Drive acceleration at ω **(d)** Direct response at ω_1 **(e)** Parametric response at ω_2
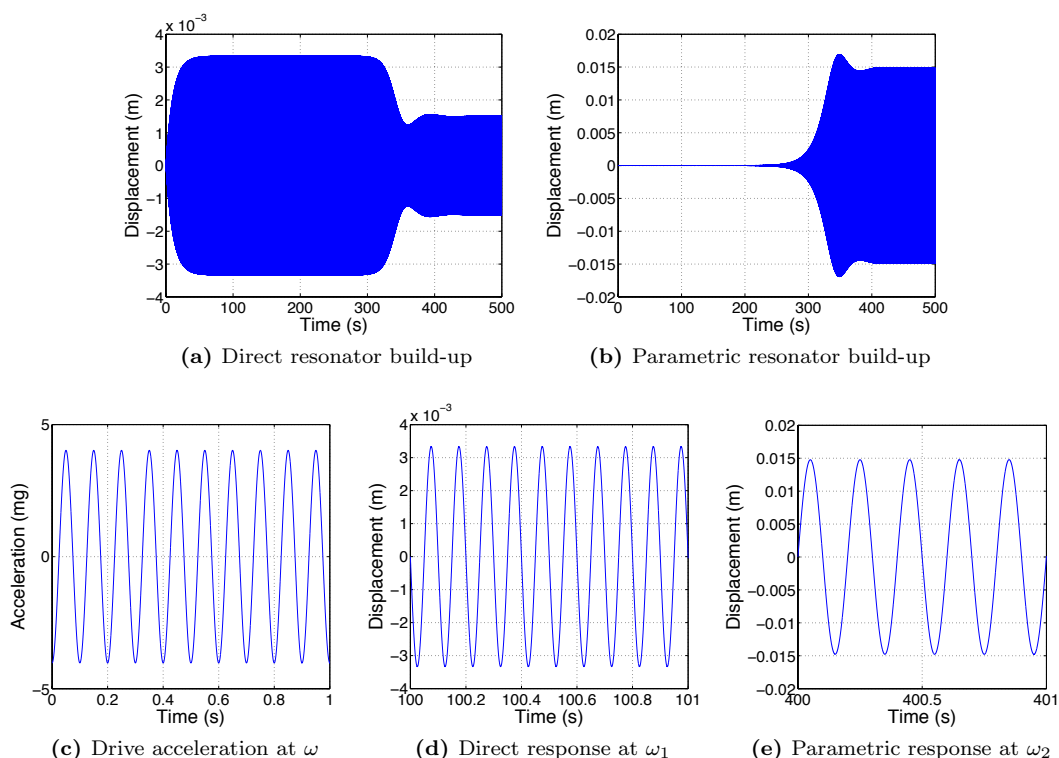
Figure 5.5: Numerical simulation of 2 degrees-of-freedom auto-parametric resonator for $\omega = \omega_1 = 2\omega_2$.

As can be seen in Figures 5.5a and 5.5b, when parametric resonance becomes dominant, oscillatory amplitude of the primary direct resonator diminishes. This demonstrates the irreversible effect of energy flow from the initial spring to the parametric resonator. In comparison to a solely parametrically excited system with the same system parameters presented in Table 5.1, the auto-parametric system numerically exhibited an initiation threshold amplitude of 2.0 mg acceleration while the onset of parametric resonance for the sole parametric resonator only took place in excess of 620 mg.

5.3   MEMS electrostatic prototype

This section explores the design, fabrication and experimentation of MEMS VEH for operation in direct and parametric resonant regimes and the inclusion of the initial spring design to minimise the initiation threshold amplitude.

5.3.1   Introduction

The three most popular VEH mechanical-to-electrical transduction mechanisms implemented in the context of MEMS are summarised below [14, 20, 9].

- *Electromagnetic:* power output does not scale down well with dimension due to diminishing coil turn density and fill factor at smaller scales using current micro-machining technologies.

- *Electrostatic:* mature MEMS technology, can be readily fabricated and integrated with IC technology. However, the peak power density, both theoretical and reported in the literature, is an order of magnitude lower than its counterparts.

- *Piezoelectric:* scales well and offers high performance, especially PZT, but MEMS fabrication is less straightforward compared to electrostatics. AlN and ZnO based harvesters are now more practically realisable with existing fabrication technology. However, the piezoelectric constant d_{31} (directly related to conversion efficiency) for PZT is approximately 1 to 2 orders of magnitude higher than that of AlN and ZnO [82].

The MEMS designs explored in this section employs the Silicon-On-Insulator (SOI) Multi-User MEMS Process (MUMPs) from MEMSCAP and adopts the parallel capacitive plate electrostatic transduction mechanism for the readily available fabrication option at the current stage.

5.3.2   Fist generation MEMS PEVEH

Design

A design model of a micro-cantilever with capacitive combs is shown in Figure 5.6a. Out-of-plane vibration is equivalent to direct excitation while an in-plane excitation force applied along the long axis of the cantilever can potentially induce parametric resonance under the right frequency and amplitude conditions. Figure 5.6b is an iteration of the second design route (Figure 3.6) by adding a double beam between the anchor and the otherwise anchored end of the cantilever, which acts as the electrically undamped additional directly excited initial spring.

(a) Micro-cantilever beam designed as part of an electrostatic transducer with out-of-plane displacement.

(b) Initial springs added to passively minimise the initiation threshold amplitude of parametric resonance.
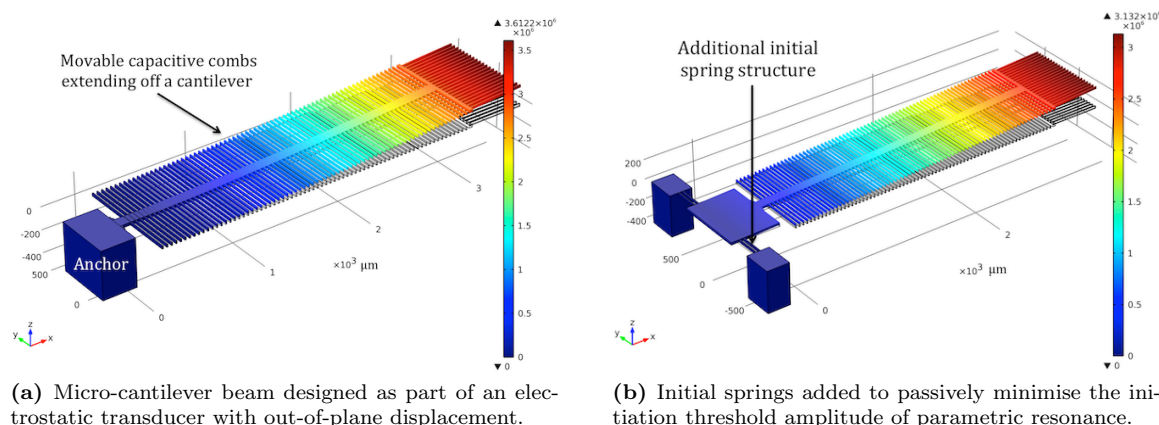
Figure 5.6: Design models of the MEMS cantilevers. Direct excitation equates to an out-of-plane driving force, whereas an in-plane excitation can potentially induce parametric resonance. Capacitive comb fingers extends off the cantilever beam but accompanying parallel fixed comb fingers are not shown here.

Various COMSOL Multiphysics simulated mode shapes of the threshold-aided parametric harvester design are shown in Figure 5.7.

(a) Cantilever 1st transverse at 763.8 Hz

(b) Initial spring 1st in-plane at 18,260.1 Hz

(c) Cantilever 1st lateral at 4569.6 Hz

(d) Cantilever 1st torsional at 12,220.3 Hz

(e) Cantilever 2nd transverse at 6402.3 Hz

(f) Cantilever 3rd transverse at 19,125.5 Hz
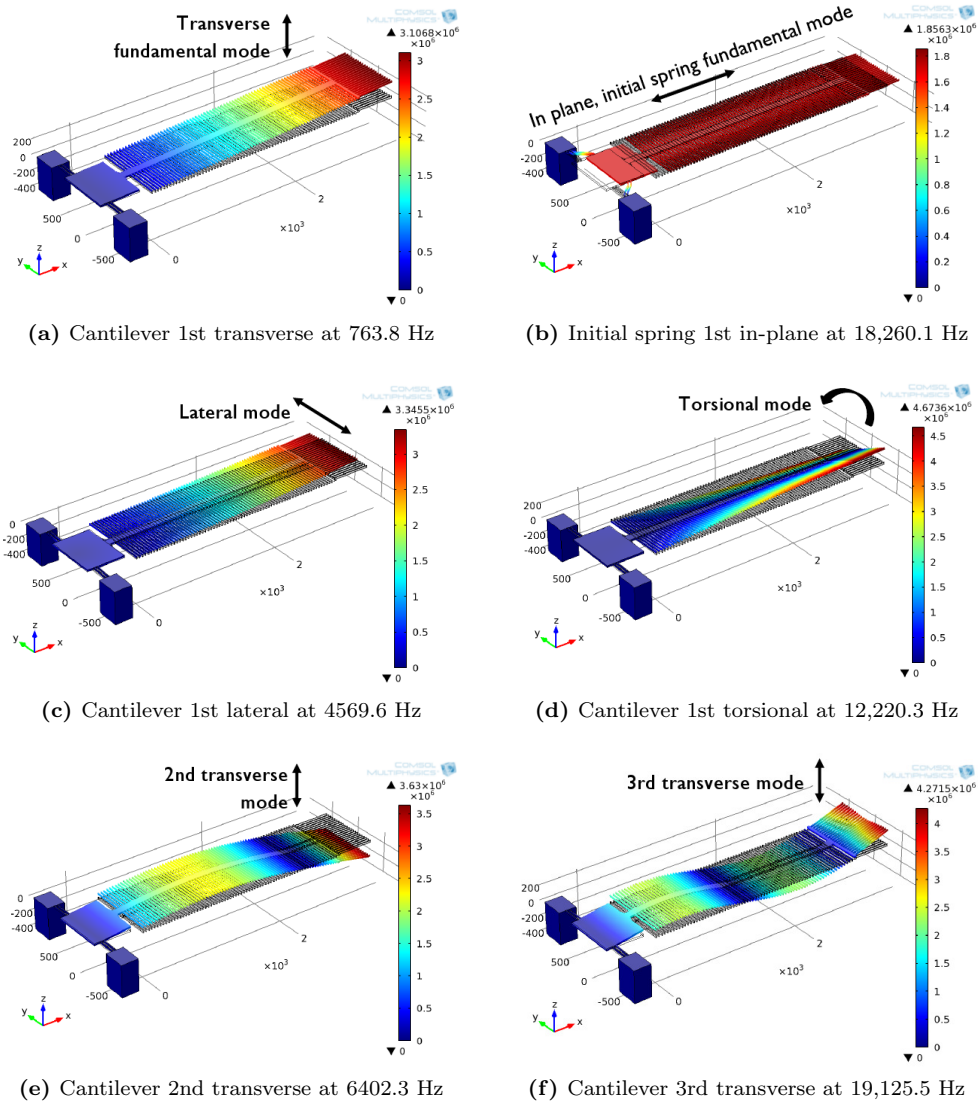
Figure 5.7: COMSOL eigenfrequency simulation of various resonant mode shapes of the threshold-aided design with 25 μm thick silicon device layer. The colour gradient bar represents displacement, which directly relates to the electrical output of electrostatic transducers.

The cantilever beam displaces with an out-of-plane gap-overlapping electrostatic motion for the fundamental mode of resonance as illustrated in Figure 5.7a. Parametric resonant modes, regardless of the order, have identical frequency and mode shape response as the out-of-plane fundamental mode shown here. This mode shape is synonymous for the solely parametric resonator as well.

The in-plane gap-closing mode Figure 5.7b arises from the fundamental mode of the initial springs under direct excitation. This mode is absent from the solely parametric harvesters due to the lack of this additional degree-of-freedom. Therefore, the electrostatic gap-closing motion is also absent from the sole cantilever design. Other higher transverse modes as well as lateral and torsional modes are present for both the threshold-aided and solely parametric resonator designs. The lateral mode (Figure 5.7c) refers to an in-plane gap-overlapping configuration similar to one of the mechanisms defined by [4]. For an electrostatic transducer, torsional and higher transverse modes (Figures 5.7d,

5.7e and 5.7f) are not expected to yield significant response due to charge neutralisation from their particular motions.

Designs were fabricated with both 25 μm and 10 μm device silicon. Although the 10 μm thickness significantly sacrificed the surface area of the capacitive plate, the overall natural frequency of the device can be minimised for realistic vibration levels. COMSOL simulation of the threshold-aided design was carried out to characterise the correlation of device thickness and resonant frequencies of various resonant modes. Figure 5.8 illustrates a summary of the simulation results for the threshold-aided design at different thickness.
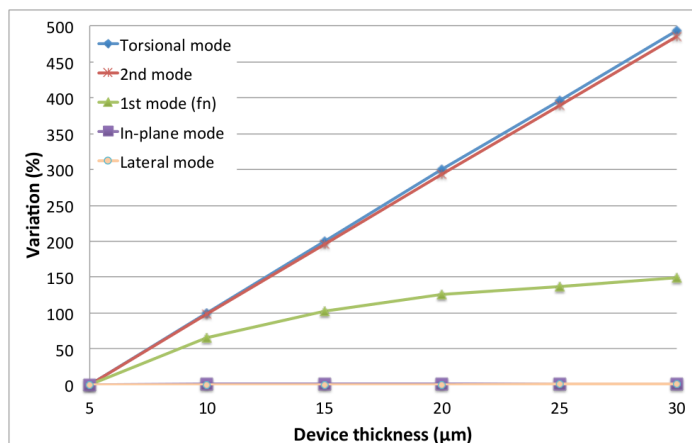
Figure 5.8: COMSOL simulated device thickness variation and correlation with ω of various modes.

The vertical axis denotes the percentage variation of the parameters of interest with device thickness of 5 μm as the initial reference. The in-plane fundamental mode of initial spring and the lateral mode of the cantilever beam were not significantly influenced by thickness. This is because both these modes displace in the directions of the length and width of the structure. On the other hand, all transverse and torsional modes either entirely or partially involve out-of-plane motion; therefore, are dependent on the thickness of the structure. The general frequency trend is a steady decrease with diminishing thickness due to reducing stiffness.

Apparatus

Three designs iterations were fabricated using the SOIMUMPs process as listed below and shown in Figure 5.9. The practical volume values include the anchors with metal pads,

- Solely parametric harvester (small) with 1000 μm in beam length (Figure 5.9a)
    - 25 μm device volume: $\sim$0.0998 mm^3
    - 10 μm device volume: $\sim$0.0785 mm^3
- Solely parametric harvester with 2000 μm in beam length (Figure 5.9b)
    - 25 μm device volume: $\sim$0.121 mm^3
    - 10 μm device volume: $\sim$0.0875 mm^3
- Threshold-aided parametric harvester with 2000 μm in beam length (Figure 5.9c)
    - 25 μm device volume: $\sim$0.147 mm^3
    - 10 μm device volume: $\sim$0.105 mm^3

(a) A smaller prototype of the parametrically excited cantilever-based vibration harvester.

(b) Parametrically excited cantilever-based vibration harvester.

(c) Threshold aided and potentially auto-parametric harvester.

(d) The initial spring (double beam) acts as the threshold-aid, amplifying base excitation.
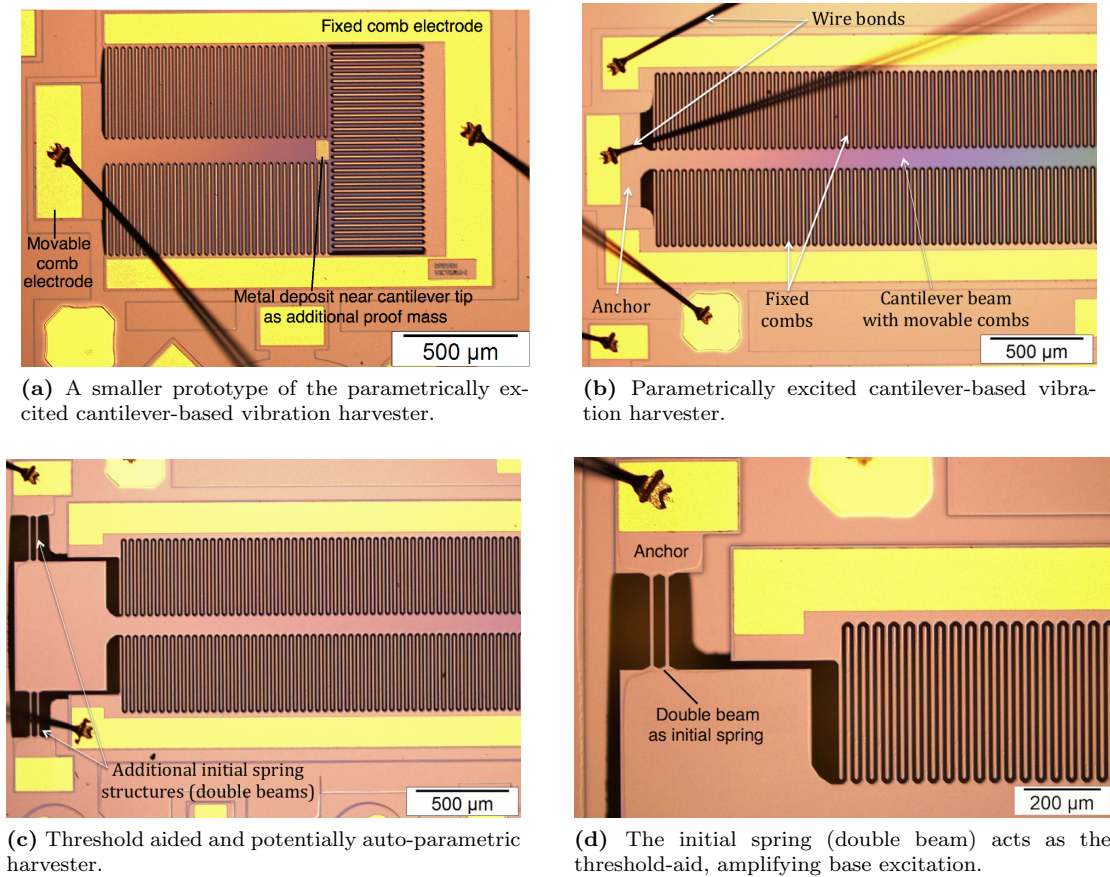
Figure 5.9: SOIMUMPs MEMS realisation of the three PEVEH prototype designs at both 25 μm and 10 μm Si device thickness.

The first two prototypes shown in Figures 5.9a and 5.9b are essentially smaller and larger versions of a cantilever beam (sole parametric resonator) respectively. Metal deposits as shown in FIgure 5.9a are also added to the free end of the cantilever beam in an attempt to minimise the resonant frequencies and maximise deflection. For each movable comb finger (10 μm wide and 400 μm long) extending from the cantilever beam, a corresponding fixed comb finger of the same dimensions is placed beside it with 10 μm air gap spacing. Therefore, a parallel capacitive plate configuration is established throughout the comb finger structures. The third prototype incorporates double beams as the initial springs. The entire shuttle is only anchored through the sets of double beams on either sides. Calculated and measured capacitance of the structures are in the order of 1's pF to 10's pF.

Experimental tests of the MEMS chips were carried out using the mechanical shaker set up shown in Figure 5.10. The shaker was driven by a digital function generator via a power amplifier. A commercial three axes MEMS accelerometer was mounted alongside the vibrating set up to measure the induced mechanical acceleration by the shaker. The measurement circuit employed for the electrostatic harvester was based on a standard voltage follower configuration with a unity gain op-amp [163]. All tests were undertaken at normal atmospheric pressure and room temperature. The cantilever was mounted with its free end upright in order to overcome the non-zero initial displacement criterion. This draws parallels from an inverted pendulum, which places the cantilever tip resting in an unstable equilibrium at zero displacement. The multi-axes vibration leakage that was insignificant at macro-scales can also help to introduce directly excited initial displacements.

(a) MEMS chip   **(b)** Experimental set up
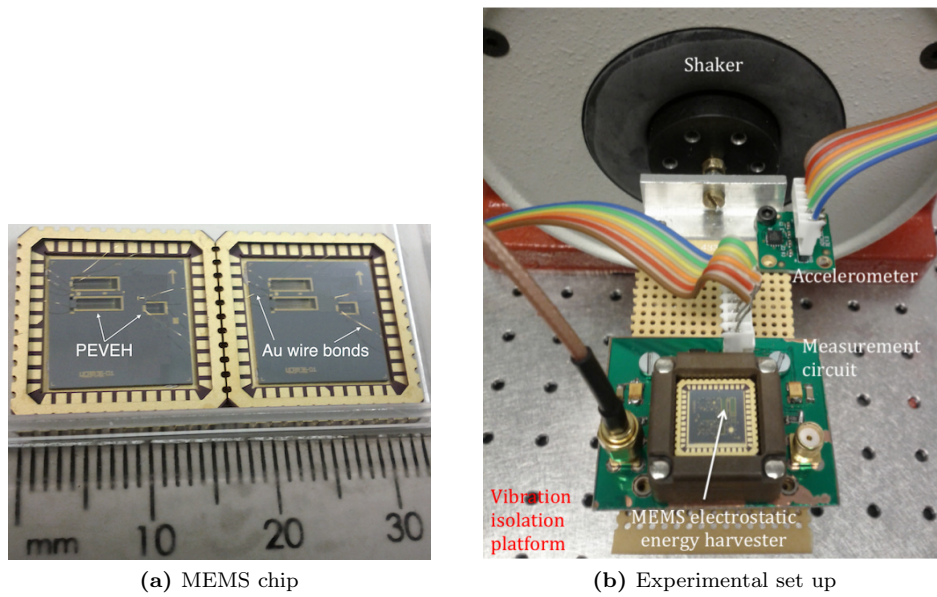
Figure 5.10: First generation MEMS PEVEH device. The MEMS chip is attached to the gold chip carrier using silver epoxy and wire bonded by gold wires.

Method

COMSOL frequency domain simulation of the 25 μm thick threshold-aided design (Figure 5.6b) is presented in Figure 5.11a and a frequency sweep by a PolyTec laser vibrometer of the real experimental device (Figure 5.9c) is shown in Figure 5.11b. These frequency domain plots revealed no harmonics or other resonant modes at either twice or half of the natural frequencies. Therefore, the possible presence of other directly excited resonant peaks within the vicinity of these frequency ranges can be excluded.

(a) COMSOL frequency sweep, $f_n = 763.8$ Hz

(b) Laser vibrometer scan, $f_n = 737.5$ Hz
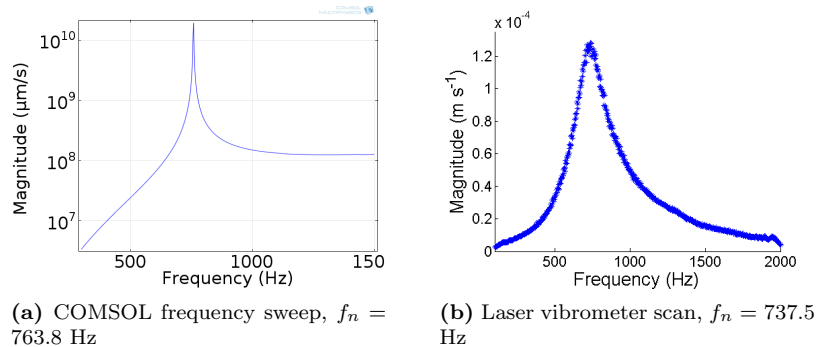
Figure 5.11: Frequency sweeps showing no harmonics or other resonant modes at twice or half of the natural frequency of the threshold-aided prototype. Experimentally measured frequency shifted by 3.44%, potentially a result of MEMS fabrication tolerance and environmental impurities.

The COMSOL simulation in Figure 5.11a had a relative tolerance of 0.9 and 745,530 degrees of freedom were solved. The Figure 5.11b vibrometer scan was carried out with 10,000 times optical magnification, driven by periodic chirp of 0.5 V and 1 V DC offset, resolution of 6400 FFT lines, complex of 100 and rectangle windowing function. The absence of the anticipated parametric resonance in the COMSOL simulation is due to the lack of this resonant phenomenon in the physics

of the simulation tool. The reason why vibrometer frequency sweeps, both sine wave sweeps and periodic chirps, also failed to reveal the parametric modes is due to the long transient state required for this resonant mode to build up.

The method employed to experimentally observe the parametric resonant peaks from mechanical excitation was to manually sweep and hold at each frequency point over a period of time for the potential oscillatory build up to take place. Once the parametric resonant regime is activated, varying frequencies within the instability region will not have to undergo the prolonged build up time again to sustain the resonance.

Power and threshold

A summary of experimentally recorded power peaks is presented in Table 5.2. The first and fourth order parametric resonances were recorded for the 25 μm thick threshold-aided parametric harvester at twice and half of the natural frequencies respectively. Although onset of the second order parametric resonance was also observed around natural frequency, steady-state response almost always converged towards the fundamental mode of resonance within the surveyed excitation amplitudes. The third order parametric resonance, theoretically residing at $2\omega_n/3$, has not yet been experimentally observed. The higher order parametric peaks were not seen for any other prototypes, including the 10 μm thick counterpart of the threshold-aided prototype.

Table 5.2: Experimental power peaks, frequencies, excitation and initiation threshold for various resonant modes of prototypes I, II and III denoting the small solely parametric, larger purely parametric and threshold-aided designs respectively. The term n/r means not recorded and n/a denotes not applicable for the given prototype.

Device	Power peak (nW); Frequency (Hz)			Acceleration (ms^{-2})	
	1st mode	1st parametric	in-plane	excitation	threshold
I 25 μm	37.7; 9100	n/r	n/a	33	n/r
II 25 μm	68.9; 1740	134; 3420	n/a	33	30
III 25 μm	10.7; 700	156; 1380	20.1; 18,200	4.2	1.3
I 10 μm	5.46; 3800	n/r	n/a	50	n/r
II 10 μm	8.94; 630	23.2; 1220	n/a	50	46
III 10 μm	2.08; 380	17.1; 750	3.34; 18,180	10	6.0

As predicted, torsional and other higher transverse modes were not recorded. While the fundamental mode was readily recorded at the respective natural frequencies of each prototype, no significant lateral mode was recorded for any of the prototypes. This could be a result of low lateral capacitive gap-overlap sensitivity for the given excitation amplitude. On the other hand, the in-plane fundamental mode of the initial spring was recorded for both 25 μm and 10 μm thick threshold-aided prototypes at approximately 18 kHz. This result, in contrast to the lateral mode, is in agreement with the higher conversion efficiency of the electrostatic gap-closing mechanism over its in-plane gap-overlapping counterpart as suggested by [4].

For the smaller solely parametric harvester, no parametric resonant peaks were observed within the surveyed excitation range of up to 60 ms^{-2}. Whereas, the larger device with comparable size to the threshold-aided prototype did exhibit principal parametric resonance; however, no higher orders were observed. The initiation thresholds of the two prototypes where parametric resonance were recorded are listed below. Over an order of magnitude decrease in this activation barrier can be observed with the addition of the initial spring for the comparable cantilever prototypes.

- Solely parametric harvester initiation threshold:
  - 25 μm 1st order: 30 ms^{-2}
  - 10 μm 1st order: 46 ms^{-2}

- Threshold-aided parametric harvester initiation threshold:
  - 25 μm 1st order: 1.3 ms^{-2}
  - 25 μm 4th order: 3.3 ms^{-2}
  - 10 μm 1st order: 6.0 ms^{-2}

The directly excited fundamental mode of resonance is always responsive to excitation even at low amplitudes while parametric resonance has zero response below a certain amplitude threshold. As soon as parametric resonance is activated beyond this activation barrier, its power output rapidly outperforms the direct excitation for the same device. Figure 5.12 illustrates this relationship for the 25 μm threshold-aided prototype, from which the best power performance amongst the experimental prototypes was recorded. The diminishing return at higher amplitudes seen from the levelling off of the graph suggest the presence of higher amplitude dependent non-linear damping factors, in electrical and/or mechanical domains, which restrict further growth of the resonant peaks.
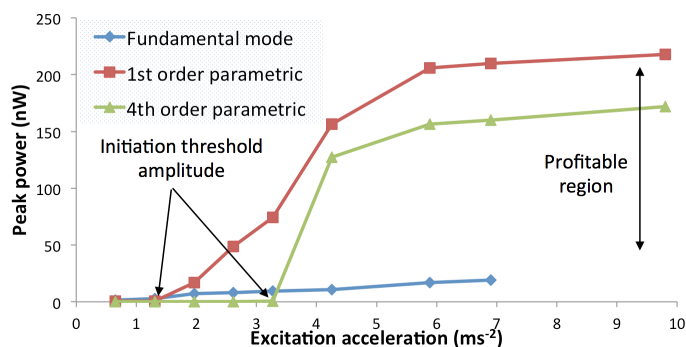
Figure 5.12: Experimental power response of the 25 μm threshold-aided parametric harvester at various resonant regimes plotted against input acceleration.

The threshold-aided prototypes exhibited over an order of magnitude higher in power peak for parametric resonance over directly excited fundamental mode of resonance for acceleration below 1 g as shown in Figure 5.13. For the 25 μm device, at 4.2 ms^{-2} of excitation, power peaks of 10.7 nW, 156 nW and 127 nW were recorded for the fundamental mode, first order parametric and fourth order parametric resonances respectively.

Qualitatively, the frequency domain power response of the solely parametric harvester is similar to that of the threshold-aided harvester. However, since the onset of parametric resonance requires an excess of 3 g of impact acceleration, the performance enhancement over its directly excited counterpart is less rewarding and unrealistic for real infrastructural applications.

Operational frequency

In terms of operational frequency bandwidth, approximately twice the half power bandwidth was recorded for the principal parametric peak (210 Hz) in contrast to the fundamental mode (100 Hz) from Figure 5.13. Furthermore, if the half power points of the fundamental mode is taken as the cut-off line for the bandwidth, a band of 1400 Hz is recorded. However, higher orders of
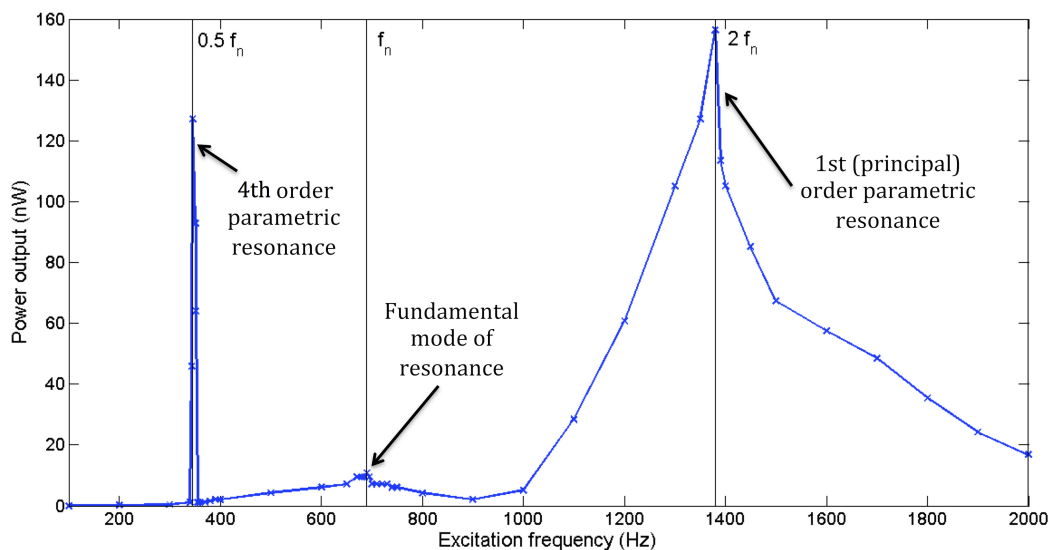
Figure 5.13: Experimental power response of the 25 μm threshold-aided parametric harvester for an input acceleration of 4.2 ms^{-2}. First and fourth order parametric resonances can be observed at twice and half of the natural frequency f_n respectively. The onset of second order parametric resonance was observed in the vicinity of f_n, appearing alternatively to the direct resonant response. However, within the surveyed amplitudes, the steady-state solution at f_n always converged towards direct resonance. The third order is yet to be observed.

parametric resonance, such as the 4th order peak (8 Hz half power band) from Figure 5.13, displayed significantly narrower bandwidth. This demonstrates the fast diminishing frequency bandwidth for the higher order instability regions, which aids to its elusiveness during vibration scans. Nonetheless, the additional peaks can potentially serve as extra power response regions for these supplementary frequency vicinities.

Summary

Introducing context to the absolute power results, Table 5.3 briefly contrasts the 25 μm threshold-aided prototype with a few selected electrostatic harvesters in the literature.

Table 5.3: Comparing the 25 μm threshold-aided parametric harvester results with selected electrostatic counterparts from the literature in terms of power density normalised against acceleration squared.

Reference	Vol. (mm^3)	Power (μW)	Acc. (ms^{-2})	Freq. (Hz)	Index (μWcm^{-3}m^{-2}s^4)
Parametric (1st order)	0.147	0.156	4.2	1380	*60.2*
Parametric (4th order)	0.147	0.127	4.2	342.5	*49.0*
Despesse *et al.* (2005) [15]	32.4	70	9.2	50	25.5
Roundy *et al.* (2002) [4]	1000	116	2.25	120	22.9
Wong *et al.* (2009) [163]	0.319	0.017	1.76	1400	17.2
Fundamental mode	0.147	0.011	4.2	700	*4.24*
Chu *et al.* (2005) [165]	19.96	32.34	40	800	1.01

The figure of merit used for comparison is calculated from power density normalised against the square of input acceleration. The parametric resonant output performs favourably while the direct resonant output performs an order of magnitude worse. Since the compared devices from the literature were all based on direct resonance, the relatively poor performance of the direct resonant

output of the prototype suggested room for device optimisation that can potentially further the power performance of parametric resonant output even more.

5.3.3 Second generation MEMS PEVEH

Design and apparatus

Carrying on the work from the previous subsection, the 2nd generation device explored here is an extended investigation into the power and frequency performance of the threshold-aided parametric resonator. Revisiting the Strutt diagram by revealing the higher orders of parametric resonance as shown in Figure 5.14, it can be seen that both the initiation threshold amplitude and the operational frequency bandwidth rapidly shy away with increasing order number and higher damping [270]. Therefore, the introduction of the threshold reduction aid: initial spring, as well as minimising parasitic damping, can help to improve the accessibility of these higher order instability regions.
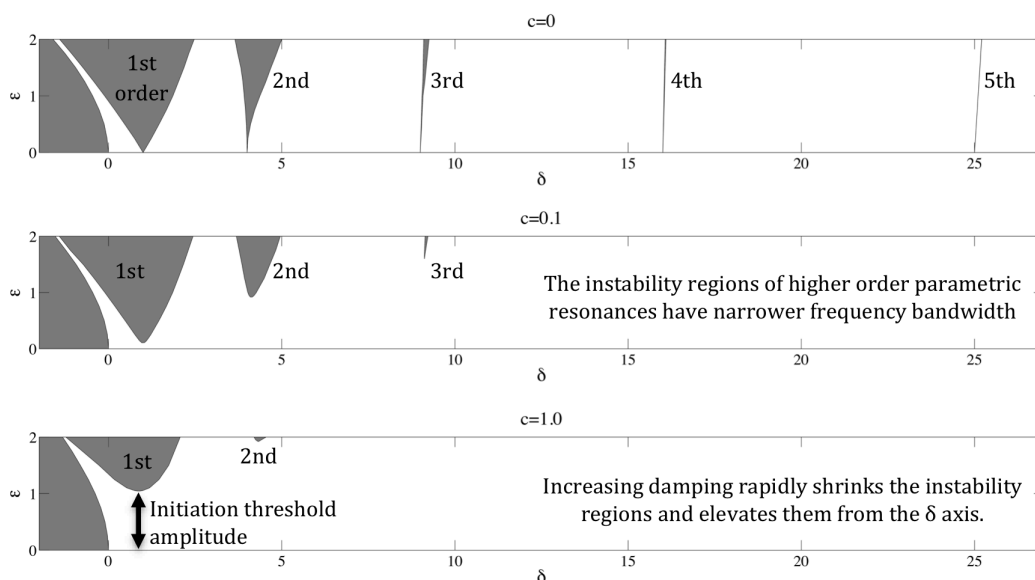
Figure 5.14: Strutt diagram showing up to 5 orders of instability regions with fast diminishing frequency bandwidth at higher orders.

For MEMS devices, damping due to air drag is an influential factor. Parasitic force from air drag is given by Equation 5.23.

$$F_d = \frac{\rho_0 S v^2 c_d}{2} \tag{5.23}$$

where, F_d is the force induced by air drag, ρ_0 is the density of air (1.225 kgm^{-3} at 288.15 K under 1 atm), S is the area of the drag surface and c_d is a dimensionless drag coefficient dependent on the geometry of the shuttle. A flat surface has a higher c_d while a sharp, circular or streamlined surface has relatively lower drag. The comb fingers are designed to be 25 μm in depth and 10 μm in width. Therefore, out-of-plane gap-overlapping motion has relatively less drag resistance than in-plane gap closing. The relative accessibility of higher order instability regions in MEMS-scale has been previously demonstrated [271].

The design iteration employed can be seen in Figure 5.15a. It is essentially the same design from the 1st generation equivalent (Figure 5.6b) where the shuttle consists of a cantilever beam with an

array of capacitive comb fingers. The initial spring double beam structure here is longer than the 1st generation prototype to allow more significant base excitation amplification. The same SOIMUMPs process was employed to produce the device shown in Figure 5.15b.

<div align="center">

(a) COMSOL Design   **(b)** Optical micrograph

</div>
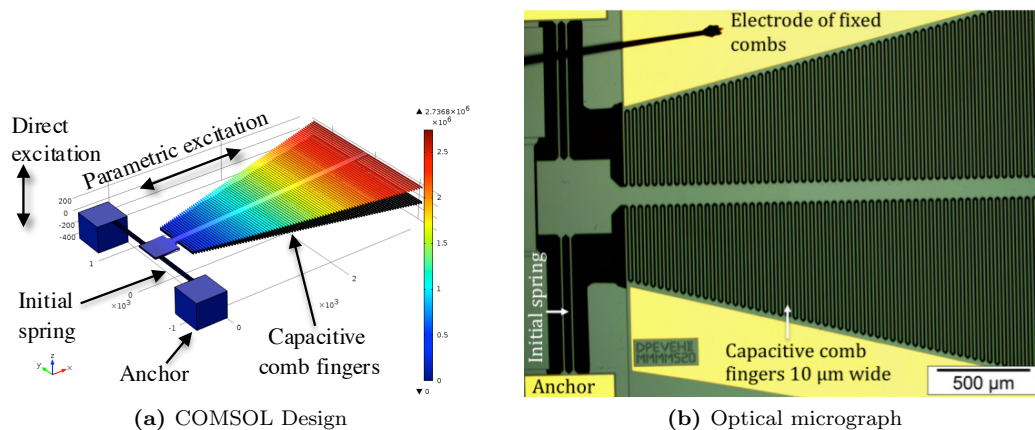
Figure 5.15: 2nd generation MEMS PEVEH with longer initial spring and tapered design.

The active device volume inclusive of the anchor is 0.278 mm^3 with 25 μm thick Si device layer and the measured and calculated capacitance is in the order of 10's pF. A tapered cantilever design is employed. Generally speaking, a tapered design with the larger breadth near the free end is suitable for maximising active regions undergoing peak displacement (ideal for electromagnetic and electrostatic transducers) while the reverse is ideal for maximising active strain regions (ideal for piezoelectric transducer) [127, 3]. Such a design here exposes larger active capacitive regions of the structure to relatively larger displacements, while the active capacitive area of the near-clamp regions are less critical due to the small-displacement and the saved space can be utilised for the placement of anchored comb fingers. However, experimental power density measurements did not yield the intended improvement compared to the constant breadth beams utilised in the first generation MEMS prototypes. This could be a result of influence from more dominating factors such as the out-of-plane alignment (and therefore spacing) of the electrostatic plates.

Vacuum packaging

In an attempt to further minimise parasitic damping caused by air drag, the MEMS device is vacuum packaged (pressure $<< 10$ torr) by an in-house process. The vacuum pressure is a conservative estimate calculated from the quality factor of a MEMS double ended tuning fork on the same chip. This minimises the ρ_0 term from Equation 5.23. The device with the vacuum seal can be seen in Figure 5.16a. Figure 5.16b contrasts the out-of-plane fundamental mode resonant peak of the room pressure (assumed to be 760 torr) and vacuumed device measured by a laser vibrometer. The COMSOL simulated eigenfrequency is approximately 303.9 Hz. The optically measured mechanical quality factor ($f_n/\Delta f$) shows an increase from around 1.5 to 9 when the device is vacuum packaged.

Results

Power response of the prototype in room and vacuum conditions per excitation acceleration is given by Figure 5.17. The plot compares the 1st mode of direct response with the various orders

(a) Vacuum seal

(b) Vibrometer scan $\sim f_n$
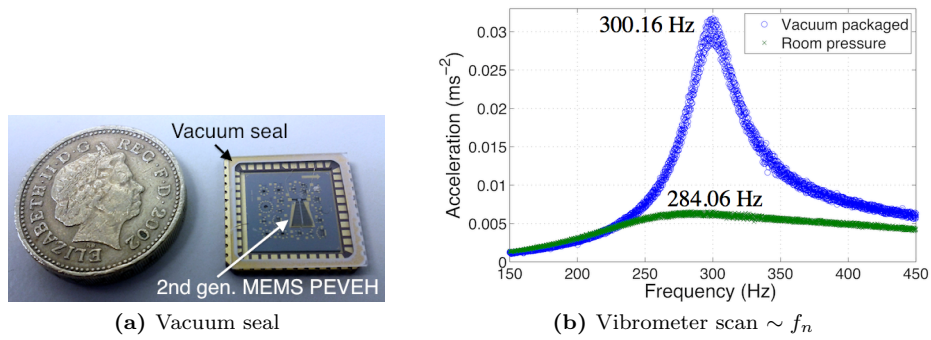
Figure 5.16: 2nd generation MEMS PEVEH with vacuum packaging.

of parametric resonance. As seen from the 1st generation device in Figure 5.12, upon activation, parametric resonant build-up at higher acceleration levels rapidly outperform its direct counterpart. However, the region before the two power curves intersect, direct resonance is the preferred option. Four orders of parametric resonance was recorded for the device in room pressure. In vacuum, an additional fifth order, albeit difficult to unveil due to its narrow bandwidth and time-dependent frequency drift, was observed.
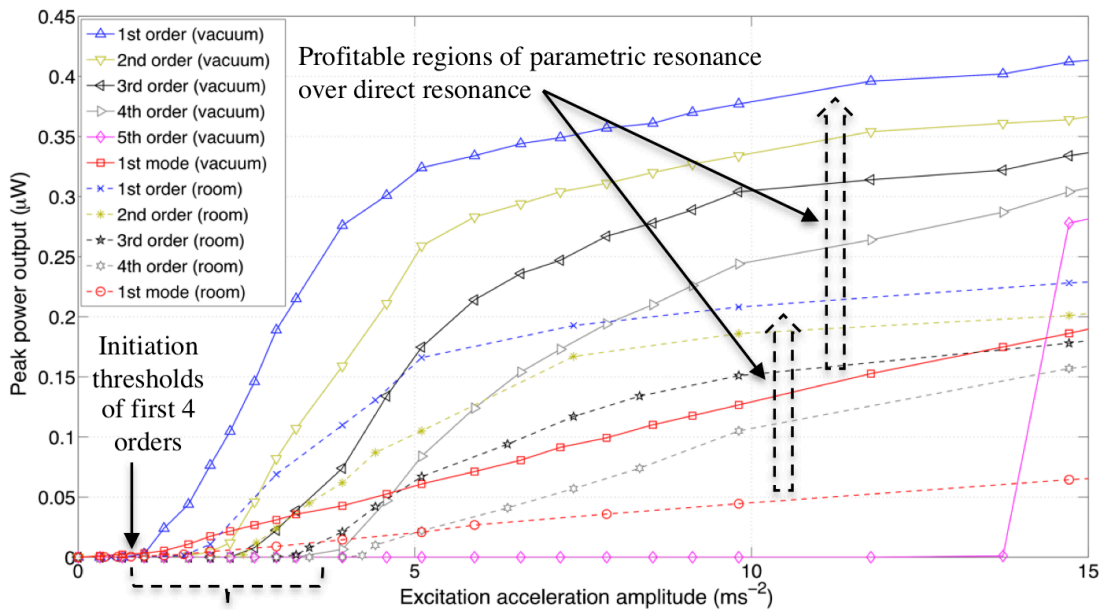
Figure 5.17: Experimental power response versus excitation acceleration. The initiation thresholds of parametric resonance decreases with lower damping in vacuum.

The onset of the fifth order for the vacuumed device was at a significantly higher amplitude than that of the first four orders and the power response rapidly attained a high level upon accessing the parametric regime. This implies a lower true initiation threshold exists for the fifth order and the potential presence of further higher orders for both room and vacuum devices within the scanned acceleration range; however, these additional instability regions have been experimentally elusive due to the impractically narrow operational frequency bandwidth for the frequency sweeps to reveal.

The diminishing frequency bandwidth and the presence of vibrational nonlinearities (inducing shifts in eigenfrequencies) increased the practical difficulty to experimentally locate the narrow bandwidth higher orders. For instance, the half power bandwidth of the fifth order parametric resonance

for the vacuumed device at ~ 1.5 g was approximately 0.7 Hz. The prolonged build-up required to accommodate the onset of parametric resonance within the instability region rendered automatic frequency sweeps impractical.

The initiation thresholds for each respective instability orders noticeably decreased at lower air density conditions as can be seen in Table 5.4. While both direct and parametric resonant peaks observed an increase in power peak at lower damping, the frequency bandwidth of parametric resonance widened instead of the narrowing peak characteristics of direct resonance. This is a result of the system moving deeper into the instability region of the Strutt diagram (vertically up). Therefore, both power and operational frequency bandwidth of the parametric peak increases with lower damping. This frequency behaviour is illustrated in Figure 5.18.

Table 5.4: The power, half power bandwidth and initiation thresholds of the 2nd generation MEMS PEVEH in room pressure and vacuum conditions. HPB is the half power bandwidth, ITA is the initiation threshold amplitude, 'n/r' denotes not recorded and 'n/a' denotes not applicable.

	Room pressure			Vacuum packaged		
	at 5.1 ms^{-2} excitation			at 5.1 ms^{-2} excitation		
	Power (nW)	HPB (Hz)	ITA (ms^{-2})	Power (nW)	HPB (Hz)	ITA (ms^{-2})
1st mode	20.8	40	n/a	60.9	11	n/a
1st order	166	80	1.57	324	160	0.98
2nd order	105	21	2.45	259	35	1.64
3rd order	67	7	3.24	175	9.8	2.62
4th order	22	2.7	4.22	84	3.5	3.92
5th order	n/r	n/r	n/r	0	0	13.73
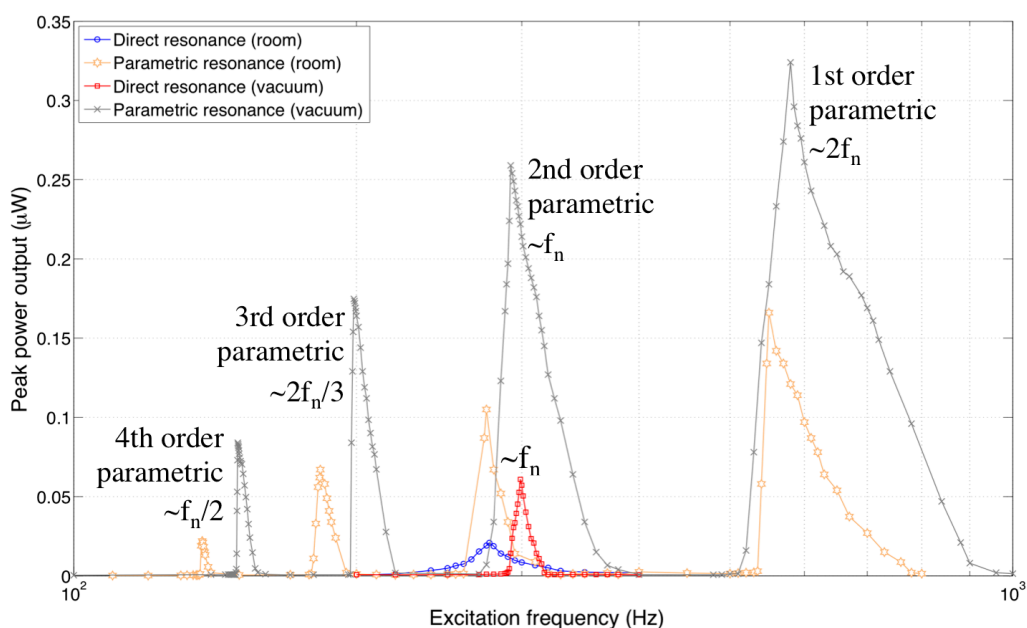
Figure 5.18: Power spectrum at an acceleration of 5.1 ms^{-2}.

Figure 5.18 demonstrates various supplementary operational frequency regions. However, only the principal order parametric resonance is relatively easy to access. The second order overlaps with the fundamental mode and a timed modulation between the linear harmonic and parametric motion takes place, which usually returns to the direct resonant regime. The third and higher orders have narrow frequency bands and longer transient build-up time (> 1 minute) for a given excitation level. Therefore, the higher orders are practically less accessible for real VEH applications.

Comparing the performance of the 2nd generation harvester with the 1st generation in terms of power density normalised against acceleration squared revealed no observable increase despite the relatively larger capacitive area from the tapered design. This could be a result of misalignment of the moveable and fixed comb fingers in the vertical axis arising from the sagging deflection of the shuttle tip. Therefore, although capacitive area is larger, distance is also great, which results in a weaker electric field.

5.3.4   Summary

Power performance

Parametric resonance has proven its superiority than direct resonance in MEMS devices. In contrast to macro-scale devices, the non-zero initial displacement criteria appears to be less of an issue due to multi-axes vibrational leakage that was negligible for macro devices. MEMS structures also allow the implementation of thin initial spring structures compared to the entire device, which would otherwise be impractical in larger scales. The possibility of vacuum packaging for MEMS devices further enables the reduction of parasitic damping leading to lower initiation thresholds, larger power peaks and wider frequency bandwidth for parametric resonance.

The decision of employing an electrostatic transducer in this study rather than a more effective transduction mechanism such as piezoelectric was purely due to the fabrication constraints imposed by the foundry process. Absolute power output is less crucial for the current proof-of-concept investigation for accessing the practicality of parametric resonance for MEMS VEH. However, further investigations can involve various MEMS and/or thin/thick-film piezoelectric devices to explore the absolute power attainable in micro-scales.

Auto-parametric resonance

Initial springs explored in the fabricated devices have significantly higher (about an order of magnitude) natural frequency than the parametric resonator. Therefore, the base excitation amplification is non-resonant. In order to maximise the base excitation amplification effect and minimise the initiation threshold amplitude, auto-parametric design can be employed. However, designing the natural frequency of the initial spring to precise twice the natural frequency of the parametric resonator has proven to be less than trivial.

The first issue is the impractically large design space required to accommodate a long enough initial spring to bring down its natural frequency. A potential solution is to use folded springs. However, the increased additive displacement from the folded spring might cause the comb fingers to over travel within the allocated air gap spacing.

A second issue is the inherent fabrication tolerance of any process, which could cause frequency mismatch in contrast to the simulated design. Although frequency tuning techniques such as applying additional electrostatic forcing can help to match the required 2:1 frequency ratio, the additional power expenditure to enable this tuning mechanism is impractical for VEH applications.

5.4   Macro-scale piezoelectric prototype

This section explores the implementation of piezoelectric transducers in cantilever-based parametric resonators. The motivation arises from the higher conversion efficiency over electrostatic generators. However, instead of displacement, strain maximisation is required.

5.4.1   First generation: piezoelectric sensors

Piezoceramic strips of dimensions 60 mm by 20 mm as well as 40 mm by 20 mm from APC International were employed. These transducers were composed of bi-morph piezoelectric layers separated by a common ground electrode. The bi-morph is in turn sandwiched between poling electrodes and an electrically insulating varnish coating on the outer most structure. The total thickness is approximately 0.7 mm with capacitance in the order of 100's nF. The calculated (Equation 5.24 [78]) and measured standalone intrinsic natural frequencies of the 60 mm strip is ∼60 Hz and that of the 40 mm strip is ∼140 Hz.

$$f_n = 3.2E + 05\frac{h}{l^2} \tag{5.24}$$

where, f_n is the intrinsic natural frequency of the piezoceramic strip, h is the thickness of the strip and l is the active length of the strip.

Cutoffs from stainless steel and mild steel shim of varying thickness (50 μm, 100 μm, 200 μm and 300 μm) were employed as the spring of the resonator. Through attaching the piezoceramic onto the shim substrate using epoxy adhesive, various iterations of piezoelectric cantilever-based prototypes were constructed. Two main designs were employed: a sole cantilever beam as well as a parametric resonator with orthogonal initial spring as shown in Figure 5.19. The mounted prototype device of the later is shown in Figure 5.20a.

Although easy to construct and cut the desired shape of the resonator from the shim, this prototype suffers from the following.

- Stiff nature of piezoceramic compared to the spring base restricts strain on the active transducer layer.

- In practical implementation, epoxy adhesive further increases stiffness and introduces additional damping between the spring and piezo layers.

- The flexible nature of the steel spring results in the piezoceramic to behaviour like a loose clamp for the free end of the spring.

Despite the shortcomings of this apparatus, which would compromise the absolute power output, the piezoceramic can still act as a vibration sensor to qualitatively characterise parametric resonators. A relative quantitative comparison was also done between the prototype itself when driven in direct and parametric resonance. Ideal resistive load was experimentally found to be in the order of 0.2 to 0.4 MΩ. Figure 5.21 presents the peak power response per excitation acceleration for a sole cantilever and a cantilever with initial spring structure.

Within the scanned acceleration of up to 2 g, no onset of parametric resonance was observed for the sole cantilever. On the other hand, onset of parametric resonance for the cantilevers with initial springs initiated around 0.4 g. It can be seen that the initial-spring-cantilever (ISC) has lower

(a) Sole cantilever

(b) Cantilever with initial spring
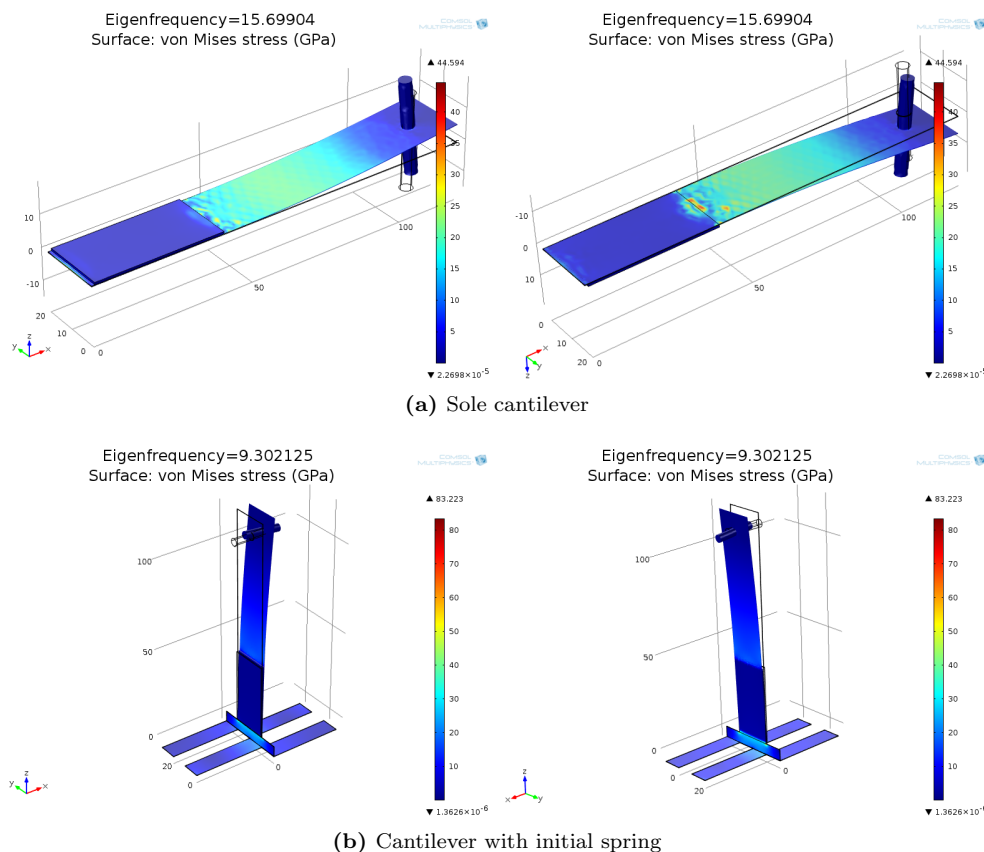
Figure 5.19: COMSOL model of sole cantilever and initial-spring-cantilever resonators with piezoceramic strips away from the free end.

conversion efficiency than the sole cantilever (SC) counterpart. This is because in addition to the base excitation amplification effect of the initial spring, this additional degree-of-freedom also acts as a dashpot. For excitation in excess of 0.5 g of acceleration, the parametric resonant response of ISC outraced the direct resonant response of SC.

Figure 5.22 presents the ISC prototype. Piezoelectric transducer was responsive to 1st mode transverse mode of the cantilever beam and the 1st mode transverse mode of the orthogonal clamped-clamped beam (CCB) initial spring. Through tuning the natural frequency of CCB to match with twice the natural frequency of the cantilever, auto-parametric resonance can be achieved with the following initiation threshold amplitude.

- Parametric resonance: ~ 4.0 ms^{-2}

- Auto-parametric resonance: ~ 0.6 ms^{-2}

The identifier of parametric resonance is where response frequency is half of the excitation frequency. Within the auto-parametric vicinity, an alternating modulation of energy transfer between the parametric resonant regime of the cantilever and linear harmonic resonant regime of the CCB takes place. The two fundamentally distinct regimes are not capable of super-positioning co-existence. At higher excitation levels, the system operates deeper into the instability region and auto-parametric resonance becomes irreversibly dominant over direct resonance of CCB.

Despite the lower initiation threshold required to activated auto-parametric resonance from the resonant-based base excitation, mismatching the frequencies as shown in Figure 5.22a can offer

(a) Experimental prototype   **(b)** COMSOL frequency domain response
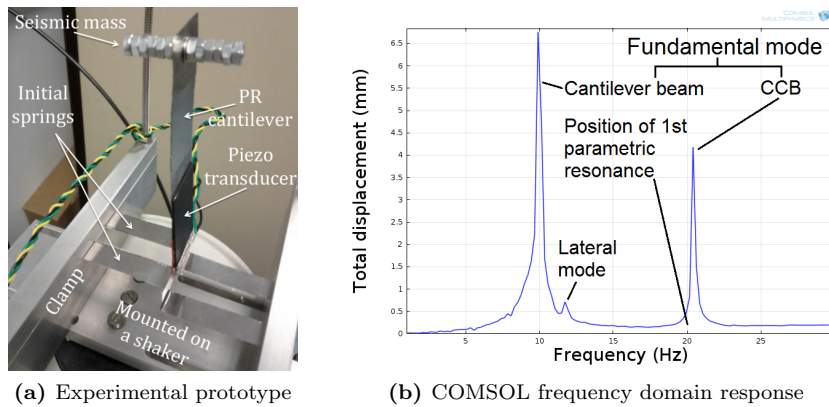
Figure 5.20: 1st generation piezoelectric cantilever-based PEVEH with orthogonal initial spring structure. Excitation is applied vertically. The upright beam acts primarily as a parametric resonator (PR), while the clamped-clamped beam (CCB) has a natural frequency approximately twice that of PR.
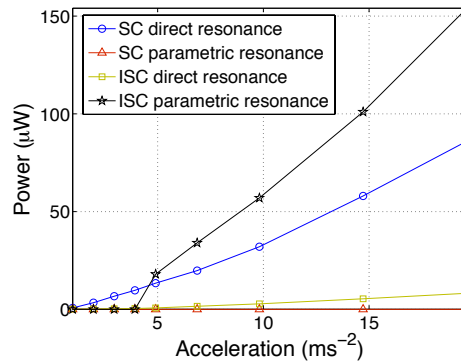
Figure 5.21: Comparison of 1st generation piezoelectric prototype between sole cantilever (SC) and cantilever with initial spring structure (ISC).

additional frequency bandwidth for broadband operation.

5.4.2   Second generation: PZT VEH

This section further explores the various design iterations of piezoelectric cantilever-based harvesters using commercial off-the-shelf PZT VEH beams to better understand the behavioural trends of tuning various system parameters.

Apparatus

Figure 5.23 presents the piezoelectric cantilever-based harvester set up for both direct and parametric excitations. Sole cantilever beam configuration and the addition of a clamped-clamped beam (single or double) as the initial spring have been investigated

Volture Systems V21BL from MIDE have been employed as the piezoelectric transducer. The transducer is made from a flexible laminate substrate, PZT with piezoelectric constant d_{31} of -190×10^{-12} C N^{-1} as well as an electromechanical coupling coefficient k_{31} of 0.36 and FR4 as the outer insulator coating. The electrodes sandwich respectively sandwich a set of piezoelectric bi-morph and primary strain is along the transverse direction of the beam, therefore, the primary operational mode utilises the d_{31} constant.

(a) Parametric resonance   **(b)** Auto-parametric resonance
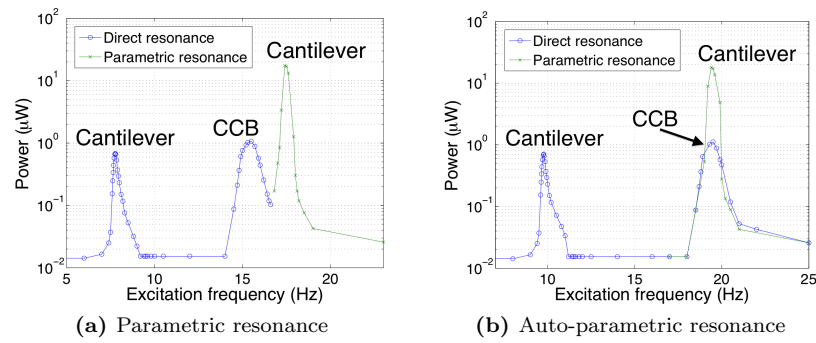
Figure 5.22: 1st generation piezoelectric initial spring cantilever with frequency tuned to exhibit parametric and auto-parametric resonance at ~ 5.0 ms^{-2}. CCB is the clamped-clamped beam initial spring.

(a) Sole cantilever   **(b)** With initial spring   **(c)** With double beam
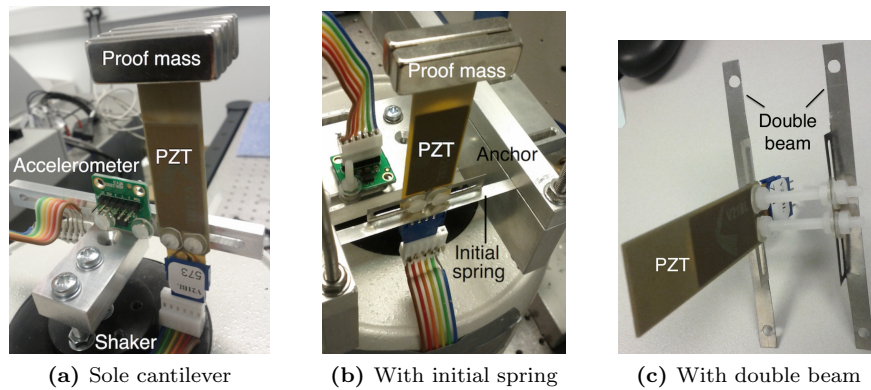
Figure 5.23: 2nd generation piezoelectric cantilever-based harvester with initial spring to reduce the initiation threshold amplitude. Transverse forcing relates to direct excitation while acceleration along the long length of the beam can potentially represent parametric excitation.

The beam is approximately 33.8 mm long and 14.2 mm wide of active piezoelectric bi-morph area near the supposedly clamped-end and a further $\sim$20.8 mm by $\sim$17.0 mm of non-piezoelectric beam area near the free end for the placement of proof mass. This design enables maximum strain near the clamped end of the beam, which is ideal for the piezoelectric transduction mechanism.

Multiple units of NdFeB magnets with dimensions of 30 mm by 10 mm by 5 mm and density of 7.4 gcm^{-3} were used as the proof mass. Initial beams were manufactured from stainless steel shim with various thickness iterations. A 3-axis accelerometer was used to control the acceleration fed into the vibratory system by a function generator controlled mechanical shaker fixed on a vibration isolation platform.

A number of system parameters and configurations were explored, which included:

- Effective mass (mainly relating to natural frequency and maximum strain)
    - Number of magnets attached and positioning along the beam length
    - Asymmetry induced from uneven number of magnets on either sides.

- Initial spring (mainly relating to initiation threshold of parametric resonance)
    - 3 thickness of beam: 101.6 μm, 152.4 μm and 203.2 μm
    - Active length of the clamped-clamped beam: 60 mm, 55 mm and 50 mm
    - Either single beam or double beam
    - Distance between the double beam

Initial spring thickness

Initial spring made from stainless steel shim had maximum active length of 60 mm and breadth of 5 mm with three thickness iterations of 101.6 μm, 152.4 μm and 203.2 μm. The configuration from Figure 5.23b was setup with four pieces of symmetrically placed magnets near the free end of the beam.
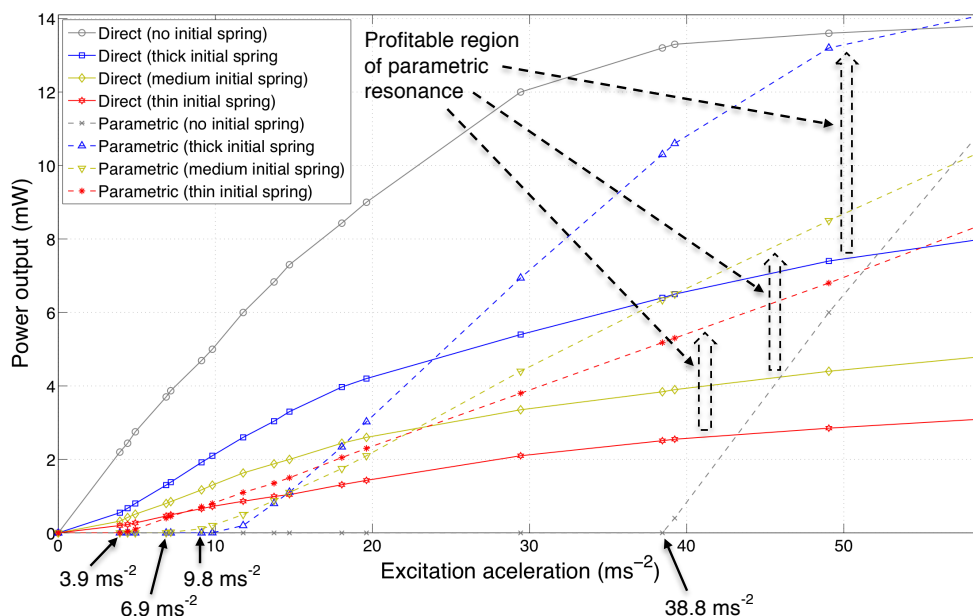
Figure 5.24: Power output per acceleration for 2nd generation piezoelectric cantilevers with and without the threshold-reducing initial spring structure.

It can be seen from Figure 5.24 that the onset acceleration for parametric resonance is significantly reduced with the initial spring; from 38.8 ms^{-2} (no initial spring) to 9.8 ms^{-2} (thick initial spring), 6.9 ms^{-2} (medium initial spring and 3.9 ms^{-2} (thin initial spring). However, this additional degree-of-freedom also acts as an energy dissipator. Stiffer the initial spring, more of the vibrational energy can propagate towards the subsidiary resonator and higher the quality factor. On the other hand, the earlier initiation of parametric resonance from more flexible initial springs maximises the profitable regions over direct resonance. Therefore, an optimal balance exist where this superior resonant phenomenon can be activated at relatively low acceleration while not sacrificing too much energy to the initial spring.

Direct resonant power output steadily increases with input acceleration until the approaching the physical limits of the piezoelectric transducer. The power slopes for both direct and parametric resonances flatten with thinner initial springs. Although the initial spring parametric curves demonstrated large profitable regions over direct counterparts, improvement over the sole cantilever structure was only observed for the thick initial spring iteration in excess of 56 ms^{-2}. Further widening of the profitable region was limited by the transducer limits employed here.

Further stiffness variation

The similar trend from Figure 5.24 was observed where the stiffness of the initial spring was further tuned either by changing the active length or by varying the proof mass. While shorter beam corresponds to lower flexibility, larger proof mass yields the opposite result. The addition of a

second parallel initial spring was aimed to provide additional stiffness variation. However, the double beam structure appears to worsen in both power output and initiation threshold amplitude from the increased damping and energy dissipation. Nonetheless, as the distance between the double beam widens, the experimental trend projects a decrease in initiation threshold amplitude.

Transient state

The transient build-up time required for parametric resonance is almost always longer than direct resonance and is directly dependent on the acceleration amplitude relative to the initiation threshold amplitude. As acceleration increases beyond this threshold and move deeper into the instability region of the Strutt diagram, shorter time is required to reach the non-trivial steady-state solution.

Variation in T-shape

The transverse mode of the cantilever beam here is along the narrow breadth of the clamped-clamped initial spring instead of the long length. The later configuration was investigated in the 1st generation piezoelectric harvester in Subsection 5.4.1, but was difficult to achieve with the Volture piezoelectric beam employed here. As the cantilever beam vibrates along the more flexible plane of the clamped-clamped beam, more energy is lost to displacement rather than strain on the piezoelectric and therefore compromises the quality factor.

Additionally, the transverse mode of the cantilever resonator triggers torsional twist in the clamp-clamped beam. Therefore, as the cantilever is in motion, the torsional vibration of the initial spring restricts the transverse base excitation amplification operation of the initial spring. On the other hand, the transverse motion of the 1st generation setup did not interfere with the transverse motion of the initial spring.

Mass and frequency tuning

All variable parameters investigated can tune the natural frequency of the system. However, the positioning and size of the proof mass are by far the most influential factors. Larger lumped mass and longer active length not only reduces the natural frequency but also yield greater power output per acceleration from the increased deflection.

Another initiation criterion of parametric resonance is a non-zero initial displacement. The vertically upright mount over other mounting configurations have been experimentally shown to be the best candidate for overcoming this limitation, from which comparisons can be drawn to an inverted pendulum. Asymmetrical proof mass further introduces an initial deflection, which allows multi-axes direct vibration leakage to help push the system into the instability region when the excitation is close to the initiation threshold.

Auto-parametric resonance

The base excitation amplification exercised by the initial spring here is non-resonant. The 1st generation piezoelectric harvester in Subsection 5.4.1 has demonstrated the potential of further lowering the initiation threshold amplitude by employing auto-parametric resonance. However, the variability of the tuneable system parameters here did not accommodate for the natural frequency

of the initial spring to match twice the natural frequency of the cantilever resonator. A several folds longer clamped-clamped beam is required to satisfy the frequency ratio matching.

Frequency domain characteristics

Figure 5.25 presents frequency domain voltage outputs (rectified across an ideal load ~250 kΩ) recorded from continuous frequency sweeps around the natural frequency. Apart from the expected linear resonant peak of the 1st transverse mode of the cantilever beam, a second smaller resonant peak in the lateral plane (twisting) was also observed but the strain on the piezoelectric layers was indirect and minuscule in comparison.
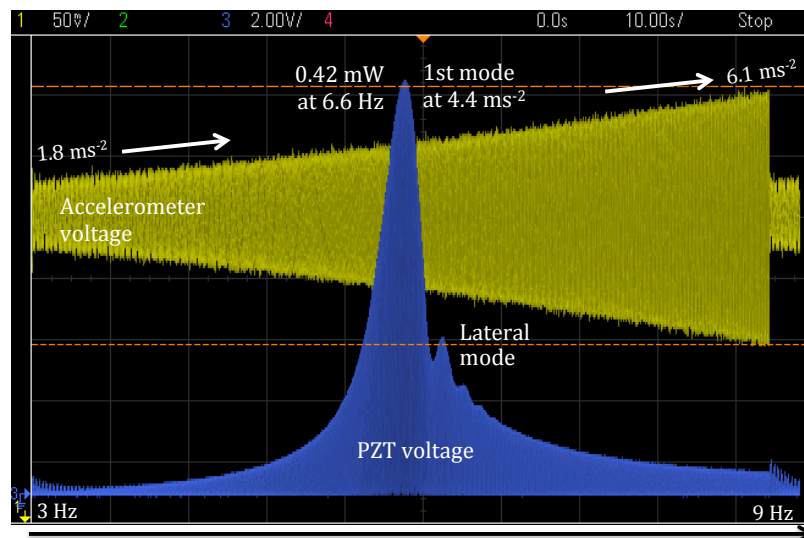
(a) 0.42 mW at 4.4 ms^{-2}
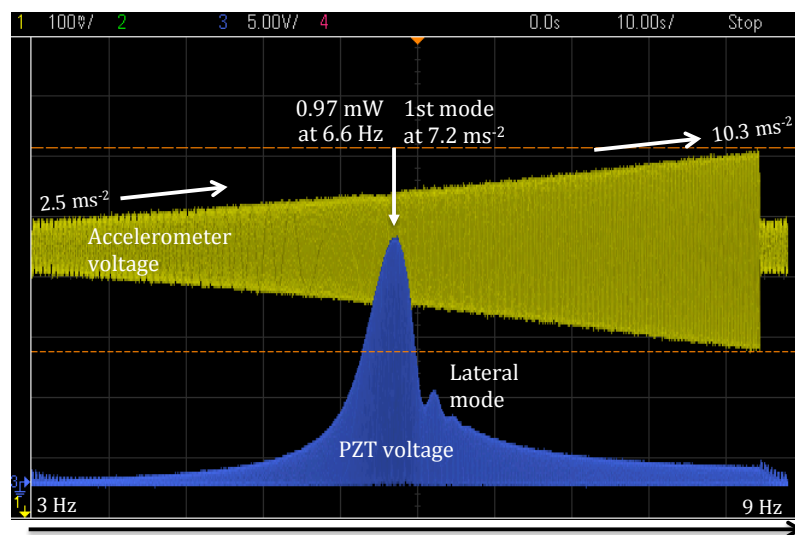
(b) 0.97 mW at 7.2 ms^{-2}

Figure 5.25: Oscilloscope voltage response from frequency sweep from 3 Hz to 9 Hz (around 1st mode of direct resonance ~6.6 Hz) in the time domain.
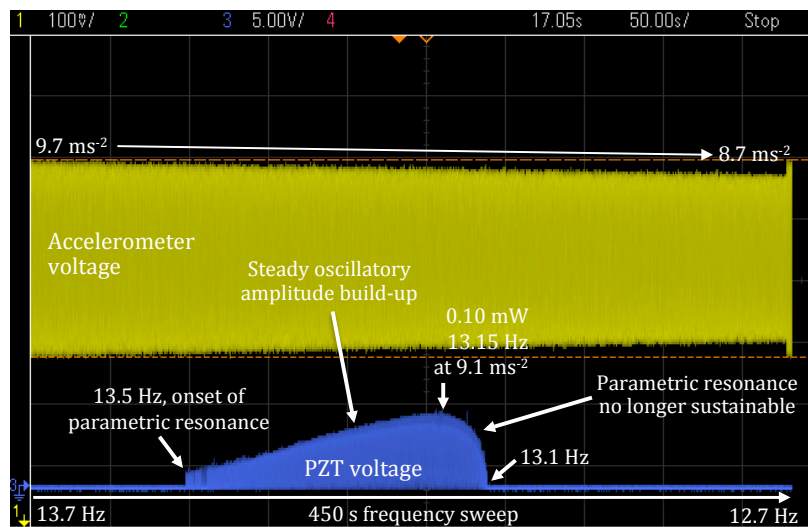
(a) Linear build-up
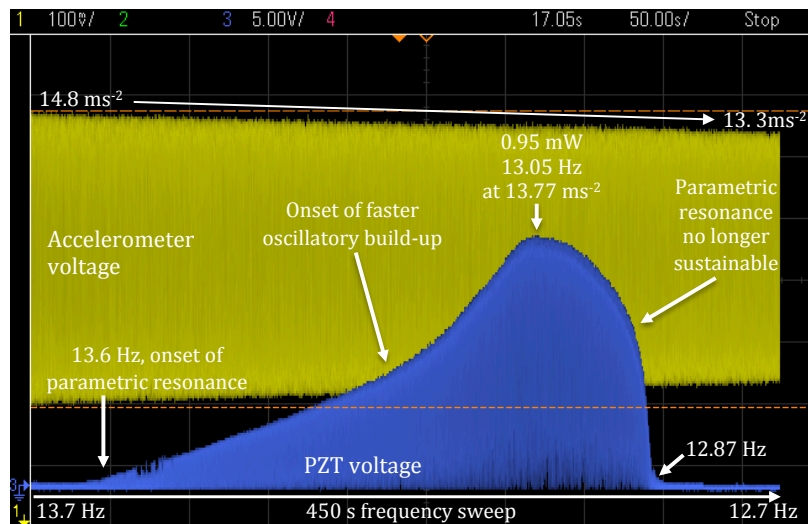
(b) Onset of steeper peak
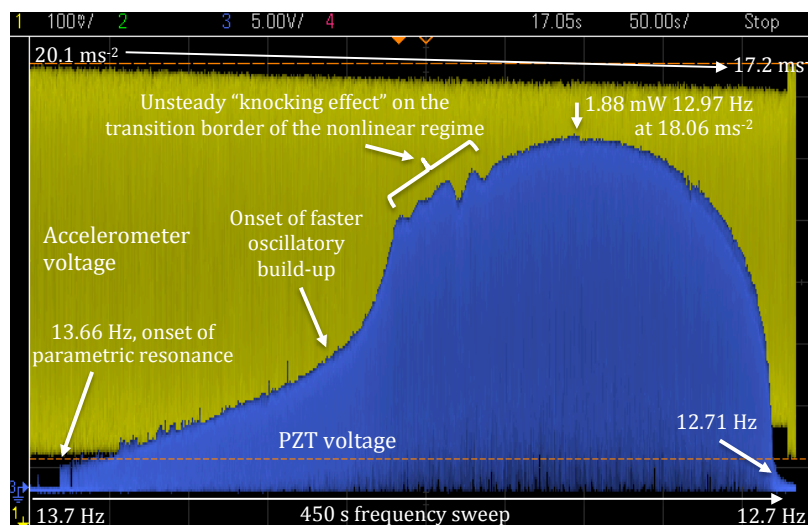
(c) Onset of unsteady state

Figure 5.26: Oscilloscope voltage response of frequency sweep from 13.7 Hz to 12.7 Hz (around principal (1st order) parametric resonance) in the time domain with varying acceleration levels.

Figure 5.26 illustrates downwards frequency sweeps around twice the natural frequency. Due to the nature of parametric resonance, a downward sweep reveals all the non-trivial bifurcation points in the nonlinear resonant regime for frequency regions below twice the eigenfrequency. A slow 450 s sweep was undertaken to accommodate the long transient build-up required for parametric resonance. Once inside the instability region, frequency shifts within this region do not need to undergo this long build-up again.

Generally, significant portions of the nonlinear power response at frequency regions below the natural frequency (right-hand side) do not show up during an upward sweep unless a significant displacement is already present. The onset of a steeper increase in response beyond a certain excitation amplitude was seen (Figure 5.26b), which was absent for lower amplitudes (Figure 5.26a). This indicates higher power efficiency as the system moves deeper into the dominance of the instability region of the Mathieu equation.

At even higher amplitudes (Figure 5.26c), a region of unsteady response can be seen prior to attaining the peak of the nonlinear region. This 'knocking effect' in the otherwise steady-state is absent on either sides of this fluctuating frequency region. Figure 5.27 is a time domain scan at a fixed frequency within this unsteady band. A repetitive pattern of local minima and maxima can be observed. A potential explanation is that this band is within a nonlinear transition region for an amplitude dependent eigenfrequency shift. For a specific fixed excitation frequency, as the eigenfrequency begins to shift away from the core of the instability region, the response amplitude drops, which in turn restores the eigenfrequency before the next cycle. An alternative physical explanation is the possible modulated energy drain to another nonlinear coupled mode that becomes significant at specific amplitude and frequency conditions
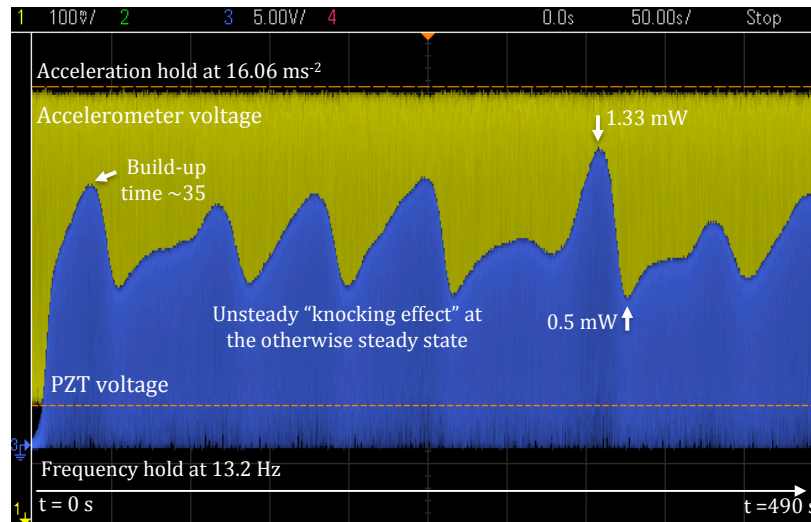
Figure 5.27: Unsteady state for certain frequencies of the parametric resonant response at high amplitudes.

Discussion

The overall efficiency of the piezoelectric transducer with the addition of initial spring worsened as the transducer is no longer positioned at the points of maximum strain. A system with electrically damped initial spring and electrically undamped parametric resonator as seismic mass can potentially serve as an alternative solution.

5.5   Summary

This chapter has explored the potential of incorporating an additional orthogonal initial spring structure parallel to the direction of the excitation in an attempt to activate the parametric resonator at a relatively lower excitation acceleration. Although appreciable reduction in the threshold have been observed in the mechanical structure, a notable loss of conversion efficiency of the active transducer mechanism, especially for macro-scale piezoelectric devices, have recorded.

The reduced conversion efficiency disadvantages the parametric resonator where a larger and steeper power gap needs to be closed in contrast to a sole direct resonator. Despite the faster growth rate of parametric resonance over direct resonance at higher excitation, this artificially disadvantaged gap has proven to be relatively restrictive to accessing the profitable parametric regions at low accelerations (1's ms^{-2}).

This loss in conversion efficiency derives from the change in strain concentration from the clamped end of the cantilever to the clamped ends of the clamped-clamped initial spring. Therefore, the electrostatic transducer in MEMS devices, which relies on free end deflection, were not affected. Comparable electromagnetic cantilever-based parametric resonators with initial springs would also be immune to this strain-related loss in efficiency.

While higher orders of instability regions of the Mathieu equation was observed for the MEMS prototypes, the macro-scale prototypes failed to unveil these higher orders. This can potentially be a result of various damping factors imposing a high initiation threshold amplitude for these higher orders or a result of a narrow frequency bandwidth in the context of the already low frequency range of the macro-scales that restricts the practical revelation of these hidden regimes.

Chapter 6

Multi-regime and multi-domain investigation

This chapter further the investigation into the potential of coupling parametric resonance with other resonant regimes and the potential of incorporating the parametric resonant phenomenon in the electrical domain with the mechanical parametric amplification effect.

6.1 Multi-regime harvester

While the potential advantages of parametric resonance for VEH have been extensively demonstrated in previous chapters, it is far from flawless. The presence of initiation threshold intrinsically dictates the presence of an operational region where direct resonance is preferably. The non-zero initial displacement criterion and prolonged build-up time also disadvantage parametric resonance. Therefore, instead of replacing direct resonance, this section explores the potential of a multiple resonant regime VEH for direct and parametric resonance to complement each other.

6.1.1 Bi-stability through axial pre-stress

Chapter 5 explored the employment of a clamped-clamped beam (CCB) initial spring to minimise the initiation threshold of the parametric resonator (PR), either by resonant (auto-parametric) or non-resonant base excitation amplification. This subsection explores the possibility of employing a third vibrational phenomenal option: snap-through motion of a bi-stable initial spring, to achieve the base excitation amplification. Introducing bi-stability, Equations 6.1 to 6.3 can be observed.

$$m\ddot{x} + c\dot{x} + \frac{\mathrm{d}U(x)}{\mathrm{d}x} = F(t) \tag{6.1}$$

$$\text{where, } U(x) = -0.5kx^2 + 0.25\mu x^4 \tag{6.2}$$

where, U is the potential energy, k is the negative spring constant and μ is the duffing coefficient.

$$\text{therefore, } m\ddot{x} + c\dot{x} - kx + \mu x^3 = F(t) \tag{6.3}$$

When $k \leq 0$, the system is mono-stable, while when $k > 0$, the system is bistable where $x = 0$ is an unstable equilibrium. When $\mu \approx 0$, cubic geometric non-linearity is negligible, $\mu < 0$ results in spring softening non-linear response and $\mu > 0$ yields spring hardening non-linear response.

Equations 6.4 and 6.5 define the local minima positions of the potential intra-wells $\pm x_s$ and the height of the potential barrier ΔU (energy required to hop across o the neighbouring stable state).

$$\pm x_s = \pm\sqrt{k/\mu} \tag{6.4}$$
$$\Delta U = k^2/4\mu \tag{6.5}$$

Figure 6.1 illustrates the introduction of bi-stability into the inverse T-shaped threshold-aided parametric resonator by applying axial pre-stress into the clamped-clamped initial spring.

(a) Axial pre-stress

(b) Bi-potential well
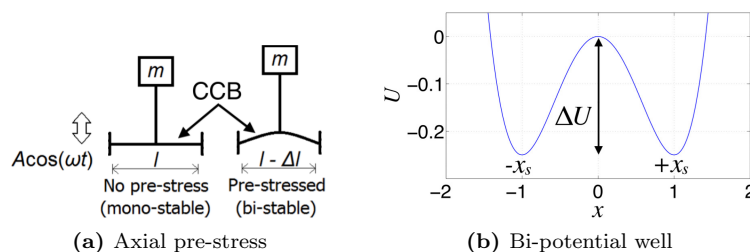
Figure 6.1: Bi-stability can be introduced through axial pre-stress of the clamped-clamped beam (CCB) initial spring of the parametric resonator.

With application of a sinusoidal periodic forcing with amplitude A as shown in Equation 6.6, the potential intra-wells modulate with time as shown in Figure 6.2. If the forcing amplitude is large enough to overcome the potential barrier, the system can hop to the neighbouring intra-well. In the physical system, this corresponds to an instantaneous energy release from the snap-through state. However, if the amplitude of the periodic forcing

$$U(x,t) = -0.5kx^2 + 0.25\mu x^4 - Ax\sin(\omega t) \tag{6.6}$$

(a) t = 0 to 0.25 T

(b) t = 0.5 to 0.75 T
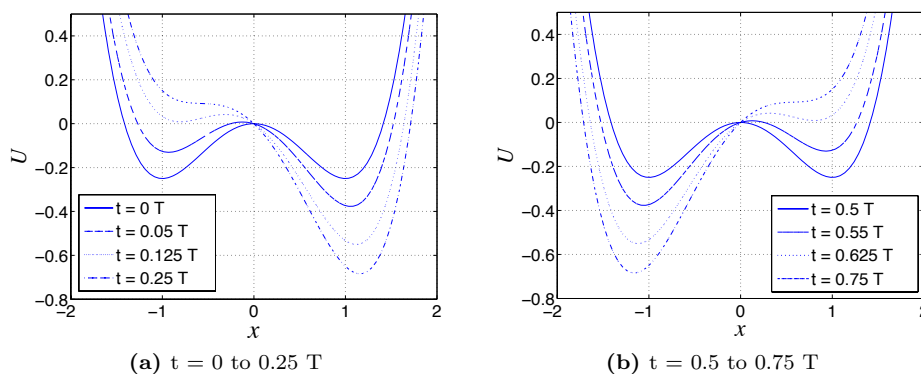
Figure 6.2: Modulation of potential well when subjected to a periodic forcing whose amplitude is just enough to match the potential well. T is the time period of the forced periodic oscillation and $k = \mu = 1$.

An example of time domain response of a bi-stable system is shown in the simulated response in

Figure 6.3. At low forcing amplitude, the system is trapped in one potential well and is incapable of crossing over. However, when the amplitude is in the vicinity of ΔU, the system can occasionally cross from stochastic effects to release the potential energy during crossing.

(a) Insufficient amplitude to cross potential barrier

(b) Barely sufficient amplitude to occasionally cross potential barrier

(c) Sufficient amplitude to always cross potential barrier
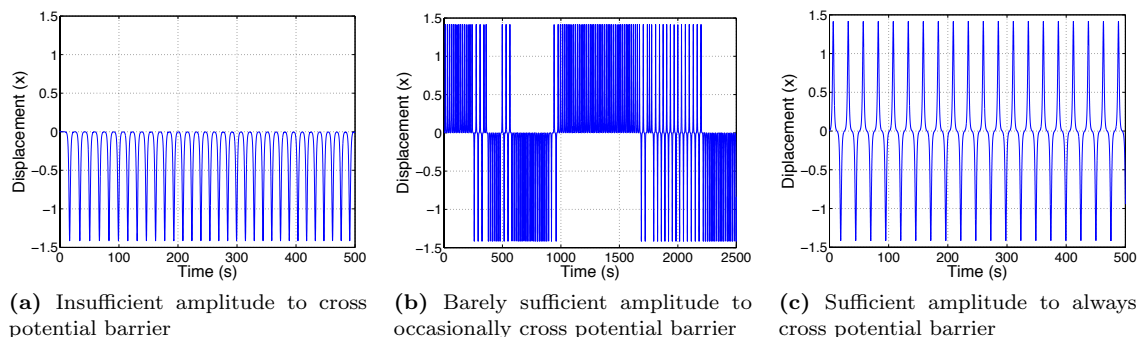
Figure 6.3: Time domain response of a bi-stable system ($k = \mu = 1$) with different forcing amplitude.

The 1st generation piezo-ceramic prototype from Subsection 5.4.1 is employed for this investigation as shown in Figure 6.4. The clamp-to-clamp gap distance is altered while maintaining the same spring length to give rise to three settings: 80 mm gap (mono-stable), 70 mm gap (mildly bi-stable) and 60 mm gap (highly bi-stable).
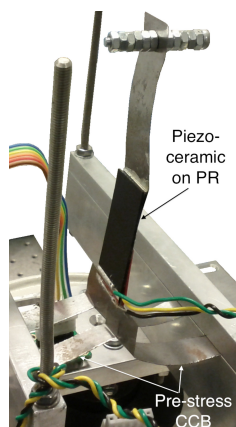
Figure 6.4: Experimental prototype of a primarily parametric resonator (PR) resting on an axial pre-stressed clamped-clamped beam (CCB) initial spring.

Figure 6.5 and Table 6.1 present the experimental results of the inverse T-shaped cantilever-based VEH subjected to various axial pre-stress settings for the initial spring. For this instance, system parameters are tuned to exhibit auto-parametric resonance.

Table 6.1: Power peaks of various fundamental modes of PR and CCB as well as principal parametric mode of PR at varying levels of bi-stability driven at $\sim$5 ms^{-2}.

Peak power (μW)	Mono-stable 80 mm gap	Mildly bi-stable 70 mm gap	Highly bi-stable 60 mm gap
PR (direct resonance)	0.70	3.20	11.8
CB (direct resonance)	1.11	0.61	0.21; 0.41
PR (parametric resonance)	18.0	53.9	92.8

As shown, with higher axial pre-stress, the 1st mode of direct resonance and 1st order of parametric resonance for the cantilever parametric resonator (PR) experienced an improvement of power
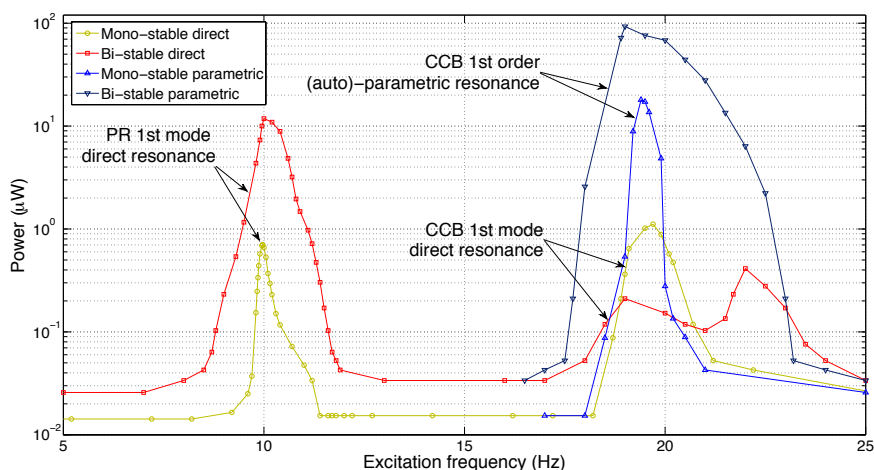
Figure 6.5: Experimental power correlation with the application of axial pre-stress on the clamped-clamped beam (CCB). PR is the subsidiary cantilever resonator that displaces orthogonal to the excitation.

efficiency. This is a result of an increasing stiffness in the initial spring with higher axial pre-stress, therefore, promoting energy propagation onto the PR. This also restricts the displacement of the clamped-clamped beam (CCB) initial spring, resulting in lower power output from the 1st mode direct resonance of CCB. At a high bi-stable state, the resonant peak of CCB decends to become twin peaks. This observation agrees with the COMSOL simulation, where a slightly off symmetry CCB appears to possess slightly different resonant frequencies associated with the different potential intra-wells.

Although once activated, the PR (operated at parametric resonance) performed substantially better with higher bi-stability, the limiting barrier of the initiation threshold required to activate it also increased as follows.

- Mono-stable: 3.60 ms^{-2}

- Mildly bi-stable: 4.05 ms^{-2}

- Highly bi-stable: 4.58 ms^{-2}

This higher initiation threshold is a result of lower base excitation amplification effect from the less flexible initial spring at higher axial pre-stress. The potential presence of snap-through states can activate large energy release in the direction of parametric excitation and help to overcome the initiation threshold, this effect is yet to be experimentally observed. This is partially due to an inadequate periodic forcing amplitude to hop through the potential barrier and partially due to the stiff tethering of the electrical wires. Additionally, although the occasionally rare up-to-down snap through state took place at a large enough impact energy, the down-to-up snap-through state was inaccessible within the physical limits due to the gravitational force.

6.1.2   Multi-regime incorporation

All resonators can potentially exhibit both direct and parametric resonance, but any system is only most responsive to a particular resonant phenomenon depending on the geometric setup and excitation criteria. Here, a resonator that displaces parallel to the forced excitation is defined as a

primarily direct resonator (DR) and a resonator configured to displace perpendicular to the driving force is a primarily parametric resonator (PR).

This subsection explores the employment of a coupled DR and PR to simultaneously access both direct and parametric resonant regimes. Figure 6.6a presents the mass-spring-damper model of such a system resting on a bi-stable initial spring where both DR and PR have very close natural frequencies. Additional side springs are added to modulate the potential barrier and promote the probability of snap-through states. Figure 6.6b is a design iteration of such a system.

(a) Mass-spring-damper model　　　　**(b)** COMSOL design iteration
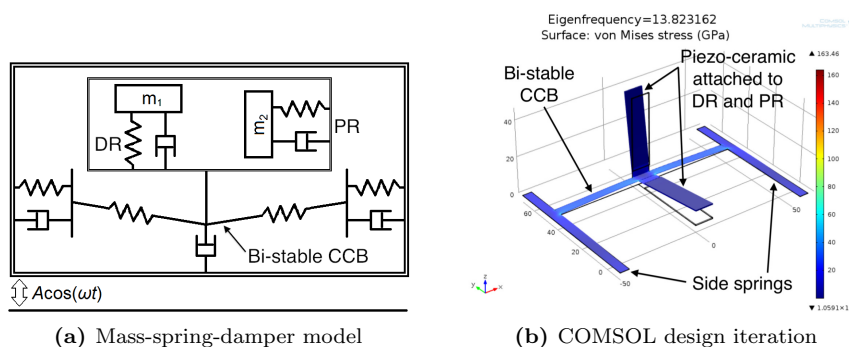
Figure 6.6: Directly and parametrically excited bi-stable system with side springs.

Side springs: to enhance stochastic excitation

As the side springs vibrate, the introduced pre-stress in the CCB varies. This helps to increase the sensitivity of the system to stochastic excitations in order to help it to cross the potential barrier even when the amplitude of the periodic forcing is barely enough such as the case in Figure 6.3b. Such a design approach can potentially enable the system to systematically hop between the two potential intra-wells with insufficient periodic forcing amplitude and the presence of white noise. Such a phenomenon where a typically insignificant excitation yields a large response over time is known as stochastic resonance and the Kramers rate (Equation 6.7) is used to describe the rate of intra-well hoping in the absence of a meaningful forcing term [240].

$$r_k = \frac{1}{\sqrt{2\pi}} \exp\left(-\frac{\Delta U}{D}\right) \tag{6.7}$$

where, r_k is the Kramers rate and D is the noise intensity. If $W(t)$ is a zero-mean Gaussian white noise, its autocorrelation function can be represented by Equation 6.8.

$$\langle W(t)W(0) \rangle = 2D\delta(t) \tag{6.8}$$

where, $\delta(t)$ is the dirac delta function with the properties defined in Equations 6.9 to 6.11.

$$\delta(t) \to \infty \; ; \quad \text{if } t = 0 \tag{6.9}$$

$$\delta(t) = 0 \; ; \quad \text{if } t \neq 0 \tag{6.10}$$

$$\int_{-\infty}^{\infty} \delta(t)\mathrm{d}t = 1 \tag{6.11}$$

The overall system takes the form of Equation 6.12 with the presence of both the periodic forcing and stochastic excitation.

$$m\ddot{x} + c\dot{x} + \frac{\mathrm{d}U(x)}{\mathrm{d}x} = F(t) + W(t) \tag{6.12}$$

Figure 6.7 illustrates a system ($k = \mu = 1$) whose periodic forcing amplitude $A = 0.01$ is barely enough to overcome ΔU (Figure 6.7a) and the alternative sole application of white noise with amplitude of its power spectral density of 5E-06 also failed to yield fruitful results (Figure 6.7b). However, with the combination of both periodic forcing and white potential, Figure 6.7c demonstrates a much improved potential barrier crossing yield.

(a) Sole periodic forcing   **(b)** Sole white noise   **(c)** Forced and stochastic excitations
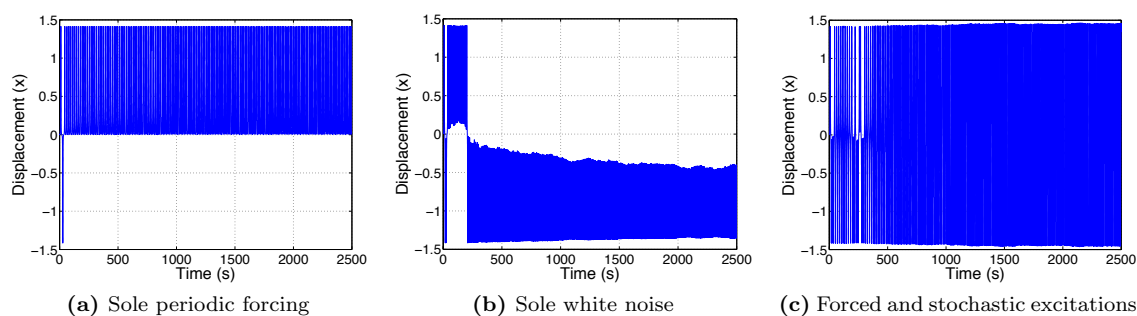
Figure 6.7: The incorporation of stochastic excitation to promote the rate of potential intra-well hopping.

Multi-frequency operation

Figure 6.8 presents the experimental prototype of the coupled DR and PR on a bi-stable CCB supported by side springs; while the driving force is applied vertically. Piezo-ceramic transducers are attached to DR and PR. Therefore, vibration in the CCB or the side springs relies on propagation towards DR and PR in order to be electrically harvested.
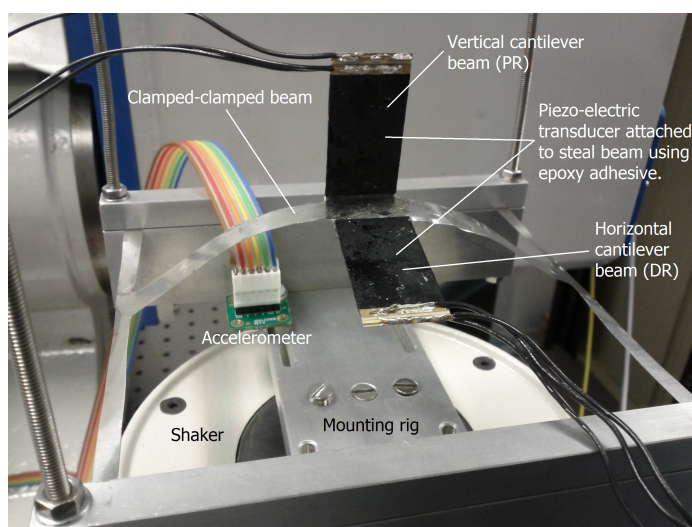
Figure 6.8: Experimental prototype of orthogonally coupled primarily direct resonator (DR) and parametric resonator (PR) resting on an axial pre-stressed loosely clamped-clamped beam (CCB) initial spring, which in turns rests on clamped-clamped side beams. The side springs aid the modulation of the potential barrier of the pre-stressed bi-stable CCB in order to promote the snap-through probability.

The power response at 3 g of acceleration is given in Figure 6.9. Due to the lack of seismic end mass for the resonators in this prototype iteration due to construction practicality, the piezoelectric strain concentration and therefore the absolute power level attainable were significantly lower than the previous prototype iteration.
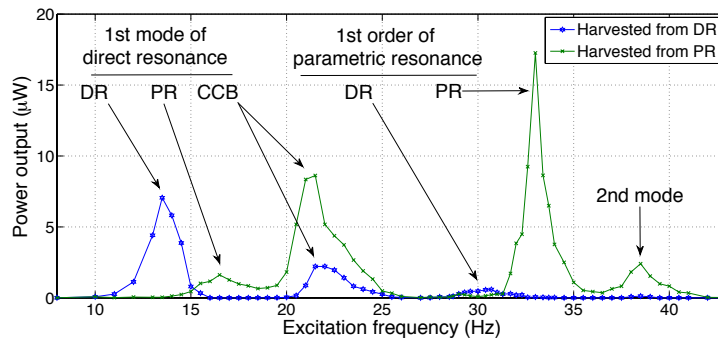
Figure 6.9: Experimentally measured power spectrum for the directly and parametrically excited VEH at 3 g of acceleration.

Direct resonant peaks for DR, PR and CCB, harvested from the piezo-ceramic transducers on DR and PR can be seen. DR fundamental mode exhibited a slight Duffing nonlinearity with spring softening effect where the resonant peak bent towards the lower frequency. The PR fundamental mode is less responsive since the excitation and response are approximately orthogonal to each other and the response was possible in the first place due to multi-axial vibration leakage (due to unintentional less-than-perfect upright mounting). The CCB response is comparable to a frequency down conversion system where the excitation of a resonator with a higher natural frequency yields a response from a subsidiary resonator with a lower natural frequency.

The first order parametric response for PR was recorded at twice the natural frequency of PR as expected. A small first order parametric resonant peak for DR can also be seen arising from the vibration leakage, but at a frequency slightly higher than twice of its fundamental mode peak; therefore confirming the nonlinear spring softening effect of its fundamental mode. Additionally, a second direct resonant mode for PR can be seen just beyond the the principal parametric resonant regime. The absolute power values for these resonant peaks are presented in Table 6.2.

Table 6.2: Power peaks of various resonant modes within between 10 and 40 Hz of the directly and parametrically excited VEH at 3 g of acceleration.

Resonant peak (harvested from)	Frequency (Hz)	Power (μW)
DR 1st mode direct (DR)	13.5	7.06
PR 1st mode direct (PR)	16.5	1.62
CCB 1st mode direct (DR)	21.5	2.21
CCB 1st mode direct (PR)	21.5	8.62
DR 1st order parametric (DR)	30.7	0.59
PR 1st order parametric (PR)	33	17.3
PR 2nd mode direct (PR)	38.5	2.41

No regular and repeatable snap-through motion was recorded for this particular setup due to the stiff tethering of the transducer wires. The simulated vibrational modes of the side springs are an order of magnitude higher than the other resonators for this prototype. Further design explorations are required to maximise the effects of the side springs described earlier.

Taking half power bands of each respective resonant peaks, an accumulated frequency bandwidth of ~10 Hz was measured between 10 Hz and 40 Hz.

6.1.3 Real vibration performance

Direct versus parametric

Unlike coupled director resonators, the coupling of direct and parametric resonators yields a fundamentally different internal energy flow. For an auto-parametric response such as Figure 6.5, where the natural frequency of an initial direct resonator and the principal parametric frequency band of the subsidiary parametric resonator fall within the same frequency vicinity, superposition of vibration as expected in coupled harmonic resonators do not take place. When operating deep into the instability region, energy from other coupled linear vibrating elements are absorbed by the dominant parametric resonator.

However, parametric resonators require a longer transient build-up time and any variations in the excitation frequency away from the desired excitation criteria would interrupt the precise onset conditions. Direct resonators on the other hand, although still possess a transient build-up time that cannot be ignored, it is usually significantly shorter than parametric resonance and is less sensitive to time-dependent frequency variations.

This shortcoming of the the parametric resonator is significantly reduced when the system already possess a relatively large initial displacement, especially a notable periodic oscillatory response at natural frequency. Since parametric resonant response is always in the vicinity of the natural frequency, such an initial oscillatory response allows the system to avert the prolonged build-up state and directly operate at a dominant state within the instability region. If a coupled direct resonator near the desired response frequency (half the parametric excitation) is activated, which allows a relatively faster energy flow towards the parametric resonator once the onset criteria are met.

Real vibration data

Figure 6.10 presents samples of vibration data in the time domain and frequency domain calculated from fast Fourier transform (FFT) measured (by the Cambridge University Geotechnical research team) from a Japanese railway bridge. Significant peaks can be seen in the vicinity of 50 Hz to 70 Hz. Vibration from the passing train lasts only for a few seconds and vibration peaks experience fast variations in frequency. Although acceleration peaks around 1's ms^{-2}, but these are only instantaneous peaks within the already short excitation.

The nature of real vibration from infrastructural systems and its bearing on direct and parametric resonant VEH are summarised as below.

- Broadband frequency
    - Direct: limited response with confined bandwidth
    - Parametric: limited response with confined bandwidth
- Fast time-varying frequency
    - Direct: limited, but forced response still exists
    - Parametric: disrupts the prolonged build-up state and response dependent on the direction of frequency change
- Relatively low amplitude
    - Direct: limited response
    - Parametric: A non-trivial task to attain initiation threshold amplitude

(a) Time domain for train at 18.1 km/h

(b) FFT for train at 18.1 km/h

(c) Time domain for train at 23.8 km/h

(d) FFT for train at 23.8 km/h

(e) Time domain for train at 26.3 km/h

(f) FFT for train at 26.3 km/h
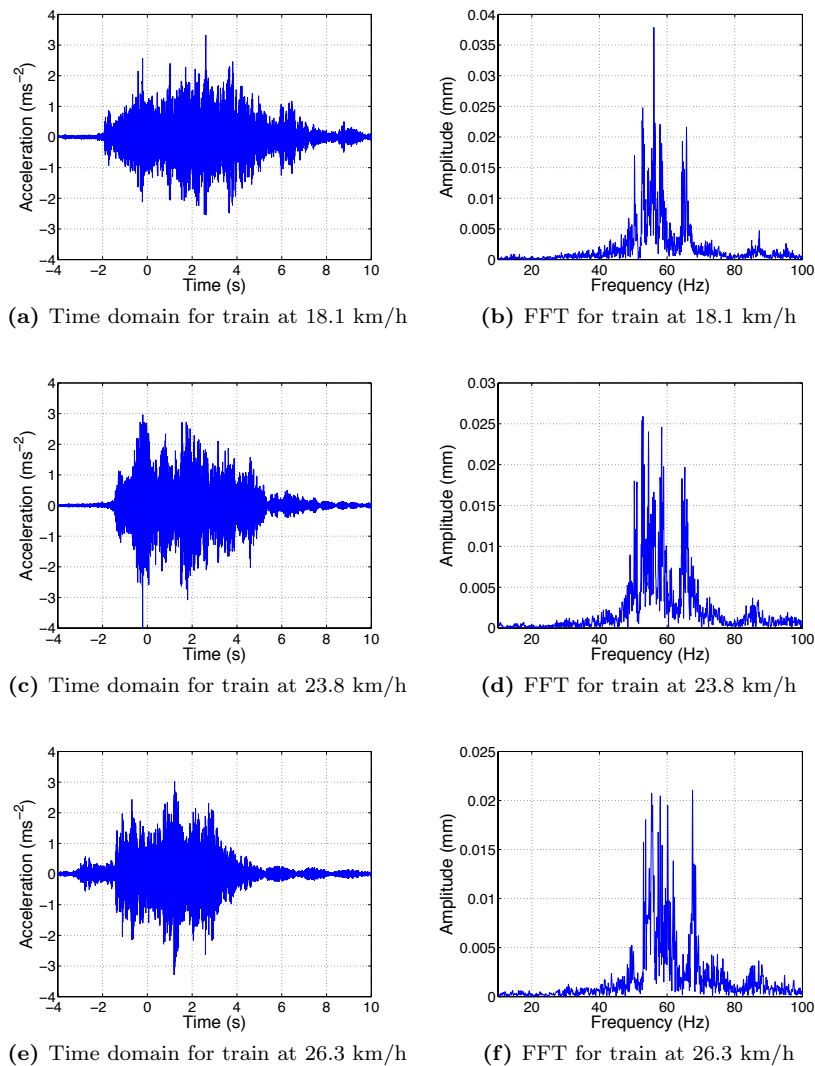
Figure 6.10: Typical samples of real vibration of a two-carriage train passing a railway bridge (measured from the main girder 1 inch away). Random vibration can be observed with several significant peaks covering a broad frequency range between ∼50 Hz and ∼70 Hz.

Numerical

Employing the numerical model developed in Chapter 4 and natural frequency tuned to match its primary response to the excitation, the simulated response of a sole direct resonating VEH and a coupled direct and parametric VEH are shown in Figure 6.11. The real vibration data in Figure 6.11a is combined from 8 different train passings with velocities ranging from 18.1 km/h to 29.2 km/h.

While a sole parametric resonator has difficulty to overcome its prolonged build-up state to attain its potentially high response, the combination of a direct resonator complements its ability to operate readily into the instability region with a faster response time. The presented model adjusts the system parameters to suit the real vibration data, but does not represent realistic system parameters. The response given in Figure 6.11b and 6.11c however, are comparable systems subjected to the same excitation.

(a) Combined real vibration data

(b) Direct resonator response

(c) Coupled direct and parametric response
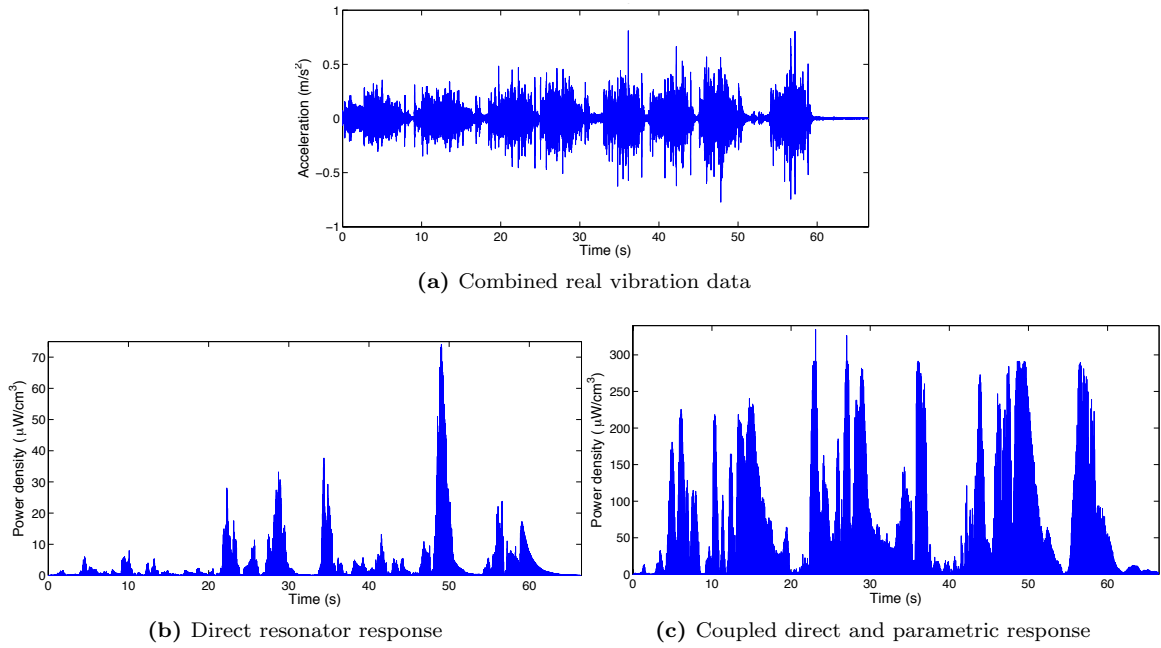
Figure 6.11: Simulated vibration response of a sole direct VEH (f_n tuned to 60 Hz) and a coupled direct and parametric VEH (f_n tuned to 30 Hz).

Experimental

Adopting the multi-regime harvester presented in Figure 6.8, the device was driven with numerically adjusted vibration data to suit its operating frequency and response amplitude. The vibration data measured from the railway bridge was numerically manipulated by a waveform editor where the excitation peaks fall in the vicinity of the direct and parametric frequencies. The amplitude was amplified 12 times for the current prototype. As discussed earlier, this prototype lacks the seismic mass due to practicality issues, which restricts its sensitivity, maximum deflection and absolute power output. The edited vibration trace is fed into the arbitrary wave function of a function generator, which in turn drives the mechanical shaker.

Figures 6.12 and 6.13 present the response from a single train passing over 20 s and multiple numerically connected train passing over 200 s. Energy harvested from DR and PR are respectively shown. Apart from the vibration of DR and PR themselves, the direct vibration of CCB is also included in the DR and PR response.

(a) Accelerometer (300 mV/g) response of adjusted vibration data

(b) DR response, 20 s average power = 5.6 μW

(c) PR response, 20 s average power = 6.0 μW
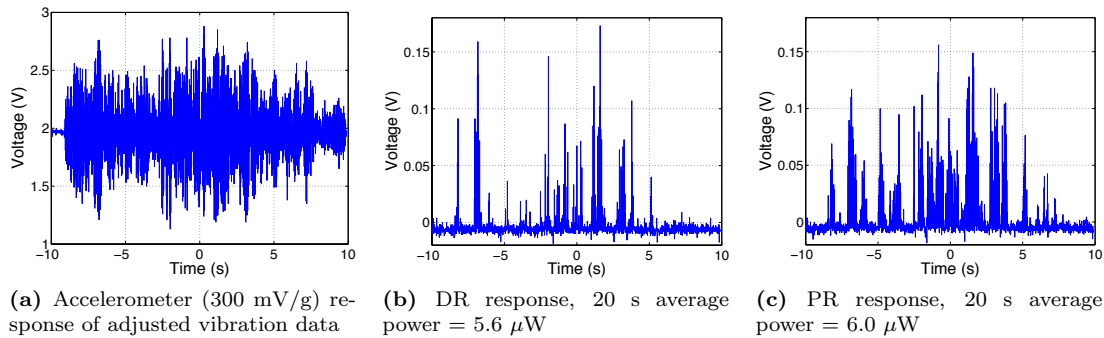
Figure 6.12: Experimentally recorded voltage response of the multi-regime VEH prototype to an adjusted vibration data of a single train passing.

(a) Accelerometer (300 mV/g) response of adjusted vibration data

(b) DR response, 200 s average power = 0.54 μW

(c) PR response, 200 s average power = 0.87 μW
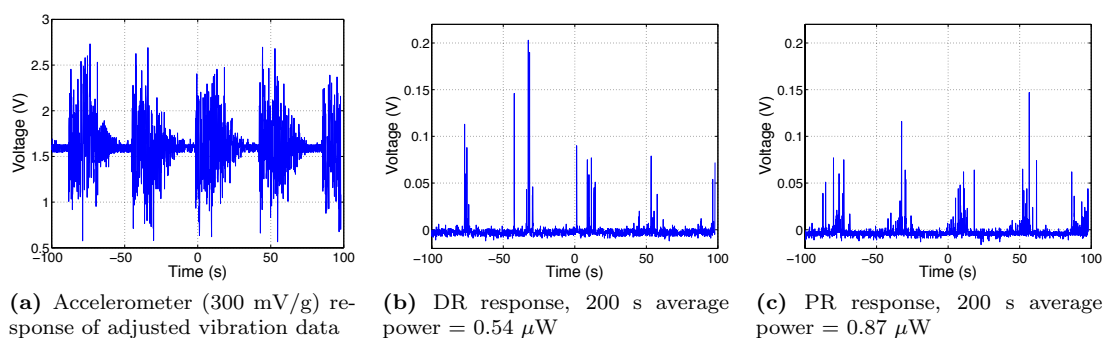
Figure 6.13: Experimentally recorded voltage response of the multi-regime VEH prototype to an adjusted vibration data of multiple train passings.

The average power, calculated from V_{rms} over the given timeframe, PR usually performs marginally better than DR. The parametric peak should outperform the direct peak in terms of absolute power as previously shown in Figure 6.9, but the response in Figures 6.12c and 6.13c failed to notably demonstrate this. Therefore, the full potential of the parametric resonant regime has yet to be activated due to the resonant build-up interruption from the fast time-varying nature of the drive vibration.

6.1.4 Discussion

While both direct and parametric resonators have their own merits and shortcomings, incorporated multiple resonant regime harvester can serve as a mutually complementing solution. While direct resonator is relatively more responsive to the fast varying broadband excitation, the multi-regime harvester incorporates the possibility of activating the high conversion efficiency associated with parametric resonance when boundary conditions become favourable.

6.2 Parametric resonance in the electrical domain

This section explores the potential of employing parametric resonance in the electrical domain to maximise conversion efficiency for VEH.

6.2.1 Introduction

The mechanical-to-electrical transducers employed by VEH such as electromagnetic, piezoelectric and electrostatic generators [9] in the mechanical domain are conventionally viewed as voltage sources, albeit usually unstable and unregulated, in the electrical domain. A power conditioning circuit is then attached to this voltage source in order to optimally capture the generated electrical charge into an electrical energy storage [28].

This section reports an alternative approach where the transducers are viewed as variable electrical elements. The capacitive nature of piezoelectric and electrostatic harvesters can act as variable capacitors, electromagnets can be variable inductors and variable resistors can derive from piezoresistive material. These transducers can be designed to generate a change in the value of their electrical parameters with response to a periodic mechanical excitation. This corresponds to a time-dependent

modulation in one or more of the homogenous system parameters in an RLC (resistor, inductor and capacitor) circuit and is described as parametric excitation [272].

When the excitation amplitude is large enough and the frequency of parameter modulation is in the vicinity of $2\omega_0/n$, parametric resonance can onset [8, 273]; where ω_0 is the natural frequency of the RLC circuit and n is a positive integer denoting the order number. This internal parameter modulation induced resonant phenomenon can potentially outperform the energy efficiency of linear direct resonance, as the resonant amplitude growth is not confined by linear damping and only saturate at high amplitude nonlinearities [219].

A seminal experimental study [256] on an electric motor driven macro-scale variable capacitor accessing the electrical principal (1st order) parametric resonance have demonstrated voltage build-up across a resistive load until the thermal destruction of the RLC circuit. Along with the superiority of parametric resonance over direct resonance in the mechanical domain as previously demonstrated in Chapters 4 and 5 the combined employment of parametric resonance in the electrical domain can further maximise the energy conversion efficiency for vibration energy harvesting.

6.2.2   Mechanical and electrical domains

Mechanical

A system model of mechanically induced variable RLC is shown in Figure 6.14. The mechanical domain can be represented by a mass-spring-damper system. Oscillatory response of this system from vibration drives periodic variation of the RLC elements.
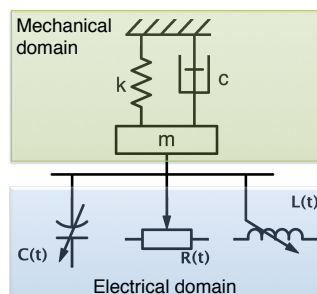
Figure 6.14: Model of vibration driven variable RLC elements, where k, c and m are stiffness, damping and mass in the mechanical domain, and $C(t)$, $R(t)$ and $L(t)$ are variable capacitance, resistance and inductance in the electrical domain respectively.

The mechanical system under direct forcing along the same plane as the oscillatory displacement is governed by Equation 6.13.

$$\frac{\mathrm{d}^2 x}{\mathrm{d}t^2} + 2\omega_0 \zeta_m \frac{\mathrm{d}x}{\mathrm{d}t} + \omega_0^2 x = \omega^2 A \cos(\omega t) \tag{6.13}$$

where, x is the oscillatory displacement, ζ_m is the mechanical damping ratio, ω_0 is the natural frequency, ω is the driving frequency, A is the driving displacement and t is the time domain. Natural frequency of the system is given by $\omega_0 = \sqrt{k/m}$. On the other hand, Equation 6.14 represents the system under parametric forcing.

$$\frac{\mathrm{d}^2 x}{\mathrm{d}t^2} + 2\omega_0 \zeta_m \frac{\mathrm{d}x}{\mathrm{d}t} + (\omega_0^2 + \omega^2 A \cos(\omega t))x = 0 \tag{6.14}$$

Electromechanical

The electrical parameter values can be calculated from the mechanical parameters of the transducers. The resistance of any electrical conductor is given by $R = \rho_0 l/S$, where, ρ_0 is the electrical resistivity of the material, l is the length of the conductor and S is the cross-sectional area. The mechanical strain induced change in resistivity of piezoresistive materials leads to a time-dependent variation: $R(t) = \rho_0(t)l/S$. The inclusion of volumetric strain and Poisson's effect would further introduce time-dependent variations in l and S.
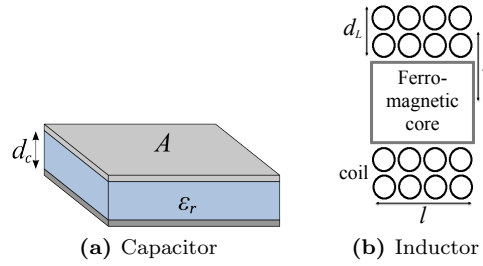
Figure 6.15: Calculating capacitance of parallel plate capacitors and inductance of ferromagnetic inductors based on their respective mechanical parameters.

For a parallel-plate capacitors (Figure 6.15a), such as that found in comb drive structures, capacitance C can be calculated by $C = \varepsilon_r \varepsilon_0 S/d_c$. Where, ε_0 is the permittivity of space (8.854E-12 Fm^{-1}), ε_r is the relative permittivity of the dielectric material between the plates, S is the plate surface area and d_c is the distance between the parallel plates. ε_r is approximately 1 in air and >1 for all media. Gap closing or gap overlapping motions lead to time-dependent variation in d and S respectively: $C(t) = \varepsilon_r \varepsilon_0 S(t)/d(t)$.

The inductance L of a ferromagnetic core inductor (Figure 6.15b,) with multi-layer and multi-row coil configuration is given by $L = 0.8(r^2 \times n^2)/(6r + 9l + 10d)$. Where, r is radius, n is number of coil turns, l is the coil thickness and d_L is the coil depth. Similar time-dependent modulations of L can take place depending on the motion of the ferromagnetic core against the coil, directly influencing the active dimensions and regions of the coil.

Electrical

The electrical domain of a series variable RLC is shown in Figure 6.16.
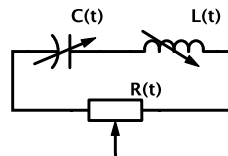
Figure 6.16: A series circuit with variable capacitor $C(t)$, inductor $L(t)$ and resistor $R(t)$.

First assuming constant values for RLC, the circuit is governed by Equations 6.15 to 6.18 according to Kirchhoff's voltage law.

$$V_L + V_R + V_C = 0 \tag{6.15}$$

where, V_L is the voltage across the inductor L, V_R is the voltage across the resistor R and V_C is the voltage across the capacitor C.

$$L\frac{\mathrm{d}i}{\mathrm{d}t} + Ri + \frac{1}{C}\int i\mathrm{d}t = 0 \tag{6.16}$$

where, i is the current through the series circuit.

$$\frac{\mathrm{d}^2i}{\mathrm{d}t^2} + \frac{R}{L}\frac{\mathrm{d}i}{\mathrm{d}t} + \frac{1}{LC}i = 0 \tag{6.17}$$

$$\frac{\mathrm{d}^2i}{\mathrm{d}t^2} + 2\omega_0\zeta_e\frac{\mathrm{d}i}{\mathrm{d}t} + \omega_0^2 i = 0 \tag{6.18}$$

where, ζ_e is the electrical damping ratio given by $\zeta_e = \frac{R}{2}\sqrt{\frac{C}{L}}$ and the electrical natural frequency of the circuit is given by $\omega_0 = (\sqrt{LC})^{-1}$. Introducing time-dependent variation to the RLC components, equations 6.19 and 6.20 can be observed.

$$L(t)\frac{\mathrm{d}i}{\mathrm{d}t} + R(t)i + \frac{1}{C(t)}\int i\mathrm{d}t = 0 \tag{6.19}$$

$$(L_1 + L_v\sin{(\omega t)})\frac{\mathrm{d}i}{\mathrm{d}t} + (R_1 + R_v\sin{(\omega t)})i + \frac{1}{C_1 + C_v\sin{(\omega t)}}\int i\mathrm{d}t = 0 \tag{6.20}$$

where, L_1, R_1 and C_1 are constant inductor, resistor and capacitor respectively, while L_v, R_v and C_v are modulation amplitudes of the variable RLC and ω is the frequency of this periodic modulation. An initial charge can be stored in L_1 and C_1 and parameter modulation can build-up further electrical charge in the circuit.

6.2.3 Numerical model

An iteration of a mechanical resonator driven variable capacitor is shown in Figure 6.17. The shaded region represent the electrical equivalent of a mechanical resonator [274, 275], such as a MEMS (micro-electro-mechanical system) capacitive comb drive, where C_g is the air gap capacitance, R_m, C_m and L_m are the motional parameters, C_1 is a capacitor with initial charge such as a supercapacitor while R_1 and L_1 are constant resistor and inductor. Voltage across C_1 can then be connected to a power conditioning circuit and an electrical load.
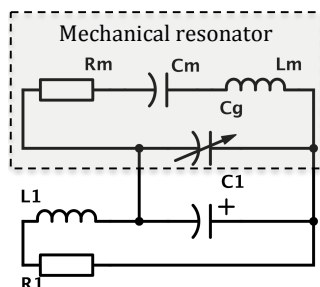
Figure 6.17: Mechanically driven variable capacitor connected with an RLC, where C_g is the variable capacitor, R_m, L_m and C_m are the motional parameters, C_1 is a partially charged capacitor whereas L_1 and R_1 are constant inductor and resistor.

Figure 6.18 presents the MATLAB numerical model built using Simscape and Simulink with a consistency tolerance of 1E-9. R_1, R_m, C_m and L_m are assumed to be negligible while a resistive load R_{load} is connected parallel to the circuit via a bridge rectifier. C_1 and L_1 are set to 0.05 F and 1 H respectively. C_g has a minimum capacitance of 0.05 F and is modulated by a sinusoidal input of $A\cos\omega t$, where A is the modulating capacitive amplitude in farads. This yields a static and undamped eigenfrequency of 0.5 Hz.
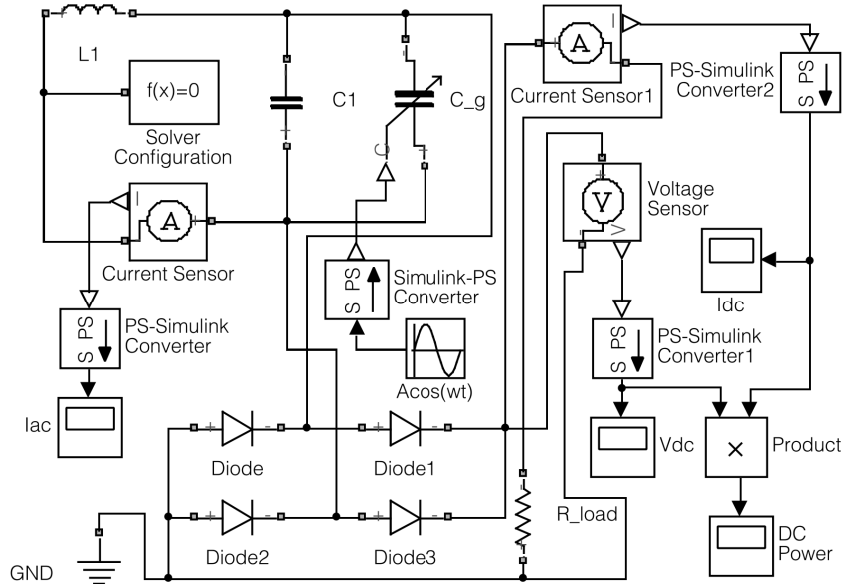
Figure 6.18: MATLAB Simscape-Simulink model of a variable capacitor C_g connected parallel to a partially charged capacitor C1, an inductor L1 and with a resistive load R_load via a bridge rectifier. DC Power measured across R_load.

Additionally, series resistance and parallel conductance for C_1, L_1 and C_g representing the parasitic effects are set to 1E-06 Ω and 1E-06 S respectively. The initial voltage across C_1 is 0.1 V and no initial current is set for L_1. The diodes used in the model have a forward voltage of 0.6 V, an on resistance of 0.3 Ω and an off conductance of 1E-06 S.
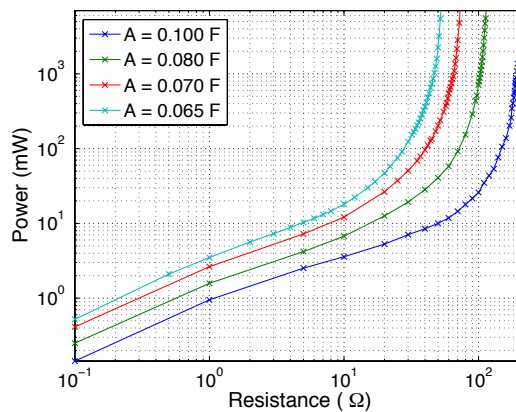
Figure 6.19: Power per load resistance. Above a certain amplitude (higher A) and below a certain damping (higher R_{load}), electrical power rapidly approaches infinity.

Figure 6.19 show the DC power output response per load resistance for varying capacitive drive amplitude A (farads) in the electrical domain. Below a certain resistance-dependent critical amplitude, the activation of parametric resonance was not observed. This is analogous to the damping-

dependent initiation threshold amplitude observed in the mechanical domain [276, 277]. Beyond this threshold, power output rapidly increases at higher capacitive variation amplitude A.

At higher load resistance values, the system approaches an open circuit configuration and corresponds to a lower damping scenario. Electrical power output can rapidly accumulate to a large and potentially undesirable value due to the system operating at a deeper and more dominant instability region. Figure 6.20 presents the frequency domain characteristics for $A = 0.07$ F and parallel $R_{load} = 100$ Ω.
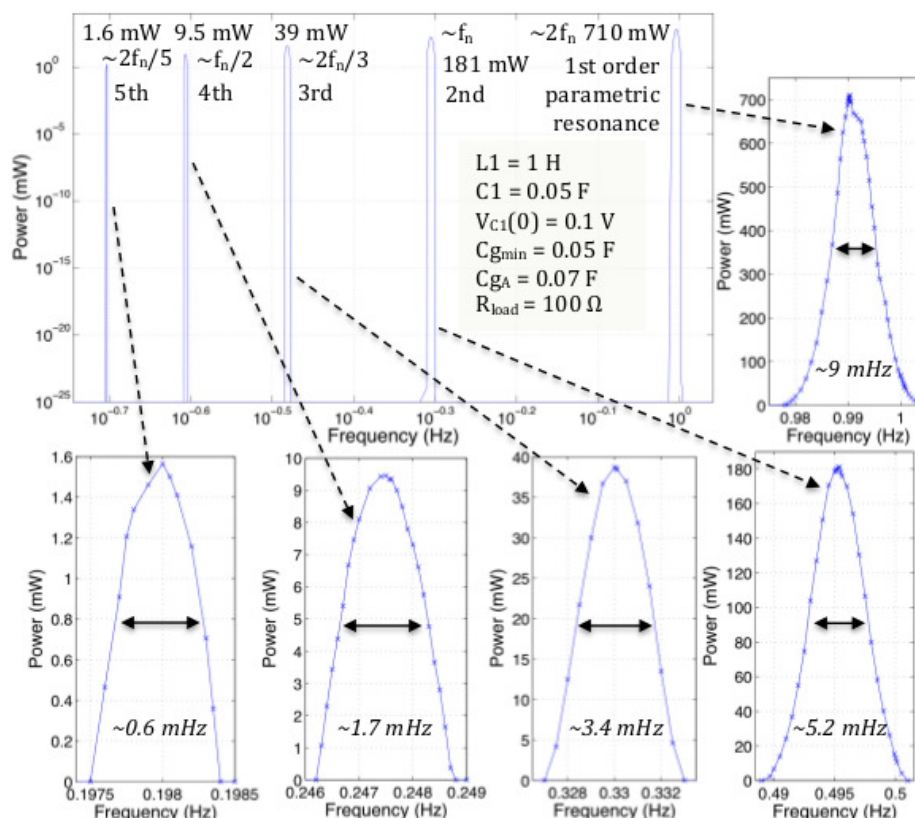
Figure 6.20: Power in the frequency domain revealing 5 orders of parametric resonance.

Within the prescribed damping, 5 orders of parametric resonance were revealed with rapidly decreasing power peak and half power bandwidths when approaching the higher instability orders. Note the logarithmic scales in the main plot. At lower damping, further higher orders of parametric resonance are theoretically possible. The response frequency of all 5 resonant orders are around the natural frequency, further confirming the parametric nature of these resonant regimes rather than forced response.

Similar frequency and resistance characteristics were observed from comparable simulations of variable inductors and variable resistors, where $L(t)$ and $R(t)$ were connected in series with constant L and R in the RLC circuit. Potentially, with matching natural frequencies for the mechanical resonator, the instability regions of parametric resonance can be activated in both the mechanical and electrical domains to maximise the conversion energy efficiency for vibration energy harvesting.

6.2.4 Summary

Conventionally, kinetic energy harvesters are viewed as voltage sources in the electrical domain, while this section assumes these transducers as variable resistors, inductors and capacitors. Mechanical resonators can drive the periodic modulation of these variable RLC elements. Upon accessing parametric resonance, potentially large electrical energy accumulation can be achieved over time as this resonant phenomenon does not saturate due to linear damping. This section has numerically demonstrated the potential of accessing these Mathieu instability regions at certain amplitude and resistance conditions. The promising results motivate further experimental investigations. Further work can involve experimental verification and incorporation with frequency matched mechanical resonators driving the variable electrical elements, which can themselves be driven into mechanical parametric resonance.

Conclusion

This thesis proposed and investigated the employment of parametric resonance as a fundamentally alternative resonant mechanism for maximising the mechanical-to-electrical conversion efficiency of vibration energy harvesters. Motivation, challenges and remedial solutions have been explored to realise and converge the two thus-far distinct interests of research in an attempt to access a large and previously untapped nonlinear region of the available power spectrum.

Despite the promising nature of parametric resonance to outperform direct resonance, it is limited by a damping-dependent initiation threshold amplitude. Two separate design routes have been investigated to minimise this activation barrier, namely: coupling an intrinsically lowly (electrically) damped parametric resonator with a secondary mechanical oscillating element from where the energy is extracted and the addition of an electrically undamped initial mechanical amplifier to magnify the input parametric excitation for a subsidiary electrically damped parametric resonator.

Various electromagnetic, piezoelectric and electrostatic devices have been realised, at both macro and MEMS scales, to explore these two design routes, alongside theoretical and numerical analysis of the various design iterations. Numerical and experimental results have generally shown an order of magnitude improvement in power output for the parametric resonator in contrast to direct linear resonator, as well as an order of magnitude lower initiation threshold amplitude for devices with the threshold-reducing designs when compared against basic parametric resonators. The absolute power results of some prototypes already compare favourably against the current state-of-the art.

Ultimately, the aim is not to replace direct resonators but to realise a multi-resonant regime VEH were various resonant and vibration phenomena, including linear, non-linear, parametric, bi-stability and stochastic, to complement each other and together exploit a wider region of the available power spectrum.

Suggestions for future work

Parametric resonant VEH prototype

While the initiation threshold-reducing mechanisms have shown promising results, further work can be done to realise the profitable regions of parametric resonance at more accessible and lower excitation amplitudes through continued design explorations and parameter optimisations. The frequency range revealed, although is typically wider than linear counterparts, is still quite confined.

A crucial research direction required to further the technological readiness level towards real site deployable prototypes involve both design and analysis to cater to the random and fast varying nature of many real world vibration profiles. While certain vibration sources such as that of industrial machinery and turbine engines are more predictable, that of civil infrastructure are more erratic. Therefore, a sole resonator, both direct and parametric, will only be able to capture a fraction of the available power spectrum.

Further work can be carried out on improving multi-regime harvesters to exploit the advantages of various resonant and vibration phenomena simultaneously. This could involve coupled linear, nonlinear and parametric resonators to employ multi-frequency ranges and internal flow of energy from the frequencies of linear resonators to that of the coupled parametric resonators. Furthermore, the incorporation of stochastic resonance into a directly and parametrically driven bi-stable VEH can potentially yield further mechanical amplification and promote sensitivity towards white-noise like vibration profiles.

Transducer design and material optimisation

While electromagnetism is already a mature technology, further design explorations, miniaturisation and parameter optimisation is still warranted to perfect the incorporation with parametric resonance for a robust and practical device in alignment with current commercial and research competitors in the field of electromagnetic VEH.

In terms of piezoelectric transducers, the incorporation of PZT in MEMS in a popular ongoing research interest within the wider VEH community and can serve as a favourable candidate to realise parametric resonance for practical applications. The possibility incorporation of other piezoelectric material with a high piezoelectric strain constant, especially unleaded options, can be of research interests.

The piezoelectric implementations explored thus far have been disadvantaged by the T-shaped cantilever implementation due to the strain concentration around the initial springs rather than the

active piezoelectric elements on the beam, despite the high attainable oscillatory amplitude within the parametric resonant regime. Therefore, alternative threshold-reducing techniques or design iterations need to be explored to tailor the requirements of piezoelectric transducers and replicate the success of its electromagnetic and electrostatic counterparts.

Electrical domain

In this work, only a preliminary theoretical and numerical analysis of integrating VEH to generate parametric resonance in the electrical domain have been explored. Further work can be done to experimentally validate the electrical version of this amplification phenomenon, driven from a vibrational source in the electrical domain. The experimental investigation would shed light into the practicality of realising the proposed system as well as providing a quantitative analysis to the profitability of employing the electrical version of parametric resonance.

Bibliography

[1] J. Kymissis, C. Kendall, J. Paradiso, and N. Gershenfeld, "Parasitic power harvesting in shoes," in *Proceedings of the 2nd IEEE International Conference on Wearable Computing (ISWC)*, Pittsburgh, Pennsylvania, 19-20 October 1998, p. 8pp.

[2] P. Glynne-Jones, "Vibration powered generators for self-powered microsystems," Ph.D. dissertation, University of Southampton, 2001.

[3] P. Glynne-Jones, S. Beeby, and N. White, "Towards a piezoelectric vibration-powered microgenerator," *IEE Science Measurement and Technology*, vol. 148, no. 2, pp. 68–72, 2001.

[4] S. Roundy, P. Wright, and K. Pister, "Micro-electrostatic vibration-to-electricity converters," in *Proceedings of IMECE*, 2002, p. 10pp.

[5] M. Muriuki, "An investigation into the design and control of tunable piezoelectric resonators," Ph.D. dissertation, School of Engineering, University of Pittsburgh, 2004.

[6] A. Frederick, "Analysis and fabrication of mems tunable piezoelectric resonators," Master's thesis, School of Engineering, University of Pittsburgh, 2006.

[7] D. Charnegie, "Frequency tuning concepts for piezoelectric cantilever beams and plates for energy harvesting," Master's thesis, School of Engineering, University of Pittsburgh, 2007.

[8] A. Nayfeh and D. Mook, *Nonlinear Oscillations*. New York: Wiley-Interscience, 1979.

[9] S. Priya and D. Inman, *Energy Harvsting Technologies*. New York: Springer US, 2009.

[10] S. Chalasani and J. Conrad, "A survey of energy harvesting sources for embedded systems," in *Proceedings of IEEE SoutheastCon*, Huntsville, Alabama, 3-6 April 2008, pp. 442–447.

[11] F. Yildiz, "Potential ambient energy-harvesting sources and techniques," *J. Technol. Studies*, vol. 35, no. 1, pp. 40–48, 2009.

[12] S.Roundy, "Energy scavenging for wireless sensor nodes with a focus on vibration to electricity conversion," Ph.D. dissertation, University of California, Berkeley, 2003.

[13] S. Roundy and P. Wright, "A piezoelectric vibration based generator for wireless electronics," *Smart Mater. Struct.*, vol. 13, no. 5, pp. 1131–1142, 2004.

[14] S. Beeby, M. Tudor, and N. White, "Energy harvesting vibration sources for microsystems applications," *Meas. Sci. Technol.*, vol. 17, no. 12, pp. R175–R195, 2006.

[15] G. Despesse, T. Jager, J. Chaillout, J. Leger, A. Vassilev, S. Basrour, and B. Chalot, "Fabrication and characterisation of high damping electrostatic micro devices for vibration energy scavenging," in *Proc. Design, Test, Integration and Packaging of MEMS and MOEMS*, 2005, pp. 386–390.

[16] S. Senturia, *Microsystem design*. Dordrecht: Kluwer Academic Publishers, 2001.

[17] S. Beeby, G. Ensell, M. Kraft, and N. White, *MEMS mechanical sensors*. Norwood: Artech House, 2004.

[18] N. Maluf and K. Williams, *An introduction to microelectromechanical systems engineering*, 2nd ed. Norwood: Artech House, 2004.

[19] C. Williams, C. Shearwood, M. Harradine, P. Mellor, T. Birch, and R. Yates, "Development of an electromagnetic micro-generator," *IEE Proceedings of Circuits Devices System*, vol. 148, no. 6, pp. 337–342, 2001.

[20] P. Mitcheson, E. Yeatman, G. Rao, A. Holmes, and T. Green, "Energy harvesting from human and machine motion for wireless electronic devices," *Proc. IEEE*, vol. 96, no. 9, pp. 1457–1486, 2008.

[21] G. Ye and K. Soga, "Energy harvesting from water distribution systems," *J. Energy Eng.*, p. 30pp., 2011, in press.

[22] E. Butikov, "Parametric resonance in a linear oscillator at square-wave modulation," *Eur. J. Phys.*, vol. 26, no. 1, pp. 157–174, 2005.

[23] D. Carr, S. Evoy, L. Sekaric, H. Craighead, and J. Parpia, "Parametric amplification in a torsional microresonator," *Appl. Phys. Lett.*, vol. 77, no. 10, pp. 1545–1547, 2000.

[24] M. Requa and K. Turner, "Electromechanically driven and sensed parametric resonance in silicon microcantilevers," *Appl. Phys. Lett.*, vol. 88, no. 26, p. 263508 (3pp), 2006.

[25] M. Thompson and D. Horsely, "Parametrically amplified mems magnetometer," in *Proc. Transducers 2009*, Denvor, CO, 21-25 June 2009, pp. 1194–1197.

[26] M. Daqaq and D. Bode, "Exploring the parametric amplification phenomenon for energy harvesting," *Proc. Inst. Mech. Eng. I J. Syst. Control Eng.*, vol. 225, no. 4, pp. 456–466, 2011.

[27] A. Erturk and D. Inman, *Piezoelectric energy harvesting.* New Delhi, India: Wiley, 2011.

[28] T. Kazmierski and S. Beeby, Eds., *Energy Harvesting Systems Principles, Modeling and Applications.* Springer US, 2011.

[29] T. Starner and J. Paradiso, *Human Generated Power for Mobile Electronics, Low Power Electronics Design*, C. Piguet, Ed. Boca Raton, Florida: CRC Press, 2004.

[30] H. Kim and S. Priya, "Piezoelectric microgenerator - current status, challenges and applications," in *Proceedings of the 17th IEEE International Symposium on the Applications of Ferroelectrics*, Santa Re, New Mexico, USA, 23-28 February 2008, pp. 1–2.

[31] C. Williams and R. Yates, "Analysis of a micro-electric generator for microsystems," *Sens. Actuators A*, vol. 52, no. 1-3, pp. 8–11, 1996.

[32] D. Arnold, "Review of microscale magnetic power generation," *IEEE Transactions on Magnetics*, vol. 43, no. 11, pp. 3940–3951, 2007.

[33] Iet archives biographies: Michael faraday. [Online]. Available: http://www.theiet.org/about/libarc/archives/biographies/faraday.cfm

[34] Smithsonian institution archives: The papers of joseph henry. [Online]. Available: http://siarchives.si.edu/history/jhp/papers01.htm

[35] C. Williams, A. Pavic, R. Crouch, and R. Woods, "Feasibility study of vibration-electric generator for bridge vibration sensors," in *16th International Modal Analysis Conference (IMAC XVI)*, Santa Barbara, CA, USA, February 1998, pp. 1111–1117.

[36] Seiko kinetic. [Online]. Available: http://www.seikowatches.com/technology/kinetic/

[37] C. Williams, R. Woods, and R. Yates, "Feasibility study of a vibration powered micro-electric generator," in *IEE Colloquium on Compact Power Sources*, London, UK, 08 May 1996, pp. 7/1–7/3.

[38] I. Sari, T. Balkan, and H. Kulah, "A micro power generator with planar coils on parylene cantilevers," in *Research in Microelectronics and Electronics*, Istanbul, 2008, pp. 133–136.

[39] H. Kulah and K. Najafi, "An electromagnetic micro power generator for low-frequency environmental vibrations," in *17th IEEE International Conference on MEMS*, Maastricht, 25-29 January 2004, pp. 237–240.

[40] I. Sari, T. Balkan, and H. Kulah, "An electromagnetic micro power generator for low-frequency environmental vibrations based on the frequency upconversion technique," *J. Microelectromech. Syst.*, vol. 19, no. 1, pp. 14–27, 2010.

[41] W. Huang, K. Tzeng, M. Cheng, and R. Huang, "Design and fabrication of a vibrational microgenerator for wearable mems," in *Proceedings of the 17th European conference on sensors and actuators (Eurosensors XVII)*, Guimaraes, Portugal, 21-24 September 2003, pp. 695–697.

[42] A. Perez-Rodriguez, C. Serre, N. Fondevilla, C. Cereceda, J. Morante, J. Esteve, and J. Montserrat, "Design of electromagnetic inertial generators of energy scavenging applications," in *Proceedings of Eurosensors XIX*, Barcelona, Spain, 11-14 September 2005, p. MC5.

[43] C. Serre, A. Perez-Rodriguez, N. Fondevilla, E. Martincic, J. Morante, and J. Montserrat, "Design and implementation of mechanical resonators for optimized inertial electromagnetic microgenerators," *Microsyst. Technol.*, vol. 14, no. 4-5, pp. 653–658, 2008.

[44] S. Scherrer, D. Plumlee, and A. Moll, "Energy scavenging device in ltcc materials," in *Proceedings of IEEE Workshop on Microelectronics and Electron Devices*, Boise, Idaho, US, 15 April 2005, pp. 77–78.

[45] P. Wang, K. Tanaka, S. Sugiyama, X. Dai, X. Zhao, and J. Liu, "A micro electromagnetic low level vibration energy harvester based on mems technology," *Microsyst. Technol.*, vol. 15, no. 6, pp. 941–951, 2009.

[46] W. Li, Z. Wen, P. Wong, G. Chan, and P. Leong, "A micromachined vibration-induced power generator for low power sensors of robotic systems," in *Proceedings of the 8th International Symposium on Robotics and Applications*, Manui, Hawaii, 11-16 June 2000, p. 7pp.

[47] N. Ching, H. Wong, W. Li, P. Leong, and Z. Wen, "A laser-micromachined multi-modal resonating power transducer for wireless sensing systems," *Sens. Actuators A*, vol. 97-98, no. 1, pp. 685–690, 2002.

[48] R. Waters, B. Chisum, H. Jazo, and M. Fralick, "Development of an electro-magnetic transducer for energy harvesting of kinetic energy and its' applicability to a mems-scale device," in *Proceedings of Nanopower Forum 2008*, Costa Mesa, California, 02-04 June 2008, pp. 359–374.

[49] Lumedyne technolgies - energy harvester. [Online]. Available: http://www.lumedynetechnologies.com/EnergyHarvester.html

[50] B. Peterson, W. Patterson, F. Herrault, D. Arnold, and M. Allen, "Laser-micromachined permanent magnet arrays with spatially alternating magnetic field distribution," in *PowerMEMS*, Atlanta, Georgia, USA, Dec. 02 - 05 2012, pp. pp. 318–321.

[51] Z. Li, M. D. Han, and H. Zhang, "A novel mems electromagnetic energy harvester with series coils," in *Transducers*, Barcelona, Spain, June 16-20 2013, pp. pp. 2245–2248.

[52] M. Mizuno and D. Chetwynd, "Investigation of a resonance microgenerator," *J. Micromech. Microeng*, vol. 13, no. 2, pp. 209–216, 2003.

[53] M. El-Hami, P. Glynne-Jones, N. White, M. Hill, S. Beeby, E. James, A. Brown, and J. Ross, "Design and fabrication of a new vibration-based electromechanical power generator," *Sens. Actuators A*, vol. 92, no. 1-3, pp. 335–342, 2001.

[54] P. Glynne-Jones, M. Tudor, S. Beeby, and N. White, "An electromagnetic, vibration powered generator for intelligent sensor systems," *Sens. Actuators A*, vol. 110, no. 1-3, pp. 344–349, 2004.

[55] R. Torah, S. Beeby, M. Tudor, T. O'Donnell, and S. Roy, "Development of a cantilever beam generator employing vibration energy harvesting," in *Proceedings of the 6th International Workshop on Micro and Nanotechnology for Power Generation and Energy Conversion Applications (PowerMEMS 2006)*, Berkeley, USA, 29 Novemeber - 1 December 2006, pp. 181–184.

[56] Perpetuum - products, pmg-17. [Online]. Available: http://www.perpetuum.com/products.asp

[57] S. Beeby, M. Tudor, E. Koukharenko, N. White, T. O'Donnell, C. Saha, S. Kulkarni, and S. Roy, "Micromachined silicon generator for harvesting power from vibrations," in *Proceedings of the 4th International Workshop on Micro and Nanotechnology for Power Generation and Energy Conversion Applications (PowerMEMS 2004)*, Kyoto, Japan, 28-30 November 2004, pp. 104–107.

[58] S. Beeby, R. Torah, M. Tudor, P. Glynne-Jones, T. O'Donnell, C. Saha, and S. Roy, "A micro electromagnetic generator for vibration energy harvesting," *J. Micromech. Microeng*, vol. 17, no. 7, pp. 1257–1265, 2007.

[59] R. Torah, P. Glynne-Jones, M. Tudor, T. O'Donnell, S. Roy, and S. Beeby, "Self-powered autonomous wireless sensor node using vibration energy harvesting," *Meas. Sci. Technol.*, vol. 19, no. 12, p. 8pp, 2008.

[60] D. Zhu, S. Beeby, M. Tudor, and N. Harris, "A planar electromagnetic vibration energy harvester with a halbach array," in *PowerMEMS*, Seoul, Korea, Nov. 15 - 18 2011, pp. pp. 347–350.

[61] ——, "Vibration energy harvesting using the halbach array," *Smart Mater. Struct.*, vol. 21, no. 7, p. 11pp, 2012.

[62] ——, "Electromagnetic vibration energy harvesting using an improved halbach array," in *PowerMEMS*, Atlanta, Georgia, USA, Dec. 02 - 05 2012, pp. pp. 251 – 254.

[63] E. Yeatman, "Rotating and gyroscopic mems energy scavenging," in *International workshop on wearable and implantable body sensor networks*, Cambridge, MA, 3-5 April 2006, pp. 45 – 48.

[64] T. Toh, P. Mitcheson, A. Holmes, and E. Yeatman, "A continuously rotating energy harvester with maximum power point tracking," *J. Micromech. Microeng*, vol. 18, no. 10, pp. 171–179, 2008.

[65] Kinetron. [Online]. Available: http://www.kinetron.nl/default.htm?loadurl=http%3A//www.kinetron.nl/cms/publish/content/showpage.asp%3Fthemeid%3D1&inframe=content

[66] A. Trimble, "A device for harvesting energy from rotational vibrations," *J. Mech. Des.*, vol. 132, no. 9, p. 6pp, 2010.

[67] B. Bowers and D. Arnold, "Spherical, rolling magnet generators for passive energy harvesting from human motion," *J. Micromech. Microeng*, vol. 19, no. 9, p. 7pp, 2009.

[68] P. Pillatsch, E. Yeatman, and A. Holmes, "Piezoelectric impulse-excited generator for low frequency non-harmonic vibrations," in *PowerMEMS*, Seoul, Korea, Nov. 15 - 18 2011, pp. pp. 245–248.

[69] S. Ju, S. Chae, Y. Choi, S. Jun, S. Park, S. Lee, H. Lee, and C. Ji, "Harvesting energy from low frequency vibration using msma/mfc laminate composite," in *Transducers*, Barcelona, Spain, June 16-20 2013, pp. pp. 1348–1351.

[70] P. Pillatsch, E. Yeatman, and A. Holmes, "A model for magnetic plucking of piezoelectric beams in energy harvesters," in *Transducers*, Barcelona, Spain, June 16-20 2013, pp. pp. 1364 – 1367.

[71] S. Ju, S. Chae, Y. Choi, S. Jun, S. Park, S. Lee, H. Lee, and C. Ji, "Low frequency vibration energy harvester using msma/pzt laminate structure and ball magnet," in *PowerMEMS*, Atlanta, Georgia, USA, Dec. 02 - 05 2012, pp. pp. 2–5.

[72] Ferro solutions veh-460. [Online]. Available: http://www.ferrosi.com/files/VEH460_May09.pdf

[73] D. Zhu, M. Tudor, and S. Beeby, "Strategies for increasing the operating frequency range of vibration energy harvesters - a review," *Meas. Sci. Technol.*, vol. 21, no. 2, p. 022001, 2010.

[74] Z. Hadas, M. Kluge, V. Singule, and C. Ondrusek, "Electromagnetic vibration power generator," in *Proceedings of IEEE Symp. Diagn. Electr. Mach. Power Electron. Drives 2007*, Cracow, 6-8 September 2007, pp. 451–455.

[75] H. Liu, L. Dhakar, and C. Lee, "Multi-frequency mems-based electromagnetic energy harvester," in *PowerMEMS*, Atlanta, Georgia, USA, Dec. 02 - 05 2012, pp. pp. 14–17.

[76] C. Shearwood and R. Yates, "Development of an electromagnetic micro-generator," *Electron. lett.*, vol. 33, no. 22, pp. 1883–1884, 1997.

[77] Q. Zhang, S. Chen, L. Baumgartel, A. Lin, and E. Kim, "Microelectromagnetic energy harvester with integrated magnets," in *Transducers*, Beijing, China, June 5-9 2011, pp. pp. 1657–1660.

[78] A. International, *Piezoelectric ceramics: principles and applications.* Pennsylvania: APC International, Ltd, 2002.

[79] M. E. Ceramics, *Piezoelectric Ceramics Data Book for Designers.* Shanghai: The Morgan Crucible Company plc, 2007.

[80] A. Erturk and D. Inman, "Issues in mathematical modeling of piezoelectric energy harvesters," *Smart Mater. Struct.*, vol. 17, no. 6, p. 14pp, 2008.

[81] J. Gonzalez, A. Rubio, and F. Moll, "Human powered piezoelectric batteries to supply power to wearable electronic devices," *Computing*, vol. 10, no. 1, pp. 1–3, 2002.

[82] H. Bardaweel, O. A. Hattamleh, R. Richards, D. Bahr, and C. Richards, "A comparison of piezoelectric material for mems power generation," in *PowerMEMS*, Berkeley, USA, Nov. 29 - Dec. 1 2006, pp. 207–210.

[83] M. Umeda, K. Nakamura, and S. Ueha, "Analysis of the transformation of mechanical impact energy to electrical energy using piezoelectric vibrator," *Japanese J. Appl. Phys.*, vol. 35, no. 5B, pp. 3267–3273, 1996.

[84] ——, "Energy storage characteristics of a piezo-generator using impact induced vibration," *Japanese J. Appl. Phys.*, vol. 36, no. 5B, pp. 3146–3151, 1997.

[85] B. Cavallier, P. Berthelot, H. Nouira, E. Foltete, L. Hirsinger, and S. Ballandras, "Energy harvesting using vibrating structures excited by shock," in *IEEE International Ultrasonics Symposium*, Rotterdam, the Netherlands, 18-21 September 2005, pp. 943–945.

[86] C. Xu, M. Akiyama, K. Nonaka, and T. Watanabe, "Electrical power generation characteristics of pzt piezoelectric ceramics," *IEEE Transactions on Ultrasonics, Ferroelectrics and Frequency Control*, vol. 45, no. 4, pp. 1065–1070, 1998.

[87] N. Shenck and J. Paradiso, "Energy scavenging with shoe-mounted piezoelectrics," *IEEE Micro*, vol. 21, no. 3, pp. 30–42, 2001.

[88] A. Erturk and D. Inman, "An experimentally validated bimorph cantilever model for piezoelectric energy harvesting from base excitations," *Smart Mater. Struct.*, vol. 18, no. 2, p. 18pp, 2008.

[89] G. Sebald, H. Kuwano, D. Guyomar, and B. Ducharne, "Experimental duffing oscillator for broadband piezoelectric energy harvesting," *Smart Mater. Struct.*, vol. 20, no. 10, p. 10pp., 2011.

[90] D. Zhu, S. Beeby, M. Tudor, and N. Narris, "A credit card sized self powered smart sensor node," *Sens. Actuators A*, p. 9pp, 2011.

[91] N. Besse, A. Quintero, D. Briand, P. Janphuang, R. Lockhart, J. Ruan, and N. de Rooij, "Pzt-based energy harvesters on plastic foil optimized through theoretical modeling and fabrication improvements," in *PowerMEMS*, Atlanta, Georgia, USA, Dec. 02 - 05 2012, pp. pp. 42–45.

[92] T. Funasaka, M. Furuhata, Y. Hashimoto, and K. Nakamura, "Piezoelectric generator using a linbo3 plate with an inverted domain," in *Proceedings of IEEE International Ultrasonics Symposium*, vol. 1, Sendai, Japan, 5-8 October 1998, pp. 959–962.

[93] R. Xu and S. Kim, "Figures of merits of piezoelectric materials in energy harvesters," in *PowerMEMS*, Atlanta, Georgia, USA, Dec. 02 - 05 2012, pp. pp. 464–467.

[94] Y. Tsujiura, E. Suwa, H. Hida, K. Suenaga, K. Shibata, and I. Kanno, "Lead-free piezoelectric mems energy harvesters of stainless steel cantilevers," in *Transducers*, Barcelona, Spain, June 16-20 2013, pp. pp. 474–477.

[95] M. Marzencki, Y. Ammar, and S. Basrour, "Design, fabrication and characterization of a piezoelectric microgenerator including a power management circuit," in *Proceedings of Dans Symposium on Design, Test, Integration and Packing of MEMS/MOEMS*, Stresa, Italy, 25-27 April 2007, p. 4pp.

[96] R. van Schaijk, R. Elfrink, T. Kamel, and M. Goedbloed, "Piezoelectric aln energy harvesters for wireless autonomous transducer solutions," in *IEEE Sensors*, Lecce, Italy, Oct 26 - 29 2008, pp. pp. 45–48.

[97] D. Shen, J. Park, J. Ajitsaria, S. Choe, H. W. III, and D. Kim, "The design, fabrication and evaluation of a mems pzt cantilever with an integrated si proof mass for vibration energy harvesting," *J. Micromech. Microeng*, vol. 18, no. 5, p. 7pp., 2008.

[98] Y. Tsujiura, K. Adachi, and I. Kanno, "Piezoelectric mems energy harvesters of pzt thin films on stainless steel cantilevers," in *PowerMEMS*, Atlanta, Georgia, USA, Dec. 02 - 05 2012, pp. pp. 500–5003.

[99] A. Hajati and S. Kim, "Ultra-wide bandwidth piezoelectric energy harvesting," *Appl. Phys. Lett.*, vol. 99, no. 8, p. 3105 (3pp), 2011.

[100] E. Aktakka, R. Peterson, and K. Najafi, "Thinned-pzt on soi process and design optimization for piezoelectric inertial energy harvesting," in *Transducers*, Beijing, China, June 5-9 2011, pp. pp. 1649–1652.

[101] S. Kok, N. White, and N. Harris, "Fabrication and characterization of free-standing thick-film piezoelectric cantilevers for energy harvesting," *Meas. Sci. Technol.*, vol. 20, no. 12, p. 13pp., 2009.

[102] A. Khaligh, P. Zeng, and C. Zheng, "Kinetic energy harvesting using piezoelectric and electromagnetic technologies—state of the art," *IEEE Trans. Ind. Electron.*, vol. 57, no. 3, pp. pp. 850 – 860, 2010.

[103] R. Elfrink, T. M. Kamel, M. Goedbloed, S. Matova, D. Hohlfeld, Y. van Andel, and R. van Schaijk, "Vibration energy harvesting with aluminum nitride-based piezoelectric devices," *J. Micromech. Microeng*, vol. 19, no. 9, p. 8pp., 2009.

[104] Q. Wang, Z. Cao, and H. Kuwano, "Vibration energy harvesters based on c-axis tilted aln thin films," in *PowerMEMS*, Atlanta, Georgia, USA, Dec. 02 - 05 2012, pp. pp. 327–330.

[105] Z. Wang, R. Elfrink, M. Renaud, R. Vullers, and R. van Schaijk, "Study of piezoelectric vibration harvester based on clamped-clamped beams under shock excitation," in *PowerMEMS*, Atlanta, Georgia, USA, Dec. 02 - 05 2012, pp. pp. 46–49.

[106] Y. Lai, W. Li, C. Lin, V. Felmetsger, and A. Pisano, "High-temperature stable piezoelectric aluminum nitride energy harvesters utlizing elastically supported diaphragms," in *Transducers*, Barcelona, Spain, June 16-20 2013, pp. pp. 2268–2271.

[107] L. Minh, M. Hara, and H. Kuwano, "Miniaturised multi-beam (k,na)nbo3-based energy harvester," in *PowerMEMS*, Atlanta, Georgia, USA, Dec. 02 - 05 2012, pp. pp. 34–37.

[108] I. Kanno, T. Mino, S. Kuwajima, and T. Suzuki, "Piezoelectric properties of (k,na)nbo3 thin films deposited on (001)srruo3/pt/mgo substrates," *IEEE Transactions on Ultrasonics, Ferroelectrics and Frequency Control*, vol. 54, no. 12, pp. pp. 2562–2556, 2007.

[109] H. Mgbemere, R. Herber, and G. Schneider, "Investigation of the dielectric and piezoelectric properties of potassium sodium niobate ceramics close to the phase boundary at (k0.35na0.65)nbo3 and partial substitutions with lithium and antimony," *J. Eur. Ceram. Soc.*, vol. 29, no. 15, pp. pp. 3273–3278, 2009.

[110] T. Yamashita, S. Takamatsu, T. Kobayashi, and T. Itoh, "Development of a fabrication process for a piezoelectric harvesting film using a reel-to-reel continuous fier process," in *Transducers*, Barcelona, Spain, June 16-20 2013, pp. pp. 1561–1564.

[111] D. Zhu, A. Almusallam, S. Beeby, M. Tudor, and N. Narris, "A bimorph multi-layer piezoelectric vibration energy harvester," in *Proceedings of the 10th International Workshop on Micro and Nanotechnology for Power Generation and Energy Conversion Applications (Power MEMS 2010)*, Leuven, Belgium, 30 November - 3 December 2010, p. 4pp.

[112] A. Elliott, D. Zhu, S. Beeby, and P. Mitcheson, "Multilayer piezoelectric energy harvesting using single supply pre-biasing for maximum power generation," in *PowerMEMS*, Atlanta, Georgia, USA, Dec. 02 - 05 2012, p. pp. 141.

[113] L. Rome, L. Flynn, E. Goldman, and T. Yoo, "Generating electricity while walking with loads," *Science*, vol. 309, no. 5741, pp. 1725–1728, 2005.

[114] J. Antaki, G. Bertocci, E. Green, A. Nadeem, T. Rintoul, R. Kormos, and B. Griffith, "A gait powered autologous battery charging system for artificial organs," *J. Am. Soc. Art. Int. Org.*, vol. 41, no. 3, pp. M588–M595, 1995.

[115] J. Feenstra, J. Granstrom, and H. Sodano, "Energy harvesting through a backpack employing a mechanically amplified piezoelectric stack," *Mech. Syst. Signal Pr.*, vol. 22, no. 3, pp. 721–734, 2008.

[116] Parasitic power shoes project. [Online]. Available: http://www.media.mit.edu/resenv/power.html

[117] K. Mossi, G. Selby, and R. Bryant, "Thin layer composite unimorph ferroelectric driver and sensor," *Materials Letters*, vol. 35, no. 1-2, pp. 39–49, 1998.

[118] A. Erturk and D. Inman, "A distributed parameter electromechanical model for cantilevered piezoelectric energy harvesters," *J. Vib. Acoust.*, vol. 130, no. 4, p. 15pp, 2008.

[119] T. Ng and W. Liao, "Sensitivity analysis and energy harvesting for a self-powered piezoelectric sensor," *J. Intel. Mat. Syst. Str.*, vol. 16, no. 10, pp. 785–797, 2005.

[120] Face international corporation. [Online]. Available: http://www.faceinternational.com/

[121] (2009) Battery free soldiers power their own equipment. [Online]. Available: http://www.epsrc.ac.uk/newsevents/news/2009/Pages/batteryfree.aspx

[122] A. Bell. Mobile energy harvesting systes. [Online]. Available: http://eh-network.org/events/dissemination2011/presentations/Andrew%20Bell.pdf

[123] M. Pozzi and M. Zhu, "Plucked piezoelectric bimorphs for knee-joint energy harvesting: modelling and experimental validation," *Smart Mater. Struct.*, vol. 20, no. 5, p. 10pp., 2011.

[124] S. Anton and H. Sodano, "A review of power harvesting using piezoelectric materials (2003-2006)," *Smart Mater. Struct.*, vol. 16, no. 3, pp. R1–R21, 2007.

[125] Y. Jeon, R. Sood, J. Jeong, and S. Kim, "Mems power generator with transverse mode thin film pzt," *Sens. Actuators A*, vol. 122, no. 1, pp. 16–22, 2005.

[126] V. Challa, M. Prasad, Y. Shi, and F. Fisher, "A vibration energy harvesting device with bidirectional resonance frequency tunability," *Smart Mater. Struct.*, vol. 17, no. 1, p. 015035 (10pp), 2008.

[127] N. White, P. Glynne-Jones, and S. Beeby, "A novel thick-film piezoelectric micro-generator," *Smart Mater. Struct.*, vol. 10, no. 4, pp. 850–852, 2001.

[128] H. Sodano, G. Park, and D. Inman, "An investigation into the performance of macro-fiber composites for sensing and structural vibration applications," *Mech. Syst. Signal Pr.*, vol. 18, no. 3, pp. 683–697, 2002.

[129] S. Kim, W. Clark, and Q. Wang, "Piezoelectric energy harvesting with a clamped circular plate: analysis," *J. Intel. Mat. Syst. Str.*, vol. 16, no. 10, pp. 847–854, 2005.

[130] ——, "Piezoelectric energy harvesting with a clamped circular plate: experimental study," *J. Intel. Mat. Syst. Str.*, vol. 16, no. 10, pp. 855–863, 2005.

[131] A. Arrieta, P. Hagedorn, A. Erturk, and D. Inman, "A piezoelectric bistable plate for nonlinear broadband energy harvesting," *Appl. Phys. Lett.*, vol. 97, no. 10, pp. pp. 104 102 – 104 102–3, 2010.

[132] N. Elvin, A. Elvin, and M. Spector, "A self-powered mechanical strain energy sensor," *Smart Mater. Struct.*, vol. 10, no. 2, pp. 293–299, 2001.

[133] H. Kim, V. Bedekar, R. Islam, W. Lee, D. Leo, and S. Priya, "Laser-machined piezoelectric cantilevers for mechanical energy harvesting," *IEEE Transactions on Ultrasonics, Ferroelectrics and Frequency Control*, vol. 55, no. 9, pp. 1900–1905, 2008.

[134] D. Borca-Tasciuc, M. Hella, and A. Kempitiya, "Micro-power generators for ambient intelligence applications," in *Proceedings of 4th International Workshop on Soft Computing Applications (SOFA)*, New York, 15-17 July 2010, pp. 19–24.

[135] S. Meninger, J. Mur-Miranda, R. Amirtharajah, A. Chandraskasa, and J. Lang, "Vibration-to-electric energy conversion," *IEEE Transactions on Very Large Scale Integration (VLSI) Systems*, vol. 9, no. 1, pp. 64–76, 2001.

[136] V. Kaajakari, *Practical MEMS: Analysis and Design of Microsystems, MEMS Sensors (accelerometers, Pressure Sensors, Gyroscopes), Sensor Electronics, Actuators, RF MEMS, Optical MEMS, and Microfluidic Systems.* Small Gear Publishing, 2009.

[137] S. Meninger, "A low power controller for a mems based energy converter," Masters thesis, Massachusetts Institute of Technology, Cambridge, Massachusetts, US, June 1999.

[138] R. Tashiro, N. Kabei, K. Katayama, Y. Ishizuka, F. Tsuboi, and K. Tsuchiya, "Development of an electrostatic generator that harnesses the motion of a living body (use of a resonant phenomenon)," *JSME International Journal, Series C: Mechanical Systems, Machine Elements and Manufacturing*, vol. 43, no. 4, pp. 916–922, 2000.

[139] M. Miyazaki, H. Tanaka, G. Ono, T. Nagano, T. Kawahara, and K. Yano, "Electric-energy generation using variable-capacitive resonator for power-free lsi: Efficiency analysis and fundamental experiment," in *International Symposium on Low Power Electronics and Design*, Seoul, 25-27 August 2003, pp. 193–198.

[140] P. Mitcheson, B. Stark, P. Miao, E. Yeatman, A. Holmes, and T. Green, "Analysis and optimisation of mems electrostatic on-chip power supply for self-powering of slow-moving sensors," in *Proceedings of the 17th European conference on sensors and actuators (Eurosensors XVII)*, Guimaraes, Portugal, 21-24 September 2003, pp. 48–51.

[141] Y. Arakawa, Y. Suzuki, and N. Kasagi, "Micro seismic power generator using electret polymer film," in *PowerMEMS*, 2004, pp. 187–190.

[142] T. Sterken, P. Fiorini, K. Baert, G. Borghs, and R. Puers, "Novel design and fabrication of a mems electrostatic vibration scavenger," in *Proceedings of the 4th International Workshop on Micro and Nanotechnology for Power Generation and Energy Conversion Applications (PowerMEMS 2004)*, Kyoto, Japan, 28-30 November 2004, pp. 18–21.

[143] W. Ma, M. Wong, and L. Ruber, "Dynamic simulation of an implemented electrostatic power microgenerator," in *Proceedings of the Symposium on Design, Test, Integration and Packaging of MEMS/MOEMS*, Montreux, Switzerland, 1-3 June 2005, pp. 380–385.

[144] R. Tashiro, N. Kabei, K. Katayama, F. Tsuboi, and K. Tsuchiya, "Development of an electrostatic generator for a cardiac pacemaker that harnesses the ventricular wall motion," *J. Artif. Organs*, vol. 5, no. 4, pp. 239–245, 2002.

[145] Y. Minakawa and Y. Suzuki, "Low-resonant-frequency mems electret energy harvester with x-shaped high-aspect ratio parylene spring," in *PowerMEMS*, Atlanta, Georgia, USA, Dec. 02 - 05 2012, pp. pp. 133–136.

[146] Y. Minakawa, R. Chen, and Y. Suzuki, "X-shaped-spring enhanced mems electret generator for energy harvesting," in *Transducers*, Barcelona, Spain, June 16-20 2013, pp. pp. 2241–2244.

[147] J. Lin, J. Zhu, Z. Feng, and M. Almasri, "Electrostatic micro power scavenger with dual cavities," in *PowerMEMS*, Atlanta, Georgia, USA, Dec. 02 - 05 2012, pp. pp. 460–463.

[148] P. Miao, P. Mitcheson, A. Holmes, E. Yeatman, T. Green, and B. Stark, "Mems inertial power generators for biomedical applications," *Microsyst. Technol.*, vol. 12, no. 10-11, pp. 1079–1083, 2006.

[149] Y. Suzuki, D. Miki, M. Edamoto, and M. Honzumi, "A mems electret generator with electrostatic levitation for vibration-driven energy-harvesting applications," *J. Micromech. Microeng*, vol. 20, no. 10, p. 8pp., 2010.

[150] T. Takahashi, M. Suzuki, T. Nishida, Y. Yoshikawa, and S. Aoyagi, "A miniature harvester of vertical vibrotory capactive type achieving several tens microwatt for broad frequency of 20-40 hz," in *Transducers*, Barcelona, Spain, June 16-20 2013, pp. pp. 1340–1343.

[151] F. Wang and O. Hansen, "Electrostatic energy harvesting device with out-of-the-plane gap closing scheme," in *Transducers*, Barcelona, Spain, June 16-20 2013, pp. pp. 2237–2240.

[152] F. Peano and T. Tambosso, "Design and optimization of a mems electret-based capacitive energy scavenger," *J. Microelectromech. Syst.*, vol. 14, no. 3, pp. 429–435, 2005.

[153] S. Boisseau, G. Despesse, T. Ricart, E. Defay, and A. Sylvestre, "Cantilever-based electre energy harvesters," *Smart Mater. Struct.*, vol. 20, no. 10, p. 11pp., 2011.

[154] S. Genter and O. Paul, "Parylene-c as an electret material for micro energy harvesting," in *PowerMEMS*, Atlanta, Georgia, USA, Dec. 02 - 05 2012, pp. pp. 129–132.

[155] M. Suzuki, H. Hayashi, A. Mori, T. Sugiyama, and G. Hashiguchi, "Electrostatic micro power generator using potassium ion electret forming on a comb-drive actuator," in *PowerMEMS*, Atlanta, Georgia, USA, Dec. 02 - 05 2012, pp. pp. 247–250.

[156] H. Hayashi, M. Suzuki, A. Mori, T. Sugiyama, and G. Hashiguchi, "Electrostatic micro transformer using potassium ion electret forming on a comb-drive actuator," in *Transducers*, Barcelona, Spain, June 16-20 2013, pp. pp. 442–445.

[157] M. Renaud, G. Altena, M. Goedbloed, C. de Nooijer, S. Matova, Y. Naito, T. Yamakawa, H. Takeuchi, K. Onishi, and R. van Schaijk, "A high performance electrostatic mems vibration energy harvester with corrugated inorganic sio2-si3n4 electret," in *Transducers*, Barcelona, Spain, June 16-20 2013, pp. pp. 693–696.

[158] H. Asanuma, H. Oguchi, M. Hara, and H. Kuwano, "A spontaneous polarization electre for electrostatic vibration energy harvesting," in *Transducers*, Barcelona, Spain, June 16-20 2013, pp. pp. 1332–1335.

[159] Y. Chiu, R. Bargayo, and H. Hong, "Stacked electret energy harvesting system fabricated with folded flexible printed circuit board," in *PowerMEMS*, Atlanta, Georgia, USA, Dec. 02 - 05 2012, pp. pp. 149–152.

[160] Y. Wada, H. Oguchi, M. Hara, H. Asanuma, and H. Kuwano, "Stacking electres for electrostatic vibration energy harvesters," in *PowerMEMS*, Atlanta, Georgia, USA, Dec. 02 - 05 2012, pp. pp. 504–507.

[161] T. Fujita, T. Onishi, K. Fujii, K. Sonoda, H. Katsuma, K. Kanda, K. Higuchi, and K. Maenaka, "Bipolar electret charging method for energy harvester," in *PowerMEMS*, Atlanta, Georgia, USA, Dec. 02 - 05 2012, pp. pp. 436–439.

[162] S. Boisseau, J. Chaillout, J. Danel, J. Legras, and G. Despesse, "Stable drie-patterend sio2/si3n4 electrets," in *Transducers*, Barcelona, Spain, June 16-20 2013, pp. pp. 1942–1945.

[163] Z. Wong, J. Yan, K. Soga, and A. Seshia, "A multi-degree-of-freedom electrostatic mems power harvester," in *PowerMEMS*, Washington, 1-4 December 2009, pp. 300–303.

[164] K. Fujii, T. Toyonaga, T. Fujita, Y. Jiang, K. Higuchi, and K. Maenaka, "Electret based energy harvester using a shared si electrode," in *Transducers*, Beijing, China, June 5-9 2011, pp. pp. 2634–2637.

[165] Y. Chu, C. Kuo, and Y. Chiu, "A mems electrostatic vibration-to-electricity energy converter," in *PowerMEMS*, Tokyo, 28-30 November 2005, pp. 49–52.

[166] R. Guillemet, P. Basset, D. Galayko, F. Marty, and T. Bourouina, "Efficient in-plane gap-closing mems electrostatic vibration energy harvester," in *PowerMEMS*, Atlanta, Georgia, USA, Dec. 02 - 05 2012, pp. pp. 137–140.

[167] L. Mateu and F. Moll, "Review of energy harvesting technologies for microelectronics," in *Proceedings of SPIE Microtechnologie for the New Millenium*, Sevilla, Spain, 09 May 2005, pp. 359–374.

[168] V. Challa, M. Prasad, and F. Fisher, "A coupled piezoelectricñelectromagnetic energy harvesting technique for achieving increased power output through damping matching," *Smart Mater. Struct.*, vol. 18, no. 9, p. 095029(11pp), 2009.

[169] A. Erturk, J. Hoffmann, and D. Inman, "A piezomagnetoelastic structure for broadband vibration energy harvesting," *Appl. Phys. Lett.*, vol. 94, no. 25, p. 3pp, 2009.

[170] J. Huang, R. O'Handley, and D. Bono, "New high-sensitivity hybrid magnetostrictive/electroactive magnetic field sensors," in *Proceedings of the Smart Structures and Materials 2003: Smart Sensor Technology and Measurement Systems*, San Diego, CA, USA, 3 March 2003, pp. 229–237.

[171] A. Bayrashev, W. Robbins, and B. Zlale, "Low frequency wireless powering of microsystems using piezoelectric-magnetostrictive laminate composites," *Sens. Actuators A*, vol. 114, no. 2-3, pp. 244–249, 2004.

[172] L. Tang, Y. Yang, and C. Soh, "Toward broadband vibration-based energy harvesting," *J. Intel. Mat. Syst. Str.*, vol. 21, no. 18, pp. pp. 1867–1897, 2010.

[173] S. Roundy and Y. Zhang, "Toward self-tuning adaptive vibration based micro-generators," *Proc. SPIE*, vol. 5649, pp. 373–384, 2005.

[174] Eh network data repository. [Online]. Available: http://eh-network.org/data/

[175] A. Weddell, D. Zhu, G. Merrett, S. Beeby, and B. Al-Hashimi, "A practical self-powered sensor system with a tunable vibration energy harvester," in *PowerMEMS*, Atlanta, Georgia, USA, Dec. 02 - 05 2012, pp. pp. 105–108.

[176] V. Challa, M. Prasad, and F. Fisher, "Towards an autonomous self-tuning vibration energy harvesting device for wireless sensor network applications," *Smart Mater. Struct.*, vol. 20, no. 2, p. 025004 (11pp), 2011.

[177] X. Wu, J. Lin, S. Kato, K. Zhang, T. Ren, and L. Liu, "A frequency adjustable vibration energy harvester," in *Proceedings of PowerMEMS 2008+ microEMS2008*, Sendai, Japan, 9-12 November 2008, pp. 245–248.

[178] J. Gieras, J. Oh, M. Huzmezan, and H. Sane, "Electromechanical energy harvesting system," Patent Publication Number: WO/2007/070022, 2007.

[179] E. Leland and P. Wright, "Resonance tuning of piezoelectric vibration energy scavenging generators using compressive axial preload," *Smart Mater. Struct.*, vol. 15, no. 5, pp. 1413–1420, 2006.

[180] I. Garcia, D. Zhu, M. Tudor, and S. Beeby, "A tunable kinetic energy harvester with dynamic over range protection," *Smart Mater. Struct.*, vol. 19, no. 11, pp. 1–10, 2010.

[181] Y. Hu, H. Xue, and H. Hu, "A piezoelectric power harvester with adjustable frequency through axial preloads," *Smart Mater. Struct.*, vol. 16, no. 5, pp. 1961–1966, 2007.

[182] C. Eichhorn, F. Goldschmidtboeing, and P. Woias, "Bidirectional frequency tuning of a piezoelectric energy converter based on a cantilever beam," *J. Micromech. Microeng*, vol. 19, no. 9, p. 094006 (6pp), 2009.

[183] D. Zhu, S. Roberts, M. Tudor, and S. Beeby, "Closed loop frequency tuning of a vibration-based micro-generator," in *PowerMEMS*, Sendai, Japan, Nov. 09 - 12 2008, pp. pp. 229–232.

[184] ——, "Design and experimental characterization of a tunable vibration-based electromagnetic micro-generator," *Sens. Actuators A*, vol. 158, no. 2, pp. pp. 284–293, 2010.

[185] P. M. A.G. Mukherjee, S. Wright, E. Yeatman, D. Zhu, and S. Beeby, "Magnetic potential well tuning of resonant cantilever energy harvester," in *PowerMEMS*, Atlanta, Georgia, USA, Dec. 02 - 05 2012, pp. pp. 480–483.

[186] C. Peters, D. Maurath, W. Schock, and Y. Manoli, "Novel electrically tunable mechanical resonator for energy harvesting," in *Proceedings of PowerMEMS 2008+ microEMS2008*, Sendai, Japan, 9-12 November 2008, pp. 253–256.

[187] C. Peters, D. Maurath, W. Schock, F. Mezger, and Y. Manoli, "A closed-loop wide-range tunable mechanical resonator for energy harvesting systems," *J. Micromech. Microeng*, vol. 19, no. 9, p. 094004 (9pp), 2009.

[188] D. Scheibner, J. Mehner, D. Reuter, T. Gessner, and W. Dotzel, "A spectral vibration detection system based on tunable micromechanical resonators," *Sens. Actuators A*, vol. 123-124, no. 23, pp. 63–72, 2005.

[189] K. Lee, L. Lin, and Y. Cho, "A closed-form approach for frequency tunable comb resonators with curved finger contour," *Sens. Actuators A*, vol. 141, no. 2, pp. 523–529, 2008.

[190] R. Syms, "Electrothermal frequency tuning of folded and coupled vibrating micromechanical resonators," *J. Microelectromech. Syst.*, vol. 7, no. 2, pp. 164–171, 1998.

[191] T. Remtema and L. Lin, "Active frequency tuning for micro resonators by localized thermal stressing effects," *Sens. Actuators A*, vol. 91, no. 3, pp. 326–332, 2001.

[192] W. Wu, Y. Chen, B. Lee, J. He, and Y. Peng, "Tunable resonant frequency power harvesting devices," in *Proceedings of the SPIE*, vol. 6169, 2006, pp. 55–62.

[193] G. Feng and J. Hung, "Optimal fom designed piezoelectric microgenerator with energy harvesting in a wide vibration bandwidth," in *Proceedings of the 2nd IEEE International Conference on Nano/Micro Engineered and Molecular Systems*, Bangkok, 16-19 January 2007, pp. 511–514.

[194] S. Shahruz, "Design of mechanical band-pass filters for energy scavenging," *J. Sound Vib.*, vol. 292, no. 3-5, pp. pp. 987–998, 2006.

[195] ——, "Design of mechanical band-pass filters with large frequency bands for energy scavenging," *Mechatronics*, vol. 16, no. 9, pp. pp. 523–531, 2006.

[196] ——, "Design of mechanical band-pass filters for energy scavenging: multi-degree-of-freedom models," *J. Vib. Control*, vol. 14, no. 5, pp. 753–768, 2008.

[197] J. Liu, H. Fang, Z. Xu, X. M. X. Shen, D. Chen, H. Liao, and B. Cai, "A mems-based piezoelectric power generator array for vibration energy harvesting," *Microelectron. J.*, vol. 39, no. 5, pp. pp. 802–806, 2008.

[198] H. Xue, Y. Hu, and Q. Wang, "Broadband piezoelectric energy harvesting devices using multiple bimorphs with different operating frequenciesple bimorphs with different operating frequencies," *IEEE Transactions on Ultrasonics, Ferroelectrics and Frequency Control*, vol. 55, no. 9, pp. 2104–2108, 2008.

[199] I. Sari, T. Balkan, and H. Kulah, "A wideband electromagnetic micro power generator for wireless microsystems," in *Transducers*, Lyon, France, 10-14 June 2007 2007, pp. 275–278.

[200] M. Ferrari, V. Ferrari, M. Guizzetti, D. Marioli, and A. Taroni, "Piezoelectric multifrequency energy converter for power harvesting in autonomous microsystems," *Sens. Actuators A*, vol. 142, no. 1, pp. 329–335, 2008.

[201] T. Petropoulos, E. Yeatman, and P. Mitcheson, "Mems coupled resonators for power generation and sensing," in *Micromechanics Europe*, Leuven, Belgium, 05-07 September 2004, pp. 261–264.

[202] A. Erturk, J. Renno, and D. Inman, "Modeling of piezoelectric energy harvesting from an l-shaped beam-mass structure with an application to uavs," *J. Intel. Mat. Syst. Str.*, vol. 20, no. 5, pp. 529–544, 2009.

[203] M. Soliman, E. Abdel-Rahman, E. El-Saadany, and R. Mansour, "A wideband vibration-based energy harvester," *J. Micromech. Microeng*, vol. 18, no. 11, p. 115021 (11pp), 2008.

[204] ——, "A design procedure for wideband micropower generators," *J. Microelectromech. Syst.*, vol. 18, no. 6, pp. pp. 1288–1299, 2009.

[205] J. Rastegar, C. Pereira, and H.-L. Nguyen, "Piezoelectric-based power sources for harvesting energy from platforms with low-frequency vibration," *Proc. SPIE*, vol. 6171, no. 617101-1-7, 2006.

[206] D. Lee, G. Carman, D. Murphy, and C. Schulenburg, "Novel micro vibration energy harvesting device using frequency up conversion," in *Transducers*, Lyon, France, 10-14 June 2007 2008, pp. pp. 871–874.

[207] M. Ferrari, F. Cerini, and V. Ferrari, "Autonomous sensor module powered by impact-ehanced energy harvester from broadband low-frequency vibrations," in *Transducers*, Barcelona, Spain, June 16-20 2013, pp. pp. 2249–2252.

[208] B. Edwards, M. Xie, K. Aw, A. Hu, and W. Gao, "An impact based frequency up-conversion mechanism for low frequency vibration energy harvesting," in *Transducers*, Barcelona, Spain, June 16-20 2013, pp. pp. 1344–1347.

[209] S. Priya, "Modelling of electric energy harvesting using piezoelectric windmill," *Appl. Phys. Lett.*, vol. 87, no. 18, p. 3pp., 2005.

[210] J. Rastegar and R. Murray, "Novel two-stage piezoelectric-based electrical energy generators for low and variable speed rotary machinery," *SPIE Proc.*, vol. 7288, pp. 72 880B–1–8, 2009.

[211] A. Wickenheiser and E. Garcia, "Broadband vibration-based energy harvesting improvement through frequency up-conversion by magnetic excitation," *Smart Mater. Struct.*, vol. 19, no. 6, p. 11pp., 2010.

[212] H. Kulah and K. Najafi, "Energy scavenging from low-frequency vibrations by using frequency up-conversion for wireless sensor applications," *IEEE Sensors J.*, vol. 8, no. 3, pp. pp. 261–268, 2008.

[213] S. Jung and K. Yun, "A wideband energy harvesting device using snap-through buckling for mechanical frequency-up conversion," in *IEEE 23rd International Conference on Micro Electro Mechanical Systems (MEMS)*, 24-28 Jan 2010, pp. 1207–1210.

[214] ——, "Energy-harvesting device with mechanical frequency-up conversion mechanism for increased power efficiency and wideband operation," *Appl. Phys. Lett.*, vol. 96, no. 11, p. 3pp., 2010.

[215] W. Bian, X. Wu, L. Bu, X. Wang, and L. Liu, "Multiple axes vibration energy harvester based on ptfe and metal balls," in *Transducers*, Barcelona, Spain, June 16-20 2013, pp. pp. 2253–2256.

[216] S. Roundy and J. Tola, "An energy harvester for rotating environments using offset pendulum dynamics," in *Transducers*, Barcelona, Spain, June 16-20 2013, pp. pp. 689–692.

[217] R. Ramlan, M. Brennan, B. Mace, and I. Kovacic, "Potential benefits of a non-linear stiffness in an energy harvesting device," *Nonlinear Dynam.*, vol. 59, no. 4, pp. pp. 545–558, 2010.

[218] N. Minorsky, *Introduction to Non-linear Mechanics.* Michigan: Edwards Brothers, 1947.

[219] ——, *Nonlinear Oscillations.* New York: Robert E. Krieger, 1974.

[220] M. Cartmell, *Introduction to linear, parametric and nonlinear vibrations.* London: Chapman and Hall, 1990.

[221] W. Thomson, *Theory of Vibration with Applications 5th Edition*, M. Dahleh, Ed. New Jersey: Prentice-Hall, Inc., 1998.

[222] S. Stanton, C. McGehee, and B. Mann, "Reversible hysteresis for broadband magnetopiezoelastic energy harvesting," *Appl. Phys. Lett.*, vol. 95, no. 17, p. 3pp., 2009.

[223] S. Burrow and L. Clare, "A resonant generator with non-linear compliance for energy harvesting in high vibrational environments," in *Proceedings of the IEEE International Electric Machines and Drives Conference*, Antalya, 3-5 May 2007, pp. 715–720.

[224] S. Burrow, L. Clare, A. Carrella, and D. Barton, "Vibration energy harvesters with non-linear compliance," *Proc. SPIE*, vol. 6928, pp. 692 807–1–10, 2008.

[225] D. Spreemann, B. Folkmer, D. Maurath, and Y. Manoli, "Tunable transducer for low frequency vibrational energy harvesting," in *Proceedings of Eurosensors XX*, Goteborg, Sweden, 17-20 September 2006, pp. 17–20.

[226] B. Mann and N. Sims, "Energy harvesting from the nonlinear oscillations of magnetic levitation," *J. Sound Vib.*, vol. 319, no. 1-2, pp. 515–530, 2009.

[227] M. Daqaq, "Response of uni-modal duffing-type harvesters to random forced excitations," *J. Sound Vib.*, vol. 329, no. 18, pp. pp. 3621–3631, 2010.

[228] B. Marinkovic and H. Koser, "Smart sand—a wide bandwidth vibration energy harvesting platform," *Appl. Phys. Lett.*, vol. 94, no. 10, p. 3pp., 2009.

[229] R. Ramlan, "Effects of non-linear stiffness on performance of an energy harvesting device," Ph.D. dissertation, Institute of Sound and Vibration Research, University of Southampton, 2009.

[230] A. Triplett and D. Quinn, "The effect of non-linear piezoelectric coupling on vibration-based energy harvesting," *J. Intel. Mat. Syst. Str.*, vol. 20, no. 16, pp. pp. 1959–1967, 2009.

[231] K. Dogheche, B. Cavallier, P. Delobelle, L. Hirsinger, E. Cattan, D. Remiens, M. Marzencki, B. Charlot, S. Basrour, and S. Ballandras, "A bi-stable micro-machined piezoelectric transducer for mechanical to electrical energy transformation," *Integrated Ferroelectrics*, vol. 80, no. 1, pp. 305–315, 2006.

[232] J. Moehils, J. Rogers, B. DeMartini, and K. Turner, "Exploiting nonlinearity to provide broadband energy harvesting," in *Proc. ASME DSCC*, Hollywood, California, USA, Oct 12 - 14 2009, p. 3pp.

[233] F. Formosa, T. Bussing, A. Badel, and S. Marteau, "Energy harvesting device with enlarged frequency bandwidth based on stochastic resonance," in *PowerMEMS*, Washington DC, USA, Dec. 1 - 4 2009, pp. pp. 229–2232.

[234] F. Cottone, H. Vocca, and L. Gammaitoni, "Nonlinear energy harvesting," *Phys. Rev. Lett.*, vol. 102, no. 8, p. 4pp., 2009.

[235] S. Stanton, C. McGehee, and B. Mann, "Nonlinear dynamics for broadband energy harvesting: Investigation of a bistable piezoelectric inertial generator," *Physica D*, vol. 239, no. 10, pp. pp. 640–653, 2010.

[236] J. Lin, B. Lee, and B. Alphenaar, "The magnetic coupling of a piezoelectric cantilever for enhanced energy harvesting efficiency," *Smart Mater. Struct.*, vol. 19, no. 4, p. 7pp., 2010.

[237] D. Zhu and S. Beeby, "A coupled bistable structure for broadband vibration energy harvesting," in *Transducers*, Barcelona, Spain, June 16-20 2013, pp. pp. 446–449.

[238] C. Trigona, F. Maiorca, B. Ando, and S. Baglio, "Tri-stable behaviour in mechanical oscillators to improve the performance of vibration energy harvesters," in *Transducers*, Barcelona, Spain, June 16-20 2013, pp. pp. 458–461.

[239] B. Ando and S. Graziani, *Stochastic Resonance.* Dordrecht, The Netherlands: Kluwer Academic Publishers, 2000.

[240] L. Gammaitoni, P. Hanggi, P. Jung, and F. Marchesoni, "Stochastic resonance," *Rev. Modern Phys.*, vol. 70, no. 1, pp. 223–287, 1998.

[241] H. Droogendijk, M. de Boer, R. Brookhuis, R. Sanders, and G. Krijnen, "Stochastic resonance in voltage-controlled mems-slider: increasing the signal-to-noise ratio with noise," in *Transducers*, Barcelona, Spain, June 16-20 2013, pp. pp. 1707–1710.

[242] C. McInnes, D. Gorman, and M. Cartmell, "Enhanced vibrational energy harvesting using nonlinear stochastic resonance," *J. Sound Vib.*, vol. 318, no. 4-5, pp. pp. 655–662, 2008.

[243] L. Gammaitoni, I. Neri, and H. Vocca, "Nonlinear oscillations for vibration energy harvesting," *Appl. Phys. Lett.*, vol. 94, no. 16, p. 3pp., 2009.

[244] L. Gammaitoni, F. Cottone, , I. Neri, and H. Vocca, "Noise harvesting," *AIP Conf. Proc.*, vol. 1129, pp. pp. 651–654, 2009.

[245] N. McLachlan, *Theory and applications of Mathieu functions.* UK: Oxford University Press, 1947.

[246] A. Tondl, T. Ruijgrok, F. Verhulst, and R. Nabergoj, *Autoparametric resonance in mechancial systems.* Cambridge, UK: Cambridge University Press, 2000.

[247] T. Fossen and H. Nijmeijer, Eds., *Parametric resonance in dynamical systems.* Springer US, 2012.

[248] S. Kelly, *Fundamentals of Mechanical Vibrations.* Singapore: McGraw-Hill Book Co., 1993.

[249] Y. Lee, "A study of parametric excitation applied to a mems tuning fork gyroscope," Ph.D. dissertation, University of Missouri, 2007.

[250] M. Faraday, "On a peculiar class of acoustical figures and on certain forms assumed by a group of particles upon vibrating elastic surfaces," *Phil. Trans.*, pp. 299–318, 1831.

[251] M. Mathieu, "Memoire sur le mouvement vibratoire d'une membrane de forme elliptique," *J. Math. Pures Appl.*, vol. 13, pp. 137–203, 1868.

[252] G. Floquet, "Sur les equations differentielles lineaires a coefficients periodiques," *Ann. Sci. Ec. Norm. Sup.*, vol. 12, pp. 47–88, 1883.

[253] G. Hill, "On the part of the motion of the lunar perigee which is a function of the mean motions of the sun and moon," *Acta Math.*, vol. 8, no. 1, pp. 1–36, 1886.

[254] J. Strutt, "On maintained vibration," *Philos. Mag.*, vol. 15, no. 94, pp. 229–235, April 1883.

[255] ——, "On the maintenance of vibrations by forces of double frequency, and on the propagation of waves through a medium endowed with a periodic structure," *Philos. Mag.*, vol. 24, no. 147, pp. 145–159, 1887.

[256] L. Mandelstam, N. Papalexi, A. Andronov, S. Chaikin, and A. Witt, "Expose des recherches recentes sur les oscillations non lineaires," *Techn. Phys. USSR*, vol. 2, no. 2-3, pp. 81–134, 1935.

[257] M. Daqaq, C. Stabler, Y. Qaroush, and T. Seuaciuc-Osorio, "Investigation of power harvesting via parametric excitations," *J. Intel. Mat. Syst. Str.*, vol. 20, no. 5, pp. 545–557, 2009.

[258] T. Ma, H. Zhang, and N. Xu, "A novel parametrically excited non-linear energy harvester," *Mech. Syst. Signal Pr.*, vol. 28, pp. 323–332, 2010.

[259] F. Elmer. (1998) Parametric resonance. [Online]. Available: http://www.elmer.unibas.ch/pendulum/parres.htm

[260] L. Mandelstam and N. Papalexi, "On the establishment of vibrations according to a resonance of the nth form," *J. Tech. Phys.*, vol. 4, pp. 67–77, 1934.

[261] M. Requa, "Parametric resonance in microcantilevers with application in mass sensing," Ph.D. dissertation, University of California, Santa Barbara, 2006.

[262] M. Ishihara, "Effects of nonlinear terms on parametric resonance in the $\lambda\phi^4$ model," *Prog. Theor. Phys.*, vol. 112, no. 3, pp. 511–532, 2004.

[263] B. DeMartini, J. Rhoads, K. Turner, S. Shaw, and J. Meohlis, "Linear and nonlinear tuning of parametrically excited mems oscillators," *J. Micromech. Microeng*, vol. 16, no. 2, pp. 310–318, 2007.

[264] L. Oropeza-Ramos and K. Turner, "Parametric resonance amplification in a memgryoscope," in *Proceedings of IEEE Sens.*, Irvine, CA, 30 October - 3 November 2005, p. 4pp.

[265] M. Sharma, E. Sarraf, and E. Cretu, "Parametric amplification/damping in mems gyroscopes," in *IEEE MEMS*, 17 March 2011, pp. 617–620.

[266] S. Arora, A. Arora, and P. George, "Design of mems based microcantilever using comsol multiphysics," *Int. J. Appl. Eng. Res.*, vol. 7, no. 11, p. 3pp., 2012.

[267] B. Donaldson, Ed., *Introduction to Structural DDynamic.* Cambridge University Press, 2006.

[268] B. Bhushan, Ed., *Springer Handbook of Nanotechnology.* Springer, 2007.

[269] M. Cartmell, "The equations of motion for a parametrically excited cantilever beam," *J. Sound Vib.*, vol. 143, no. 3, pp. 395–406, 1990.

[270] D. Levy and J. Keller, "Instability intervals of the hill's equation," *Commun. Pure Appl. Math.*, vol. 16, no. 4, pp. 469–476, 1963.

[271] K. Turner, S. Miller, P. Hartwell, N. MacDonald, S. Strogatz, and S.G.Adams, "Five parametric resoannces in a microelectromechanical system," *Nature*, vol. 396, pp. 149–152, 1988.

[272] W. Barrow, D. Smith, and F. Baumann, "A further study of oscillatory circuits having periodically varying parameters," *J. Franklin Inst.*, vol. 221, no. 3, pp. 403–416, 1936.

[273] L. Falk, "Student experiments on parametric resonance," *Am. J. Phys.*, vol. 47, no. 4, pp. 325–328, 1979.

[274] S. Kalicinski, T. Bieniek, P. Janus, and P. Grabiec, "Determination of electrical and mechanical parameters in capacitive mems accelerometers using electrical measurements," *Microelectron. Reliab.*, vol. 51, no. 7, pp. 1192–1197, 2011.

[275] Y. Sabry, M. Medhat, B. Saadany, T. Bourouina, and D. Khalil, "Parameter extraction of mems comb-drive near-resonance equivalent circuit: physically-based technique for a unique solution," *J. Micro/Nanolith. MEMS MOEMS*, vol. 11, no. 2, p. 021205 (10pp), 2012.

[276] Y. Jia, J. Yan, K. Soga, and A. Seshia, "A mems parametrically excited vibration energy harvester," in *PowerMEMS*, Atlanta, Georgia, 2-5 December 2012, pp. 215–218.

[277] ——, "A parametrically excited vibration energy harvester," *J. Intel. Mat. Syst. Str.*, vol. doi: 10.1177/1045389X13491637, 2013.

Appendix A

Design schematics

All the design schematics shown below are the original ideas and work of the author drawn in SolidWorks.

A.1   First generation electromagnetic VEH

Figure A.1 illustrates some of the unused first stage electromagnetic designs. Figure A.1a is a cantilever (anchor not shown) mounted on another spring to yield a 2 degrees of freedom system to achieve either additive or multi-frequency response [163]. Figure A.1b is an earlier design iteration of the pendulum-lever.

(a) Cantilever resting on spring

(b) Early pendulum-lever configuration
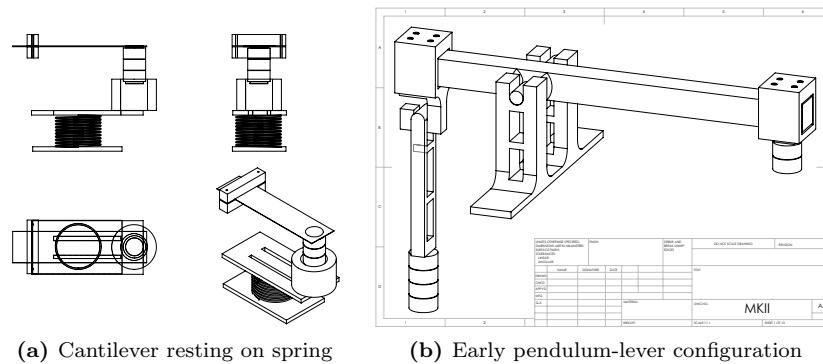
Figure A.1: Unused first stage designs.

Figures A.2 and A.3 list the macro-scale pendulum-lever VEH schematics employed in subsection 4.4.1.


(a) System overview

(b) Pivot base
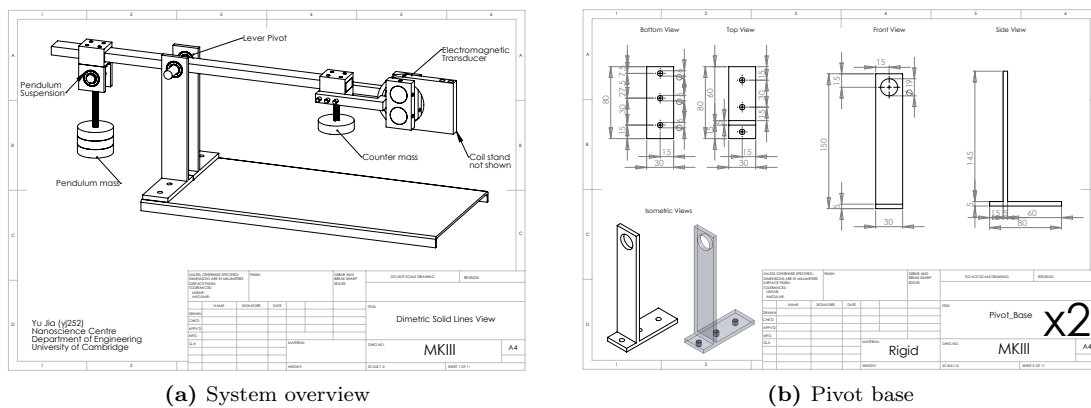
**Figure A.2:** Design schematics of the employed first generation pendulum-lever electromagnetic VEH.

I
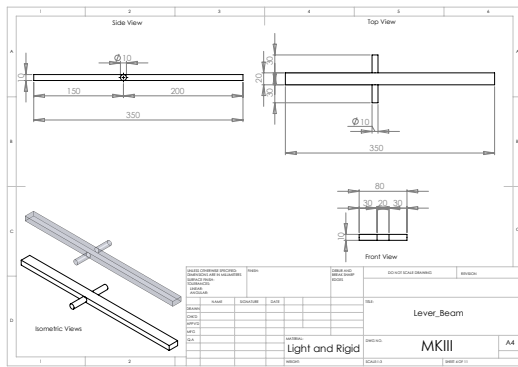
(a) Lever beam
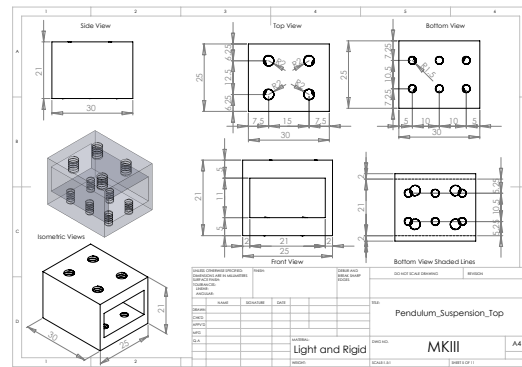
(b) Pendulum suspension lever linkage
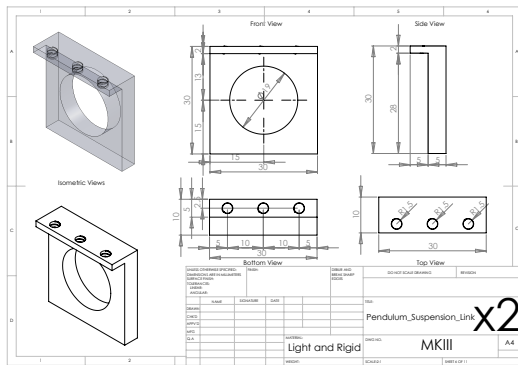
(c) Pendulum suspension bearing housing
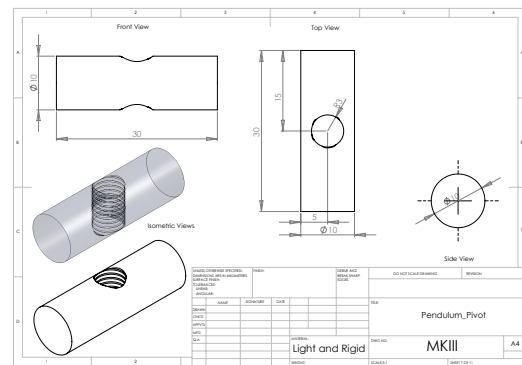
(d) Pendulum suspension bearing-pendulum linkage
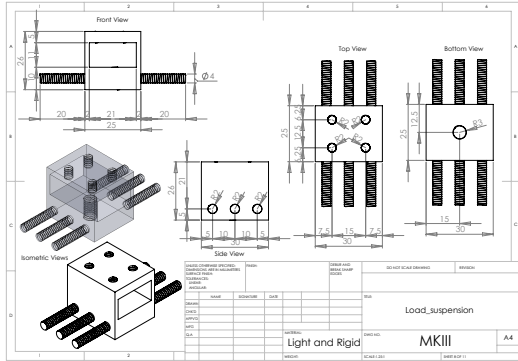
(e) Counter-weight suspension and magnet holder fixing
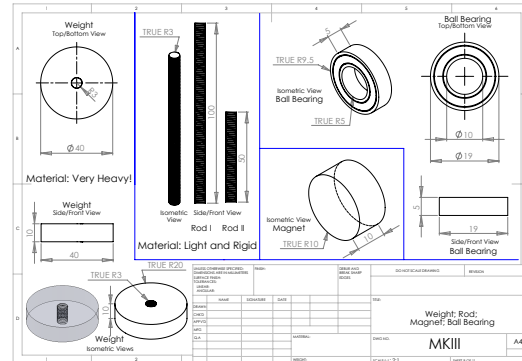
(f) Weights, threaded rods (arms of pendulum and weights), ball bearings and magnets
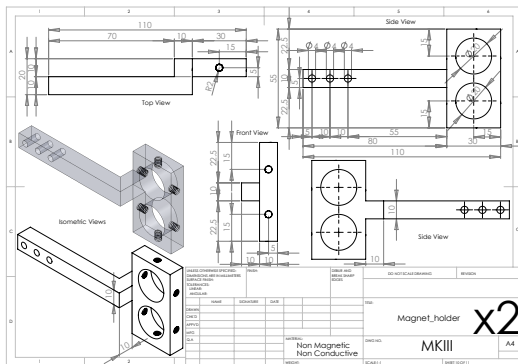

(g) Magnet holder
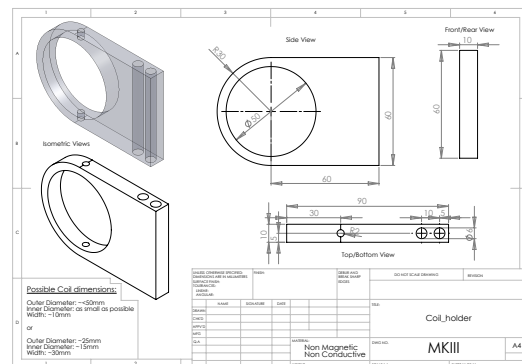
(h) Coil housing

Figure A.3: Component schematics of the employed first generation pendulum-lever electromagnetic VEH.

A.2   Second generation electromagnetic VEH: Corsair

Figure A.4 illustrates the design schematics of the prototype Corsair explored in subsection 4.4.2. While all the first generation macro-scale, Corsair and Swing prototypes shared the same coils, Corsair was the only of the three that used different dimensions of magnets. Otherwise, the transducer subsystem is of similar size and configuration between the macro-scale and the miniaturised iterations.


(a) System overview

(b) Pivot stand

(c) Lever beam

(d) Pendulum suspension housing

(e) Pivot and pendulum rod, bearing and magnetic keeper

(f) Coil, coil holder, magnet and magnetic weights
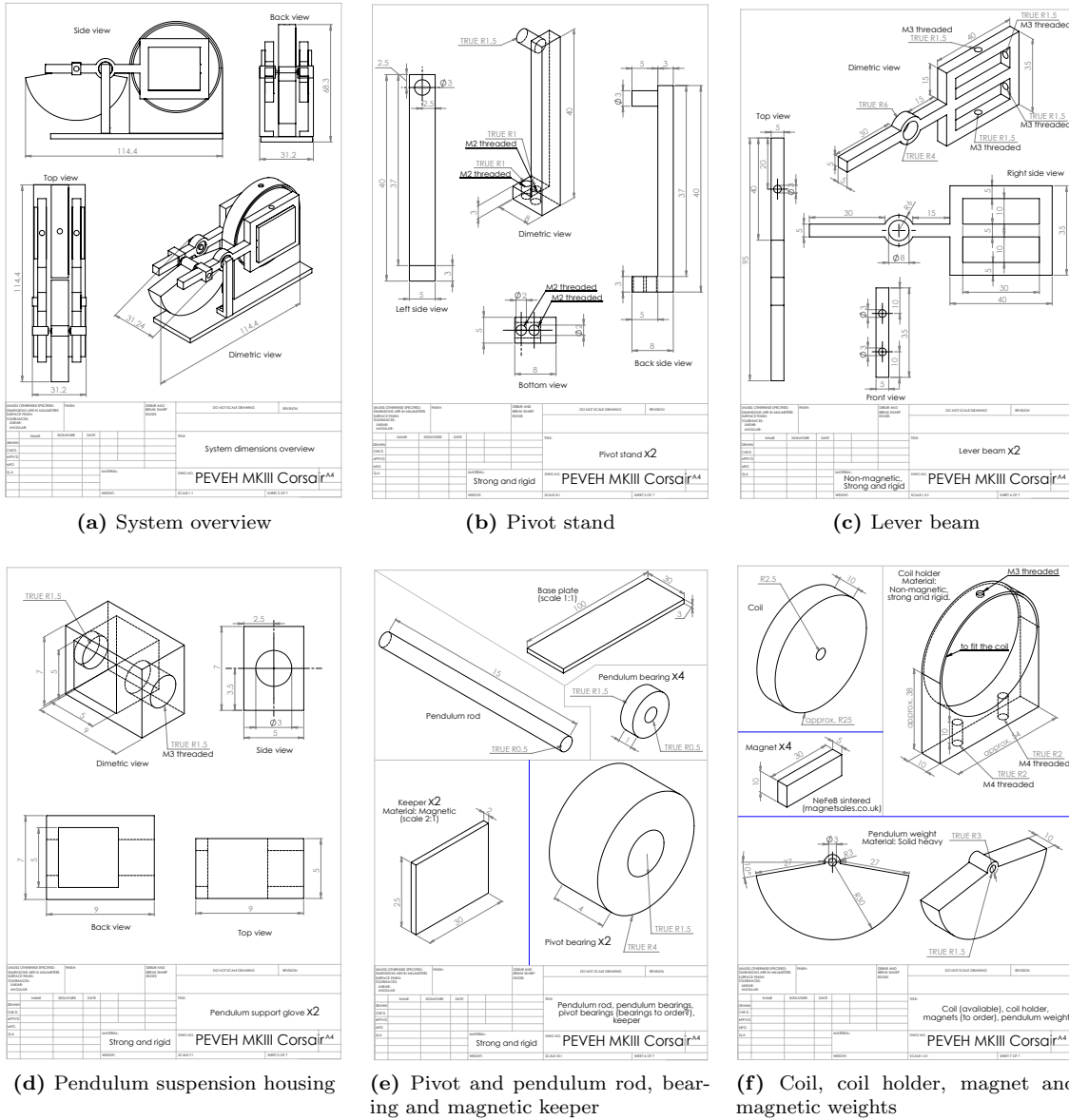
Figure A.4: Design schematics of the employed prototype: Corsair.

A.3 Second generation electromagnetic VEH: Swing

Figure A.5 illustrates the design schematics of the prototype Swing explored in subsection 4.4.2. Coil, coil holder, magnets, magnetic keepers and bearings are similar to the ones employed above.


(a) System overview

(b) Pendulum arm and magnet housing

(c) Pivot stand and pendulum suspension

Figure A.5: Design schematics of the employed prototype: Swing.

A.4 Mounting stands for cantilever-based VEH

Figure A.6 is the multi-purpose mounting stand used in Chapters 5 and MMChapter.

(a) System overview

(b) Baes plates and angled shaker mounting pieces

(c) Clamps

Figure A.6: Vertically and horizontally mounting stand for cantilever and clamped-clamped beams.

Appendix B

MEMS design and fabrication

The employed MEMS prototype realisation is the commercially available SOI-MUMPs (silicon on insulator multiple user MEMS Processes) provided by MEMSCAP. The process offers a choice of either 25 μm or 10 μm thick silicon device level. A typical multi-layer illustration of a simple cantilever structure is shown in Figure B.1.

Figure B.1: Layer outline of MEMSCAP SOIMUMPs for a simple cantilever structure.

Tanner Tools L-Edit is used to construct the MEMS design layout for the various patterned layers: doped silicon, metal pad, grounded blanket metal and trench (backside release) area. Figure B.2 illustrates an overview of the first generation and second generation MEMS VEH design layout in respect to the chip carrier. Other unrelated devices on the same chip has been photoshopped out as part of the dummy silicon.


(a) First generation MEMS VEH

(b) Second generation MEMS VEH
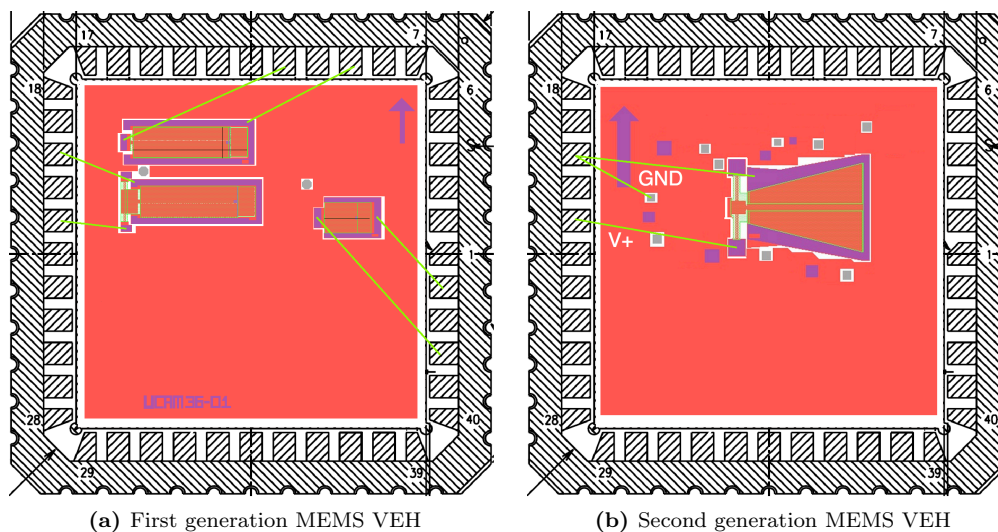
Figure B.2: Design layout and positioning on chip carrier for the MEMS VEH. Anchored electrodes are grounded while movable electrodes are treated as the DC bias and AC signal channel.

Appendix C

Vacuum packing procedure

The vacuum packing process employed is an in-house custom chip-level procedure initially devised by Dr Pradyumna Thiruvenkatanathan and colleagues within the group.

The process primarily utilises a RF probe station and a pump to create the vacuum condition for the chip while placed inside the probe station. A glass lid with solder on its perimeter edges (Figure C.1 is attached to one of the modified x-y-z staged probe heads, which is lowered onto the chip inside the vacuum condition to make physical contact seal.
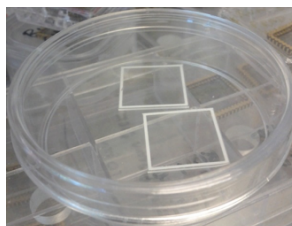

Figure C.1: Vacuum seal glass lid with white solder around its perimeter edges for solderable contact seal.

The heating element inside the chamber of the probe station is then programmed according to the specific heating cycle of the solder to make permanent seal contact. After the heating cycle is completed, the chamber is allowed to cool to room temperature before the vacuum condition inside the probe station is re-pressurised.
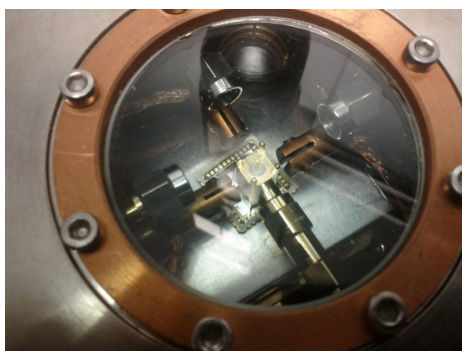

Figure C.2: Vacuum packing in progress inside the vacuum pumped RF probe station.

The quality factor of MEMS double ended tuning forks on the same chip is then used as a point of reference to estimate the pressure attained inside the seal. The estimates given in the main text are conservative estimates, which are potentially several folds to an order of magnitude higher than the actual pressure inside the vacuum seal.

The lifetime performance of the hermetic seal has not been studied and the long term leakage has not been quantified. All experiments for the vacuumed prototype were done within 2 weeks of vacuum packaging and no noticeable difference in quality factor has been observed within this time period.

Appendix D

# Piezoelectric VEH preparation

D.1   APC piezo-strip transducers

(a) Layer view (not to scale)

(b) Attaching to steel with epoxy

Figure D.1: APC Strip Transducer.

D.2   Volture piezoelectric cantilevers

(a) Horizontal mount

(b) Vertical mount


(c) Initial spring

Figure D.2: Mount for shaker and initial spring apparatus for Volture piezoelectric VEH.

Appendix E

Experimental apparatus for VEH characterisation

Figure E.1 illustrates a typical setup for characterising the frequency and power characteristics of VEH while Figure E.2 characterises the general vibration behaviour of MEMS VEH using Polytec laser vibrometer. While a macro-scale version of vibration characterisation using vibrometer is possible, the system employed have yet to be modified for macro-scale purposes.
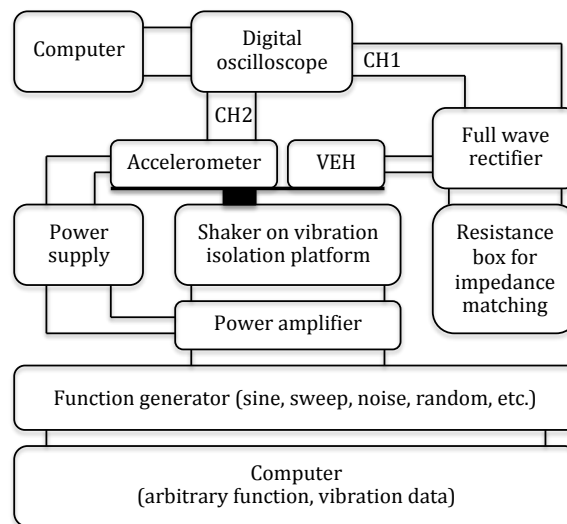

**Figure E.1:** Apparatus employed for VEH experimental characterisation.
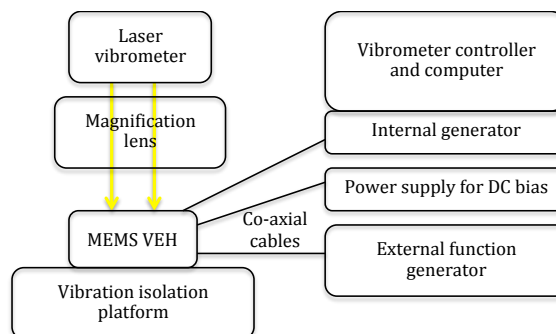
Figure E.2: Laser vibrometer setup employed for vibration characterisation.

Appendix F

Laser vibrometer noise

Although the signal measured by the vibrometer beam is already relative to the reference beam to minimise background vibration, a static noise floor with a very specific frequency characteristics was constantly observed. Multiple significant peaks can be noted (e.g. 450 Hz, 2.3 kHz, 10 kHz, etc.) as shown in Figure F.1. This specific response is always present whether the shuttle, anchor or even null regions are measured. Possible sources include electromagnetic or acoustic feedthrough, but this cannot be confirmed.
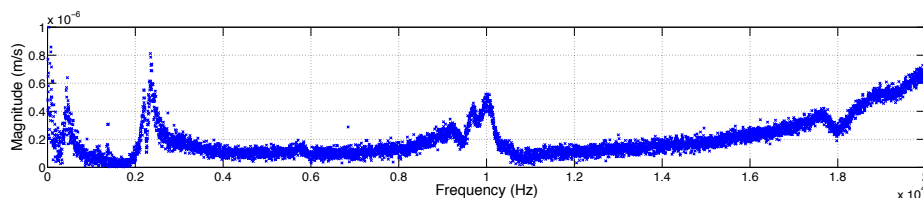

Figure F.1: Frequency response of laser vibrometer noise floor. This specific pattern is always present.

Figure F.2 compares the shuttle measurement of the 2nd generation MEMS VEH and the never-changing noise measurement, where the noise signal has falsified response of the device in multiple frequency ranges such as 2.3 kHz and 10 kHz. Due to the non-varying nature of this specific noise floor, the noise response can be simply subtracted from any vibrometer measurements. Figure F.3 shows the 'cleaned' frequency response of the MEMS VEH after subtracting the noise.
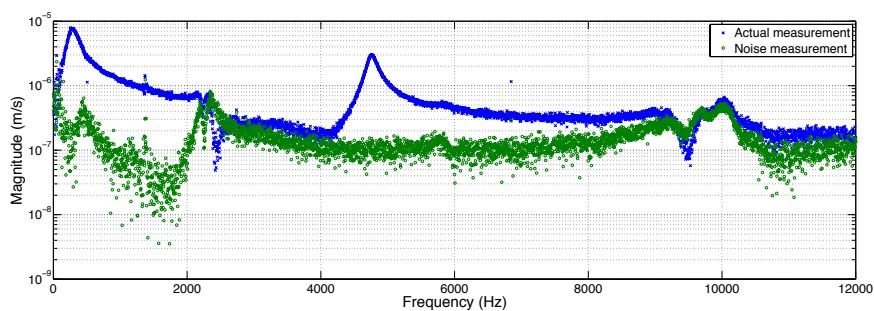

**Figure F.2:** Frequency response of actual measurement of a MEMS VEH compared to the noise signal.
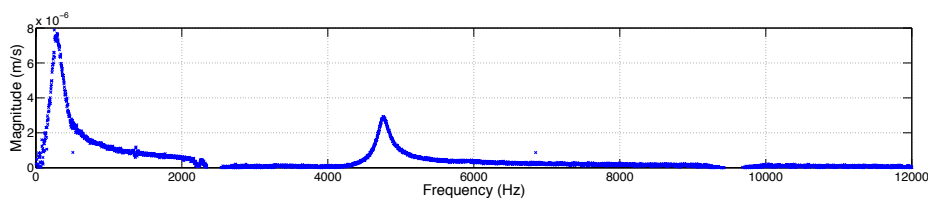
Figure F.3: Real frequency response of the MEMS VEH after subtracting he noise signal.

Appendix G

Author publication list for work related to this thesis

Peer-reviewed journal articles (published)

1. <u>Y. Jia</u>, J. Yan, K. Soga and A.A. Seshia (2013), Parametrically excited MEMS vibration energy harvesters with design approaches to overcome the initiation threshold amplitude, Journal of Micromechanics and Microengineering, Vol. 23, No. 11, 10pp. http://dx.doi.org/10.1088/0960-1317/23/11/114007 (invited article, **IOPselect**)

2. <u>Y. Jia</u>, J. Yan, K. Soga and A.A. Seshia, (2013), A parametrically excited vibration energy harvester, *Journal of Intelligent Material Systems and Structures*, 12pp., (online first 18 June 2013) http://dx.doi.org/10.1177/1045389X13491637

Journal articles (submitted for review or in preparation)

1. <u>Y. Jia</u>, J. Yan, K. Soga and A.A. Seshia (2013), Parametric resonance for vibration energy harvesting with design techniques to passively reduce the initiation threshold amplitude, 14pp. Department of Engineering, University of Cambridge, (submitted to Smart Materials and Structures, in review)

2. <u>Y. Jia</u> and A.A. Seshia (2013), Electrical domain parametric resonance for vibration energy harvesting, Nanoscience Centre, University of Cambridge, 7pp. (draft completed, yet to be submitted)

Peer-reviewed international conference proceedings (published)

1. <u>Y. Jia</u>, J. Yan, K. Soga and A.A. Seshia (2013), Multi-frequency Operation of a MEMS Vibration Energy Harvester by Accessing Five Orders of Parametric Resonance, *The 13th International Workshop on Micro and Nanotechnology for Power Generation and Energy Conversion Applications (PowerMEMS 2013)*, Royal Society, London, UK, December 3-6, Journal of Physics Vol. 476, Conference Series 1, pp. 607-611, http://dx.doi.org/10.1088/1742-6596/476/1/012126 (won Best Student Oral Presentation Award)

2. <u>Y. Jia</u> and A.A. Seshia (2013), Directly and parametrically excited bi-stable vibration energy harvester for broadband operation, *The 17th International Conference on Solid-State Sensors, Actuators and Microsystems (IEEE Transducer 2013 and Eurosensors XXVII)*, Barcelona, June 16-20, pp. 454-457, http://dx.doi.org/10.1109/Transducers.2013.6626801

3. <u>Y. Jia</u>, J. Yan, K. Soga and A.A. Seshia (2012), Parametrically excited MEMS vibration energy harvesters, *The 12th International Workshop on Micro and Nanotechnology for Power Generation and Energy Conversion Applications (PowerMEMS 2012)*, Atlanta, USA, December 2-5, pp. 215-218